UNIVERSITY OF CALIFORNIA

Santa Barbara

Saline-Alkaline Lakes of the Eocene Green River Formation and their Microbialites

A dissertation submitted in partial satisfaction of the
requirements for the degree Doctor of Philosophy
in Earth Science

by

Daniel Fontoura Cupertino

Committee in charge:

Professor Stanley M. Awramik, Chair

Professor Syee Weldeab

Professor Alexander Simms

March 2023

The dissertation of Daniel Fontoura Cupertino is approved.

Syee Weldeab

Alexander Simms

Stanley M. Awramik, Chair

March 2023

Saline-Alkaline Lakes of the Eocene Green River Formation and their Microbialites

by

Daniel Fontoura Cupertino

ACKNOWLEDGEMENTS

First, I would like to thank the postgraduate committee at Petrobras, the company I have worked for since 2006, for believing in my proposal and funding this entire process of intellectual enrichment. Another person of fundamental importance was my advisor Stan Awramik, always willing to go on a field trip in the most inhospitable places in search of good and intriguing outcrops. Without his guidance and his reviews, this PhD would not have come together. I am incredibly thankful for my "Green River mates", Mike Vanden Berg, Roberto Biaggi, Carrie Frantz, and Ken Wright for their help with data collection, guidance, scientific discussion, and companionship along the Green River outcrops. I am most grateful to the late H.P.Bucheim, whose expertise and experience in the Green River Formation greatly influenced this research. I would also like to thank Syee Weldeab and Alex Simms for serving as members on my committee. I appreciate all the scientific discussions and research directions that I received from them, and all the support they gave to me and my family as a non-traditional student (thanks to Yann Ricard, too!). I am grateful to my fellow graduate for the casual scientific discussions and social meetings.

This thesis is dedicated to my father, José A. Cupertino, who always encouraged his children to never settle down and always be in search of knowledge. I would like to thank my family for all the support they have provided me. To my parents, Jose and Angela, and my brothers, Leticia and Leandro, thank you for always being by my side. Even physically so far away, we always felt very close. Lastly, I thank my brave son Rodrigo, companion of many adventures, always in a good mood and helpful. And Manu, for her constant support and encouragement to finish this thesis from here, Brazil.

VITA OF DANIEL FONTOURA CUPERTINO
February 2023

EDUCATION

Bachelor of Science in Geology, Federal University of Rio de Janeiro, Rio de Janeiro, Brazil, June 2005 (cum laude)

Doctor of Philosophy in Earth Sciences, University of California, Santa Barbara, March 2023 (expected)

PROFESSIONAL EMPLOYMENT

August 2005-November 2005: Geophysics at WestenGeco/Schlumberger, Rio de Janeiro, Brazil Seismic data acquisition and processing.

December 2005-June 2006: Geology Specialist at Petroleum Federal Agency (ANP), Rio de Janeiro, Brazil Exploration Hydrocarbon Companies regulation. Evaluate prolific hydrocarbon areas to offer on Brazilian oil and gas bidding rounds.

July 2006-Present: Exploration Geologist at PETROBRAS S. A., Rio de Janeiro, Brazil. Evaluate plays and prospects targets for future commercial hydrocarbon development. Ability to correlate wells and interpret seismic data to incorporate into the geologic model. Prepared confidential reports for presentation to management. Coordinator of regional carbonate reservoirs projects. New ventures areas.

QUALIFICATIONS:

2007: Certificate Program focus in Basin Analysis - Petroleum Geology. Certified by Rio de Janeiro State University.
2008: Certificate Program focus in Exploration Interpretation - Petroleum Geology. Certified by Ouro Preto Federal University.
2009: Universität Potsdam, Institut für Erd und Umweltwissenschaften. Training focused in carbonates with Dr. Maria Mutti.
2011: Universidad Nacional de Córdoba, Facultad de Ciencias Exactas, Físicas y Naturales. Training focused on carbonates, field mapping and modern carbonate lakes analogous with Dr. Ricardo Astini.

FIELD STUDIES

2015-2019: Green River Basin, Buchheim, P., Awramik, S., Vanden Berg, M and Carroll, A.
2014: Basin & Range - Ancient and Modern Lakes – Scholz, C.
2013: Carbonate Reservoirs Oman Field Trip - Homewood, P. and Mettraux, M.
2012: Bahamas Chevron-Petrobras Field Trip - Harris, PM and Eberli, G.
2012: Thermal Karst Field Trip, Campo Formoso, Bahia, Brazil – Neto, P.
2011: Marnoso-Arenacea Fm. Turbidites, Apeninos Setentrionais, Italy – Tinterri, R.
2010: Thermal Karst Field Seminar, Buda Hills, Hungary – Esteban, M. et al.

ABSTRACT

Saline-Alkaline Lakes of the Eocene Green River Formation and their Microbialites

by

Daniel Fontoura Cupertino

The Eocene Green River Formation is the best studied ancient lacustrine deposit. It also contains the most diverse and abundant microbialites of any lake deposit. Unfortunately, there have been few studies of these microbialites. Microbial bioherms and biostromes formed considerable primary carbonate and rare Mg-clay, deposits in the littoral to sublittoral environments of Green River lakes. These deposits were studied in three areas: Vermillion Creek (Colorado), Evacuation Creek (Utah), and Sanpete Valley (Utah). The microbialites were formed mostly under balanced fill, saline-alkaline lake conditions and their morphology was influenced by fluctuating lake dynamics.

1. The upper LaClede Bed, Laney Member of the Eocene Green River Formation at Vermillion Creek, Colorado, contains an unusual, unique microbialite: giant columns, over 5 m tall, composed of 3-10 cm thick layers, that in turn are composed of columnar, columnar branching, domical, and shrubby stromatolites. These stromatolites are largest known lacustrine columnar stromatolites. Large coniform stromatolites also occur as do stromatolite encrusted logs. The layering patterns and their contained microbialite types resulted from lake-water fluctuations due to changing climatic conditions (primarily arid vs. humid) and provide critical indicators for paleoenvironmental analysis.

2. Two microbialite-bearing carbonate short-term cycles were examined from the upper Douglas Creek Member of the Eocene Green River Formation at Evacuation Creek, Utah. The carbonates are notable because of the number of distinctive microbialites occurring as biostromes and bioherms that are traceable over several kilometers. Nine microbialite facies were established. Unique arborescent and branched minicolumnar stromatolites, which resembles shrubs, developed within the bioherms. Each distinctive microbialite facies reflect high-frequency fluctuations of lacustrine depositional conditions. All carbonate facies successions are associated with two short-term rhythmic cycles that record periods of fluvial quiescence (aridity) represented by littoral carbonate deposition under an evaporative regime. The presence of dolomicrite mineralization within the carbonate beds and analcime within siliciclastic beds indicate a microbial and evaporative shallow depositional environment under saline alkaline conditions. Most of the identified diagenetic phases took place in near-surface and shallow diagenetic settings. The lateral extent and facies changes of the microbialite carbonate beds allow a reconstruction of a NE-SW lake shoreline at the western shoulder of the Douglas Creek Arch, and how these carbonates beds evolved.

3. In Sanpete Valley, Utah, in the upper Green River Formation, in addition to microbialites, the Mg-clay mineral stevensite (and other Mg-clay minerals) is found, in both carbonate-chert microbialites and claystone. Also, this area was subjected to volcanoclastics. Various species of Mg-clay minerals (stevensite, mixed-layer kerolite-stevensite, and sepiolite), along with calcite and dolomite, were found in four Mg-clay-bearing lithofacies: 1) Mg-Clay-bearing Stromatolites; 2) Mg-Clay Arenites; 3) Mg-Claystone with Calcite Aggregates; and 4) Intraclastic Hybrid Arenites and Conglomerates. Mg-clay bearing rocks and the microbialites from the Sanpete Valley were deposited in a southwestern, shallow

embayment of Eocene Lake Uinta along the margin of the Sevier fold and thrust belt. All the findings provide a comprehensive framework for the lithostratigraphic and chemostratigraphic evolution of the lake system, as well as texture classification, providing a unique analog for detailed correlation and comparison to other basins containing similar Mg-clay and microbialite-bearing deposits, in particular the Cretaceous pre-salt deposits in off-shore Brazil and Angola.

TABLE OF CONTENTS

LIST OF FIGURES

CHAPTER 1

1. Introduction

The diversity of lacustrine depositional systems is practically boundless. Compared to oceans, lakes are highly variable in chemical composition, in particular salinity, which results from the weathered products of drainage basin bedrock, hydrology, biology, climate, and tectonics (Renaut and Gierlowski-Kordesch, 2010). Given the wide environmental spectrum, it is not surprising that lacustrine carbonate sediments are remarkably diverse in terms of their facies, paleontology, geochemistry, stratigraphy, and mineralogy. Saline-alkaline lakes constitute a special class of carbonate lakes in closed or intermittently closed basins (Eugster and Hardie, 1978). Shallow, nearshore environments of these lakes are ideal places for the development of microbialites, especially stromatolites (Talbot and Allen, 1996).

A recent influx of interest in microbial carbonates as potential reservoirs for oil and natural gas has stemmed from the discovery of oil in the lacustrine Cretaceous pre-salt of Angola and Brazil (Carminatti et al., 2008, Awramik and Buchheim, 2014). These majors discoveries raised many questions about the carbonate reservoirs formed in lacustrine systems and associated with microbial carbonate facies, both at basin and reservoir scales. Thus, the analyses of similar ancient and recent microbial carbonates is important for developing successful models for exploration.

The Eocene Green River Basin shares close similarities with newly discovered carbonate-hosted oil and natural gas deposits in the Cretaceous “pre-salt” successions of Brazil and Angola, making it an extremely useful analog. Establishing a relationship between the porosity of microbial carbonate beds and their potential to form reservoirs aid in

forming an invaluable tool in locating, estimating, and determining potential reservoirs. The well exposed outcrops in the Green River Formation show: (a) large, multimeter-size bioherms, (b) smaller, patch-reef-like bioherms, (c) inter-biohermal facies, (d) facies transitions toward lake depocenter of bioherm-bearing successions, (e) biostromes, (f) spring deposits (tufa) associated with microbialites, (g) microbialites composed of shrubs, and (h) successions with stevensite, microbialites, and oolite. These can help uncover relationships between large-scale stratigraphic architecture, outcrop-scale microbialite forms and textures, and small-scale degrees and distributions of porosity. These relationships, though, are not well understood and require more research into their reservoir potential.

1.1 Geodynamic context and climate setting of the Green River Eocene Lakes

The North American Cordillera orogenic system developed in response to subduction of oceanic (Farallon and Kula) plates and accretion of terranes along the western margin of the North American plate margin during Jurassic to Paleogene time as a result of the Laramide orogeny (Dickinson, 2004; DeCelles, 2004) (Fig.1). The Laramide orogeny consisted of subduction-related magmatism eastward during Late Cretaceous, due a slab-shallowing of the subduction of Farallon plate (DeCelles, 2004). Interactions between the shallow subducted Farallon plate and the overlying lithosphere are thought to have been partly responsible for the development of basement-cored Laramide uplifts in the Rocky Mountain foreland. Igneous activity increased across a broad east– west zone above the northern margin of the flat slab, which then progressed southward during slab roll back and mantle lithosphere delamination (Best et al., 2009). The hinterland experienced concentrated extension in core complexes, and increased paleo-elevation and relief, which progressed

southward over time (Chamberlain et al., 2012). Eastward-thinning of Paleozoic strata may have also influenced Laramide structural styles. Numerous nonmarine basins developed within this “broken foreland”, including those that host the lacustrine Eocene Green River Formation (Miller et al, 1992). In this context, Eocene Lakes formed, in which the Green River Formation was deposited at the end of the Laramide (Fig.1).

The deposition of the Green River Formation was deposited in the early Eocene, 54 to 43 Ma, and coincided with the highest global temperatures of the Cenozoic (the Early Eocene Climatic Optimum, EECO), which was followed by a long period of climate cooling leading to Oligocene glaciations (Fig.2). During the early Eocene, following a warming trend that started in late Paleocene time, sustained warming occurred (Bijl et al., 2009) that peaked with the ~2 Myr long Early Eocene Climate Optimum (EECO) at ca 52 to 50 Ma (Zachos et al., 2001, 2008). This warming was followed by a cooling trend throughout the middle to late Eocene (starting at the termination of the EECO, ca 50 Ma; Bohaty and Zachos, 2003; Bijl et al., 2009).

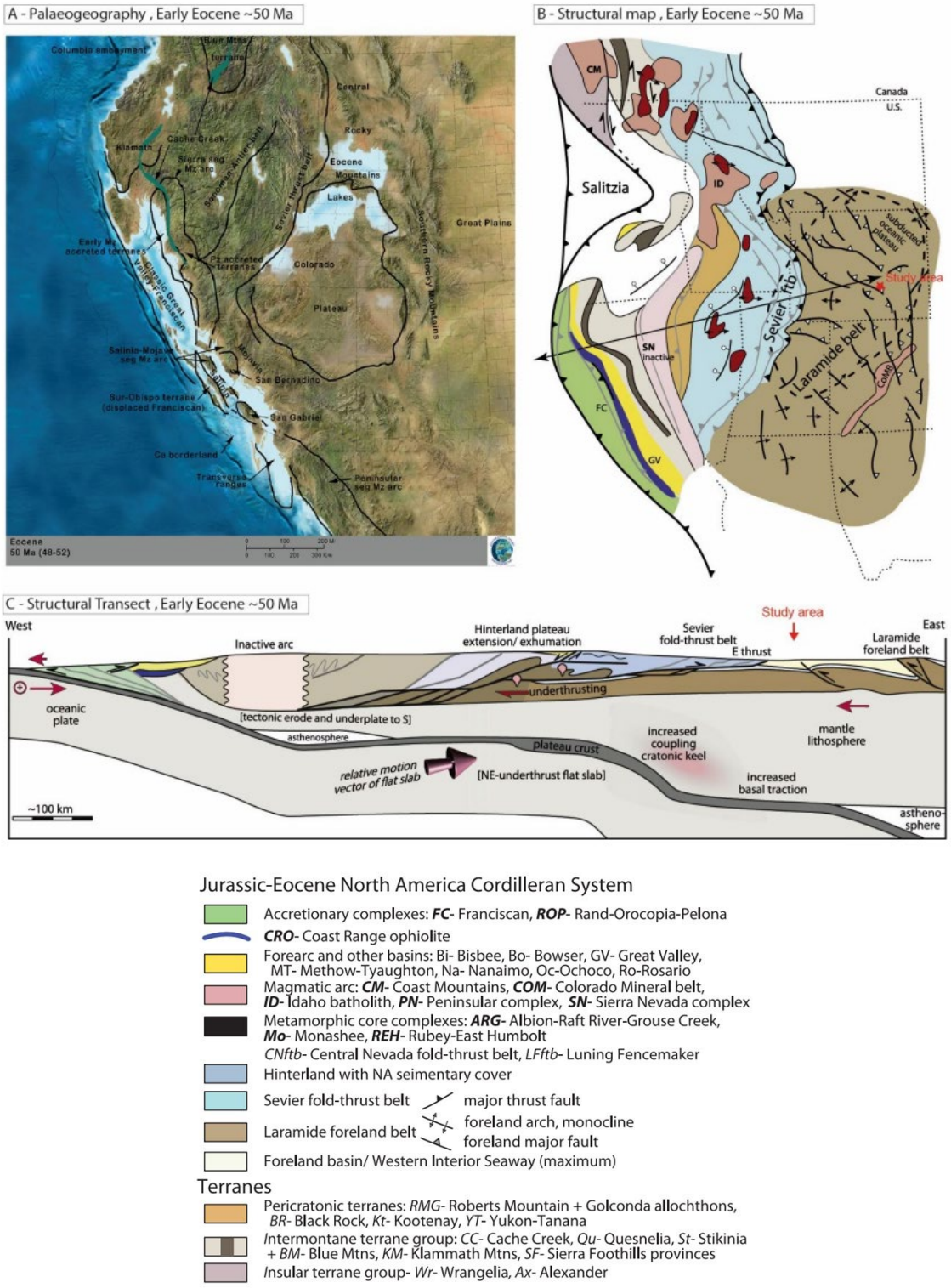

Figure 1. A) Palaeogeographic reconstruction of Western US at Paleogene (Early Eocene) times (Blakey and Ranney, 2017), note Green River Eocene Lakes; B) Palinspastically restored tectonic domains of the North American Cordilleran orogenic system for end of Laramide deformation (Early Eocene ~50 Ma); C) Lithospheric cross sections for Paleogene (~50 Ma). Modified from Yonkee and Well, 2015.

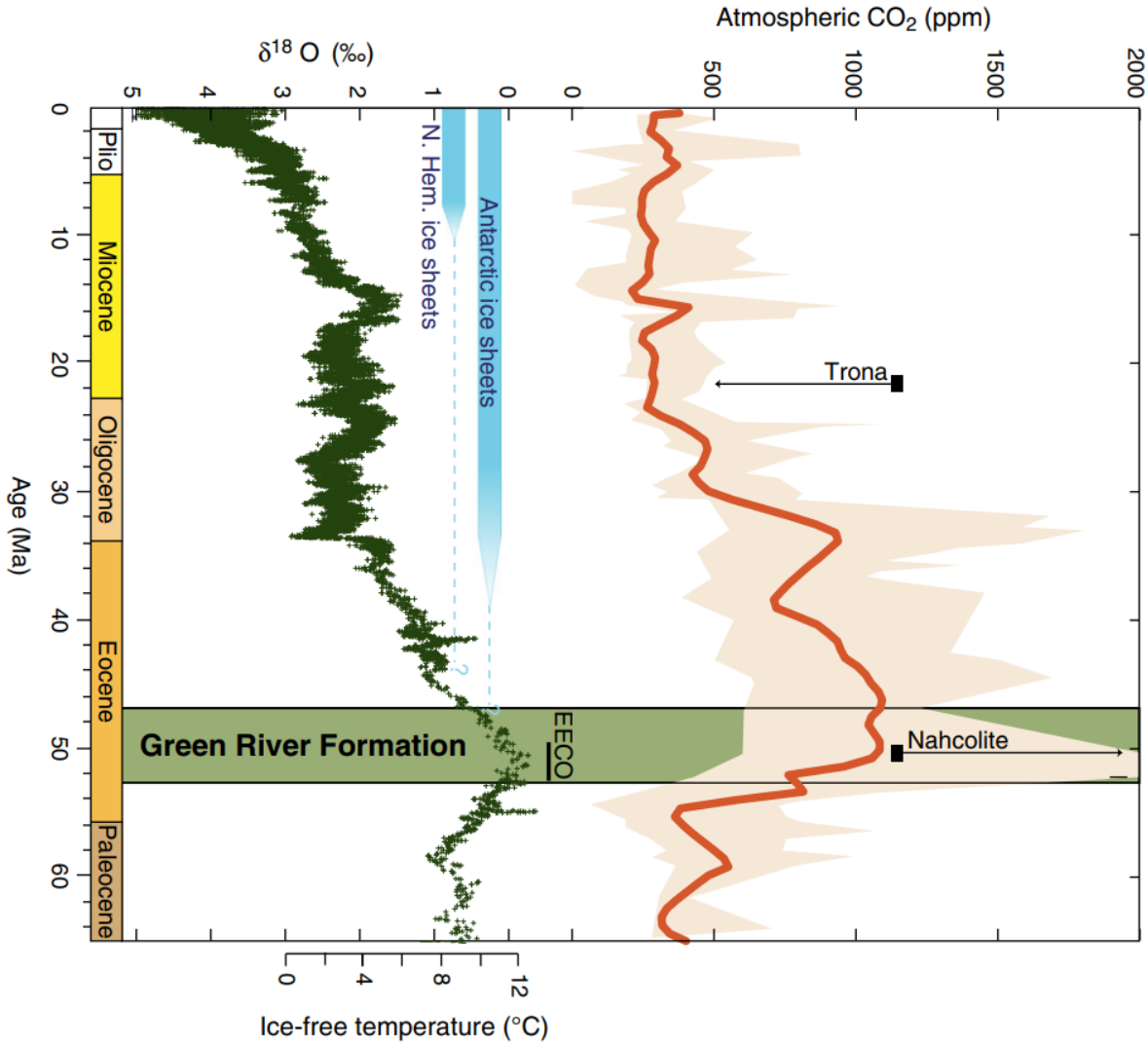

Figure 2. Temperature and CO_2 context of the Paleogene (Frantz et al, 2014). Cenozoic CO2 (top, red) and temperature (bottom, green) estimates. The time period represented by Green River Formation deposits are highlighted in green, with the Early Eocene Climatic Optimum (EECO) highlighted. The CO_2 plot is modified from Beerling and Royer (2011) and depicts the range of CO_2 values allowed by several different proxies, with the best fit line suggested by Beerling and Royer (2011). The lower temperature plot based on $\delta^{18}O$ from benthic foraminifera is modified from Zachos et al. (2008).

The greater Green River Basin of southwestern Wyoming is one of the best areas in the Rocky Mountains for paleobotanical investigation of the Paleocene-Eocene climate (Wilf, 2000). Intensive sampling has resulted in the recovery of an estimated 189 species of plant macrofossils from the Tiffanian, Clarkforkian, Wasatchian, and Bridgerian land mammal "ages". Based on leaf margin and leaf area analysis, conditions in the Green River Formation were generally warm and frost-free. Mean temperatures were near 20 C and mean annual precipitation in the range of 80-100 cm/yr. Long term changes were generally consistent with global changes, becoming slightly warmer and drier between about 59 and 50 Ma (Wilf, 2000) (Fig.3).

Thrasher and Sloan (2009) used an embedded climate model with 50x50 km resolution to examine regional variation within the western U.S. This analysis shows strong contrasts in temperature and precipitation with elevation. A pronounced rain shadow effect developed in the mountainous area northwest of the Green River lakes. The rain shadow formed at minimum altitudes of >3000 m for the mountains encircling the Green River basin (Norris et al, 1996). The model predicts cooler temperatures at basin level that indicated by leaf analysis, suggesting that additional climate forcing factors nor incorporated to the model must be involved (Fig.4).

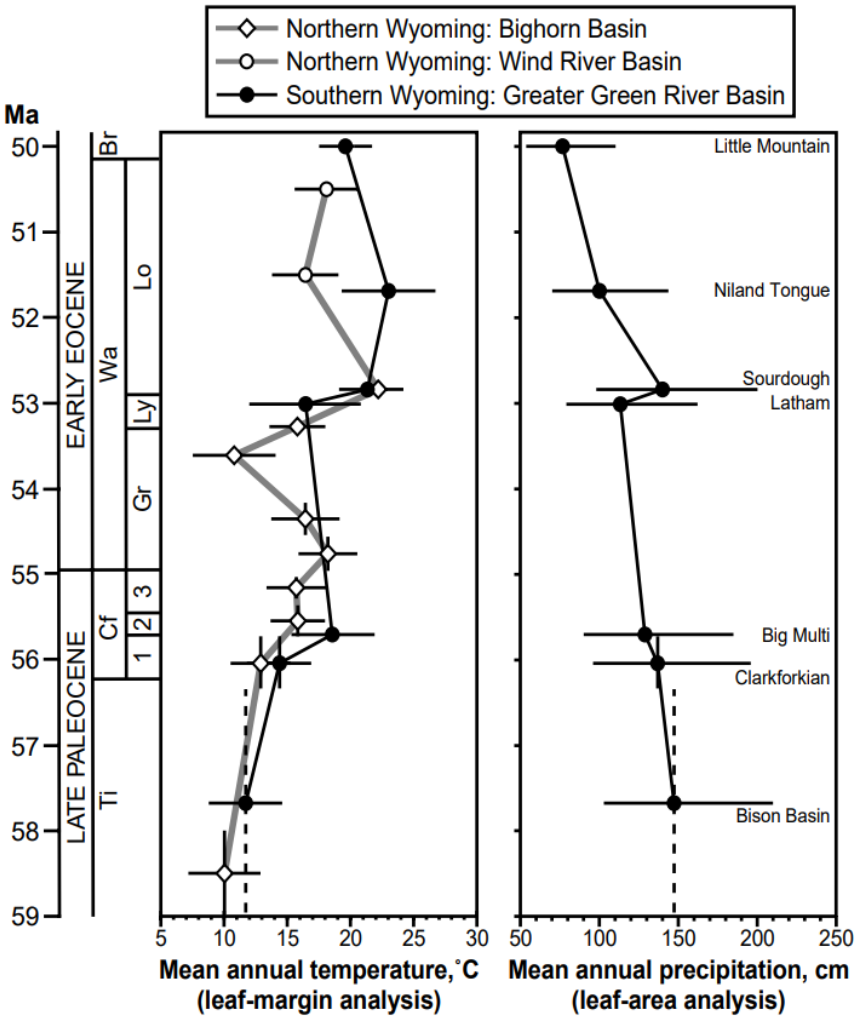

Figure 3. Paleocene-Eocene climate history of southern and northern Wyoming, estimated from leaf-margin and leaf-area analysis (Wilf, 2000).

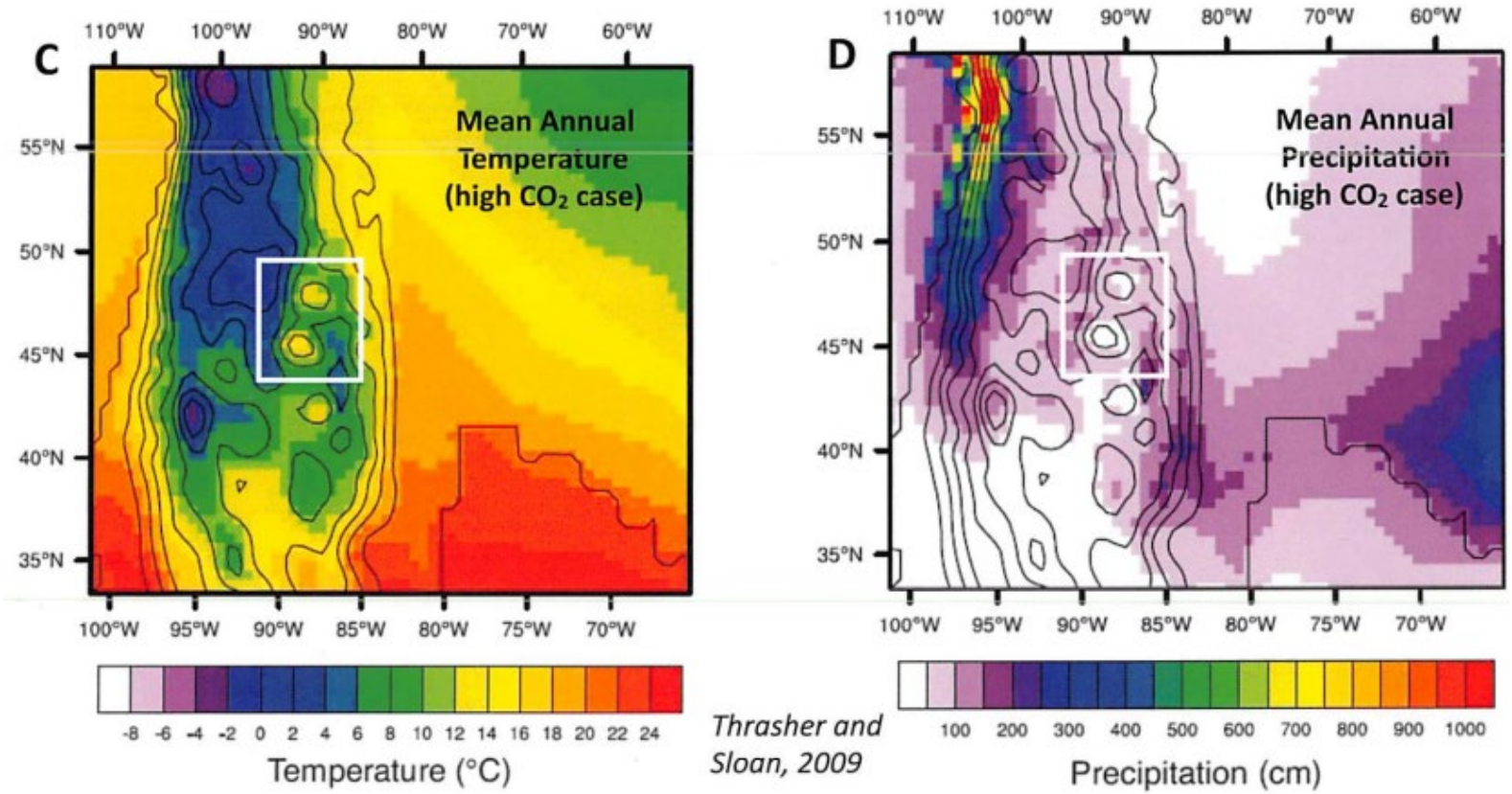

Figure 4. Paleocene-Eocene climate model: white rectangles equal the approximate area of the Green River Formation lakes (Thrasher and Sloan, 2009).

1.2 Green River Formation and the paleolakes Gosiute and Uinta

The Eocene Green River Formation (GRF) of Wyoming, Colorado, and Utah was deposited over a period of approximately 5 Ma (53.5 to 48.5 Ma) in a series of continental basins that occupy a broken foreland province to the east of the Cordilleran fold and thrust belt (Dickinson et al., 1988) (Fig.5). These basins are separated from one another by chains of anticlinal basement-cored uplifts that occurred during the Laramide orogeny (Dickinson et al., 1988). The entire GRF was deposited during the late phase of Laramide orogeny of the Rocky Mountains and records a mixed carbonate-siliciclastic fluvio-lacustrine system, with extensive carbonate shoals and microbial carbonates deposits (Tänavsuu-Milkeviciene and Sarg, 2012) (Fig.6).

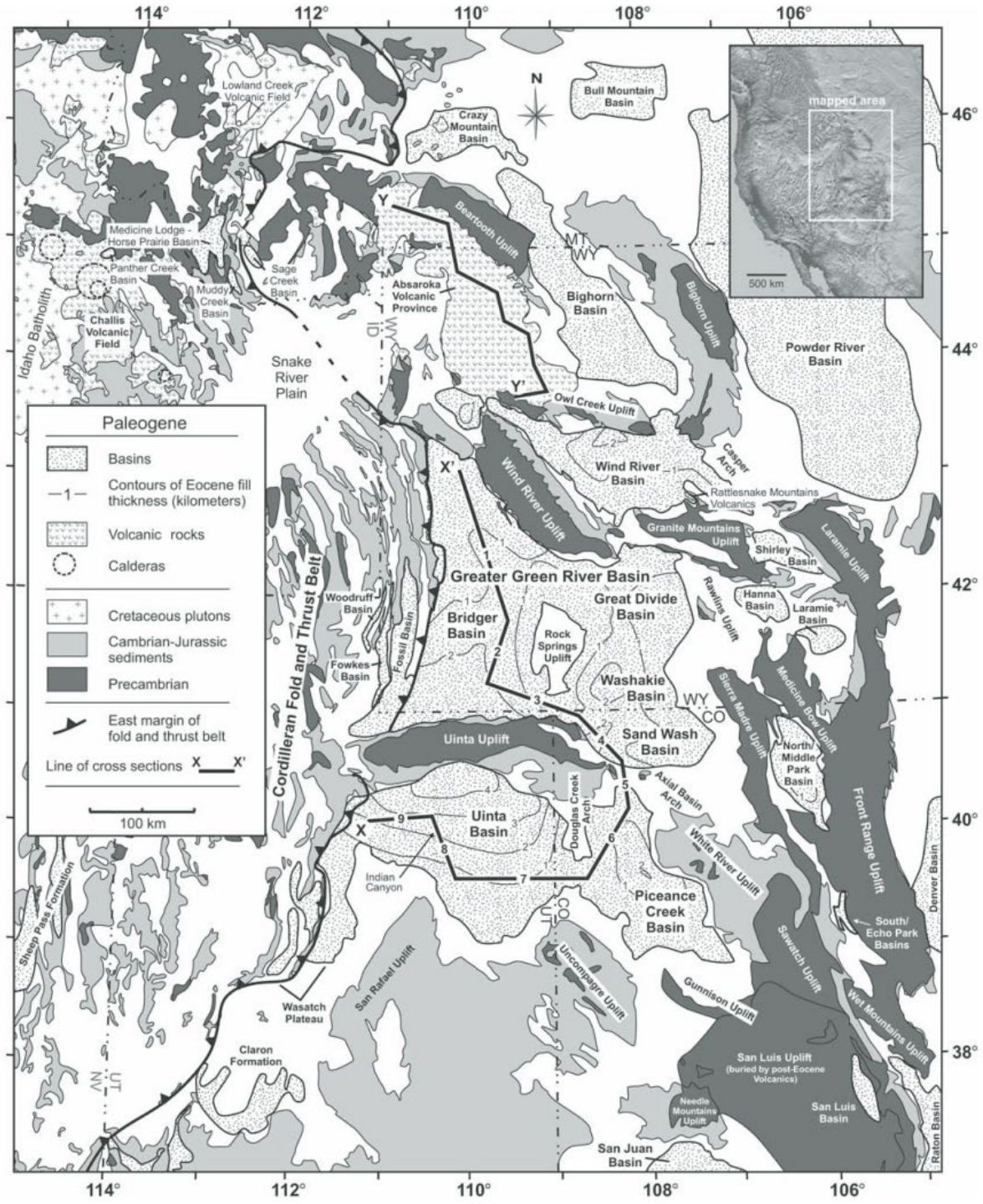

Figure 5. Map showing the location of Eocene basins and basin-bounding uplifts within the broader Laramide orogeny, showing the thickness of Eocene strata (Smith et al., 2008).

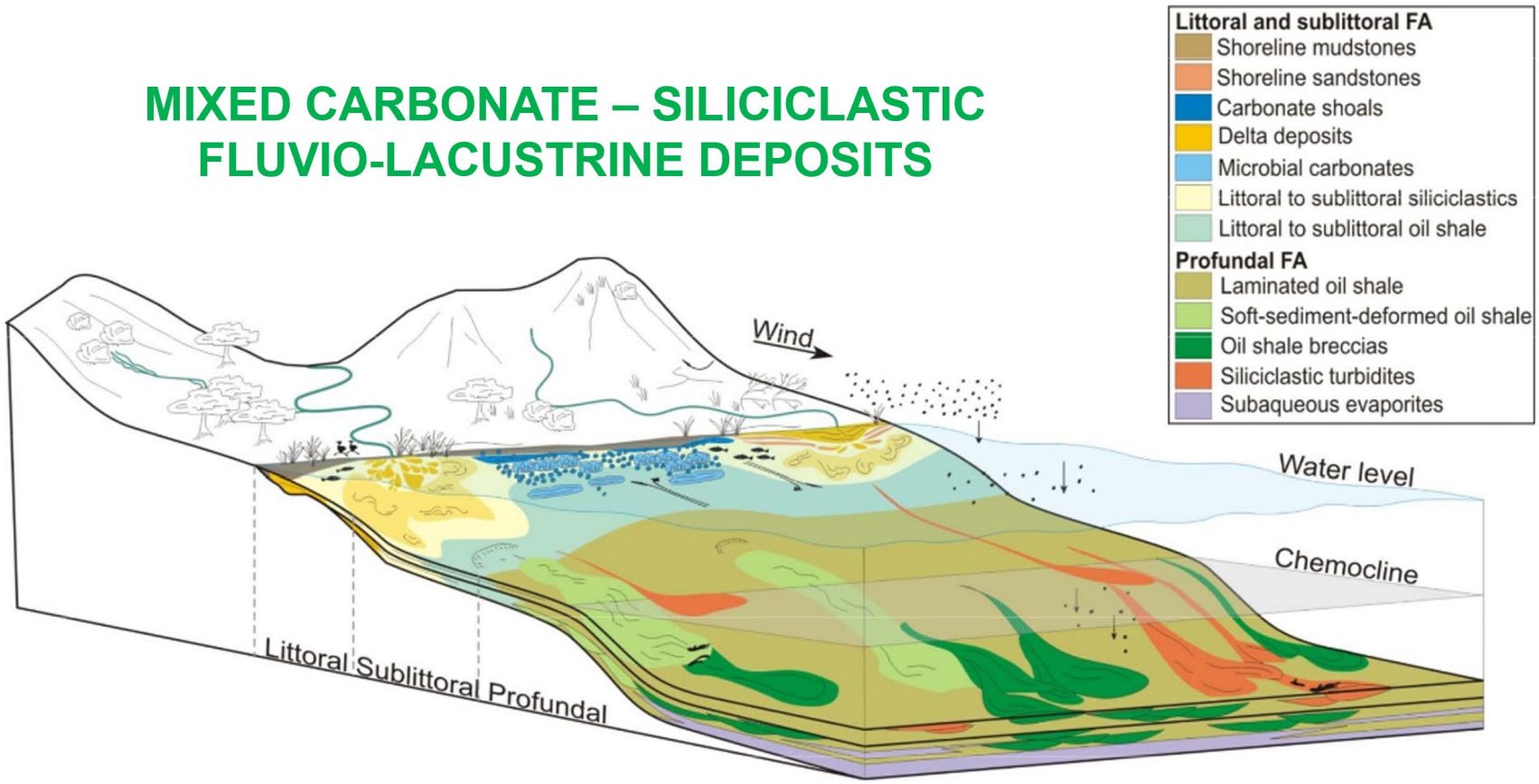

Figure 6. Depositional model for the Green River lake basins (modified from Tänavsuu-Milkeviciene and Sarg, 2012)

Volcanism occurred over broad areas of the northwestern United States during the Eocene and provided both fallout tuffs and volcaniclastic sediment to the GRF lake basins (Surdam and Stanley, 1980). Major volcanic centers include the Absaroka Volcanic Province, Challis volcanic field, Lowland Creek Volcanics and minor fields are scattered throughout the region (Smith et al., 2008). Precise age dating has allowed the first direct comparison of time equivalent deposits in different basins of the GRF. From this analysis it is becoming apparent that its diversity is not random, but instead reflects predictable regional patterns of basin accommodation, hydrologic relationships, and magmatism. Lake types evolve from overfilled (fluvial-lacustrine facies) to underfilled (evaporative facies) as accommodation increased and sediment supply decreased (Bohacs et al., 2000). The principal genetic controls on these successions are inferred to be potential accommodation, which determines the volume of the "hole" that a lake occupies, and water + sediment fill. This determines how completely that hole is filled. The balance between these two controls determines lake basin type (or lake type). Fluvial-lacustrine facies are thus associated with overfilled lake basins, fluctuating profundal facies with balanced-fill lake basins, and evaporative facies with underfilled lake basins (Fig.7, 8). Note that these terms refer to time-averaged rock successions, rather than to "snapshots" of how the lake looked at one moment. Lake types therefore do not necessarily have modern analogues. For example, individual lakes occupying a balanced-fill basin may oscillate between hydrologically open and closed and between hypersaline and brackish (or even fresh), due to the influence of short-term climate cycles.

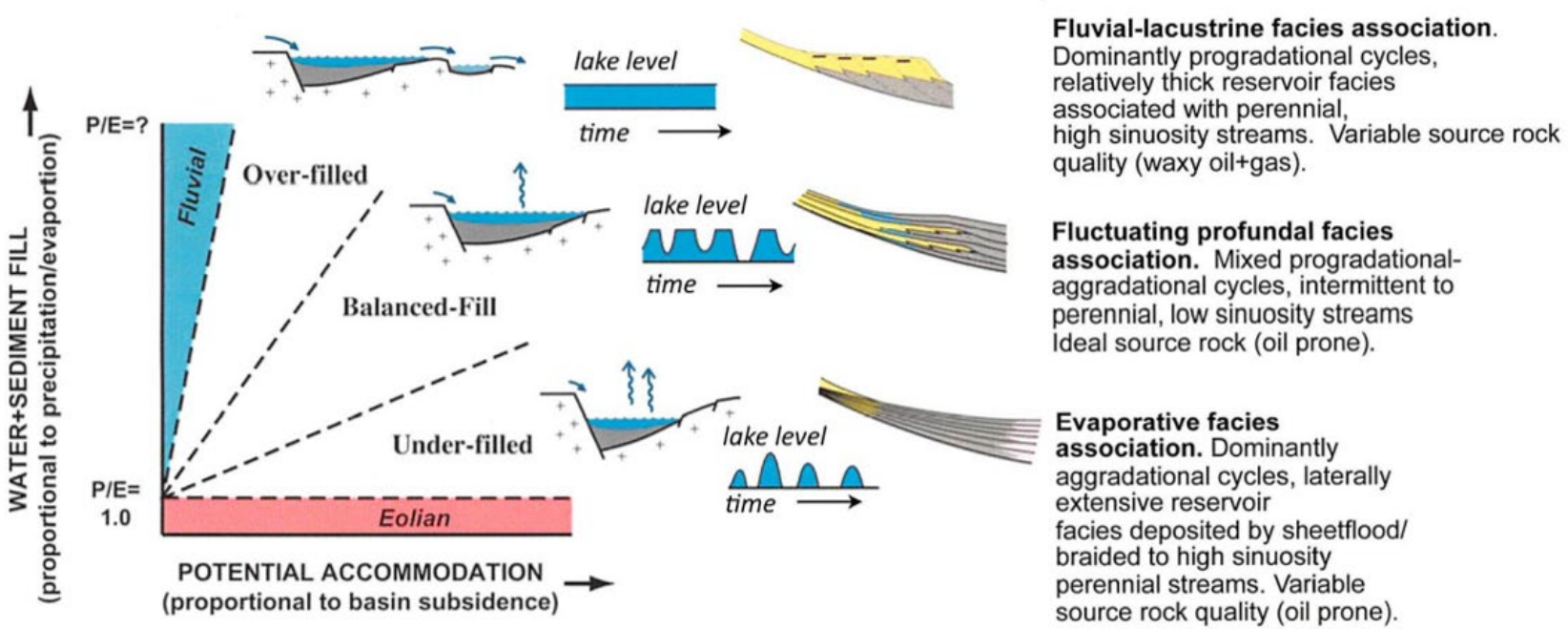

Figure 7. Lake-basin type diagram showing the character of lacustrine strata as a function of both sediment + water supply and potential accommodation (Bohacs et al., 2000).

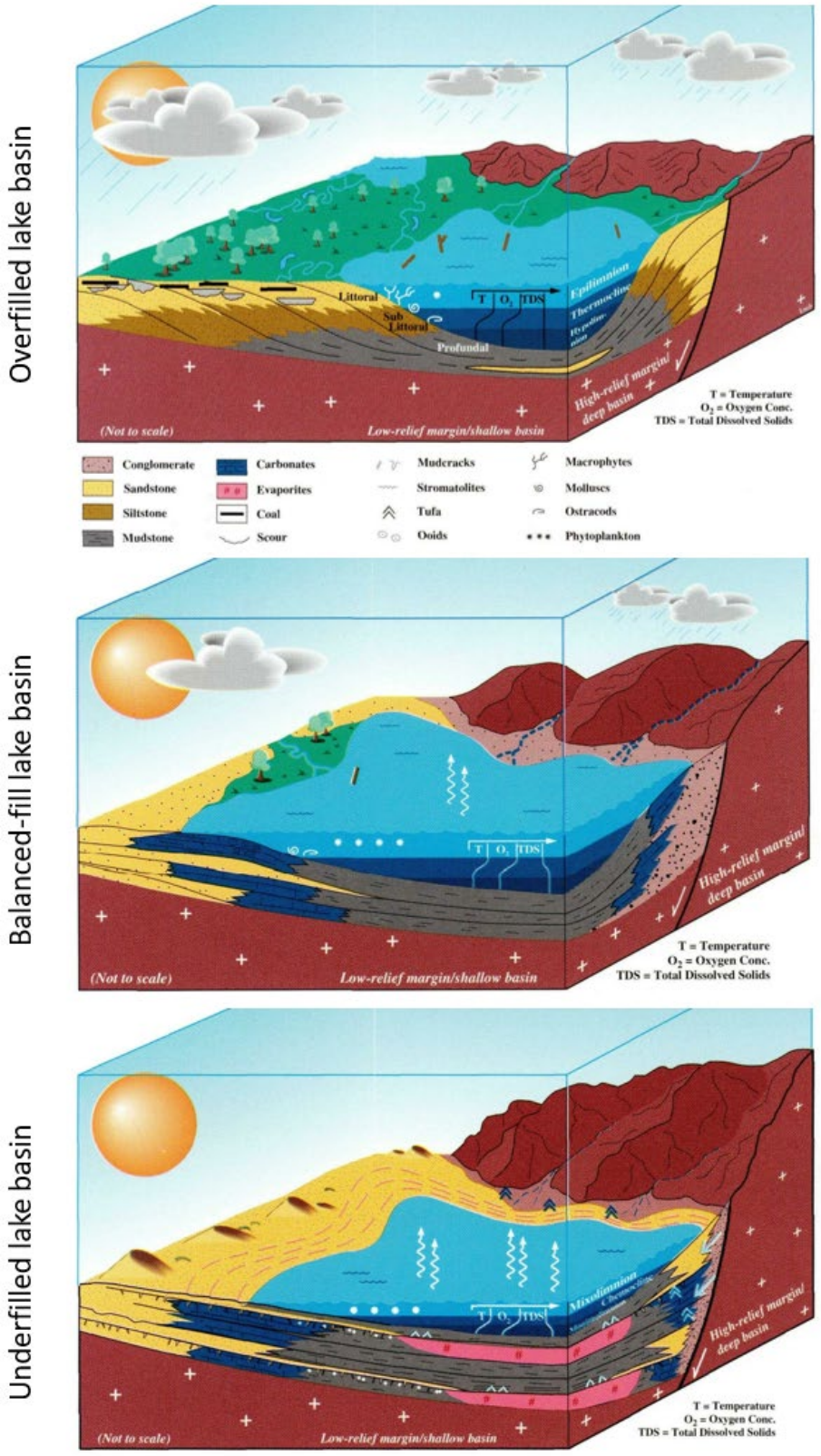

Figure 8. Schematic diagram highlights major features of overfilled, balanced-fill and underfilled lake basin types, which lake-level fluctuations are climatically driven (Bohacs et al., 2000).

Distinctive assemblages of lithologies and fossils within the Green River Formation allow for its subdivision into three principle lacustrine facies associations: fluvial lacustrine, fluctuating profundal, and evaporative (Carroll and Bohacs, 1999). The evaporative facies is best recognized via the presence of bedded evaporites and absence of fish fossils. It is interpreted to represent deposits of hypersaline lakes within underfilled basins in which water rarely rose above the level of the downstream sill. Fluvial-lacustrine facies preserves abundant mollusc and occasional fish fossils and are interpreted to have been deposited in freshwater lakes in overfilled basins where water consistently spilled over the downstream sill. Fluctuating profundal facies is typically composed of laminated, organic-rich carbonate mudstones intercalated with thin desiccation horizons and are interpreted to represent the deposits of brackish to saline lakes that occupied balanced-fill basins where water oscillated near the sill level. Assignments of facies association and lake type in most cases correspond to previously identified stratal units and are primarily employed to help standardize terminology between the basins (Fig.8).

The Green River Formation has a maximum thickness of nearly 2 km and was deposited into two main basins, separated by the E-W Uinta uplift (Fig.9):

- The Greater Green River Basin, to the north, including Bridger (Green River), Great Divide, Washakie, and Sand Wash sub-basins, corresponding to the depositional system of the paleolake Gosiute.

- The Uinta Basin and Piceance Creek Basin (sometimes considered one basin, the Uinta Basin), to the south, and correspond to the depositional system of the paleolake Uinta.

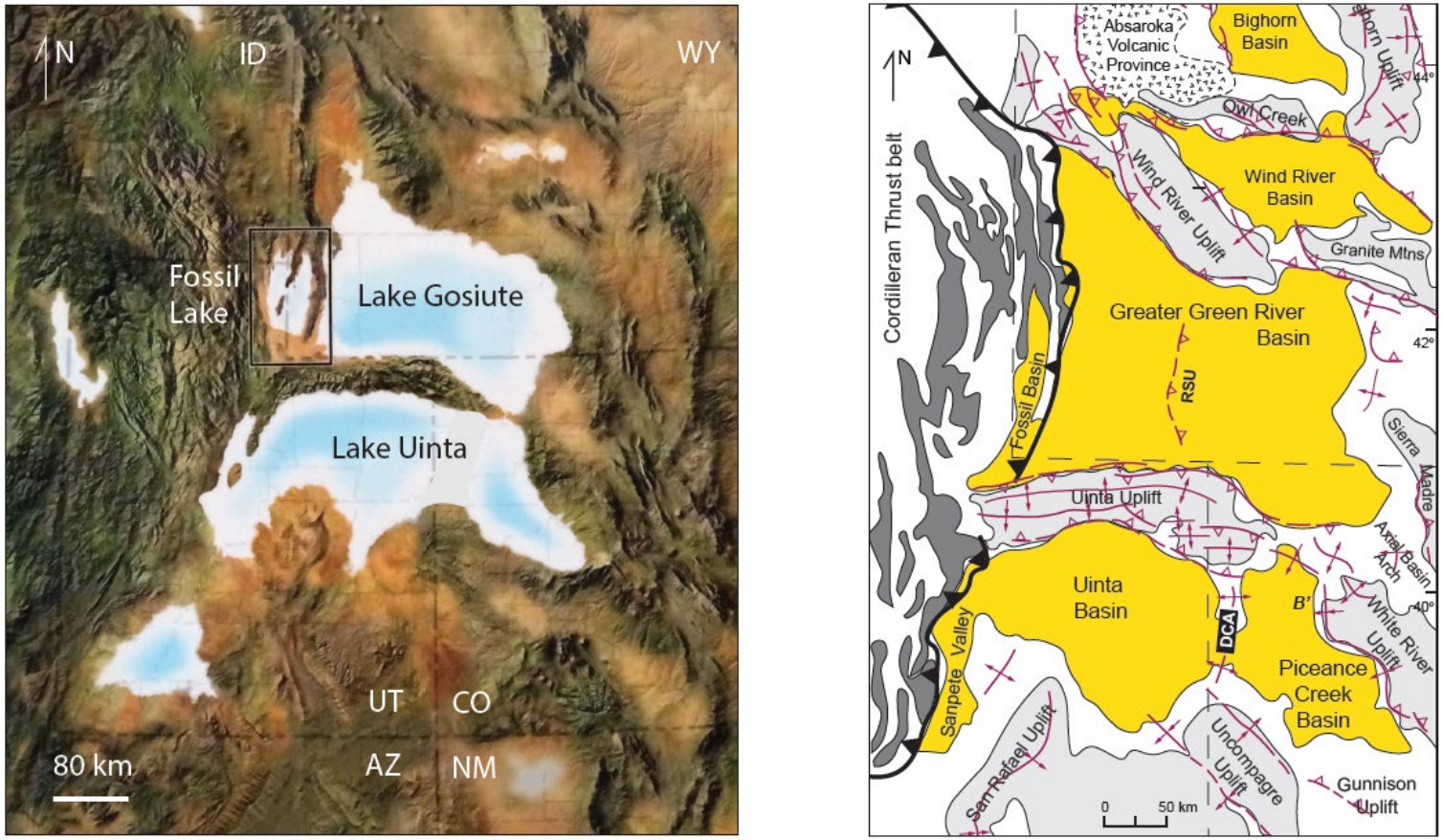

Figure 9. A) Two main Eocene lakes in which the Green River Formation was deposited: Lake Gosiute and Lake Uinta (modifed from Blakey and Ranney, 2018). B) Cordilleran thrust belt (dark gray), intermontane basins (yellow) and basin-bounding uplifts (light gray) (modified from Dickinson et al. 1988, Smith and Carroll, 2015).

The Green River Formation lakes had a hydrographic basin of 349,000 km2, with Lake Gosiute covering a maximum extent of 40,150 km2 (Bradley and Eugster, 1969) This lake varied in its extent due to its response to climatic and tectonic events. These influenced variation in microbialite bioherms as they responded to water levels and climatic conditions. A broad palaeogeographic evolution of Lake Gosiute (Greater Green River Basin) and Lake Uinta (Uinta and Piceance Creek Basins) have been proposed by Smith et al. (2008). Note, the literature has treated the Piceance Creek Basin as a sub-basin of the Uinta Baisn. Lake type observations have been combined with paleocurrent indicators and provenance data to reconstruct the paleo-hydrologic configuration of the Laramide landscape for eight discrete time slices (Fig.10).

Sedimentation in the Green River Formation is dominated by alluvial facies (Roehler, 1992). Alluvial deposits are subdivided into three broad facies associations according to their mode of deposition: deltaic, alluvial plain, and alluvial fan. However, these clastic dominated strata are interbedded by carbonate-dominated intervals. These carbonate-dominated intervals mainly correspond to balanced-fill lake basin defined by Bohacs et al. (2000), and are characterized by fluctuating facies associations, dominated by stromatolite-rich deposits at the lake margins. Thinly laminated marly mudstones occur in the basin center, known to be the main source rocks and oil shale bearing strata of the Green River Formation.

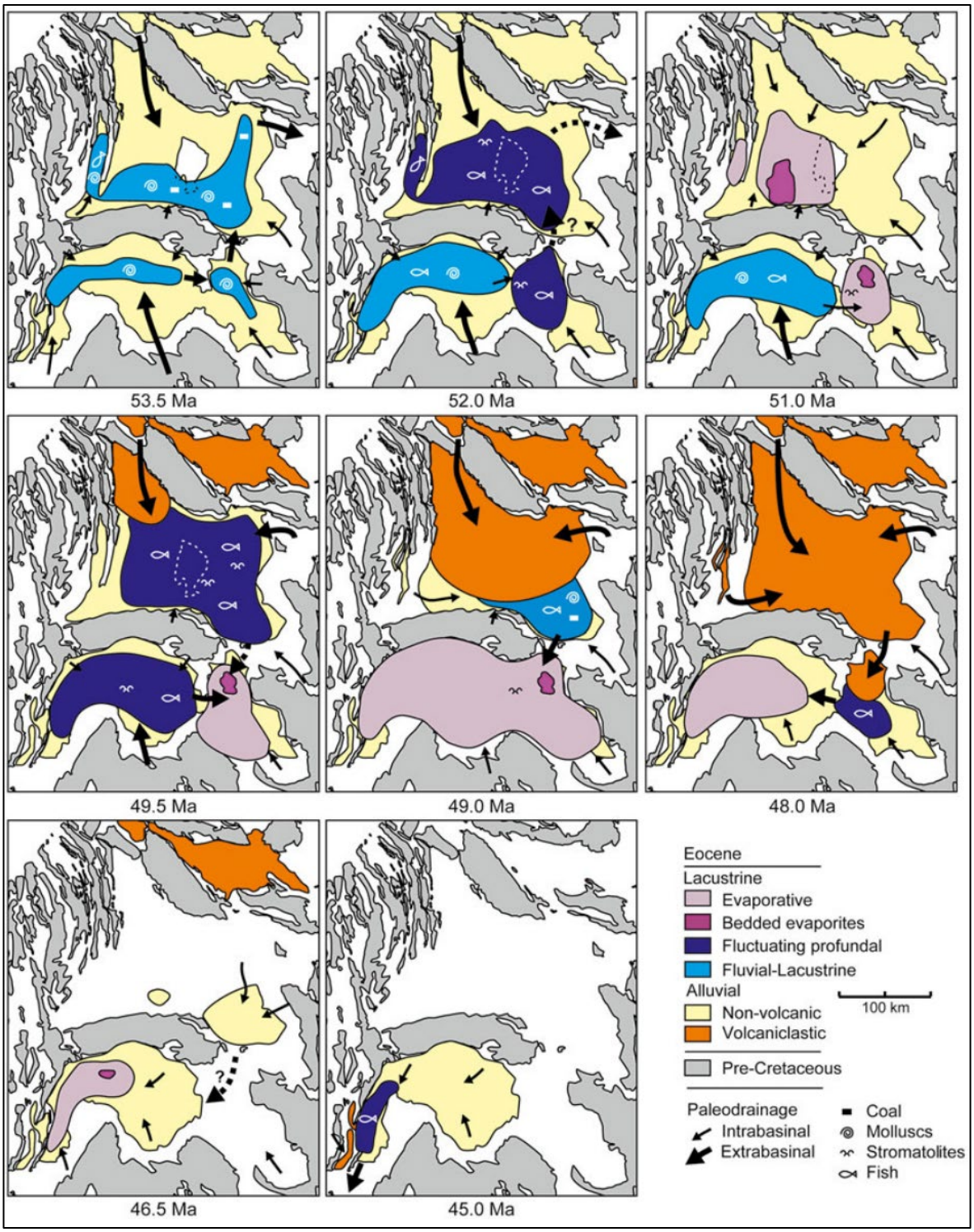

Figure 10. Green River paleohydrology from 53.5 Ma to 45.0 Ma. (Smith and Carroll, 2015).

The main stratigraphic occurrences of extensive carbonate shoals and microbial carbonate deposits are associated with three major transgressive systems tracts in balanced-fill lake type (Fig.11). Models for the origin of the carbonate-rich Green River Formation have long been debated and are subject to ongoing discussion. During the 1970s, this debate primarily focused on arguments for a deep, stratified lake with anoxic bottom waters (Bradley, 1929, 1964), versus a playa-lake system in which a relatively shallow, evaporative lake was surrounded by exposed mudflats (Eugster and Surdam, 1973; Eugster and Hardie, 1975). Several excellent studies conducted a documented sedimentologic details of the trona-rich Wilkins Peak Member (Smoot, 1983) and the oil shale-rich Laney Member (Surdam and Wolfbauer, 1975; Buchheim and Surdam, 1977; Surdam and Stanley, 1979).

The debate concerning an appropriate depositional model arises in part from the fact that the Green River Formation exhibits a remarkable degree of internal diversity, ranging in lithology from bedded evaporite to coal. No one depositional model can adequately account for all these variations (Carrol and Bohacs, 1999), and in fact it is questionable whether the Green River should be considered a “formation” at all. Several of its included “members” appear to meet the basic definition of a formation as a rock unit that is sufficiently distinctive to be regionally mapped. The GRF probably would more appropriately be considered a group, although this change has not yet been proposed formally.

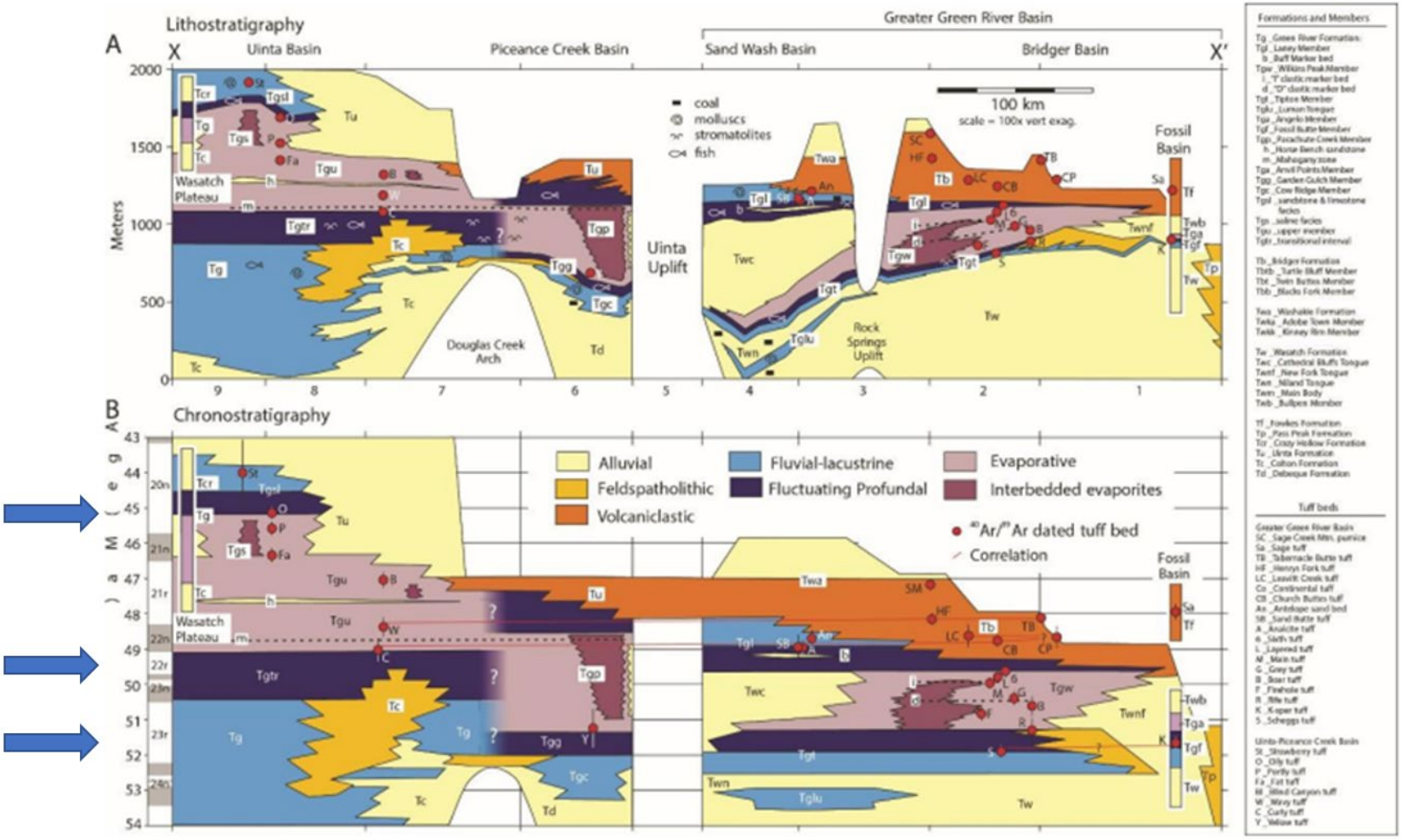

Figure 11. Lithostratigraphic and time stratigraphic cross sections of Eocene strata in the Greater Green River, Piceance Creek, and Uinta Basins (Modified from Smith et al, 2015).

1.3 Green River Formation and its microbialite occurrences

The Eocene Green River Formation contains what may be the richest and most diverse record of non-marine microbialites including biostromes and, bioherms (Fig.12). Stromatolites dominate, but shrubs, oncoids, thrombolites, and tufa-like microbialites occur. Some studies use these microbialites in making interpretations about the depositional system (Roehler, 1993); however, few studies have described and analyzed the microbialites in detail (Bradley, 1929; Frantz et al., 2014; Jagniecki et al, 2021).

The GRF contains what may be the most varied microbialite forms and distribution of any lacustrine deposit (Awramik and Buchheim, 2014) (Fig.13, 14). Laterally extensive biostromes are common, some traceable for over 70 km (Surdam and Stanley, 1979) (Fig.15). It also contains multimeter-size bioherms, with springs often associated with bioherms and large microbialites (Awramik and Buchheim, 2015; Jagniecki et al, 2021). An example of some possibly unique microbialites are the giant, multi-meter size, columnar stromatolites (Awramik and Buchheim, 2015; Ingalls et al., 2022). Columns are up to 5.5 m high and up to 7 m in diameter (the largest lacustrine columnar stromatolites known) and have continuous layers that can be traced from the base to the top of the column (Awramik and Buchheim, 2015).

The distinctive microbialites megastructure shapes (Grey and Awramik, 2000) appear to develop in the transgressive phases of the lake. Most microbialites of the GRF formed in a transgressive system tract with their megastructure controlled by the gradient of the lake bottom and the balance of sediment and water supply (Fig.16). The biostrome facies association was deposited in balanced-fill lakes and on low-gradient lake bottoms. The bioherm facies association represents aggradational stacking and the bioherms are restricted

to localized build-ups in a near-shore, littoral setting. This association was deposited in overfilled lakes or balanced-fill lakes with stable shorelines. Tufa-like microbialite facies association is frequently associated with spring-inflow features. This association was deposited in overfilled to balanced-fill lakes.

If the lake type is known (filled status) predications can be made about the potential for the development of thick biohermal sequences, assuming steady subsidence and sufficient accommodation space. If it is concluded that the lake was underfilled, the potential for microbialite growth is severely limited. Abundant ground water in the form of sub-lacustrine springs can have a significant influence on the type of microbialite growth (Jagniecki et al., 2021), such as the tufa-like microbialites (Fig.16). Conversely, if we know the microbialite facies type from a limited perspective, such as a core, we can predict the lake-type.

Figure 12. Some of the microbialite outcrop localities of the Eocene Green River Formation (Utah, Colorado, and Wyoming). Blue lines outline the ancient lakes.

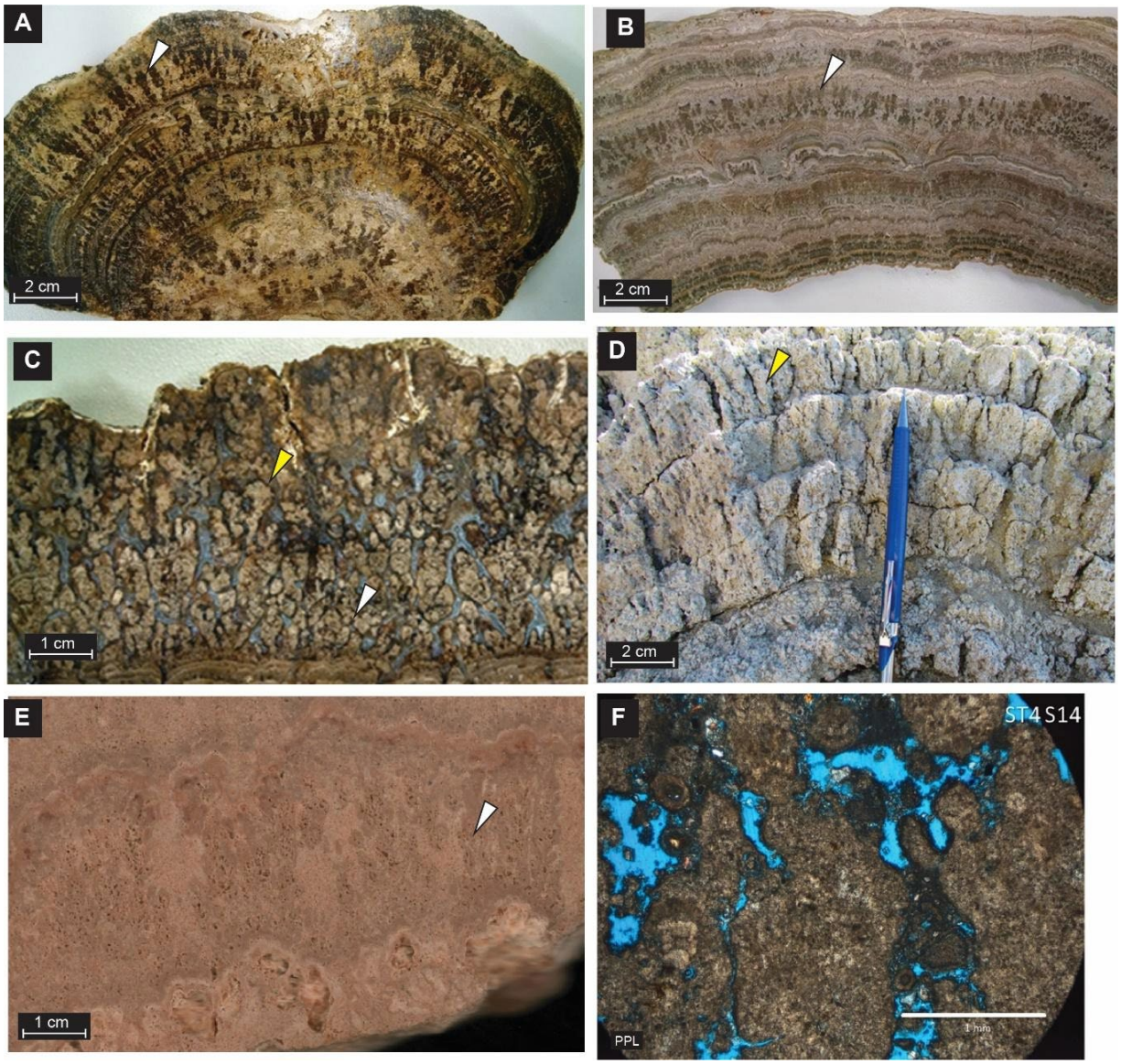

Figure 13. Dendrolites (Shrubs). A) White Mountain South, WY - Tipton Mb. B) Essex Mountain, WY - Tipton Mb. C) Vermillion Creek, CO - Laney Mb. D) Tipton Dugway, Delaney Rim, WY - Laney Mb. E) Vermillion Creek, CO – Laney Mb. F) Micritic microstructure of shrubs from Fig.13E (white arrow).

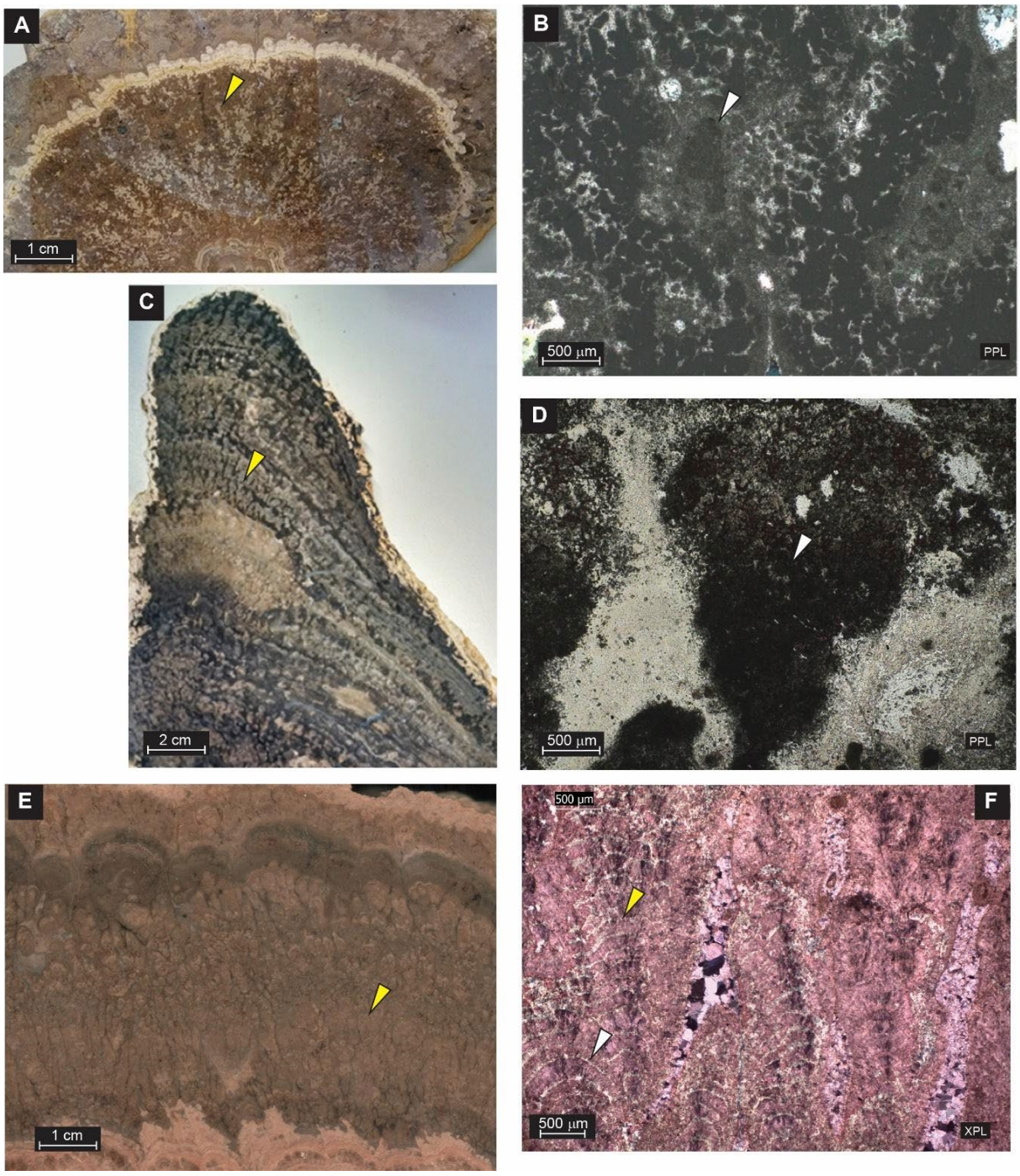

Figure 14. Dendrolites (Shrubs). A) Dripping Rock Springs, WY – Wilkins Peak Mb. B) Photomicrographs of Fig.14A, micritic microbialite microstructure (white arrow) with interspace filled up by grainstone and *Chlorellopsis coloniata* C) Donut Stromatolite, Delaney Rim, WY – Laney Mb. D) Photomicrographs of Fig.14C, micritic microbialite microstructure (white arrow). E) Vermillion Creek, CO – Laney Mb. F) Photomicrographs of Fig.14C, fibrous (yellow arrow) stromatolite (white arrow) microstructure.

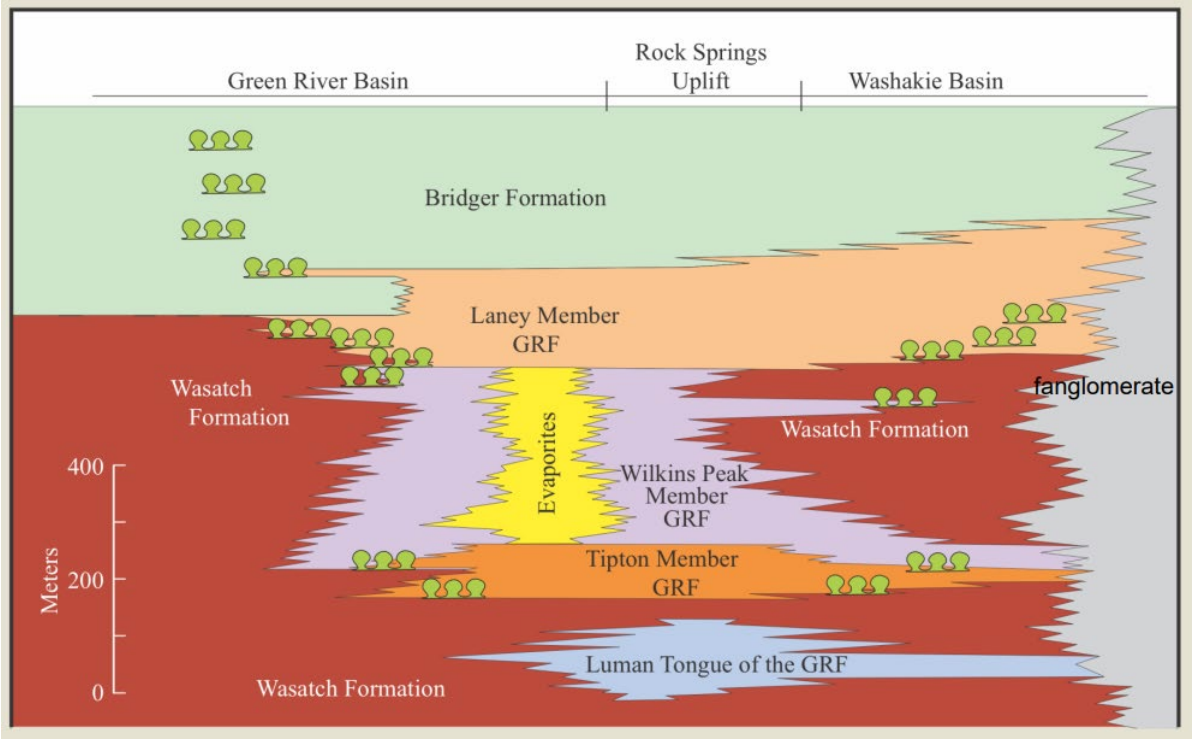

Figure 15. Stratigraphic occurrences of microbialites in the Eocene Green River Formation of Great Green River basin (Buchheim, 2014).

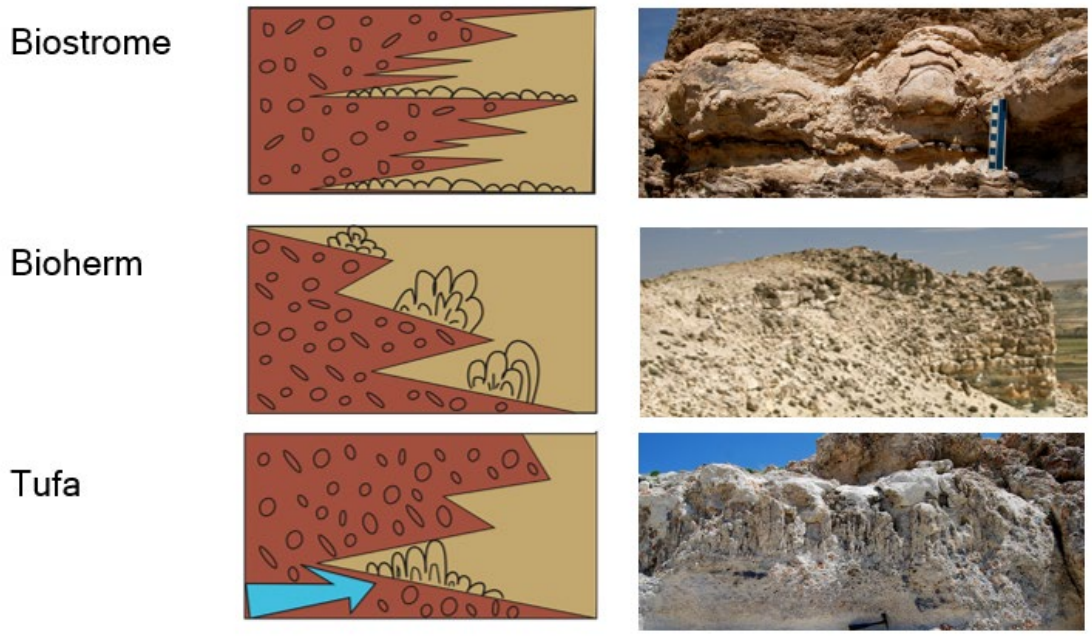

Figure 16. Stratigraphic occurrences of microbialites at transgressive phases of the Green River Formation (Buchheim, 2014).

1.4 Significance of Thesis and Conclusions

The Green River Formation contains the most diverse and abundant microbialites known from lacustrine deposits (Awramik, pers comm, 2022). Paleoenvironmental reconstructions of such microbialite-bearing successions have not been studied in great detail and require integration of various lines of information such as depositional and diagenetic features stratigraphic stacking patterns, mineralogy and geochemistry (stable isotopes, trace elements, organics). It is important to understand the factors that control initiation and development of microbialites, their development into biostromes and bioherms, and their sedimentological context, stratigraphic distribution, and facies relationships.

The objectives of this dissertation are to examine key outcrops in the Green River Formation that have microbialite bioherms and biostromes, and to place these within their stratigraphic framework, their facies architecture, lake chemistry, and relate them to the overall development of the lacustrine lakes system.

The Eocene Green River Formation of Colorado, Utah, and Wyoming is the most studied lacustrine deposit and is an excellent repository for many of the features mentioned above, especially microbialites. This study has four chapters, all dealing with the Eocene Green River Formation. The first chapter is an overview of the Green River and its microbialites. The second chapter examines the paleoenvironmental significance of the authigenic clay mineral stevensite in an embayment of Lake Uinta in Utah. The third and fourth chapters deal with determining the paleoenvironmental significance of microbialites that formed during some saline-alkaline phases of Lake Gosiute in Colorado and Lake Uinta in Utah, soon after the Early Eocene Climatic Optimum (EECO), 52.6–50.3 Ma (Lowenstein et al, 2017). All parts of the study utilize multi-proxy analyses.

Chapter 2 has been submitted to Sedimentology and is in revision, Chapter 3 has been submitted to Sedimentary Geology and is in revision, and Chapter 4 will be submitted to a journal in the near future.

CHAPTER 2

2. Mg-clay of a lacustrine microbialite-bearing carbonate deposit, Eocene Green River Formation, Sanpete Valley, Uinta Basin, Utah.

Daniel F. Cupertino [a,b], Camila Wense Ramnani [b], Michael Vanden Berg [c], and Stanley M. Awramik [a]

[a)] Department of Earth Science, 1006 Webb Hall, University of California, Santa Barbara, CA 93106, USA. (e-mail: dcupertino@petrobras.com.br)

[b)] Petrobras, Research and Development Center (CENPES), Av. Horário de Macedo, 950, Ilha do Fundão, Cidade Universitária, Rio de Janeiro-RJ, 21941-915, Brazil

[c)] Utah Geological Survey, 1594 W. North Temple, Suite 3110, Salt Lake City, UT 84116, USA.

Manuscript submitted and under revision by *Sedimentology*.

2.1 Abstract

Authigenic Mg-clays have been observed and documented in the Green River Formation, specifically as ooidal stevensite grains. Magnesian clays are a valuable proxy for reconstructing shallow-water, saline-alkaline lake paleoenvironments due their responses to chemical changes. Mg-rich clay minerals are relatively common components in modern and ancient lake systems but are unusual in carbonate rocks. A rare interaction of lacustrine magnesian clays, microbialites, carbonates and volcanoclastic deposits of the Eocene Green River Formation that crop out in Sanpete Valley, Utah. The characterization of this interaction, their genesis, the environmental controls on their distribution and accumulation is still barely understood. This study has identified various species of Mg-clay minerals

(stevensite, kerolite, sepiolite and mixed-layer kerolite-stevensite), calcite and dolomite found in four Mg-clay-bearing lithofacies: 1) Mg-Clay-bearing Stromatolites; 2) Mg-Clay Arenites; 3) Mg-Claystone with Calcite Nodules; and 4) Intraclastic hybrid arenites and conglomerates. Stevensite-bearing units record four high frequency depositional cycles defined by the amount of dolomite and their inverse relationship with clay minerals and mica. Mg-clay bearing rocks from the Sanpete Valley area were deposited in southward, shallow embayment of Lake Uinta along the margin of the Sevier fold and thrust belt. Sanpete Valley´s stevensite-bearing section shows syngenetic mineralogical paragenesis with neoformation of magnesian clays accompanied by calcite and silica. All those findings provide a comprehensive analysis of the lithostratigraphic and chemostratigraphic evolution of the lake system, as well as texture classification, providing unique analog for detailed correlation and comparison to other basins containing similar Mg-clay and microbialite-bearing deposits.

Keywords

Stevensite, Mg-clay, Stromatolite, Lacustrine Microbialite, Green River Formation, Sanpete Valley

2.2 Introduction

Lake systems, especially those that are volcanically influenced, can host carbonate and authigenic silicate minerals displaying a variety of unusual fabrics and sedimentary textures. Lake-water chemistry controls carbonate and silicate production, which is influenced by the lithology of the surrounding catchment (Wright, 2012). When waters are alkaline, aqueous silica activity is high, some dissolved magnesium (Mg) is present, and detrital input is relatively low. Substantial amounts of authigenic clay minerals can accumulate in these lakes systems (Deocampo, 2015). Magnesian clays are a valuable proxy for reconstructing saline-alkaline lake paleoenvironments due their complex and rapid response to chemical changes (Tosca and Wright, 2014). Authigenic clays are formed in situ through direct precipitation from solution (neoformation), reaction of amorphous gels, or by transformation of precursor minerals, mainly pyroclastics and detrital clays (Jones, 1986). Mg-rich clay minerals are relatively common components in modern and ancient lake systems but are unusual in carbonate rocks.

2.1.1 Green River Formation stevensite occurrences

The Eocene Green River Formation (GRF) contains excellent examples of microbial carbonates associated with authigenic Mg-clay minerals in saline-alkaline phases of the lake. Mg-clay minerals have been reported at the south margins of the Green River lakes Gosiute (Wyoming) and Uinta (Utah). Bradley and Fahey (1962) identified stevensite associated with carbonate facies of the Wilkins Peak Member of the GRF, which formed when lake Gosiute was at low level and strongly saline. Toward the center of the lake Gosiute center, Bradley and Fahey (1962) found exceedingly fine-grained dolomite, loughlinite and stevensite from Wilkins Peak Mb and interpreted them to be authigenic minerals and may have been

deposited by neoformation directly from a warm, strong brine, or by transformation, formed by a diagenetic process soon after burial (Bradley and Eugster, 1969). Loughlinite has a closed relationship with sepiolite and might have been formed as chemical precipitate under saline or alkaline lacustrine environments (Tank, 1972). Stevensite and loughlinite could form through a reaction involving dissolved Mg and Na with SiO_2 derived from devitrification of volcanic ash. Mg-clays have also been reported near-shore at the south margin of Lake Uinta. Authigenic formation by transformation was the model developed by Dyni (1976) to explain the formation of these deposits. At that area and associated with Parachute Creek member, the presence of trioctahedral illite would suggest a common origin or precursor formation of trioctahedral smectite.

Much of the Mg-Clays' research in the Green River Formation focused on mineralogical characterization, while the petrographic and morphological aspects were left aside. At the southwestern part of Lake Uinta in the Sanpete Valley area, Tettenhorst and Moore (1978, p.588), studying the “coffee-ground” beds of Faulk (1948, p.30), identified ooids composed of stevensite "in a very sparse to abundant matrix of calcite and minor quartz." These stevensite ooids were formed authigenically by precipitation in place in the ancient lake Uinta, also with authigenic quartz, due to their petrographically grain shape and relationship to the ooids (Tettenhorst and Moore, 1978). This was corroborated by SEM Elemental maps of Ca, Mg, and Si (Tettenhorst and Moore, 1978). The relationship of carbonate mineralogy and Mg-clay authigenesis due to cyclical changes in lake water balance, chemistry, and biological activity, was pointed out at the south margin of lake Uinta (Bristow et al., 2012).

Nevertheless, despite their apparent frequent occurrences in these systems, Mg-clays have received little attention from the standpoint of deposition environment. Using an integrated

approach through the application of various analytical methods (X-Ray diffraction, electron microprobe, scanning electron microscope-energy dispersive spectrometry and automated scanning electron microscopy); detailed petrographic analysis coupled with careful field methodology (sedimentary structures recognition, stacking patterns analysis, high resolution stratigraphy), a paleoenvironmental interpretation for the deposition of Mg-clay minerals in this area was carried out. Our objectives here are to characterize this rare interaction of Mg-clay and microbialite deposits and the environmental controls on their distribution and accumulation. Furthermore, by providing a comprehensive analysis of the lithostratigraphic and chemostratigraphic evolution of the lake system, as well as texture classification, this study will allow for detailed correlation and comparison to the other basins containing similar Mg-clay and microbialite-bearing deposits.

2.1.2 Sanpete Valley geology

Lacustrine magnesian clays, carbonate, and volcanoclastic deposits of the Eocene Green River Formation crop out intermittently in Sanpete Valley, Utah. These isolated exposures of the Green River Formation extend southward from the Uinta basin into central Utah along the margin of the Sevier fold and thrust belt. The sediments found there were generated and deposited at the southwestern margin of paleolake Uinta, during its final hypersaline phase. Approximately 46.5 Ma (Lutetian, Eocene), the Green River lakes were in an evaporative regime, with lake Gosiute filled with volcanic sediments from the northern Absaroka volcanic province, while lake Uinta evolved to an underfilled lake, as one broad shrinking saline lake (Smith et al, 2008; Vanden Berg and Birgenheier, 2017) (Fig.17A). Lacustrine sedimentation in the Sanpete Valley area occurred adjacent to a broad alluvial plane, very low depositional gradient, in a nearly closed hydrographic sub-basin, and influenced by a

subtropical climate (Sheliga, 1980). Like in all Green River lakes, frequent plinian eruptions in the Challis and Absaroka volcanic fields produced ash that was carried by prevailing northwest winds into lake Uinta (Smith et al, 2008).

The Green River Formation at Spring City Cuesta in the Sanpete Valley area consists of three distinct lithostratigraphic units, first described by Faulk (1948), and here named from the lower to upper beds: Stevensite-bearing unit, Microbialite-oolite unit and Buff Limestone unit (Fig.17B). The Stevensite-bearing unit corresponds to the first phase of lacustrine deposition and is composed of massive and laminated green and brown mudstones, with significant amounts of calcite and dolomite. These sediments reflect an evaporative draw on both mud flat and lacustrine environments, with authigenic clay minerals forming at the margins associated with saline-alkaline low stands (Sheliga, 1980). Volcaniclastic sedimentation is common in this unit and is recorded by yellow-brown tuff beds (Faulk, 1948). The Microbialite-oolite unit marks a dramatic environmental change with small saline-alkaline lakes being replaced by a larger, fresher lake with little or no mud flat. Sedimentation at this time was dominated by carbonate deposition, thrombolites, stromatolites, oolitic grainstones, ostracods, gastropods, caddisfly larval cases, chert beds (Faulk, 1948). Caddisfly cases also occur. At the base of the Buff Limestone unit, a tawny brown tuff marks the last lake environmental change of the GRF in the Sanpete Valley area. This tawny brown tuff records the influence of the regional north to south basin-fill of Green River lakes with volcanoclastic sediments of the Challis and Absaroka region (Fig.17A). Precise age dating allows direct comparison of the lakes to global climate changes, and of lake types associated with different coeval basins. Sanidine and biotite grains from the Green River tuff layers have been dated using $^{40}Ar/^{39}Ar$ techniques and used for strata correlation

between the greater Uinta Basin and the Sanpete Valley sub-basin $^{40}Ar/^{39}Ar$ biotite ages of the Sanpete Valley tuffs were obtained by Sheliga (1980). The coarse tuff, which corresponds to Sheliga´s WCT tuff, was reported having a $^{40}Ar/^{39}Ar$ biotite age of 46.35 ±1.12 Ma. The jutting tuff, which corresponds to Sheliga´s ET#8 tuff and Faulk's #16 tuff, was reported with a $^{40}Ar/^{39}Ar$ biotite age of 43.34 ±0.64 Ma (Fig.18).

We used U-Pb dating of detrital zircon grains to provide better resolution of two Sanpete Valley tuff beds: the coarse tuff and the tawny tuff (Fig.18, 19).

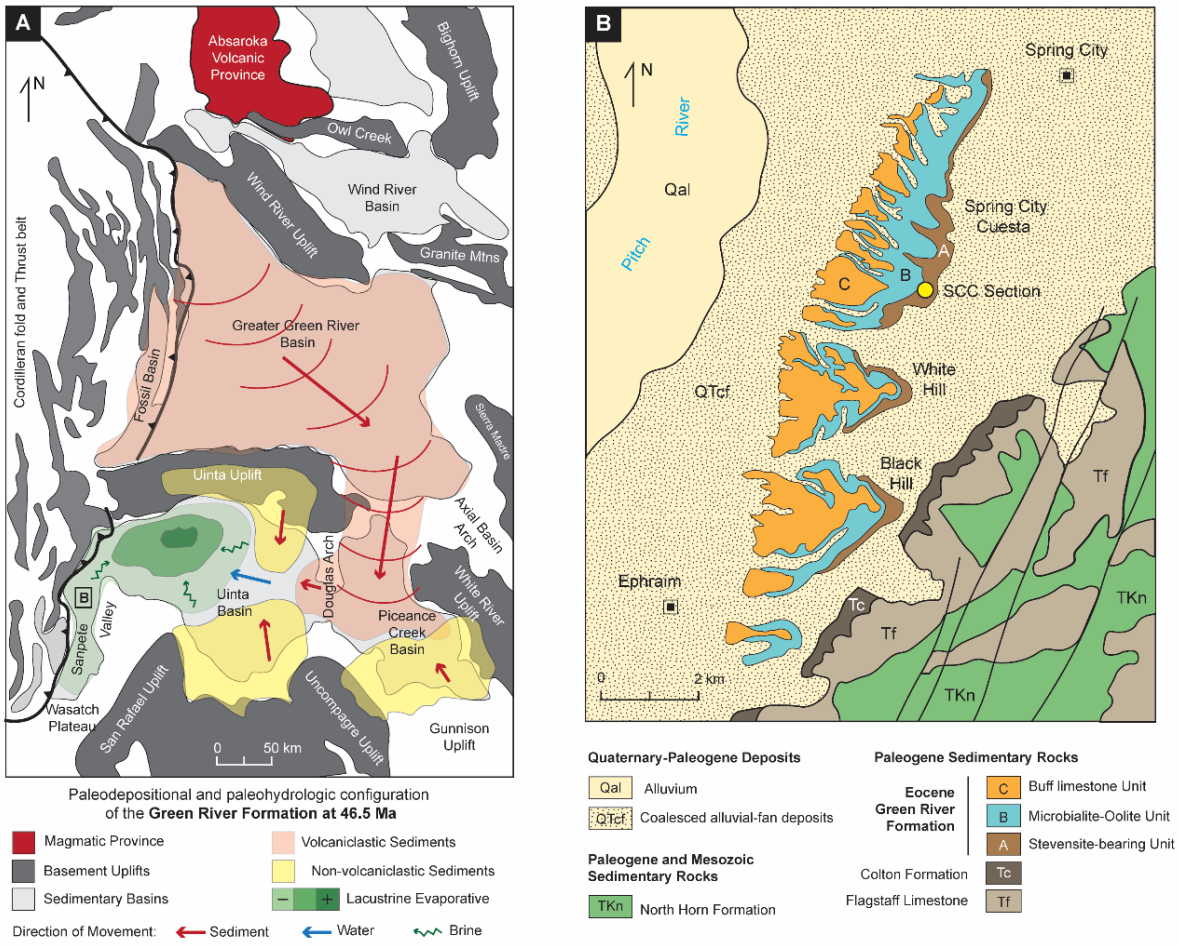

Figure 17. A) Map showing hydrology and sediment depositional patterns of the Green River Formation lakes at 46.5 Ma (modified after Smith et al., 2008; Vanden Berg and Birgenheier, 2017). B) Simplified geological map and location of the studied Spring City Cuesta section in the Sanpete Valley, Utah (modified from Faulk, 1948).

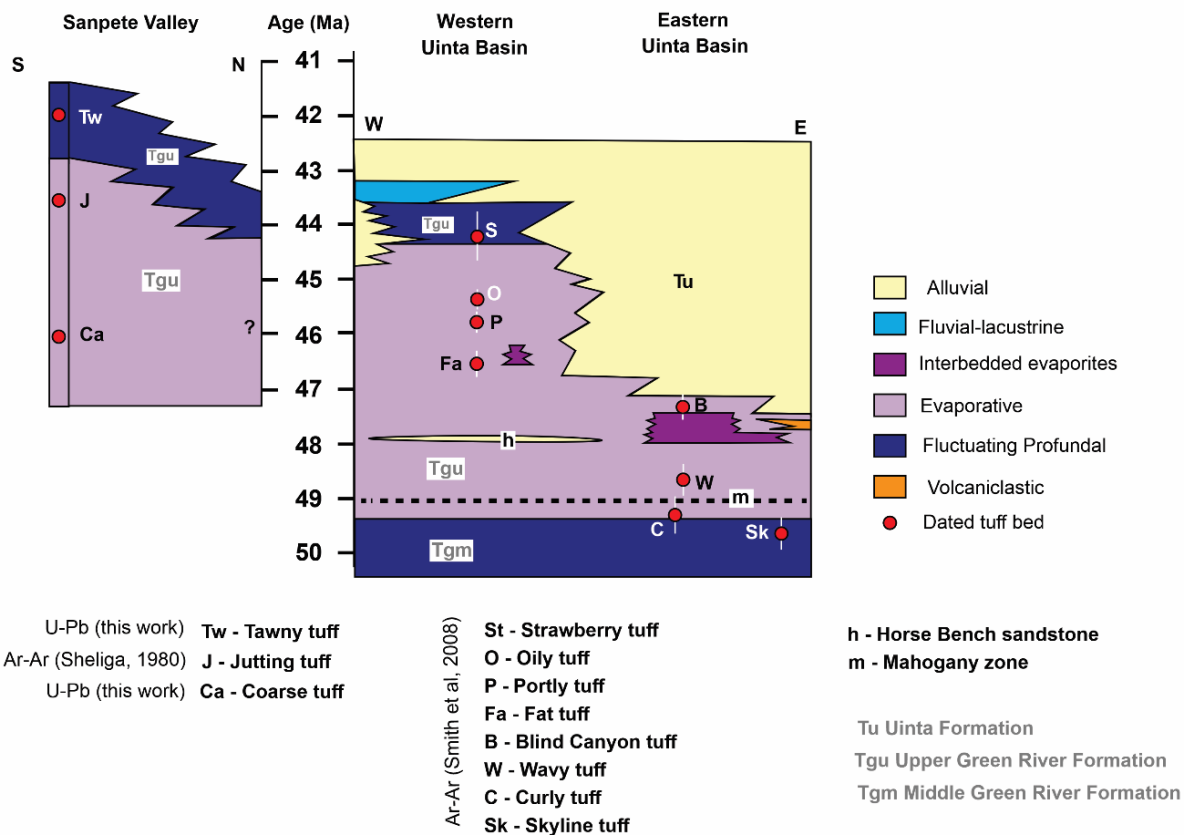

Figure 18. Chronostratigraphy of the Upper Green River Formation of Uinta Basin and Sanpete Valley, Utah using known age constraints (Smith et al., 2008, 2015) and new U-Pb geochronology data from Sanpete Valley. This figure also shows the stratigraphic position of facies associations and dated tuff beds.

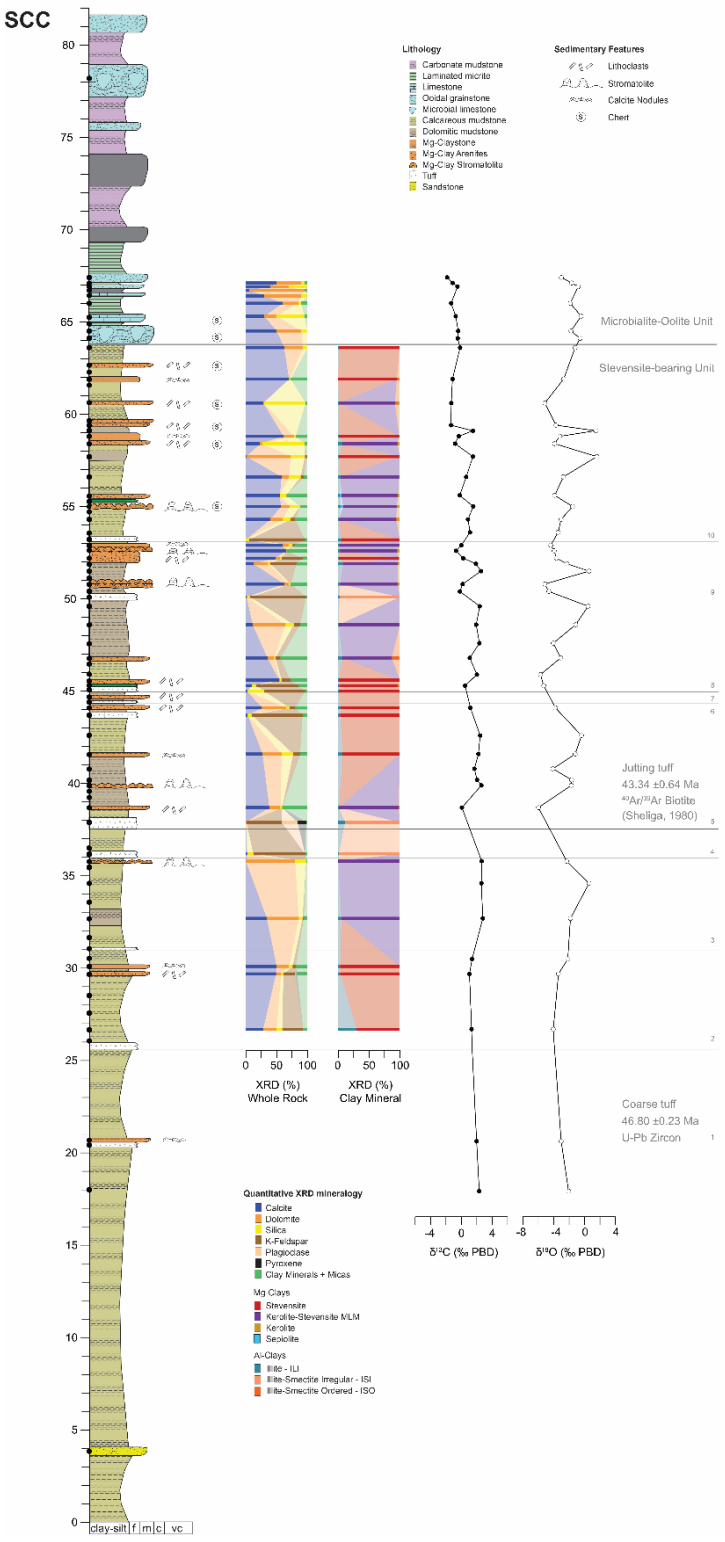

Figure 19. Spring City Cuesta measured section (SCC) of the Green River Formation in Sanpete Valley showing detailed lithology, XRD measurements bulk rock (weight percent), clay fraction (weight percent), and $\delta^{13}C$ and $\delta^{18}O$ stable isotopes. Tuff´s geochonology data: Biotite $^{40}Ar/^{39}Ar$ ages (Sheliga, 1980) and Zircon U-Pb ages (this study) are show with 2σ analytical uncertainties.

2.2 Materials and Methods

One 40 m detailed stratigraphic section was measured at Spring City Cuesta with the aim of characterizing the fine-grained sediments and Mg-clay-bearing beds. The Spring City Cuesta's measured section (Fig.19) with its description was carried out at the millimeter and centimeter scale to achieve a high-resolution stratigraphic record. Detailed facies analysis was performed using 81 hand samples collected from the outcrop at the location, and polished slabs were prepared from all the samples. Analytical methods are outlined below.

Sedimentary petrography

Petrographic analyses were conducted both macroscopically and microscopically on 40 polished slabs and 30 thin sections. A LEICA DM 2500P transmitted light petrographic microscope was used to describe the mineralogy, textures, grain types, diagenesis, and carbonate fabrics of all samples. The standard carbonate Dunham classification modified by Wright (1992) and Flügel (2010), and microbialite terminology by Grey and Awramik (2000), were used to classify carbonate samples based on meso- and micro-scale textures.

XRD

Quantitative XRD bulk mineralogical analyses were made at Materials Research Laboratory at University of California at Santa Barbara (UCSB). An aliquot of each sample was ground in an agate mortar. Randomly oriented powder was pressed in a specific sample holder for X-ray irradiation. Qualitative analysis was obtained at Petrobras Research and Development Center in Rio de Janeiro with the software Jade 9 of the Materials Data Incorporated Company (MDI, 2015) using the data base of minerals PDF-2 of the International Centre of Diffraction Data (ICDD, 2013). Quantitative analyses were realized through the Rietveld

Method (Young, 1995) with HighScore software. The analyses were performed in a Panalytical Empyrean Powder Diffractometer, under 40mA and 45kV.

Clay mineral analyses were performed at Petrobras Research and Development Center in Rio de Janeiro. The XRD patterns of the clay minerals (<2 μm fractions) were obtained from oriented preparations. The samples were crushed gently in an agate mortar and then dispersed into distilled water using ultrasonic treatment. The <2 μm fractions were separated by centrifugation and the resulting paste was smeared on glass slide for clay orientation (Thiry, 1974). The analyses were performed in the RIGAKU D/MAX – 2200/PC X-ray diffractometer under 40mA and 40kV. The oriented preparations were analyzed in air-dried state, in an ethylene glycol solvated state and heat at 490°C. The composition of mixed-layer clay minerals was estimated using NEWMOD software (Reynolds, 1985).

Carbon and oxygen stable isotopes

Forty-seven micro-powdered samples were collected using a Dremel micro-drill tool and analyzed for stable isotopes of oxygen and carbon. The isotope analyses were performed in Thermo-Finnigan DELTAplusXP MAT isotope ratio mass spectrometer (IRMS) coupled to a Finnigan™ GasBench at the Marine Science Institute Analytical Lab (UCSB). Isotope ratios ($\delta^{13}C$ and $\delta^{18}O$) are reported using the PDB standard. Analytical uncertainties (1σ) are assessed by repeat analyses of the NBS 19 standard and accounts for ± 0.07 ‰ and ± 0.18 ‰ $\delta^{13}C$ and $\delta^{18}O$, respectively.

Electron Microprobe Analysis (EMPA)

The electron microprobe analysis was undertaken by Regional Center for Technological Development and Innovation (CRTI) at Federal University of Goiás, Brazil. For the

acquisition of chemical analyses, thin sections were covered by a thin carbon layer and then examined by a JEOL JXA-8230 electron microprobe, under 15Kv and 20 nA for silicate minerals analysis and under 15kV and 5nA for carbonate minerals analysis.

To calculate the structural formula of clay minerals by EMPA, it is necessary to know the crystalline structure of the species to be analyzed (the group to which the clay mineral analyzed belongs). This information was previously obtained with XRD analysis. For the calculation of the structural formula, a dehydrated base was considered for the unit cell since the analysis by electronic microprobe does not perform the reading of hydrogen. Thus, for 2:1 type phyllosilicate, the basis for calculation was 22 oxygens for kerolite, smectites, micas and mixed-layer kerolite-smectite.

Automated Mineralogical Mapping by SEM

The automated mineralogical mapping by scanning electron microscopy was acquired at Petrobras Research and Development Center. Thin sections of five samples were covered by a thin carbon layer and analyzed with a FEI-QEMSCAN 650 scanning electron microscope operating in high vacuum at 15 kV, using backscattered electron imaging. Semi-quantitative analysis with energy dispersive X-ray spectroscopy (EDX) was performed using two detectors, with a 10 μm resolution. The mineralogical maps show the spatial distribution of rock phases (minerals and pores), the relationship between them and their abundance (area and mass percentage).

LASS zircon

U–Pb isotope and trace-element analysis of zircons were determined at University of California, Santa Barbara, following the methods outlined in Kylander-Clark et al. (2013).

The laser-ablation split-stream system combines a Photon Machines 193 nm ArF Excimer laser, equipped with a Hel-Ex ablation cell, with a Nu Instruments HR Plasma high-resolution MC-ICP-MS system for collecting U-Pb isotope data, and an Agilent 7700 quadrupole ICP-MS for determining trace-element concentrations. The laser parameters for analysis consisted of a 25 μm spot ablated at ~1 j/cm^2 and 4 Hz for 15 seconds, following a 20 second baseline and two-shot pre-ablation. Unknowns were bracketed by zircon reference material 91500 (Wiedenbeck et al., 1995); RMs GJ1 (Jackson et al., 2004), Plešovice (Sláma et al., 2008) were included occasionally for quality control; GJ1 and Plešovice yielded average ages within 2% of their accepted values. For element concentration analyses, ^{90}Zr was used as the internal standard and GJ1 (Liu et al., 2010) was used as the reference material. Raw U-Pb isotope and trace-element data were reduced using Iolite v3 (Paton et al., 2011) to correct for instrument drift, laser-ablation-induced down-hole elemental fractionation, plasma-induced elemental fractionation, and instrumental mass bias.

2.3 Results

This study has identified various species of clay minerals: stevensite, kerolite, sepiolite, illite and mixed layer kerolite-stevensite and illite-smectite distributed in distinct lithofacies in the Sanpete Valley.

2.3.1 Main Mg-clay-bearing Lithofacies

Unusual mineral assemblages of Mg-clays, calcite and dolomite are found in four Mg-clay-bearing facies: 1) Mg-Clay-bearing Stromatolites; 2) Mg-Clay Arenites; 3) Mg-Claystone with Calcite Nodules; and 4) Intraclastic hybrid arenites and conglomerates. Mg-clays

(stevensite, kerolite, and mixed-layer kerolite-stevensite) comprise most the clay fraction of all facies, except for the tuffs, where the Al-clays (Al-smectites, Al-micas, and illite-smectite) dominate.

Facies 1: Mg-Clay-bearing Stromatolites

Microbialites can form in a wide range of environments. At Sanpete Valley, unique stromatolites composed of distinct laminations of mixed-layer kerolite-stevensite intercalated with micritic laminae were found in Mg-clay-bearing unit at the lower section of Spring City Cuesta (SCC) (Fig.19, 20). Following the hierarchy of observational levels for microbialites (Grey and Awramik, 2020), the predominant macrostructure shape is domical, with rounded tops and heights up to 15cm (Fig.20A). Columnar stromatolites are the second predominant shape of occurrence at SCC Section (Fig.20B). The columns are slender and widths less than 4cm and up to 10 cm tall. At the top of the section, thrombolites co-occur with caddisfly larval cases suggesting fresher water (Faulk, 1948).

The domical-shaped stromatolites show a diverse mesostructure with distinct Mg-clay/Calcite laminae. Minicolumnar stromatolites, ranging from 2 to 4mm in diameter, are one of the stromatolitic mesostructure types and have bifurcate branching (Fig.20C). The continuity of laminae within the minicolumns is irregular especially in Mg-clay laminae. Another mesostructural type is the compound stromatolite formed by pseudocolumnar and minicolumnar stromatolites (Fig.20D). The Mg-clay laminae in this type are composed of 94% kerolite-stevensite. Nodular domical stromatolites, form the third stromatolitic mesostructured type (Fig.20E). The diameter of the base is less than the maximum diameter. Nodular domical stromatolites show higher Mg-clay/calcite ratios when compared to the other stromatolite types described above.

At the microstructure scale, in most stromatolite types, kerolite-stevensite laminae are the primary constituent, as a major matrix precursor, followed by micrite, as an early syn-depositional diagenetic constituent (Fig.21A, B). Early micritization is related to kerolite-stevensite dissolution and replacement (Fig.21C, D). Radiating or divergent kerolite-stevensite crystals, emanating from a common point, are partially dissolved and cemented by microcrystalline quartz. Some samples display microcrystalline pore-filling quartz cement (Fig.21 E, F).

Facies 2: Mg-Clay Arenites

Massive, well to moderately sorted arenites composed of coated grains of kerolite and stevensite clay minerals that are cemented by micrite (Fig.22A). These Mg-clay grains are moderately to densely packed, ranging from 1 to 4mm in size. Grain nuclei are commonly dissolved and replaced by quartz (Fig.22B). Kerolite-stevensite ooids and kerolite-stevensite coated carbonate particles are often present and have very thin alternation of light and dark asymmetric laminae and syn-depositional grain deformation by compaction (Fig.22C, D). Mg-clay ooid nuclei are heterogeneous. They are composed by an often-preserved single nucleus of skeletal grains (ostracods), lithoclasts or peloids (Fig.22E, F). Some micritic ooids have microborings. Frequently, as chemodiagenetic alteration, ooid nuclei are replaced by microcrystalline silica, and sometimes they are completely silicified. Microcrystalline silica also fills vugs, interparticle space, and fracture pores. Quartz mosaic cement occurs in small amounts filling interparticle porosity of the Mg-Clay arenites.

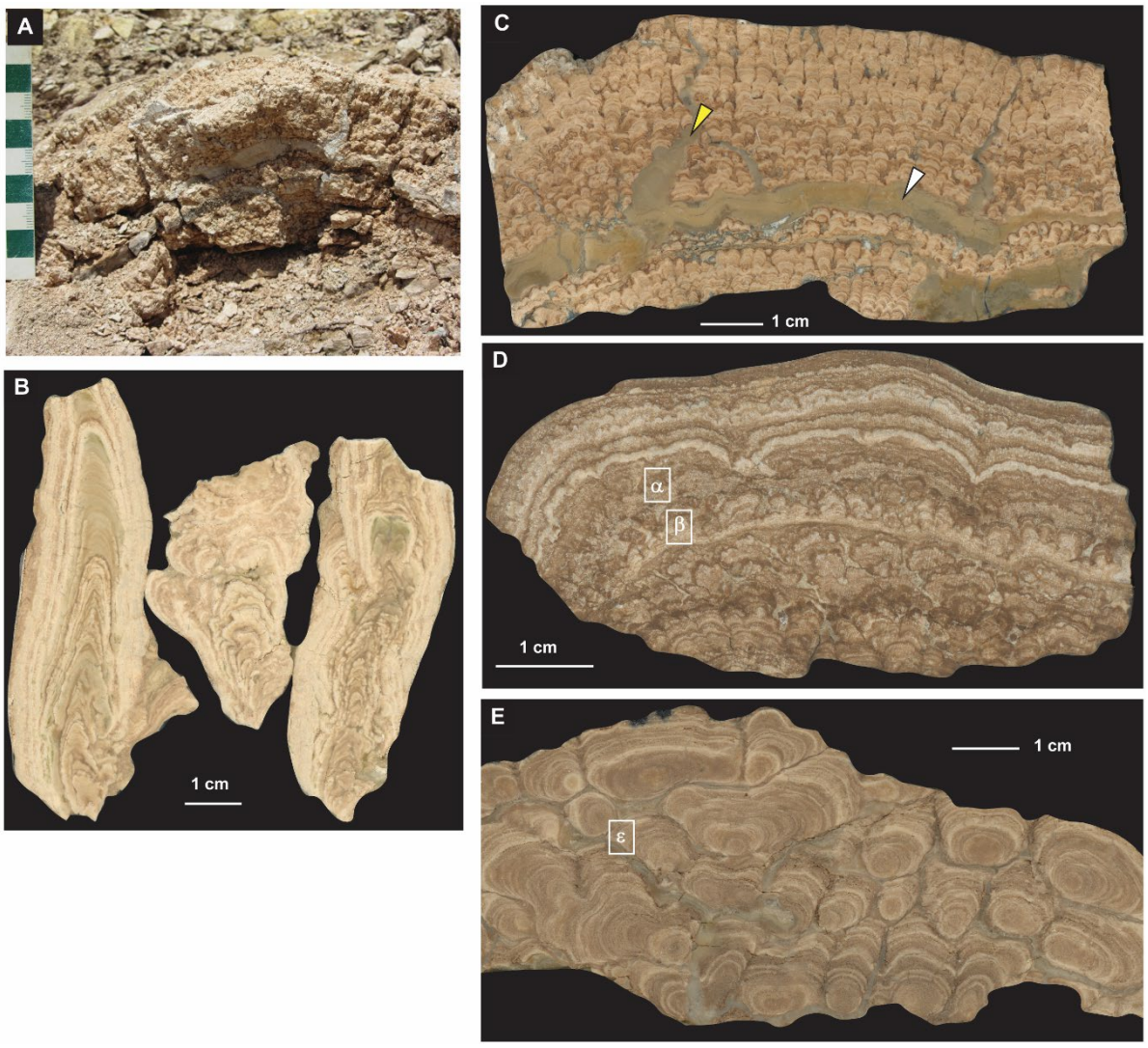

Figure 20. Types of Mg-clay stromatolites: A) Domical stromatolite (outcrop view); B) Columnar stromatolite; C) Minicolumnar stromatolites (mesostructure scale) with intercalated light (calcite) and dark (kerolite-stevensite mixed layered minerals (K-S)) laminae, early diagenetic silicification (white arrow) and late fracture-filling quartz (yellow arrow), slabbed sample of Fig.5A; D) Compound stromatolite (pseudocolumnar and minicolumnar stromatolites) with intercalated light (calcite) and dark (K-S) laminae. E) Nodular domical stromatolite.

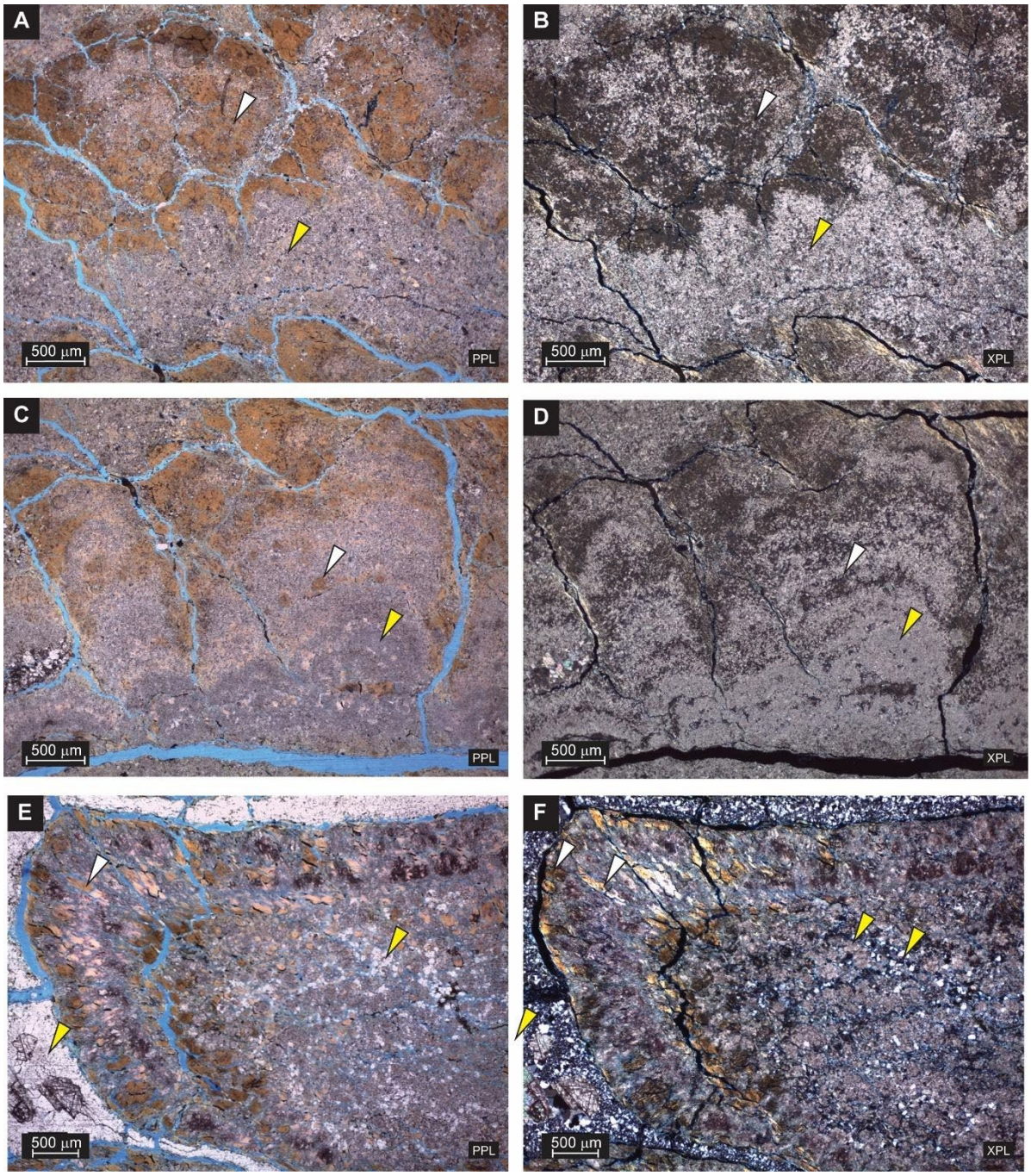

Figure 21. A) Minicolumnar stromatolite microstructure from Fig.4D(α). K-S crystal aggregates (white arrow), partially replaced by microcrystalline calcite crust (yellow arrow); plane-polarized light (PL); B) crossed-polarized light (XPL). C) Minicolumnar stromatolite microstructure from Fig.4D(β). Variable thickness of the micritic laminae (yellow arrow) intercalated with K-S crystal aggregates; some of K-S are partially replaced and engulfed by calcite crystals (white arrow) (PL); D) (XPL). E) Nodular domical stromatolite microstructure from Fig.4E(ε). Divergent radial K-S minerals (white arrow), within stromatolite nodules; partial dissolution and replacement by quartz crystals (orange arrow) and quartz mosaic cementation among nodules (yellow arrow) (PL); F) (XPL).

Facies 3: Mg-Claystone with Calcite Nodules

These syngenetic laminated magnesian clay deposits are mainly composed of kerolite-stevensite. Mg-claystones were often dissolved and/or replaced by displacive calcite nodules, microcrystalline silica, and dolomite. Calcite nodules are the most common diagenetic constituent (Fig.23A, B), sometimes in association with teepee structures (Fig.23). The diameter of the calcite nodules ranges between 0.1 to 3 mm. A few of them have recognizable nuclei made of clay peloids. A well-defined nucleus is rare. Calcite nodules frequently displace and deform what was the unconsolidated Mg-clay sediment. Shrunken and partially dissolved kerolite-stevensite laminations are common and are often replaced by recrystallized calcite rhombs and aggregates (Fig.23C-F).

Facies 4: Intraclastic Mg-clay hybrid arenites and conglomerates

Massive intraclastic hybrid arenites and massive intraclastic hybrid clayey conglomerates are the two types of intraclastic Mg-clay-bearing rocks frequently observed at SCC. The classification of hybrid rocks used followed Armelenti et al. (2016). The main constituents of intraclastic arenites are fragments of reworked Mg-claystone, calcite nodules, dolomitic marlstone, stromatolites, and tuff. They are poorly to well-sorted. Most intraclasts are rounded, ranging between 0.5 to 3 mm, with less frequent tabular 0.5 to 1 cm fragments (Fig.24A). Microcrystalline calcite commonly fills interparticle pore space. Mg-claystone and Mg-clay arenites often are deformed (Fig.24B). Mg-clay matrix is a common constituent in intraclastic rudstone (Fig.24C). Aggregates of calcite and rhombs show well defined habits and displacive features in relation to the surrounding clay matrix, suggesting it has formed in situ, as a replacive eodiagenetic process. (Fig.24D).

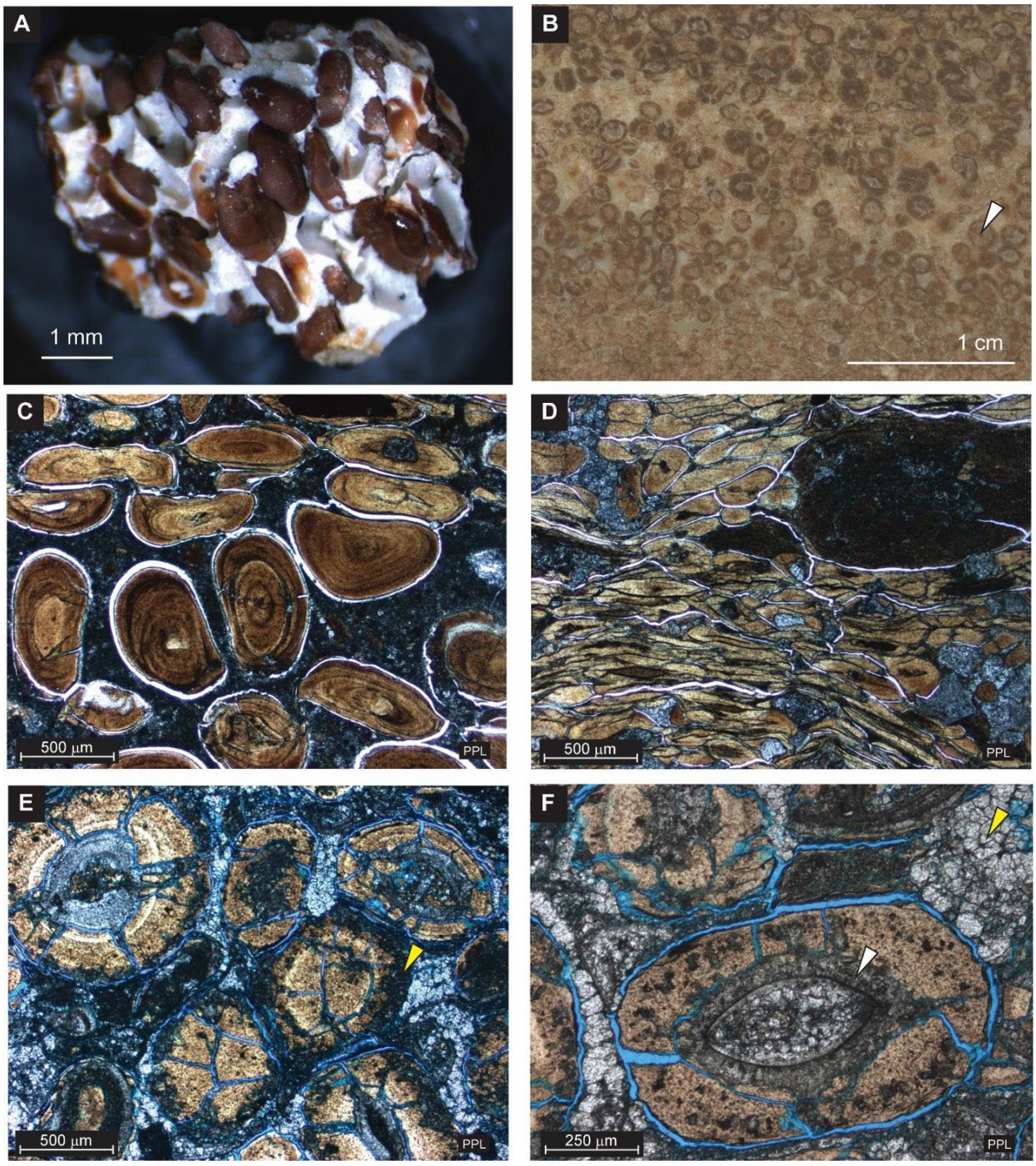

Figure 22. Mg-Clay Arenites: A) kerolite-stevensite coated grains and peloids cemented by micrite; B) Massive, well to moderately sorted Mg-clay arenites showing grain nuclei replaced by quartz. C) Kerolite-stevensite ooids; very thin alternation of light and dark laminae, often deformed. D) Strong mechanical compaction of the Mg-clay coated grains. E) Ooids nuclei formed by intraclasts and peloids. Note presence of what appears to be microborings in ooid cortex (yellow arrow) F) Single nucleus of articulated ostracod, replaced by microcrystalline silica (white arrow) and quartz mosaics filling interparticle porosity (yellow arrow).

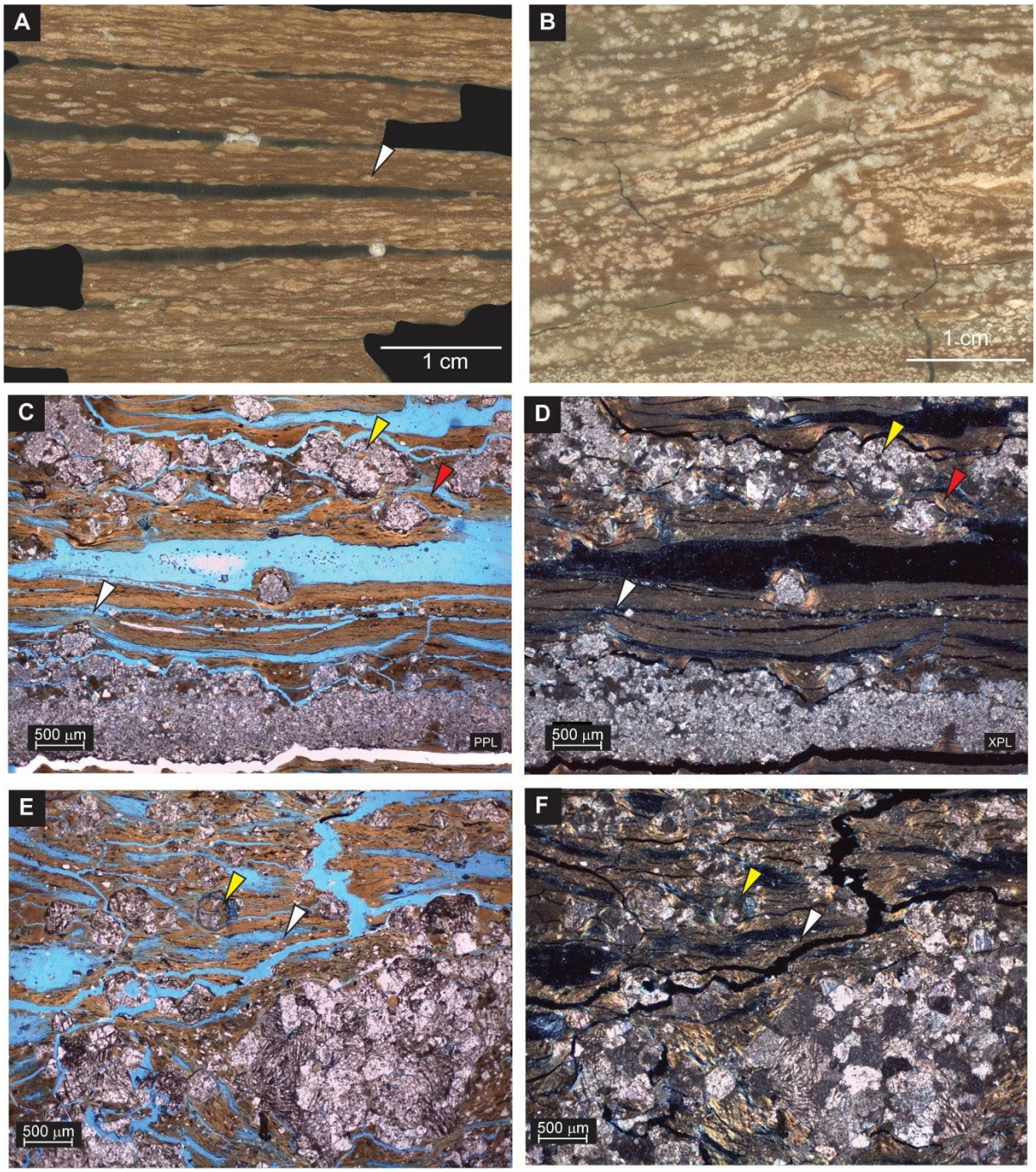

Figure 23. Mg-Claystone with Calcite Nodules. A) Laminated kerolite-stevensite claystone with calcite nodules (white arrow); B) K-S claystone with teepee structure and displacive calcite nodules and crystals; C) Micrite aggregates (nodules) displacing and replacing Mg-clay laminae (yellow arrow), that are shrunken and partially dissolved (white arrow) K-S laminations, displacing K-S laminations, and aggregates (red arrow) (PL); D) XPL; E) Calcite rhombs within K-S lamina (white arrow), K-S minerals preserved in calcite aggregates (yellow arrow) (PL); F) XPL.

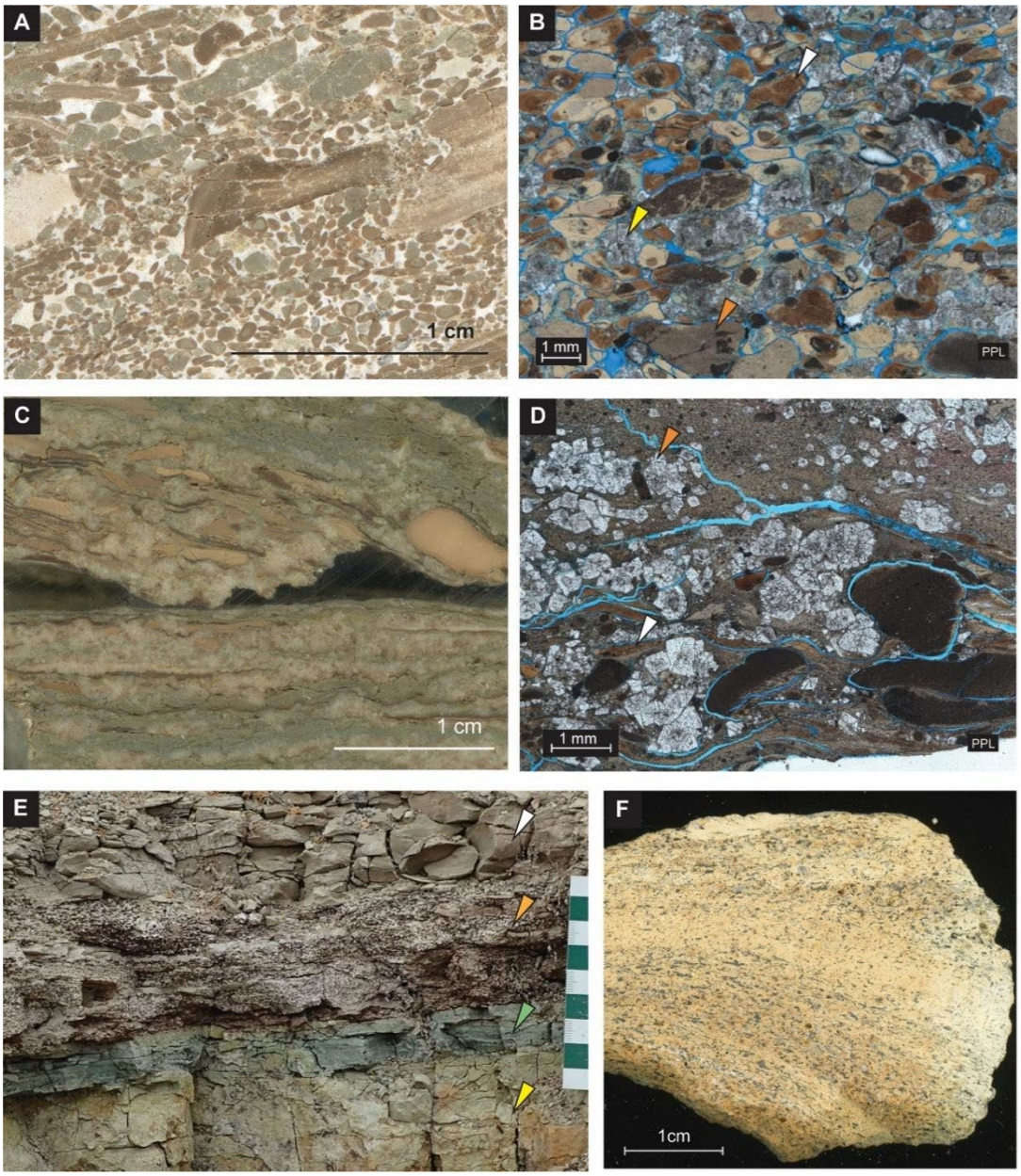

Figure 24. Mg-Clay hybrid rocks and tuff. A) Intraclastic, ooidal Mg-clay hybrid arenites with flattened and rounded Mg-clay intraclasts and ooids, besides carbonate intraclasts in a micrite cement; B) Massive intraclastic hybrid arenite composed of fragments of reworked Mg-claystones intraclasts (white arrow), calcite aggregates (yellow arrow), and dolomitized marlstone (orange arrow). Mg-clay intraclasts are commonly rounded (PL); C) Hybrid clayey conglomerate, composed of intraclasts of dolomitized marlstone, tuffs, calcite nodules and Mg-claystones; D) Mg-clay and Al-claystone intraclasts in a laminated stevensite matrix, which is partially replaced by calcite rhombs. (PL). E) Spring City Cuesta section outcrop showing sedimentary succession with tuff (yellow arrow, Fig.9F) weathered tuff (green arrow), Mg-clay arenites (orange arrow) and dolomitic marlstone (white arrow); F) Tuff showing phenocrystals of sanidine, biotite, and hornblende.

Tuff

At least ten distinct tuff beds occur in the SCC section. Most of them are associated with Mg-clay-bearing rocks and form resistant ledges, 20 to 70 cm thick. Tuff, weathered tuff, Mg-clay arenites, and dolomitic marlstone are repeated in the sedimentary succession (Fig.24E). Tuffs with dark minerals occur sporadically (Fig.24F). According to Sheliga (1980), phenocrysts of biotite, hornblende, and a mixture of sanidine and adularia occur in significant amounts, and quartz and plagioclase in minor amounts. These are the main minerals of these tuffs. Air fall is interpreted to be the most likely depositional process for these tuffs, since euhedral crystals of sanidine, biotite and hornblende are common.

2.3.2 XRD: Bulk mineralogy and Clay Fraction Mineralogy

Bulk Mineralogy

All facies, except for the tuffs, consist mainly of calcite, dolomite, clay minerals and mica, with minor feldspar and quartz. The variation of bulk mineralogy in weigh percentage per sample in relation to stratigraphic position is plotted in Figure 19. Thirty-three bulk mineralogy samples from Mg-clay-bearing units were grouped in three sets: (a) Mudstone (Calcareous mudstone, Dolomitic mudstone), (b) Mg-Clay facies (Mg-Clay Stromatolites, Mg-Clay Arenites, Mg-Claystone), and (c) Tuffs. The minerals were statistically analyzed by sets (Fig.25).

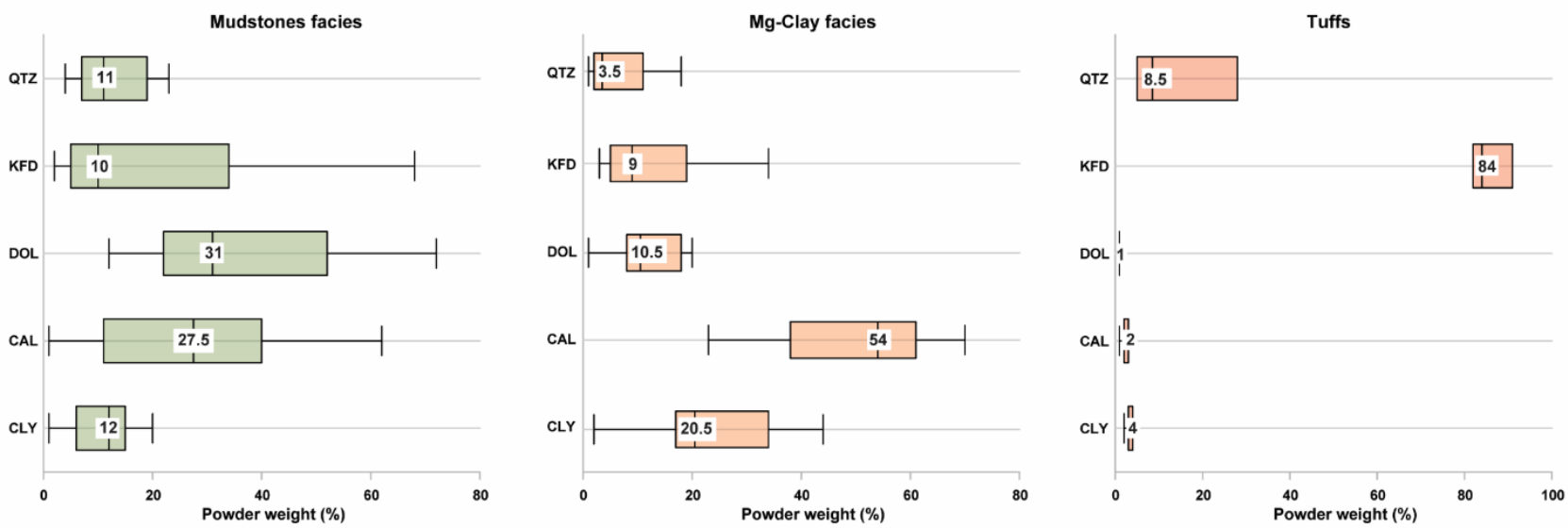

Figure 25. Bulk mineralogy from quantitative XRD analysis. Box plots showing median and interquartile range of minerals (weight percentage) grouped in three sets: Mudstone facies (Calcareous and Dolomitic mudstone), Mg-clay facies (Mg-clay stromatolite, Mg-clay arenites and Mg-claystone) and tuffs. QTZ: Quartz; KFD: k-feldspar; DOL: dolomite; CAL: calcite; CLY: clay minerals and mica.

The Mudstone facies is composed of terrigenous and chemical clay-sized material. Dolomite (31% μ) and calcite (27.5% μ) are the dominant minerals. These authigenic minerals comprise 58.5% μ of the mudstone facies. Dolomite and calcite appear to vary in abundance within mudstone facies samples in the vertical section (Fig.19). Clay minerals and mica make up 12% μ of the mudstone facies and include both terrigenous (Al-clay minerals: illite, smectite) and authigenic minerals (stevensite, kerolite) (Fig.19, 25). Similar weight percentages of quartz (11% μ) and k-feldspar (10% μ) make up the mineralogy of terrigenous minerals.

The Mg-Clay facies presents an overall mean composition of the samples of 54% calcite, 20.5% clay minerals, 10.5% dolomite, 9% k-feldspar, and 3.5% quartz (Figure 25). This composition varies in samples from the measured section, degree of diagenetic modifications and with lithofacies (Fig.19). When compared to the Mudstone facies, the Mg-clay facies shows higher calcite component percentage and a decrease in dolomite, indicating that there may be a primary control (deposition) in rock mineralogy.

The mineral assemblage of tuffs is characterized by the presence of abundant potassium feldspar (84% μ), low abundance of quartz (8.5% μ) and clay minerals and mica (4% μ), minor calcite (2% μ) and dolomite (1% μ). Significantly, authigenic potassium feldspar is the most common constituent of most of the tuffs in the evaporative phases of the Green River basins. Tuffs show a slight mineralogical variation in relation to stratigraphic position (Fig.19).

Clay Fraction Mineralogy

Mg-clay minerals (stevensite, kerolite, sepiolite and mixed-layer kerolite-stevensite) comprise most the clay fraction of all facies, except for the tuffs, where the Al-clays (Al-smectites, Al-micas, and illite-smectite) dominate (Fig.19). Stevensite and kerolite-stevensite are the two main species of clay minerals on most of the samples' diffraction patterns. Figure 26 shows some examples from the Mg-Clay arenite and Intraclastic Mg-Claystone hybrid arenite samples. The diffraction patterns of the clay fraction also show small amounts of mica, mainly illite, and illite-smectite. Kerolite-stevensite of the Mg-clay-bearing lithofacies contains a relative high fraction of stevensite (80% stevensite), as observed in the fit between experimental and calculated patterns shown in Figure 26C. Mudstone lithofacies (calcareous and dolomitic mudstones) are characterized by stevensite, kerolite-stevensite and illite. Illite has a detrital origin. Tuff lithofacies show a high abundance of irregular illite-smectite (mixed-layer rich in smectite) and low abundance of Al and Fe-smectites.

2.4.3 Electron Microprobe Analysis (EMPA): Chemical composition of Mg-Clay minerals

Chemical Compositions: M+-4Si-R2+ ternary system

Four samples [Mg-claystone (Fig.23A), Mg-clay arenite, Intraclastic Mg-claystone hybrid arenite (Fig.24C), and Mudstone] were selected for chemical analysis by electron microprobe. All the chemical composition results were graphically represented by a M+-4Si-R2+ ternary graph (Fig.27). In this diagram, two clusters of clay minerals can be seen.

In the first cluster, most of the chemical analysis results are in the field of stevensite toward kerolite and sepiolite minerals. This cluster results occurs in the Mg-clay bearing lithofacies. The second cluster is related to the tuff facies and is composed of Al-smectites and Al-micas with iron (celadonite) and magnesium (biotite).

Average Structural Formulae

Two samples [Mg-Claystone Facies (Fig.23A, Fig.28AB) and Intraclastic Mg-Claystone hybrid arenite (Fig.24C, Fig.28CD)] were selected for determination of the Mg-Clay structural formula (Tab.1). Thirty clay mineral points, 10 rhombohedral dolomite points, and 5 calcite points were performed for each sample. The hydrated phyllosilicates analyzed by electronic microprobe were: kerolite, stevensite, micas and mixed-layer kerolite-stevensite.

Stevensite (smectite group) was identified in these two samples (Mg-claystone and Intra Mg-clay). The petrographic, XRD and SEM analyses indicate that these claystones are mainly consist of calcite, dolomite, k-feldspar, Mg-smectite, illite and quartz.

Stevensite has a tetrahedral layer formed mainly by Si, with small amounts of Al (Table 1). The octahedral layer is formed mainly by Mg, with small amounts of Al, Fe, Ti and traces of Ni, Mn, V and Cr. The interlayer space is formed by Ca, Na and K, but it is possible that some of this Ca resulted from the contamination of underlying calcite, due to the large amount of this mineral in the samples (i.e., the microprobe beam picked up some Ca from the calcites). Also noted was the occurrence of small amounts of fluorine in the analyzed stevensite.

Table 1. Electron microprobe analysis of clay minerals and average structural formulae.

Sample Mg-claystone: Mg-claystone with calcite nodules (Fig.28A, B); Intra Mg-clay: Intraclastic Mg-clay hybrid arenite (Fig.28C, D).

Sample	SiO_2	Al_2O_3	Fe_2O_3	NiO	MnO	TiO_2	V_2O_3	Cr_2O_3	MgO	CaO	K_2O	Na_2O	F	Total
Mg-claystone P1	52.19	1.60	1.08	0.01		0.07	0.01	0.01	23.13	1.02	0.26	0.09	1.08	80.56
Mg-claystone P3	51.50	1.58	1.09		0.02	0.06	0.02		22.51	0.34	0.22	0.06	1.21	78.61
Mg-claystone P7	50.32	1.40	0.74		0.01	0.04	0.03		22.41	0.94	0.18	0.07	0.91	77.02
Intra Mg-clay P60	49.00	2.05	1.99	0.02	0.01	0.02			21.37	0.77	0.10	0.05	0.98	76.37
Intra Mg-clay P63	49.79	2.76	2.04			0.04			21.83	0.73	0.19	0.02	0.86	78.27
Intra Mg-clay P67	49.87	3.13	1.74						22.87	0.50	0.06	0.04	0.67	78.86

MR Molar ratio Mg/Si

	Tetrahedral			Octahedral					Interlayer			MR
Sample	Si	Al	∑Tet.	Mg	Al	Fe^{3+}	Ti	∑Oct.	Ca^{2+}	Na^{+}	K^{+}	
Mg-claystone P1	7.96	0.04	8.00	5.26	0.25	0.12	0.01	5.64	0.17	0.03	0.05	0.66
Mg-claystone P3	8.00	0.00	8.00	5.23	0.29	0.13	0.01	5.66	0.06	0.02	0.04	0.65
Mg-claystone P7	7.99	0.01	8.00	5.31	0.25	0.09	0.00	5.65	0.16	0.02	0.04	0.66
Intra Mg-clay P60	7.92	0.08	8.00	5.15	0.31	0.24	0.00	5.7	0.13	0.02	0.02	0.65
Intra Mg-clay P63	7.84	0.16	8.00	5.13	0.35	0.24	0.00	5.72	0.12	0.01	0.04	0.65
Intra Mg-clay P67	7.76	0.24	8.00	5.31	0.33	0.20	0.00	5.84	0.08	0.01	0.01	0.68

Number of cations calculated on the basis of 22 oxygens

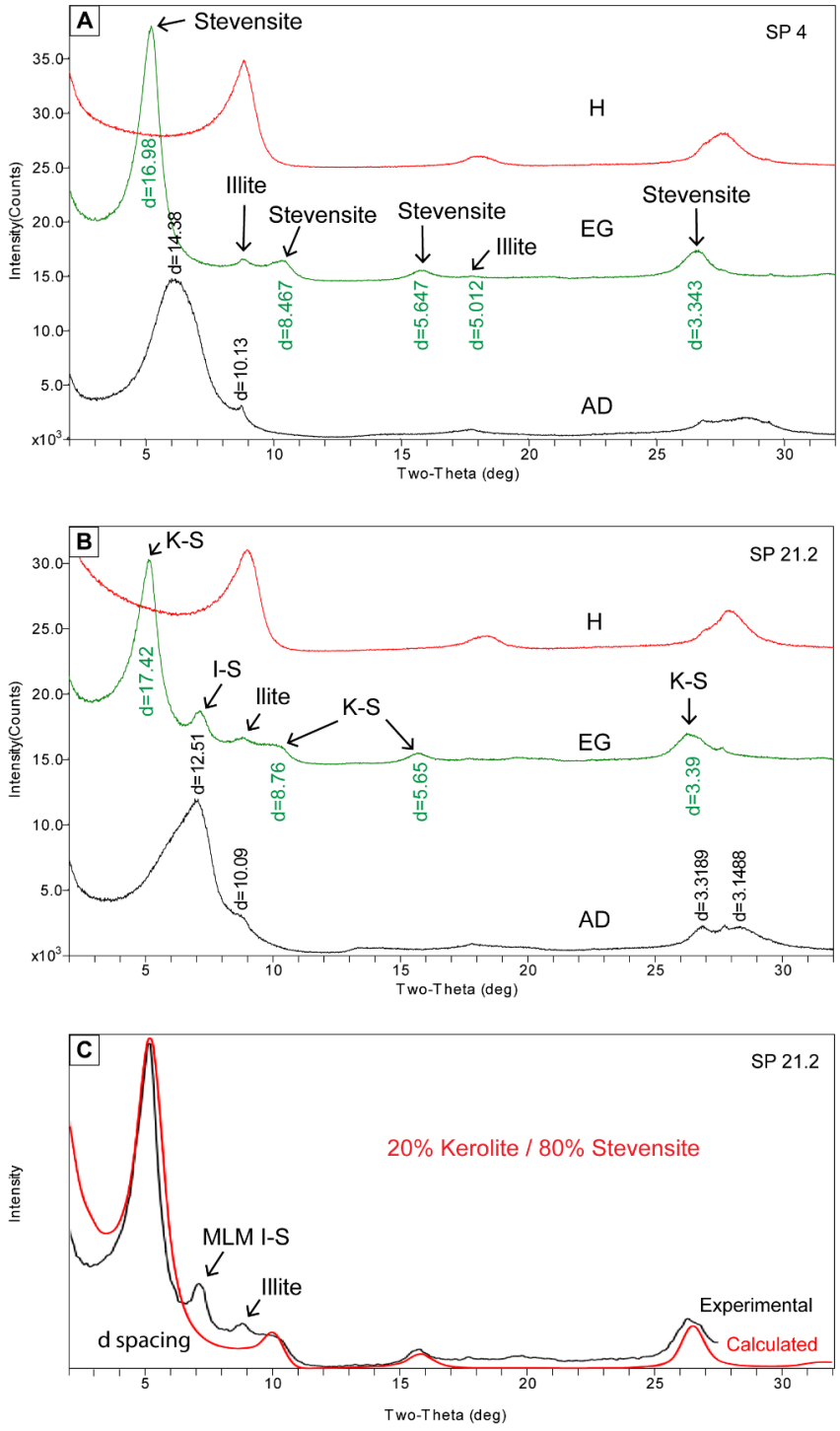

Figure 26. XRD patterns of the <2 mm fraction of intraclastic Mg-clay hybrid arenites. A) Sample with predominance of stevensite and illite. B) Sample with predominance of kerolite-stevensite mixed layered minerals (K-S), illite-smectite mixed layer minerals (I-S) and illite. AD: Oriented preparation of the <2µm fraction in air-dried state. EG: Oriented preparation of the <2µm fraction in ethylene-glycol solvated state. H: Oriented preparation of the <2µm fraction heated at 490ºC. C) Fit between experimental and calculated patterns for kerolite-stevensite mixed layer minerals using Newmod software.

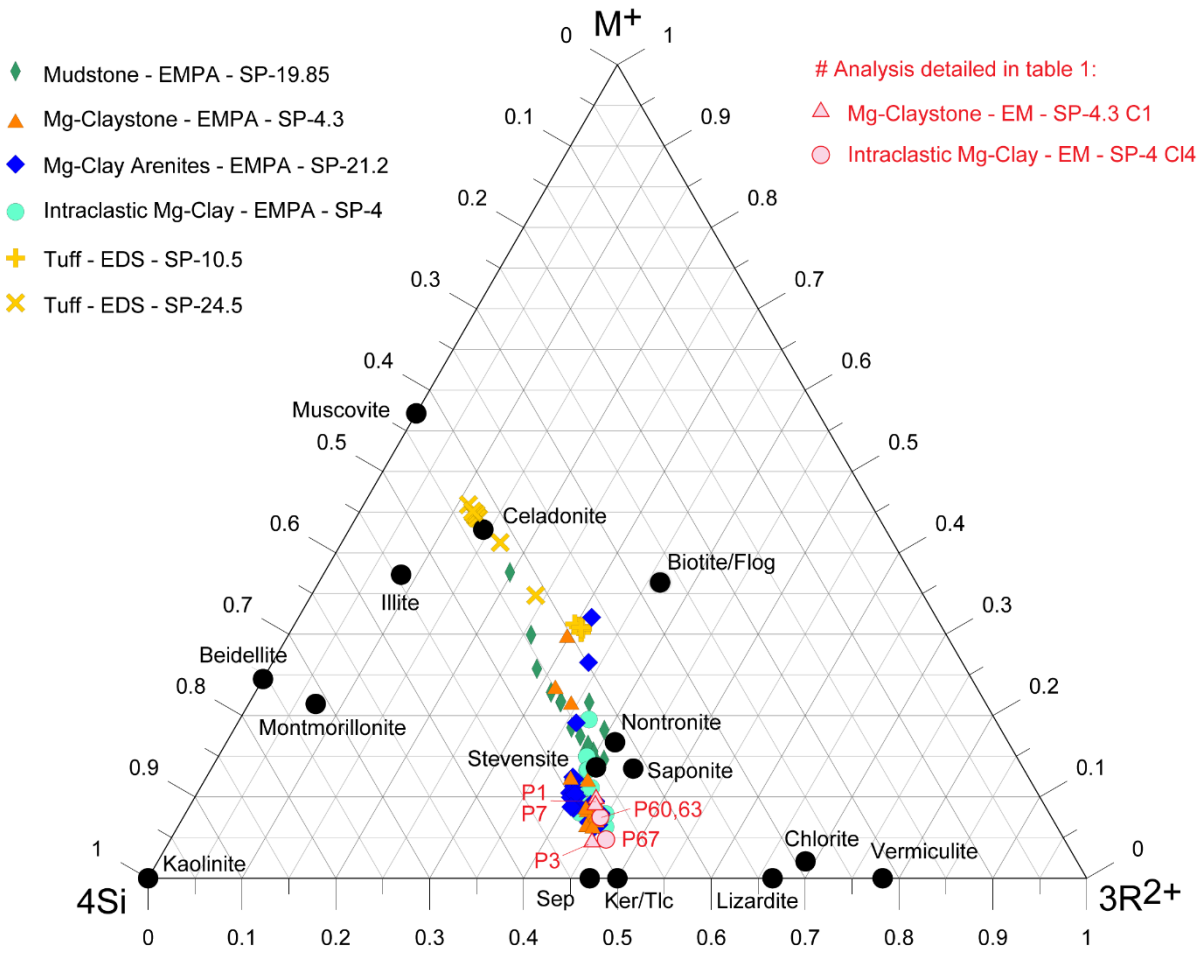

Figure 27. Chemical composition of clay minerals and micas on the ternary diagram M+-4Si-3R2+ (Meunier and Velde, 1989). 74 chemical analyzes acquired by electronic microprobe, in clay minerals and micas of Mg-clay bearing lithofacies and tuffs.

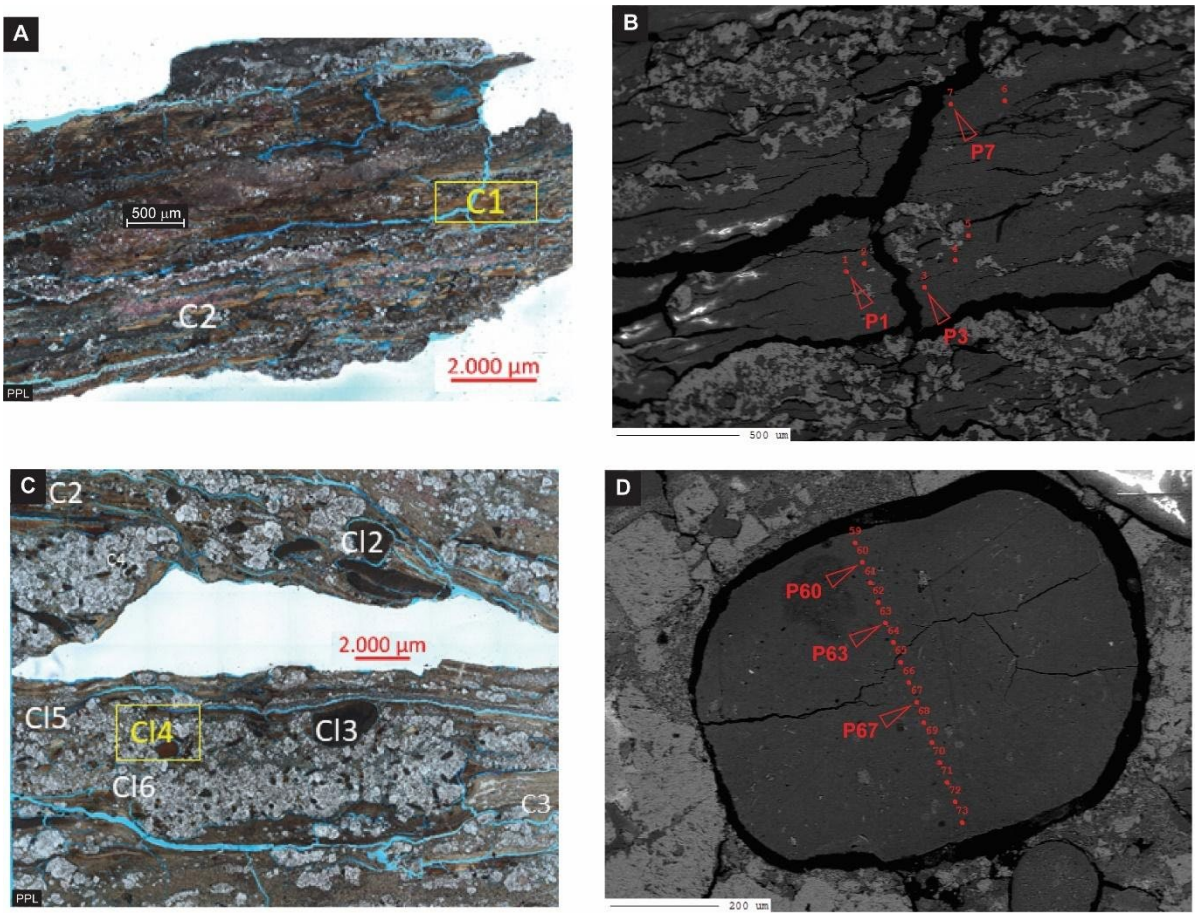

Figure 28. Electron Microprobe Analysis (EMPA). Mg-claystone with calcite nodules (Sample SP-4.3, Fig.8A): A) Photomicrograph with transmitted white light; B) SEM image with backscattered electrons, detail from C1 and chemical analysis P1, P3 and P7 detailed in table 1. Intraclastic Mg-clay hybrid arenite (Sample SP-4, Fig.9C): A) Photomicrograph with transmitted white light; B) SEM image with backscattered electrons, detail from Cl4 and chemical analysis P60, P63 and P67 detailed in Table 1.

2.4.4 Automated Mineralogical Mapping

Automated mineralogy and petrographic methods, deploying quantitative evaluation of minerals by scanning electron microscopy (QEMSCAN), where run on four lithotype samples: Mg-claystone, Mg-clay arenite, Intraclastic Mg-claystone hybrid arenite, and Tuff. These analyses show details of individual constituent minerals of each sample separated to reveal spatial distributions (Fig.29, 30).

The most abundant mineral group and largely spatially distributed within the Mg-claystone and Mg-clay arenite samples studied, are Mg-clay minerals (> 55% in area average) followed by calcite (> 20% in area average) (Fig.29). Using XRD analysis, the main Mg-clay mineral constituent of Mg-claystone is stevensite, and kerolite-stevensite for Mg-clay arenite. Calcite largely forms as diagenetic lamina or cementing matrix. The term cement, loosely used in this study, refers calcium carbonate matrix forming between Mg-clay ooids. The presence of small amounts of dolomite is recurrent in the samples studied. Dolomite is found in two different forms: (1) rhombohedral crystals (subhedral and euhedral) of early genesis (Fig.31); and (2) microcrystals replacing a pre-existing calcitic framework (Fig.29). Quartz has a spatial distribution very similar to dolomite but in smaller amounts (Fig.28). The detritus concentration is composed by quartz in silt-size grains, which occurs closely associated with Al-micas, Mg-micas, and K-feldspars. Dolomite is associated with these detrital occurrences (e.g., Mg-claystone; Figure 29). Clay clasts are observed partially replaced by calcite and authigenic quartz. Stevensite of the Mg-claystone shows dolomite rhombohedra among the laminated Mg-clays.

Intraclastic Mg-claystone hybrid arenite is formed by Al-clays, Mg-micas and Mg-smectite of volcanic fragments, with clasts and peloids of authigenic Mg-clays (stevensite and

kerolite-stevensite) and early diagenesis calcite cement (Fig.30). Two distinguished areas of Mg-smectites occurrence are highlighted, one associated with authigenic clay mineral formation (Fig.30D), and the other associated with volcaniclastic detritus (Fig.30E).

Tuff beds were also studied, and these are mainly formed by Al-clay minerals and K-feldspar, with small amounts of Mg-clay minerals, quartz and calcite (Fig.30F-J). Tuff clay minerals are dioctahedral: interstratified illite-smectite, dioctahedral smectite and illite. Electron microprobe analysis on clay minerals, show the differentiation between authigenic clay minerals from non-tuff sedimentary rocks and the clay minerals from the tuffs (Fig.27).

.

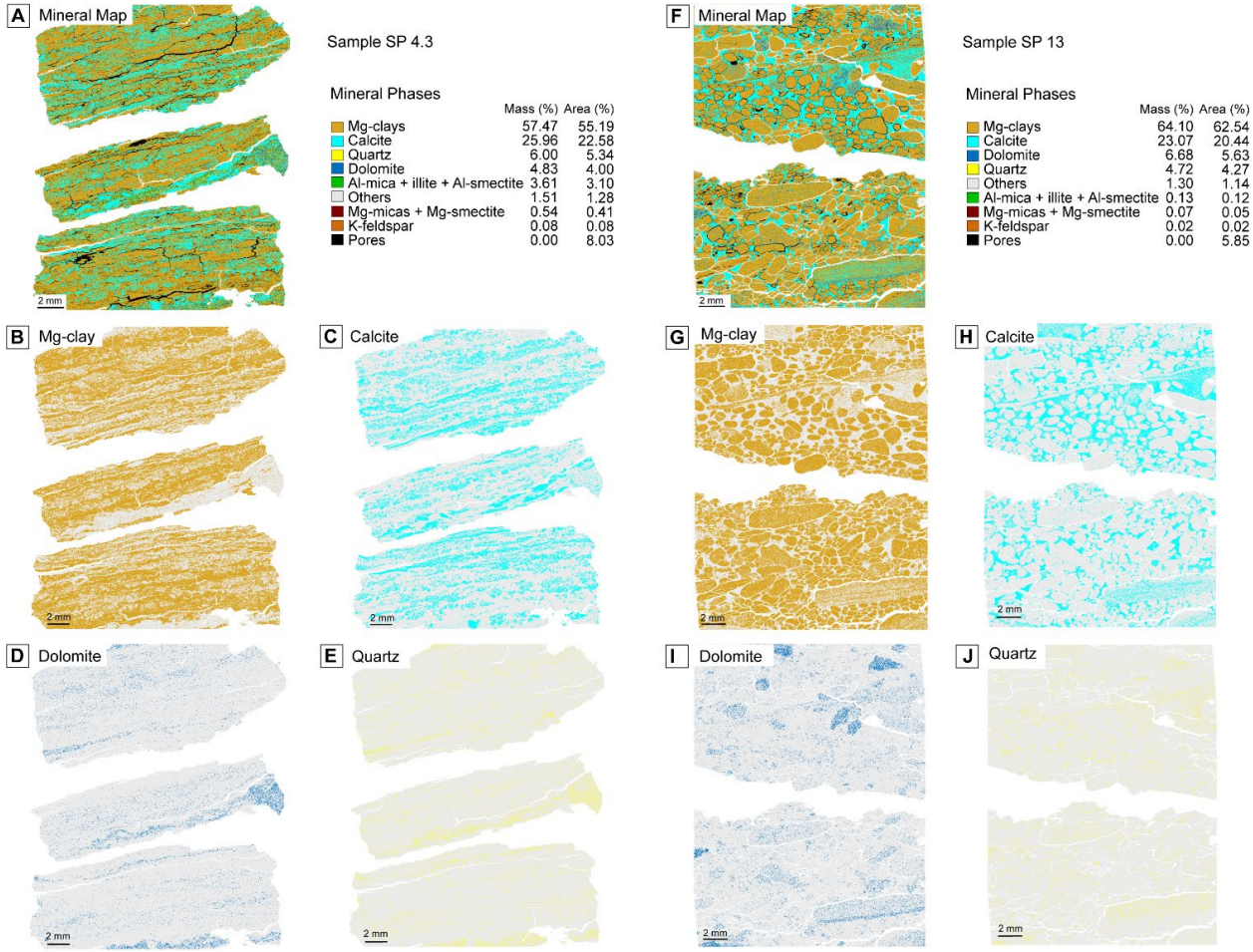

Figure 29. QEMSCAN Automated Mineralogical Mapping Results. Mg-claystone lithotype: A) Mineral spatial distribution with 10 µm resolution and quantification of mineral phases in area and mass; B to E) Mineralogical maps showing occurrance of Mg-clays, calcite, dolomite, and quartz. Mg-clay arenite lithotype: F) Mineral spatial distribution with a 10 µm resolution and quantification of mineral phases in area and mass; G to J) Mineralogical maps showing occurrance of Mg-clays, calcite, dolomite, and quartz.

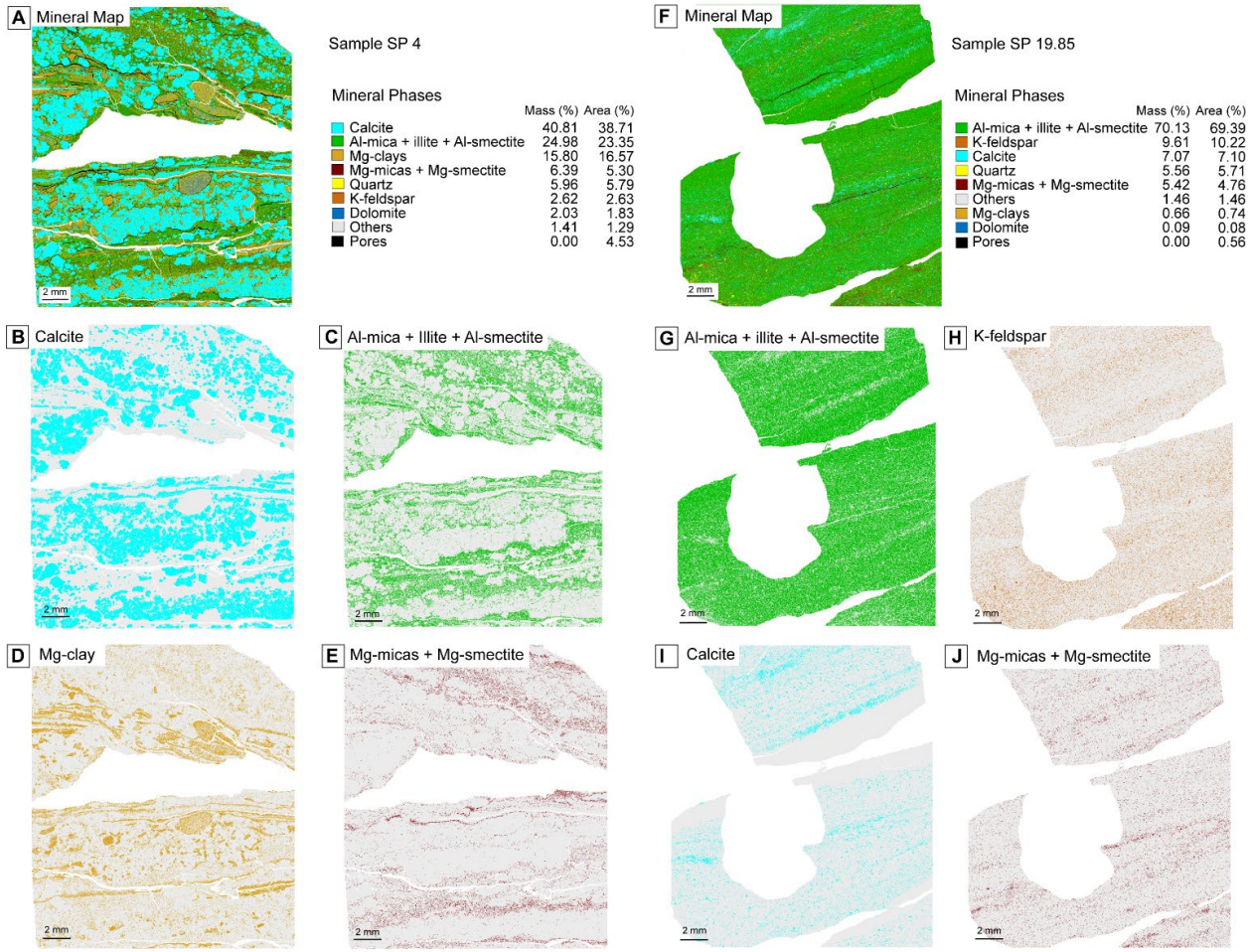

Figure 30. QEMSCAN Automated Mineralogical Mapping Results. Intraclastic Mg-claystone hybrid arenite lithotype: A) Mineral spatial distribution with a 10 µm resolution and quantification of mineral phases in area and mass; B to E) Mineralogical maps showing occurrance of Mg-clays, calcite, dolomite, and quartz. Tuff lithotype: F) Mineral spatial distribution with a 10 µm resolution and quantification of mineral phases in area and mass; G to J) Mineralogical maps showing occurrance of Mg-clays, calcite, dolomite, and quartz.

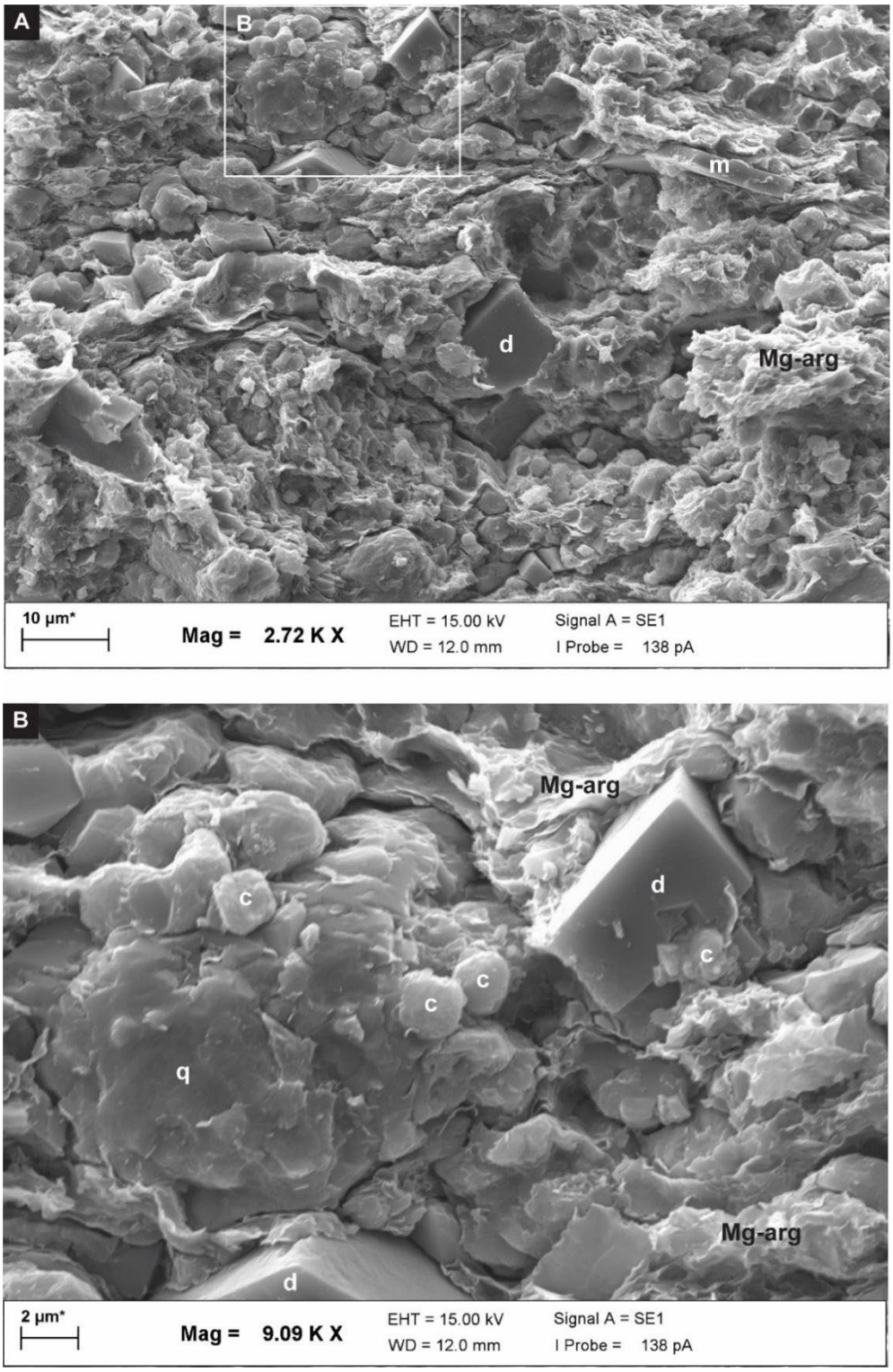

Figure 31. Backscattered Electron Image of dolomitic mudstone. A) Sample area with clay minerals (Mg-arg), dolomite (d) and mica (m). B) Image A detail: note dolomite (d) and calcite microcrystals (c) within a Mg-clay minerals matrix. Presence of quartz grain (q).

2.4.5 U–Pb geochronology

Tuff beds have been used in the Green River Formation to date horizons and correlate units due to their basin-wide occurrence (Smith et al, 2008). Tuffs at Sanpete Valley area contain variable amounts of biotite, hornblende, and sanidine feldspar (Sheliga, 1980). Generally, tuff beds in the Green River Formation have been dated by $^{40}Ar/^{39}Ar$ geochronology on biotite (Sheliga, 1980) and sanidine (Smith et al, 2008).

Laser ablation inductively coupled mass spectrometry (LA–ICP–MS) was used as an *in-situ* technique to analyze U–Pb isotope ratios in zircons, a tuff accessory mineral. Three tuff beds were selected for analysis, two samples from Spring City Cuesta (Coarse and Tawny tuffs) and one sample for quality control (Skyline tuff) at Evacuation Creek, Utah. Zircon U-Pb Tera-Wasserburg concordia and ^{207}Pb corrected error-weighted mean $^{206}Pb/^{238}U$ crystallization ages are shown in Figure 32. The Coarse tuff is lower in the section at Spring City Cuesta (Figure 19, Tuff #1) and is approximately stratigraphically equivalent to Faulk's tuff unit #2 (Faulk, 1948) and Sheliga's tuff WCT #1 (Sheliga, 1980). This tuff sample contained zircons with a weighted mean age of 46.80 ± 0.15 Ma (MSWD = 1.2, n = 113). The Jutting tuff, sample #5 from the Spring City Cuesta section (Figure 19), was the name given to Sheliga's ET#8 tuff and Faulk's #16 tuff. Sheliga's (1980) $^{40}Ar/^{39}Ar$ data on biotite places the Jutting tuff at 43.34 ± 0.64 Ma. Tawny tuff, after Faulk (1948), collected at the top of Black Hill Mountains (Sanpete Valley) yielded a population of zircons with a weighted mean of 41.97 ± 0.18 Ma (MSWD = 1.5 for n = 117).

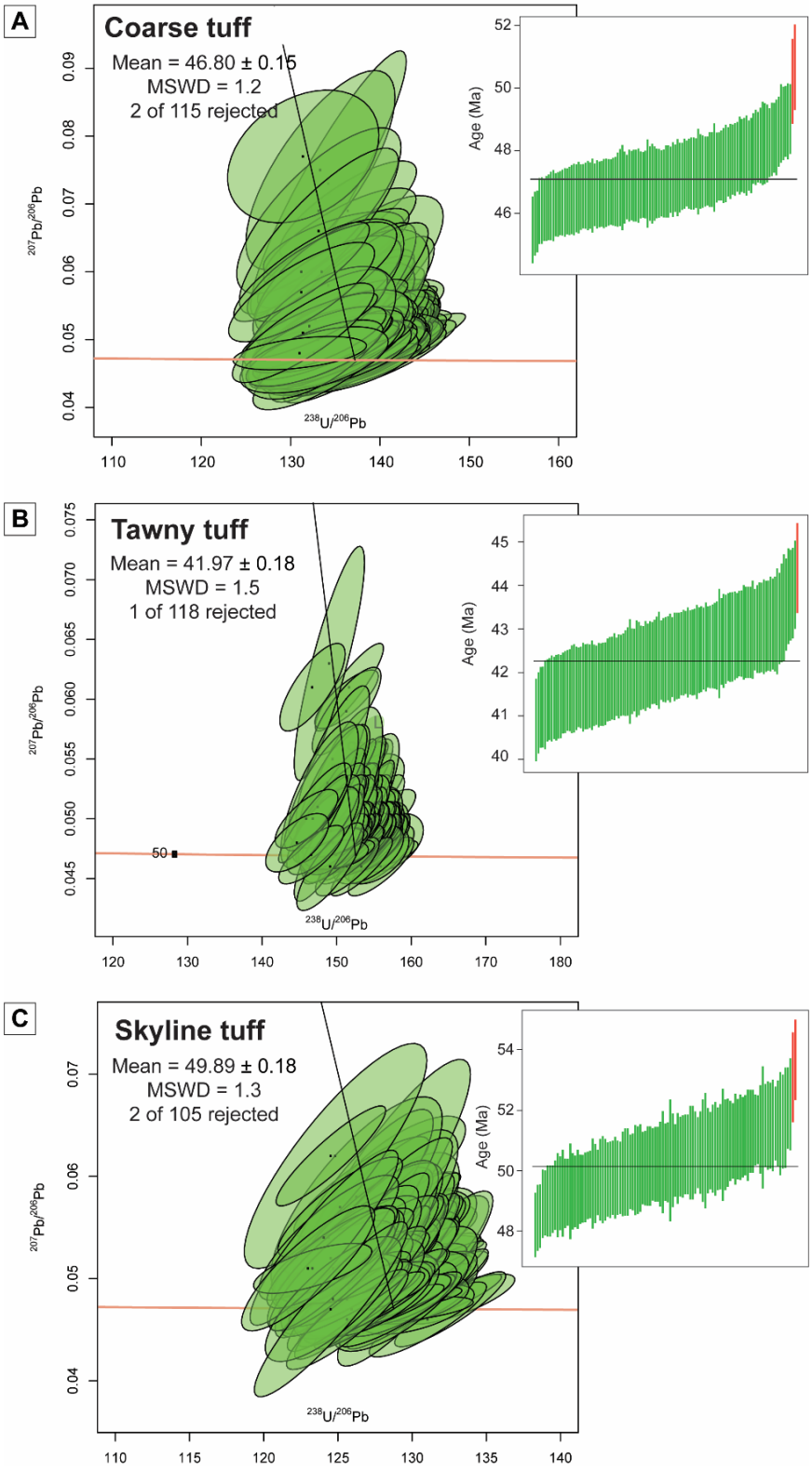

Figure 32. Zircon U-Pb geochronology data illustrated in Tera-Wasserburg Concordia plots, calculated error-weighted mean ^{207}Pb corrected-^{206}Pb/^{238}U ages.

2.5 Discussion

Lake Uinta at Sanpete Valley is interpreted to have its southern boundary in the Wasatch Plateau region extended northeastward into the Uinta Basin, with the northern boundary being the fault block mountains of the Uinta uplift (Sheliga, 1980). There is a lack of paleogeographic maps showing hydrogeologic configurations and sediment influx scenarios of Lake Uinta in the Wasatch Plateau region.

2.5.1 Calibration and correlation of Sanpete´s stevensite-bearing unit

Modern geochronology has permitted correlations of the Green River Formation between the structural subbasins (Smith et al., 2008). The results of U–Pb geochronology of two Sanpete tuff layers (Coarse Tuff, 46.8 Ma and Tawny Tuff, 42 Ma) aid in the understanding stevensite-bearing strata correlation between the Sanpete Valley subbasin and the Western Uinta basin (WUB) (Fig.18). Our results show that the Coarse tuff in the Sanpete area is similar in age and could be correlated to the Fat tuff (46.34 ± 0.13 Ma; Smith et al., 2008) at spell out (Fig.18). The Coarse tuff ages tie the lower section of the stevensite-bearing unit in the Sanpete area (Fig.18) to the evaporative lake type facies deposited at WUB, confirming Smith et al.'s (2008) interpretation of a broad evaporative lake occupying the Western Uinta basin and all the Wasatch plateau area (Fig.33A). One dated tuff result from Sheliga (1980) in the Sanpete area, here named Jutting tuff (43.34 ± 0.64 Ma), is nearly correlative with the Strawberry tuff (44.00 ± 0.92 Ma; Smith et al, 2008) at WUB (Fig.18). These correlations suggest the initiation of an interbasin sill localized at the northern portion of Wasatch plateau at 44.5 Ma (Fig.33B). It shifts from an evaporative lake-type facies related to the upper section of the stevensite-bearing Unit (Fig.19) at Sanpete, to a fluctuating profundal lake type facies in the western Uinta Basin (Fig.18) and it records an increase in available

water toward the eastern of the interbasin sill, with a drop in salinity, the WUB being first to turn from hypersaline into a freshwater lake, 1.5 my later by the Sanpete area.

The Sandstone facies (Sprinkel, 2018) records the influence of lake freshening toward Uinta basin proper (Fig.33C). In our correlation at 42 Ma, tied by the Tawny tuff (41.97 ± 0.18 Ma), we do not know if there is a lake in the Uinta Basin or not. Lake Uinta is still an intermittent lake, the Strawberry tuff (44.2 Ma) is at the base of the Sandstone and Limestone facies, but the next dated tuff bed is 41 Ma (Sprinkel, 2018), which is well into the Uinta Formation (no lake). It´s hard to know when the lake in the Uinta Basin disappeared. In summary, the correlation through time of GRF facies of the Wasatch Plateau with western Uinta Basin show distinct lake-type successions between these two basins. After 47 Ma, Uinta Lake was increasingly influenced by volcanism to the north (Smith, 2008) and evaporative strata filled western Uinta and Sanpete basins. It seems that, during all deposited evaporative lake-type facies in the Sanpete Valley basin, the influence of an interbasin sill was active, providing a local hypersaline and alkaline environment in the Sanpete Valley area, with the formation of stevensite. At the same time, the WUB was under a milder evaporation with a less alkaline environment, and with localized precipitation of interbedded evaporites (right after deposition of the Fat tuff) (Fig.18).

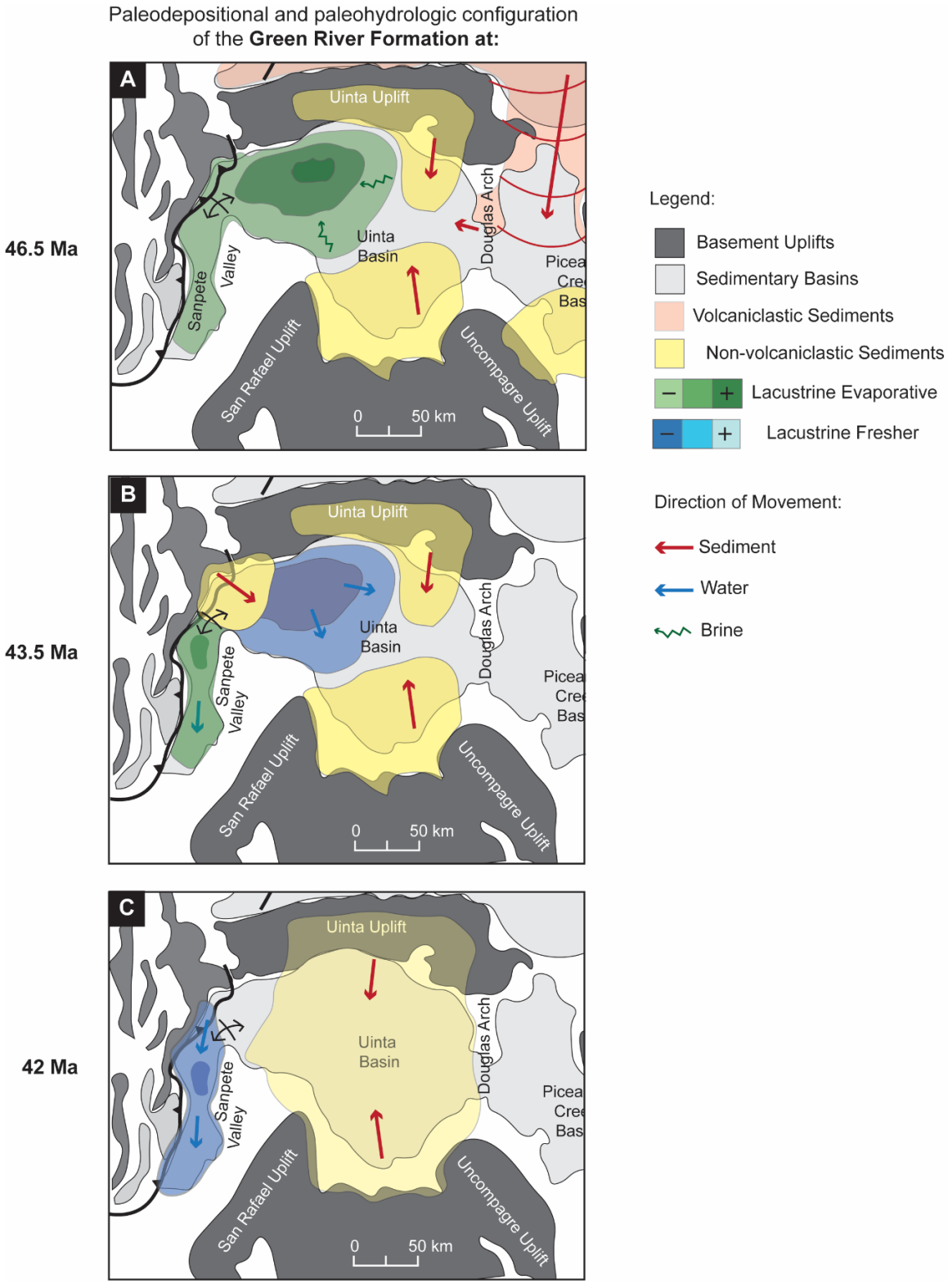

Figure 33. Maps showing hydrology and sediment depositional patterns of the Green River Formation lakes at: A) 46.5 Ma; B) 43.5 Ma and C) 42 Ma (modified after Smith et al. 2008; Vanden Berg and Birgenheier, 2017).

2.5.2 Sanpete´s stevensite-bearing unit depositional model

All the information obtained from the authigenic Mg-clay minerals analyses were used to reconstruct a depositional model for Sanpete´s stevensite-bearing unit (SBU) and infer a paleogeographic interaction between the Wasatch Plateau region and the Uinta basin during the late phase of Lake Uinta evolution, during the Lutetian (43 to 47 Ma). Mg-clay bearing rocks from the Sanpete Valley area were deposited in a southward, shallow embayment of Lake Uinta along the margins of the Sevier fold and thrust belt (Fig.17). This shallow water embayment was partially protected from the Lake Uinta's hydrochemistry regime, recording lake type facies differentiation toward the Uinta basin. Groundwater and local run-off from the surrounding areas (rich in silica and magnesium) favored a distinct hydrochemistry in a low energy sedimentary environment.

Mg-clays are a valuable proxy for reconstructing shallow-water, saline-alkaline lake paleoenvironments, due to their rapid responses to chemical changes (Tosca and Wright, 2014). Physicochemical factors, such as salinity (moderate to high salinity), pH (alkaline hydrochemistry), Mg/Si ratio, and temperature are fundamental controls on the formation of authigenic magnesian clays in sedimentary and early diagenetic environments (Pozo and Calvo, 2018). The possibility of microbial influence, volcanism, and detrital input, changing pH and silicon-magnesium ratios, are also considered. According to Calvo and Pozo (2015), evaporative conditions commonly bring about two types of authigenic process that generate magnesian clays. One is sedimentary neoformation, with homogeneous nucleation, which are directly precipitated from ionic or colloidal solutions and amorphous gel reactions (Galan and Pozo, 2011). It can evolve crystallization of a new mineral structure from ions, without the need of a pre-existing mineral structure. Or neoformation with heterogeneous

nucleation, on a pre-existing surface and generation of colloidal silica that leads to precipitation of hydrated silicates (Bontognali et al, 2010). Both cases are marked by low trace elements abundances, especially rare earths. Precursor minerals are usually absent and detrital minerals are commonly absent or low in content. The appearance is laminated and with clean textures in thin sections (Fig.23C). The occurrence of neoformed clay is considered depositional.

The second authigenic process is the transformation of precursor minerals (mainly pyroclastic sediments and detrital clays). In this case, detrital or authigenic clays could be transformed into new, authigenic clays. Transformation is commonly associated with diagenetic (post-depositional) processes. There is a moderate to high content of trace elements depending on past transformed phases. Detrital minerals are common in clay particle size fractions or larger. Precursor minerals are present. Laminations are absent or inherited. No authigenesis by transformation of samples were found at Sanpete. Chemical data corroborate this information, as the amount of aluminum identified by EMPA is low, which indicates almost no influence of detrital minerals in the formation of clay minerals.

XRD bulk mineralogy of the stevensite-bearing unit (Fig.19), comprises four high frequency depositional cycles, defined by the amount of dolomite and their inverse relationship with clay minerals and mica. Cycles start with a relative high amount of clay minerals and low amounts of dolomite, ending with a low clay minerals content and a high amount of dolomite (Fig.34). These cycles record changes in the depositional pattern of the lake in response to short-lasting shifts in evaporation rates. As for the vertical succession of these Mg-clay bearing rocks, there is an alternation of stevensite and kerolite-stevensite deposits in the whole stevensite-bearing unit (Fig.34). Changes in the relative amounts of authigenic

dolomite and calcite, which may be driven by changes in Ca and Mg availability, are notably relevant to Mg-silicate-rich systems (Tosca and Wright, 2018). The stevensite/kerolite-stevensite variation does not match the dolomite/clay mineral cycles; however, the amount of kerolite-stevensite increases in the upper part of the section, while stevensite is concentrated in the lower section. At high salinity and high Mg/Si, stevensite-like products are favored at high pH and kerolite-like products dominate at lower pH (Tosca and Masterson, 2014). Magnesian smectites tend to form in waters with high alkalinity (pH>9.5) and high salinity (Tosca and Wright, 2018). Sepiolite tends to form in waters with intermediate alkalinity (pH 8-9.5) and intermediate salinity (Pozo and Calvo, 2018). Thereby, at the SCC section, the main Mg-clay mineral shift is evidencent from stevensite in the lower section to a kerolite-stevensite upper section that is assumed to be related to pH variation as consequence of influx of acidic waters from Uinta lake's overflow or rainfall into the embayment.

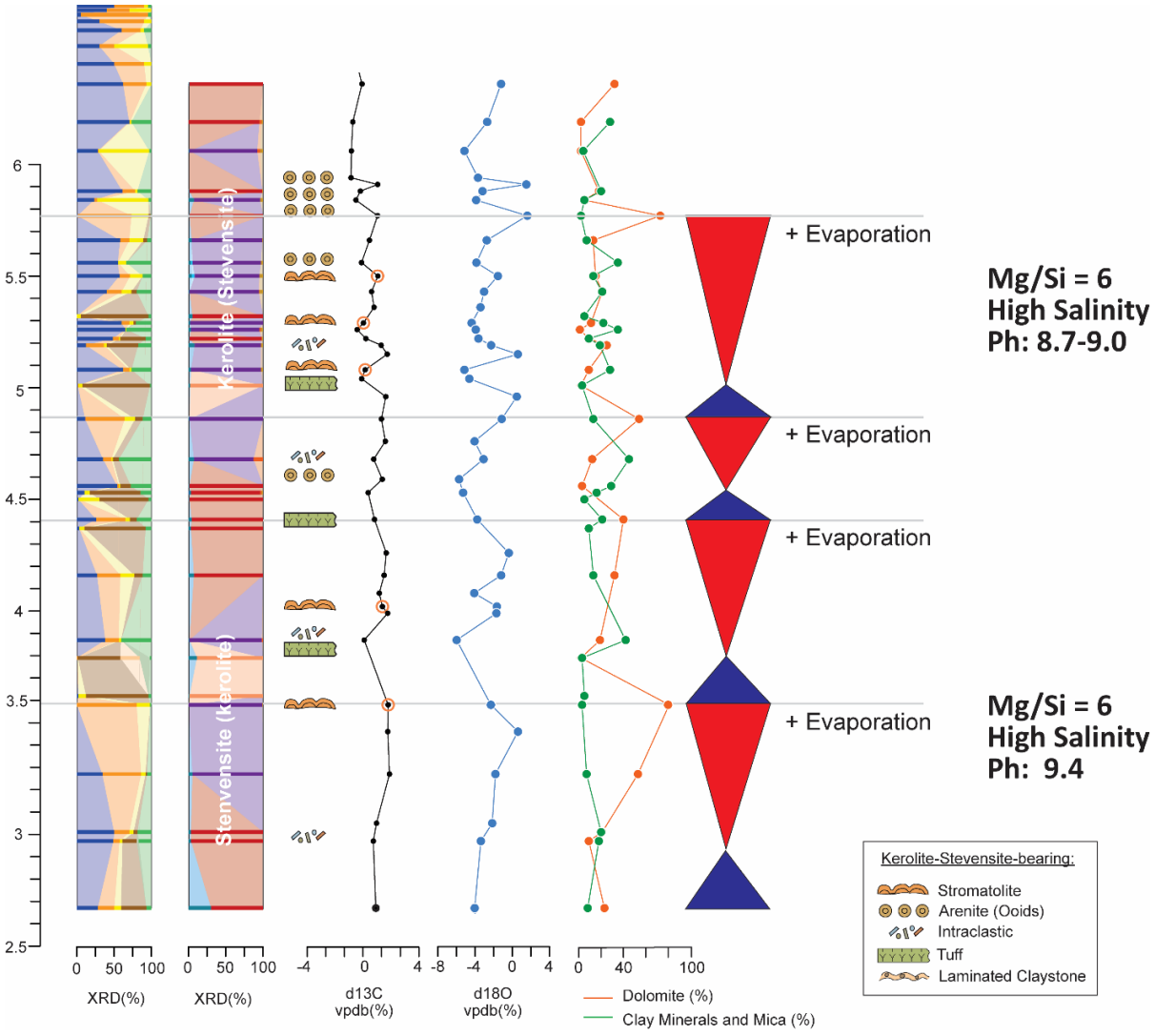

Figure 34. Stevensite-bearing Unit at Spring City Cuesta Section (SCC), showing detailed lithology, XRD measurements (see legend at Fig.3): bulk rock (weight percent) and clay fraction (weight percent), $\delta^{13}C$ and $\delta^{18}O$ stable isotopes, and dolomite and clay minerals percentage logs. High frequency cycles defined from the stacking patterns of the amount of dolomite mineral and their inverse relationship with clay minerals and mica, showing four evaporative-upward cycles.

Authigenic clay minerals are only one family of authigenic silicate minerals that may form in evaporative, siliceous basins. It is important to note that all lake basins accumulating authigenic silicates have several things in common including: (a) high aqueous silica activity due to weathered volcaniclastics and/or a hydrothermal input; (b) alkaline waters due to weathering of basic rocks and evaporative concentration; and (c) significant time intervals of relatively low detrital sediment input (Deocampo, 2015). In this context, modern alkaline brines play a fundamental role in understanding the formation of authigenic Mg-clays. For example, clay minerals of Lake Abert, a shallow alkaline, saline lake in Oregon, show an increasing neoformed Mg-clay (stevensite) from south to north (Jones and Weir, 1983). In the same direction of increasing salinity, the south fresher waters are the result of the principal inflow from the Chewaucan River. With lake-levels fluctuations of 4 m, Lake Abert dries-up periodically at the north end, forming playas (Jones and Weir, 1983).

Even with the impact of eodiagenetic processes on the Mg-clay-bearing lithofacies, oxygen stable isotopes display short-term $\delta^{18}O$ excursions associated with a saline lake under evaporation with dilution by freshwater (Fig.34). Higher concentrations of clay minerals (stevensite and/or kerolite-stevensite) are generally associated with negative $\delta^{18}O$ excursions (relative humid phases), whereas higher concentrations of dolomite minerals occurs in the intervening positive $\delta^{18}O$ excursions (higher evaporative phases) (Fig.34). The isotopic signature of Mg-clay-bearing stromatolites is characterized by no primary paleoenvironmental signal of bulk rock carbon and oxygen isotope measurements due to diagenetic overprint. No covariant trend occurs between $\delta^{13}C$ and $\delta^{18}O$ isotopes.

Stevensite-bearing unit deposits are indicative of a perennial salt lake undergoing water-level fluctuations as evidenced by the results above and by the lack of fresh water biological

assemblages. Lithofacies associations identified from the stevensite-bearing unit, allowed the development of a distinct depositional model (Fig.35). Triggered by evaporation, from north to south, moderate to high salinity controlled the formation of the Mg-clays. With Mg-claystones being precipitated in a more sheltered location of the embayment (low energy, shallower portions), while Mg-clay arenites (ooids) and Mg-clay-bearing stromatolites developed in a relatively moderate energy location at the embayment margins, close to the northern inflow (Fig.35).

The magnesium enrichment mechanism in the depositional environment can be explained through a condition of extreme aridity or the occurrence of adjacent volcanic materials responsible for the supply of Mg and Si. The occurrence of volcaniclastic rocks (tuff) intercalated with lake sediment deposits is well documented in the Green River Formation (Smith et al, 2008). The presence of thick sequences rich in magnesian phyllosilicates could be explained by localized depositional morphology and sedimentary infill constraints, which would not fully explain the source of Mg. Igneous rocks may have indirectly contributed to the precipitation of authigenic minerals, as a source of ions (e.g., Mg^{+2}, Ca^{+2} and Si^{+4}) for silica precipitation and clay minerals. Note that in basalts there are higher contents of elements such as Ca and Mg.

All unique Mg-clay-bearing stromatolites are composed by kerolite-stevensite, formed mostly under the same high salinity, high Mg/Si and relative less alkaline pH lacustrine settings, as a result of gentle water inflows. In many lake basins, authigenic clay minerals and other silicates represent a significant component of the sediment, and in a few cases, they dominate the assemblage, as in the case of stevensite-bearing unit. Stromatolites composed of non-carbonate mineralogies occur less frequently and it is difficult at times to

separate the original mineralogy from a post-depositional diagenetic one. Focusing on the primary mineralogy, there are stromatolites composed of silica (Berelson et al., 2011), gypsum (Allwood et al., 2013), iron (Brake et al., 2002; Planavsky et al., 2009) and manganese (Rossi et al., 2010). When favorable chemistry coincides with a locally confined environment, the influence or relationship of extracellular polymeric substances (EPS) produced by the microbes building the stromatolites can act as favorable surfaces for Mg-silicate nucleation, such as in the microbial mats (Tosca and Wright, 2018). In recent microbial mats, Mg and silica can be concentrated in EPS (Bontognali et al, 2010). To this date, the stromatolites from SBU are the only ones of a particular type of stromatolites primarily composed of authigenic neoformed Mg-clays, showing that an extrinsic biologically-influenced mineralization (Dupraz et al, 2009) can contribute as an alternative mechanism-driven process for the formation of kerolite-stevensite minerals. These findings expand our knowledge relating to evaporation as the sole trigger for stevensite precipitation and the direct evidence for a certain absence microbial influence in this process. Stromatolite facies with magnesian clay minerals were reported in recent Australian lakes (Burne et al, 2014), in the Neogene sequences of the Madrid basin (Calvo et al. 1999), in the Paleocene of the Salta basin (Bunevich et al. 2017), and from Aptian Barra Velha Formation at Santos basin (Carvalho et al., 2022; Ramnani et al, 2021; Silva et al., 2021; Gomes et al., 2020).

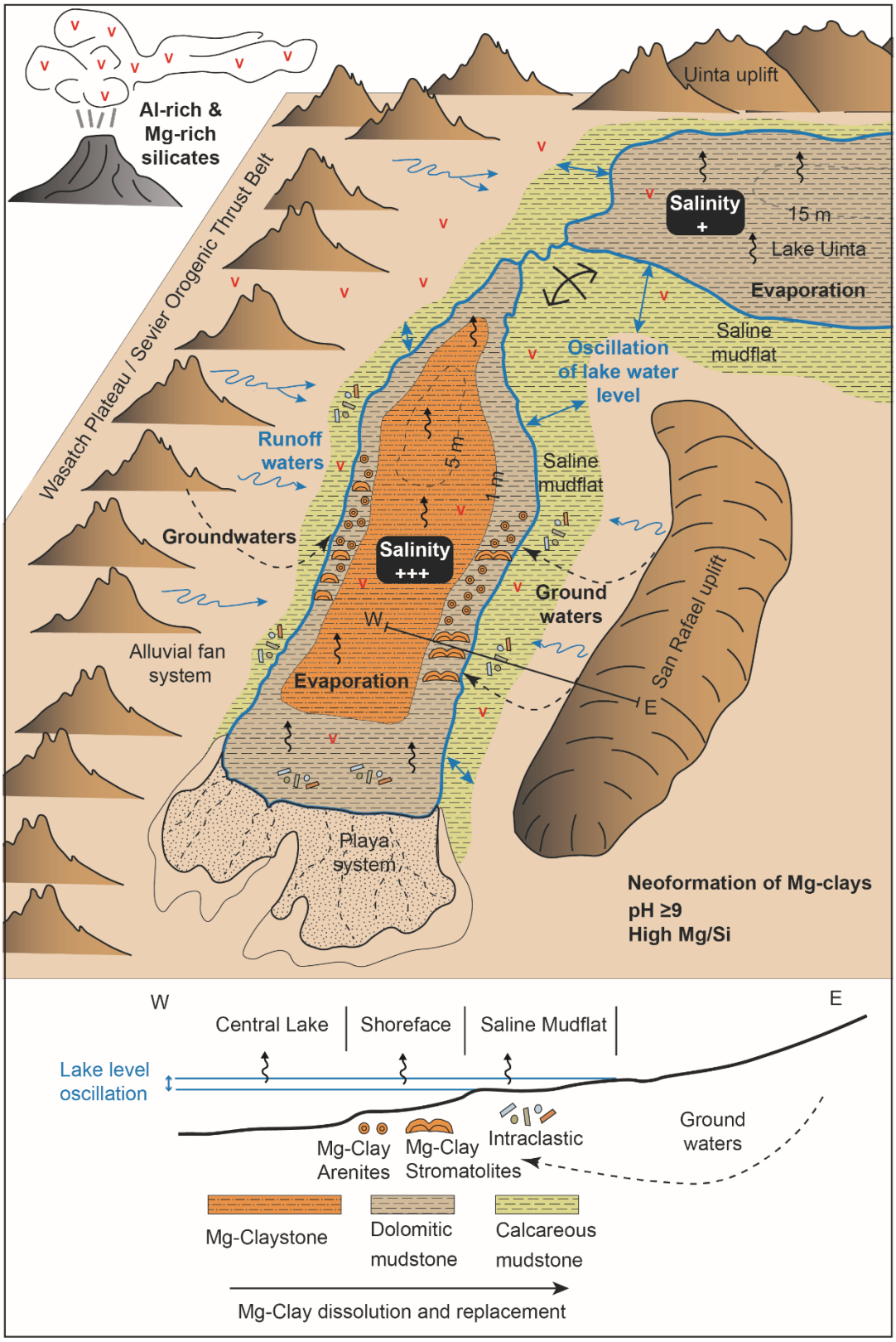

Figure 35. Depositional model for stevensite-bearing unit of Spring City Cuesta section.

The presence of beds of Mg-clay ooids (arenites), the vast majority composed of kerolite-stevensite, indicate that moderate-energy waters were present along the upper section of SBU, in part associated with Mg-clay-bearing stromatolites. Mg-clay arenites (ooids) were formed in environments with some agitation by waves, since water agitation is necessary for the development of concentric shapes (Herlinger et al., 2017; Carramal et al., 2022), while laminated Mg-claystones were certainly deposited in low-energy environments. Mg-clays in the form of ooids are neoformed stevensite and kerolite-stevensite and have a clean texture. From the marine realm, it is known that microbes are involved in precipitation that leads to ooid formation, accretion, and cementation processes, together with particular geochemical conditions (Harris et al, 2019). A similar process may be taking place in lacustrine saline alkaline environments. Mg-Clay-bearing stromatolites were probably formed in environments of an energy level intermediate between that for the formation of the ooids and that in which the laminated claystones developed.

Magnesian clay ooids, which occur preferentially in the sand fraction, can be reworked, and deposited in the form of intraclasts, along with lithoclasts of stromatolites, laminated Mg-claystones and tuffs. These rocks are prone to reworking and exposure that results in the largest and widespread accumulations of intraclastic Mg-clay facies.

The main petrographic characteristics of laminated Mg-claystones are their clean texture, presence of lamination, the absence of precursor minerals and very low amounts or absent detrital minerals, indicating deposition associated with low energy sedimentary environment control.

At the start of the sequence, sediments record the development of increasing aridity, reflected in the dominance of laminated carbonate mudstone, intraclastic grainstones and a

negative excursion of $\delta^{18}O$ isotopes (Fig.34). Tabular microbialites become more abundant toward the top of the regressive hemicycle, marked by a maximum regressive surface. During dry periods, when evaporation rates were greater than precipitation rates, the lake level gradually decreased, resulting in contraction of the lake. Although some precipitation still occurred in the catchment, most rainfall infiltrates and surface runoff into the lake became increasingly intermittent.

2.5.3 Diagenesis of the Sanpete´s stevensite-bearing unit

The GRF Mg-clay minerals present in this unit show different textures that indicate their genesis: authigenic by neoformation (syn-sedimentary direct precipitation from ionic or colloidal solutions); authigenic by transformation (early diagenesis: dissolution-precipitation from previous phases); Mg-clay intraclasts – sand size (reworked authigenic clay); and detrital clay (Al- and Mg-rich) associated with silt size siliciclastic grains. The relationship between carbonates and clay minerals shows that these clay minerals are concomitant with the carbonate sedimentation.

Sanpete Valley´s stevensite-bearing section shows syngenetic mineralogical paragenesis with neoformation of magnesian clays accompanied by calcite and silica (Fig.36). Composition of clay minerals in a saline environment is modified by a reaction with ions from the solution phase. Lake Yoa, located in the northeastern part of Chad, is surrounded by cliffs with many freshwater springs at many localities (Darragi and Tardy, 1987). These diluted waters are concentrated by evaporation and show a brine evolution with neoformation of stevensite accompanied by aragonite. The co-precipitation of these two minerals controls the increases of pH, alkalinity, and silica concentrations in solution while a depletion of Ca, Mg concentrations is also observed. The effect of mineral precipitation on

the chemistry of residual fluids is the trigger of the geochemical evolution of saline waters, which effectively eliminates the ion with lowest concentration at the time that supersaturation occurs (Deocampo, 2015). As observed in rift lakes (e.g., Renaut et al., 1986; De Wet et al., 2002), dilution of lake waters during more humid periods, or input of CO2 by magmatic and hydrothermal activity, may have promoted the dissolution of Mg-clays, releasing silica and magnesium, and favoring the precipitation of silica and dolomite (Herlinger, 2017).

The main elements of the composition of magnesian clays are Si and Mg (except for palygorskite). Concentration of Al is relevant in saponite and palygorskite. Possible sources of $Si(OH)_4$ are rainwater, groundwater, detrital and clay mineral dissolution and alteration, and volcaniclastic sediments, like ash (later to become tuff). Presumable sources for Mg^{2+} are also rainwater, groundwater, and volcanism, adding the fluid mineralization from the formation of calcite and gypsum, dedolomitization, and the dissolution of Mg rich minerals. Formation of authigenic magnesian clays is favored in areas of low subsidence and low detrital sediment input, such as in the marginal areas of playas (Warren, 2006).

Diagenetic phases replacing preexisting constituents in stevensite-bearing unit include microcrystalline calcite (Fig.31B), calcite nodules (Fig.23C), microcrystalline silica (Fig.21), calcite mosaic, and quartz mosaic (Fig.20C).

MINERAL PHASE	PROCESSES	SYNGENESIS	EODIAGENESIS	MESODIAGENESIS
STEVENSITE/KEROLITE	NEOFORMATION			
CALCITE	PRECIPTATION			
DOLOMITE	SUBSTITUTION			
MICRITE	SUBSTITUTION			
CALCITE MODULES	SUBSTITUTION			
MICROCRYSTALINE	SILICA SUBSTITUTION			
CALCITE MOSAIC	PORE FILLING			
QUATZ MOSAIC	FRACTURE FILLING			

Figure 36. Diagenetic sequences interpreted from Mg-clay-bearing lithofacies. Thicker lines correspond to main processes and products, with dashed lines showing subordinated processes.

2.6 Conclusions

Clay units associated with Sanpete's stevensite-bearing unit (SBU) deposits are constituted by neoformed authigenic magnesian clay minerals. These clay intervals occur in several areas, and their distribution is related to the physicochemical conditions of lake water, determined by the depositional paleomorphology of the lake. This work shows that there is a distinct stratigraphic sequence of occurrence of Mg-clays in the basin (stevensite-bearing unit), between 46 and 43 Ma. U–Pb geochronology of two Sanpete´s tuff layers (Coarse Tuff, 46.8 Ma and Tawny Tuff, 42 Ma) aid to fully understand the stevensite-bearing strata correlation between the Sanpete Valley subbasin and the Western Uinta basin. Stevensite-bearing unit is associated with a proper depositional environment: an evaporative shallow water embayment, partially protected from the Lake Uinta's hydrochemistry regime. At these conditions, three main authigenic magnesium clay minerals are deposited (stevensite, kerolite, and mixed-layer kerolite-stevensite) in four Mg-clay-bearing lithofacies: 1) Mg-Clay-bearing Stromatolites; 2) Mg-Clay Arenites; 3) Mg-Claystone with Calcite Nodules; and 4) Intraclastic hybrid arenites and conglomerates. These minerals with laminated and/or granular clean texture are authigenic by neoformation. Detrital Mg-clay minerals occur in the form of intraclasts in the sand fraction, as a product of reworking processes. Allochthonous detrital Al-clays also occur in the silt and clay fraction, associated with regional volcanism and suspension and settling processes in the lake.

X-ray diffractometry analyzes allowed the recognition of possible accommodation rate conditions for the occurrence of four high-frequency depositional cycles. Defined by the amount of mineral dolomite and their inverse relationship with clay minerals and mica. The different species of magnesian clay minerals do not correlate directly with the cycles. The

predominance of stevensite over kerolite occurs in the lower section indicating an environment with lower humidity, a low lake level (retraction of the lake and/or relatively shallower conditions), lower energy and a pH above 9.4. The upper section records a period of higher humidity, with a relative increase in the lake level, the formation of ooids deposited in a context of moderate energy, and with a pH between 8.7 and 9.0. The lacustrine environment of the Sanpete embayment has dimensions of hundreds of kilometers, associated to the north with inflow of waters from Lake Uinta. Groundwater and local run-off from the surrounding rocks (rich in silica and magnesium) favored a distinct hydrochemistry in a low energy sedimentary environment. Salinity, lake energy and low gradient ramp-like depositional morphologies controls Mg-clay-bearing lithofacies deposits. Triggered by the evaporation, from north to south, moderate to high salinity controlled the formation of the Mg-clays. On the lake margins in a relatively high energy regime and less alkaline pH lacustrine settings, Mg-clay ooids, oolite and stromatolites developed. Layered Mg-clays would be precipitated in a more internal position of the embedding providing low energy.

The characterization of the interaction of Mg-clay and microbialite deposits provide great insight into the sedimentation dynamics and early diagenesis of lacustrine carbonate systems, allowing for detailed correlation and comparison to the other basins containing similar Mg-clay and microbialite-bearing deposits. Sanpete Mg-clays occurrences are consistent with several sedimentary textures and minerals observed in the pre-salt carbonates of Santos and Campos basin. The understanding of the formation and preservation of Sapetes' authigenic clays within the lacustrine environment can improve the prediction of reservoir quality at other basins elsewhere. The model presented provides a novel

framework for understanding and predicting Mg-silicate-carbonate interactions and their geological consequences and yield new predictive concepts for Mg-clay formation in other lacustrine systems.

2.7 Acknowledgments

We acknowledge Petrobras (Brazil) for support and full funding this research. We are grateful to H. P. Buchheim (in memorian), M. Vanden Berg, R. Biaggi, Y. Parizek-Silva, and K. Wright for discussions, constructive reviews, and assistance in the field related to this study. We thank S.C. Anjos, P. M. Magalhaes, and R.J. Jahnert for encouraging this project to take place.

CHAPTER 3

3. Microbialite facies and environmental dynamics in a saline-alkaline lake: Douglas Creek Member, Eocene Green River Formation, Evacuation Creek area, Uinta Basin, Utah

Daniel Fontoura Cupertino [a,b]*, Michael Vanden Berg [c], Stanley M. Awramik [a]

a) Department of Earth Science, 1006 Webb Hall, University of California, Santa Barbara, CA 93106, USA.

b) Petrobras S.A., Av. Henrique Valadares, 28, Tower B, 4th floor, Rio de Janeiro, RJ, 20231-030, Brazil.

c) Utah Geological Survey, 1594 W. North Temple, Suite 3110, Salt Lake City, UT 84116, USA.

* Corresponding author: dcupertino@petrobras.com.br

Manuscript submitted and under revision by *Sedimentary Geology*.

3.1 Abstract

Two microbialite-bearing carbonate short-term cycles within the upper Douglas Creek Member of the Eocene Green River Formation were studied in detail in a 37 km^2 area at the confluence of Evacuation and Missouri Creeks, eastern Uinta Basin, Utah. The carbonates are notable because of the number of distinctive microbialites occurring as biostrome and bioherm beds traceable over several kilometers. Nine microbialite facies were established based on their distinctive microbialite content and were defined using macro-, meso- and

micro-structural features. Unique arborescent and branched minicolumnar stromatolites, which resembles shrubs, developed within the bioherms. Each distinctive microbialite facies reflect high-frequency fluctuations of lacustrine depositional conditions. All carbonate facies successions are associated with two short-term rhythmic cycles that record periods of fluvial quiescence (aridity) represented by littoral carbonate deposition under an evaporative regime.

The presence of dolomicrite mineralization within the carbonate beds and analcime within siliciclastic beds indicate a microbial and evaporative shallow depositional environment. Most of the identified diagenetic phases took place in near-surface and shallow diagenetic settings. The interchange of sedimentary deposits reflects fluctuations in the hydrologic state of the lake within a balanced-fill phase. The lake is closed during carbonate deposition with ^{18}O enrichment induced by evaporation, as compared to the siliciclastic facies deposited in an ephemeral open system. Each of these short-term cycles record high-frequency fluctuations superimposed on a long-term lake-level falling. The climatic significance and consequent fluctuating hydrology controlled the carbonate facies with the cycles manifesting in the shallow and wide shoulder of Douglas Creek Arch. The lateral extent and facies changes of the carbonate beds allow a reconstruction of a NE-SW lake shoreline at the western shoulder of the Douglas Creek Arch, and how these carbonates beds evolved.

Keywords — Microbialites, Shrubs, Ca-Dolomite, Bioherms, Douglas Creek Arch, Green River Formation.

3.2 Introduction

Lakes are dynamic systems. Unlike marine systems, lake facies can change laterally over short timescales. A few centimeters of sediment may record changes from a fresh, deeper water setting to a shallow, hypersaline brine (Kelts, 1988). Lake hydrologic state is mainly a function of the prevailing climate, which directly controls water, sediment supply and weathering rates (Bohacs et al, 2000). Tectonics are also an important factor. They form the basin, alter its shape, the surrounding drainage patterns, sediment supply, river capture and possibly triggering hydrothermal activity and sub-lacustrine volcanism (Haberyan and Hecky, 1987). Some lakes coexist under the same climate conditions with different chemical and biotic histories (Buongiorno et al, 2018). Climate influences the formation of these facies by influencing periods of biogenic activity, sediment accumulation and seasonal variance in mineral precipitation (Cohen, 2003). Carbonate sediments behave differently from siliciclastic sediments, both during and after deposition, with implications for their paleolimnological interpretation. Carbonate minerals form in near equilibrium to lake water, but are relatively reactive under diagenetic conditions, where mineral dissolution and replacement are common. These processes are particularly important near littoral zones in highly concentrated brines, and in areas of groundwater–sediment interaction (Renault and Gierlowski-Kordesch, 2010).

The Douglas Creek Member of the Green River Formation (GRF) in the Evacuation Creek area of the eastern Uinta Basin, Utah, records exceptional littoral and sublittoral cyclical lacustrine deposits (Tänavsuu-Milkeviciene et al, 2017) with unique microbialite-bearing carbonate beds. In this balanced-fill phase (Bohacs et al, 2003) of Lake Uinta, the focus of this study is the interchange of sedimentary deposits that reflects fluctuations in the

hydrologic state of the lake, which is closed during carbonate deposition and open during siliciclastic deposition. The microbial carbonates are notable because of the number of distinctive microbialites occurring as biostromes and beds with bioherms. These are traceable over several kilometers. This research determines the relationship between each distinctive microbialite bed and their relation to depositional cycles. The sedimentary lake record (authigenic mineralization, weathering intensity, sediment supply, diagenesis) is analyzedand used in the reconstruct of the depositional environment and climate control.

3.2.1 Lake Uinta at Douglas Creek Arc Area

The Green River Formation was deposited in five intermontane basins (Fossil, Greater Green River, Piceance, Uinta and Sanpete Valley) during the early Eocene (Fig.37A). These intermontane basins formed as result of the thick-skin Laramide orogeny in western North America (Lawton, 2008). Intermontane basins are closely connected to bedrock-cored uplifts. In the Rocky Mountains region, an assemblage of basins formed occupied by continental depositional environments that received detritus from the adjacent uplifted blocks. Most of the Laramide uplifts experienced episodic contractional deformation from late Cretaceous through middle Eocene time (Dickinson et al, 1988). At the early stages of the Laramide orogeny, most but not all basement-involved blocks had begun to rise. By the end of the Cretaceous, a broad continuous north-south uplift occurred, which originated the Rock Springs uplift (RSU) in southern Wyoming and the Douglas Creek Arch (DCA) in northeastern Utah and northwestern Colorado (Fig.37A, B). In the early Eocene, near the end of the Laramide orogeny, this continuous north-south uplift structure was truncated and offset by the west-east-trending uplift of the Uinta Mountains (Mederos et al., 2005) (Fig.37A).

Laramide intermontane basins record a variety of continental depositional environments, such as alluvial fans, meandering and braided rivers with extensive floodplains, open and closed lacustrine systems, carbonate lacustrine margin shoals, carbonate mudflats, and playa deposits (Lawton, 2008). During the early Eocene, two very large lakes existed north and south of the Uinta uplift: Lake Gosiute (53,000 km2 in Greater Green River Basin) and Lake Uinta (24,000 km2 in Uinta Basin. The lake that occupied the 15,000 km2 Piceance Basin early in its history is often considered an extention of Lake Gosiute while later its history is connected to Lake Uinta across the Douglas Creek arch. Each of these lakes varied greatly in chemistry and areal extent as recorded by the sediments and facies of the Green River Formation. Uplifts during late phases of the Laramide orogeny influenced the geomorphic evolution of the Green River lakes creating interbasinal (Uinta uplift) and intrabasinal structural highs (Rock Springs uplift and Douglas Creek arch). These topographic highs acted as spillways during filling of the lakes with water and sediments (Smith et al., 2008). While the Green River lakes were evolving, intermittent volcanic activity was recorded as tuff beds in the lakes (Smith et al 2008). The bulk of these volcaniclastic rocks were produced by Plinian eruptions of the Absaroka volcanic province in Wyoming (55 to 45 Ma; Lindsay and Feeley, 2003) (Fig.37A) and Challis volcanic province in Idaho (50 to 45 Ma; Smith et al, 2003). The ash was carried by prevailing winds into the Green River lakes (Smith et al, 2008). The combination of highly reactive pyroclastic material and saline-alkaline solutions in a closed phase of the hydrographic basin was ideal for the formation of authigenic minerals (e.g., analcime; Surdam and Sheppard, 1978).

A detailed stratigraphic framework for the Green River Formation in the Uinta Basin was established by Birgenheier et al. (2020), which subdivides the GRF into lower, middle, and

upper stratigraphic units (Fig.37B). After a regional lake regression, smaller freshwater lakes in the Piceance and Uinta Basins expanded and connected across the Douglas Creek arch (marked by the carbonates of Long Point transgression) to form one large lake, Lake Uinta (Johnson and Finn, 1986) (Fig.37B). Under the influence of climate changs, due to the early Eocene hyper-thermals and the subsequent Early Eocene Climatic Optimum (52.6–50.1 Ma) (Birgenheier et al, 2020), cyclical fluvial-lacustrine deposition was established. This comprises the middle Green River Formation composed of the Douglas Creek Member and Sunnyside Delta Interval (dominated by siliciclastic deposition), as well as the overlying transition interval and basal Parachute Creek Member, dominated by carbonate deposition. The Mahogany zone, an organic-rich, basin-wide carbonate mudstone, represents the climax of Lake Uinta's expansion and organic productivity (Johnson et al., 2011) and marks the boundary between the middle and upper members (Birgenheier and Vanden Berg, 2011).

The Douglas Creek Member (DCM) records a basin-wide interval, dominated by siliciclastic deposition, between the high lake level of the Carbonate Marker Unit and the carbonate dominated Parachute Creek member. The DCM constitutes littoral lacustrine environments on the Douglas Creek arch (DCA) (Fig.37B), which is bounded on the north by the Uinta uplift and to the south by Uncompahgre uplift (Fig.37A). The DCM extends approximately 75 km from north to south and is about 35 km wide (Bader, 2009) (Fig.37A, B). Lake Uinta occupied two basins, the Uinta basin and the Piceance basin separated by the arch. During a ~4.4 m.y. period, the DCA acted as a sill for Lake Uinta. Lake waters that flowed intermittently across the paleo high of the arch (Smith et al., 2008; Rosencrans, 2015). The Douglas Creek arch was an important control on local deposition between the two basins. The arch formed the main spillway between the lakes of the Uinta and Piceance Basins and

preserves phases of the two lakes as they were expanding and contracting. During expansion phases, the arch was transformed from a sill to an underwater saddle (Smith et al., 2008). The amount of oil shale is negligible within DCM (Bradley, 1931; Moncure and Surdam, 1980; Johnson et al., 2010; Tänavsuu-Milkeviciene et al., 2017). Previous authors have attempted to correlate the Uinta and Piceance Basin deposits using lithostratigraphy, tracing the lateral continuity of rich and lean zones of oil shale or thin tuff beds (Cashion and Donnell 1972, 1974; Moncure and Surdam, 1980; Cole, 1985; Johnson and Finn, 1986; Johnson et al., 1988; Johnson and Johnson, 1991). Due to the intertoging character of the oil shale units of the Parachute Creek Member, with heterolithic littoral deposits of the Douglas Creek Member, basin-wide correlation across the Douglas Creek arch has proven difficult. Among few regional marker beds, the Mahogany zone (Parachute Creek Member) is the most reliable and can be traced hundreds of km (Cashion and Donnell, 1974; Moncure and Surdam, 1980) in Uinta Basin, but not across the DCA into the Piceance Basin.

To determine the palaeoenvironmental setting of Douglas Creek Member at the Douglas Creek arch, we investigated stromatolites and their morphologies in the Evacuation Creek area, across more than 10 km of relatively continuous outcrop where the member is best preserved (Fig.37C).

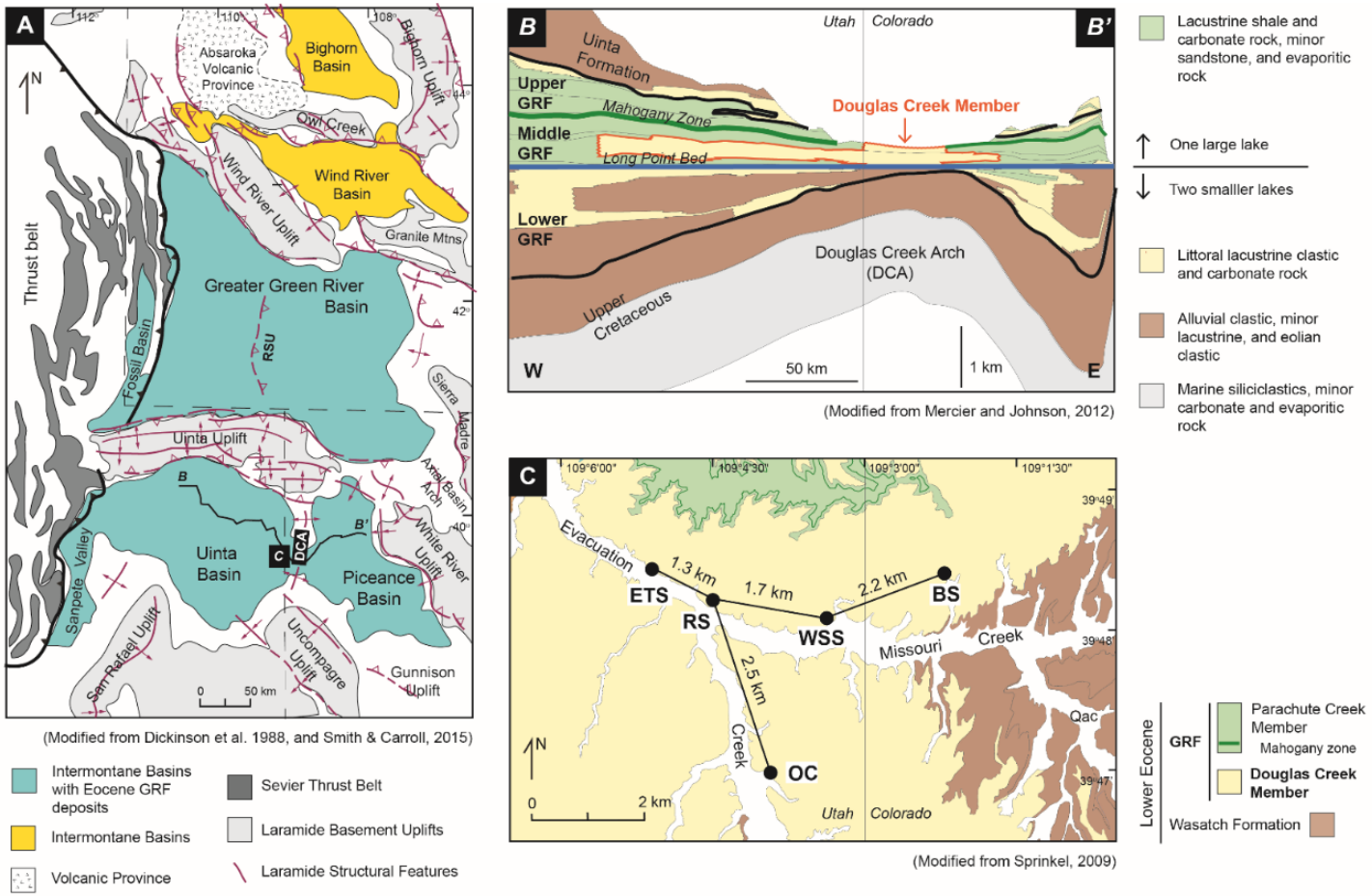

Figure 37. A) Location map of Eocene basins in yellow and basin-bounding uplifts in light gray (after Smith and Carrol, 2015). Major Laramide structural features in purple (Dickinson et al., 1988). RSU: Rock Springs uplift; DCA: Douglas Creek Arch. B) West-east (B-B') stratigraphic cross section across DCA showing correlation of Upper Cretaceous and Paleogene rocks in the Uinta and Piceance Basins. (After Mercier and Johnson, 2012). C) Geologic map of the Evacuation and Missouri Creek area (after Sprinkel, 2009) showing the location of the studied outcrops: East Temple (ETS), Rosewood (RS), West Stadium (WSS), Barrel (BS) and Ochre Cliff (OC) sections. The studied area is located at the eastern margin of the Uinta basin, on the western flank of Douglas Creek arch, Utah (black box with C in Fig 37A).

3.2.2 Douglas Creek Member and the Carbonate-rich zone (R1)

Long-term fluctuations of the Parachute Creek Member of Uinta Basin reflecting regressive/transgressive cycles were first noted by Picard and High (1968). The alternating carbonate-rich and carbonate-lean zones described by Cashion and Donnel (1972). The Evacuation Creek area displays these distinct rich-lean zones of Uinta Basin (Fig.38). They are related to a balanced-fill lake type (Bohacs et al., 2003), which intermittently overflows toward Piceance Basin over the sill of the Douglas Creek arch due to a lake level rise. The Douglas Creek Member is also cyclical, which has led to the identification of long-term and short-term depositional cycles (Bradley, 1930; Surdam and Stanley, 1979; Fischer and Roberts, 1991; Cole, 1998; Pietras et al., 2003; Machlus et al., 2008; Smith et al., 2014). Tänavsuu-Milkeviciene and Sarg (2012), in the Piceance Basin, and Rosenberg (2013), in the eastern Uinta Basin, were the first to apply concepts of genetic stratigraphy, using detailed facies association analysis as a tool to identify and correlate cyclic patterns near the DCA. Based on large-scale depositional sequences in the Uinta Basin, Birgenheier et al (2020) interpreted that after the connection of the two basins, Lake Uinta changed primarily by climatically driven influences. Evolving under highly seasonal, semi-arid subtropical climate conditions from a shallow lake through a high, stratified organic-rich lake, that ended in a closing hypersaline lake phase. During deposition of the upper part of the Douglas Creek Member, long after the lake transgressed over the Douglas Creek Arch (marked by the Long Point bed; Johnson, 1984), Lake Uinta was under highly seasonal flooding events with varying levels of salinity, but never fresh. This has been postulated to be associated with early Eocene hyperthermals and the Early Eocene climate optimum (Birgenheier et al, 2020). The Early Eocene Climatic Optimum, 51–53 Ma, had the warmest

climate of the Cenozoic (Zachos et al, 2008). The atmospheric concentration of CO_2 in this early Eocene global warm interval was elevated, ranging from 680–1260 ppm, based on the presence of nahcolite ($NaHCO_3$) in evaporite deposits in Lake Gosiute (Jagniecki et al, 2015). Based on paleobotanical and faunal assemblages, the paleoclimate in the region surrounding the lakes varied from temperate, arid conditions to warm, subtropical conditions (Norris et al, 2000). Current paleoaltitude estimates are close to 2 Km above sea level for the lake basins (Chase et al, 1998) and 4 Km of elevation above sea level for the surrounding mountains (Norris et al, 2000).

The southern shore of Lake Uinta was very broad and flat. This allowed large transgressive and regressive shifts in the shoreline in response to climatic and tectonic-induced rise and fall of the lake (Keighley et al., 2003). As the lake expanded, the DCA became a shoal area where littoral carbonate and siliciclastic sediments were deposited (Cole, 1985). Mineralogical changes started to occur, and the brackish shallow littoral zone became noticeably saline, with formation of authigenic and diagenetic minerals reflecting the increased salinity (Birgenheier et al, 2020). Douglas Creek Member deposition on the arch was characterized by a highly variable environment reflecting periods of fluvial input, but also periods ideal for carbonate formation. The first, thick microbial carbonate deposits of Lake Uinta occur in the Douglas Creek Member (Bradley, 1929; Tänavsuu-Milkeviciene et al, 2017), focus of this study, and named here carbonate-rich zone one (R1) (Fig.38). The timing of the deposition of the Douglas Creek Member has not been firmly stablished, but it is constrained by two regionally correlated markers, the base of the carbonate marker unit with an estimated age of 54 Ma (Remy, 1992) and the Skyline Tuff dated 49.6 Ma (Smith and Carroll, 2015), which is several hundred meters in Parachute Creek Member (Fig.38).

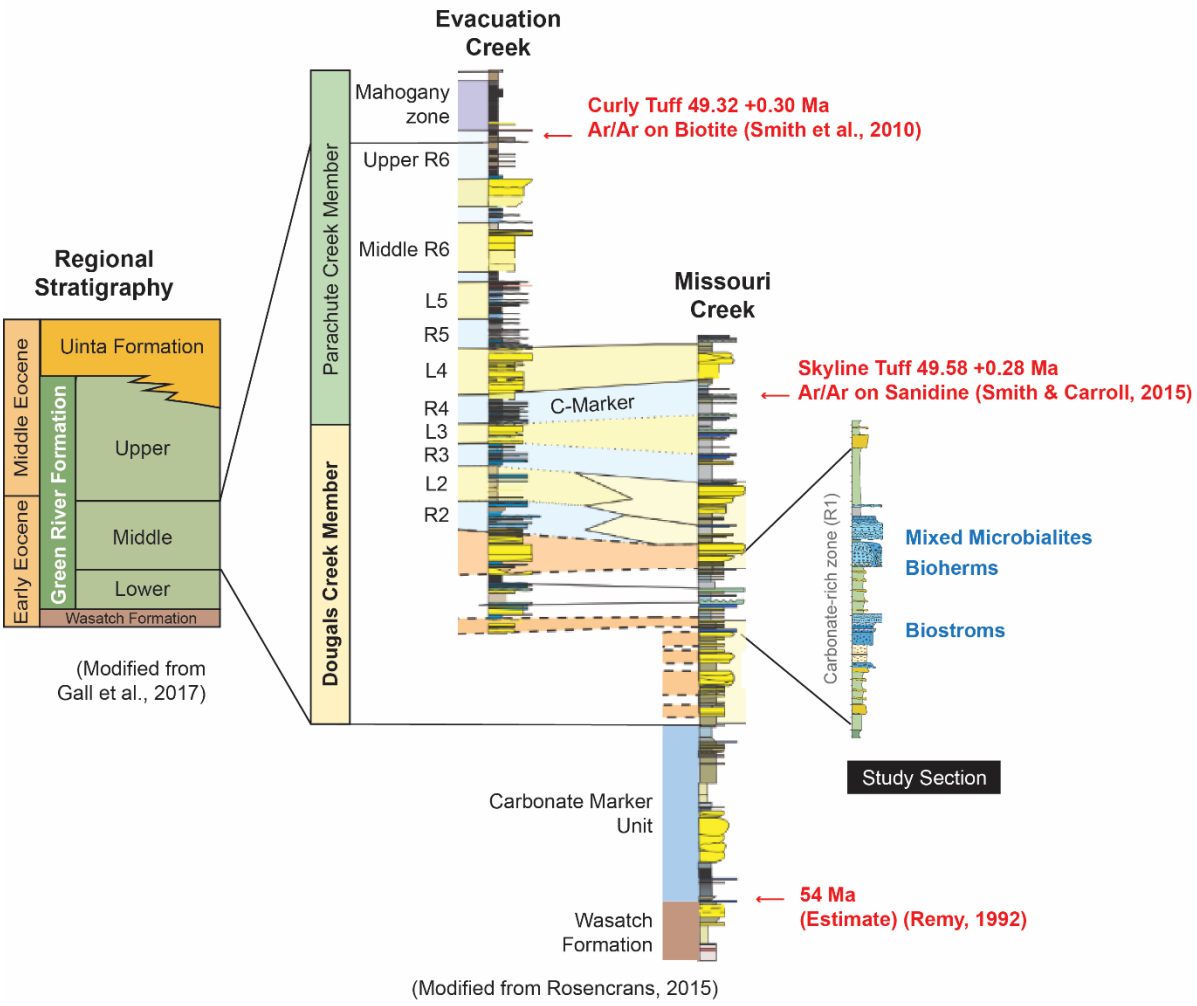

Figure 38. On the left, regional stratigraphy of the Eocene Green River Formation in the Uinta Basin (Gall et al, 2017). On center-right, Evacuation and Missouri Creeks reference sections from Rosencrans (2015), highlighting the microbialite-bearing study section located in the upper part of the Douglas Creek Member. Note alternating carbonate-rich (R) and carbonate-lean (L) zones of Cashion and Donnel (1972)

Fossil and living microbialites are abundant in littoral zones of several lakes (Casanova and Hillare-Marcel, 1993), especially in saline-alkaline lakes. Microbial carbonates provide sensitive signals of changes in inflow, precipitation, evaporation, subsidence, and sediment supply. Numerous studies have shown the potential of the microbial carbonate as a proxy to lake hydrologic state reconstructions (Abell et al., 1982; Casanova, 1986; Hillaire-Marcel and Casanova, 1987; Casanova and Thouin, 1990; Straccia et al., 1990; Talbot, 1990; Arenas et al., 1997; Petryshyn et al., 2012; Buongiorno et al, 2018). Lacustrine microbial carbonates provide information on lake-level fluctuations (Awramik and Buchheim, 2015), paleohydrology, through ^{13}C and ^{18}O analyses (Talbot, 1990), and paleoenvironments, based on their growth morphology (Cohen et al, 1997).

The Eocene Green River Formation (GRF) of Wyoming, Utah, and Colorado contains excellent examples of microbial carbonates associated with its world-class cyclical lacustrine successions (Bradley, 1929; Eugster and Hardie, 1975; Surdam and Stanley, 1979; Fischer and Roberts, 1991; Roehler, 1993). Most of the current debate about the origin of these cyclical variations has focused on relatively long-time scales: Milankovitch orbital cycles (Machlus et al., 2004; Meyers, 2008; Smith et al., 2010; Whiteside and Van Keuren, 2009; Baddouh et al, 2016) or tectonic driven cycles (Pietras et al., 2003; Doebbert et al., 2010). Higher frequency cycles, like millennial-scale and annual to centennial climatic fluctuations, lack enough characterization in the Green River Formation (Pietras et al., 2003; Machlus et al., 2008; Aswasereelert et al., 2013).

Here we show that nine distinct microbialite facies arose in different environments and developmental stages of a brackish, shallow subaqueous littoral zone on a local basement high of Douglas Creek Arch, which has acted as spillways during filling of the Lake Uinta.

We argue that Douglas Creek Member and the Carbonate-rich zone (R1) are most plausibly interpreted as a saline, mixed, siliciclastic-carbonate platform based on facies analysis, combined attributes of the microbialites, geochemistry data, and the microbialite distribution.

3.3 Methods

We examined several cliffs along Evacuation and Missouri Creeks in the eastern Uinta Basin (up to 24 km^2 in area). High-resolution stratigraphic analysis was performed based on measured sections, outcrop descriptions, hand samples, thin sections, petrology, mineralogy and O and C stable isotope data. Five detailed stratigraphic sections (Fig.37C) were measured, building on the work of Rosenberg (2013) and Rosencrans (2015) (Fig.38). Microbialites were traced laterally between sites.

Petrography

Detailed facies analysis following Dalrymple (2010) was performed using 173 hand samples collected from the measured sections. All hand samples were slabbed in vertical profile (normal to bedding) and the carbonate samples were polished. To better identify the minerals and carbonate microstructure, 48 (76.2 x 50.8 mm) and 20 (46 x 27 mm) petrographic thin sections were made. Billets were vacuum impregnated with blue epoxy for porosity type characterization. Thin sections were stained with Alizarin Red S to distinguish calcite/aragonite from dolomite and studied using a Nikon Eclipse LV100 Polarizing microscope.

Facies analysis

To interpret the sedimentary successions, the approach suggested by Dalrymple (2010) was used with the definition of the facies (fundamental building blocks). From that, the facies succession was determined to finally generate a summary of the depositional system.

Whole rock mineralogy by X-ray diffraction

Quantitative XRD bulk mineralogical determination was made by the Rietveld refinement method (Rietveld, 1969). To reduce the mean particle diameter to 5 – 10 μm of 142 samples, the Hardy and Tucker (1988) procedure was followed, with grinding in an agate mill and then grinding for 5 minutes in a McCrone Micronizing mill. Analyses of the powdered samples were performed on Panalytical Empyrean Powder Diffractometer (UCSB Material Research Laboratory) with CuKα radiation, PIXcel3d detector and Ni filter, under a 45-kV voltage and 25-mA intensity. The scanning range of the goniometer is 5° to 55° 2θ. The X-ray diffraction patterns were interpreted using MDI Jade 2010 Software (ICDD PDF-2 Database at Loma Linda University).

Scanning Electron Microscope (FEG-ESEM with EBSD, EDS and CL)

Observations by SEM of thin sections were performed using a FEI Quanta 400F field emission source equipped with an HKL Technology Nordlys 2 electron-backscatter diffraction (EBSD) camera for crystal orientation determination, an INCAx-act silicon drift detector x-ray energy spectrometer (EDS), and a cathodoluminescence (CL) detector.

Automated mineralogical mapping

Six representative polished thin sections were selected for quantitative evaluation of minerals by scanning electron microscopy (QEMSCAN) performed at the Petrobras Research Center (CENPES) in Brazil. Mineralogical mapping was performed by

QEMSCAN 650 (FEI) equipment: a scanning electron microscopy and energy dispersive X-ray spectrometry technology, combined with sophisticated software for automation and image processing. This method provides rapid, fully integrated mineralogical mapping with 10 μm resolution / pixel size.

Considering the limits of the technique, the following phases of Ca-Mg carbonates detectable by the equipment were: calcite containing 0% to 1% (mass) MgO; calcite containing 1% to 4% MgO; calcite containing 4% to 7% MgO; calcite containing 7% to 10% MgO; dolomite containing 17% to 20% MgO; and dolomite containing 20% to 22% MgO. The values of stoichiometric calcite and dolomite are 0 and 22% MgO, respectively.

Stable carbon and oxygen isotopes

$\delta^{13}C$ and $\delta^{18}O$ isotope analyses were performed on 140 carbonate powder samples. They were carefully microdrilled with a 1 mm carbide bit in Syee Weldeab's Lab (UCSB Earth Science). Care was taken to drill only the targeted areas of (microbialites or detrital infill, avoiding cements as much as possible. Analyses were obtained from 70 mg of microdrilled powder using a Thermo-Finnigan DELTAplusXP MAT isotope ratio mass spectrometer (IRMS) coupled to a Finnigan™ GasBench at the Marine Science Institute Analytical Lab (UCSB). Isotope ratios ($\delta^{13}C$ and $\delta^{18}O$) are reported using the PDB standard. Analytical uncertainties (1σ) are assessed by repeat analyses of NBS 19 standard and accounts for ± 0.07 ‰ and ± 0.18 ‰ $\delta^{13}C$ and $\delta^{18}O$, respectively.

3.4 Results

3.4.1 Facies Analysis

Facies analysis and environmental interpretations rely on the observation that biological, chemical and physical processes produce a record of their actions (Dalrymple, 2010). The interpretation of the sedimentary successions in this study follows the facies analysis approach proposed by Walker (1992) and elaborated by Dalrymple (2010). From outcrop observations and hand samples the sedimentary successions were broken down into facies. Here, the term facies is used in a descriptive sense and defined by a combination of lithologic, physical and biologic attributes that are genetically significant, such as composition, presence or absence of matrix, grain size, texture, sedimentary structures (Dalrymple, 2010). In the case of the carbonates, the microbialite content. However, individual facies can have ambiguous environmental interpretations. Combining facies into groups genetically related to one another as facies associations and/or facies successions is essential for a more accurate environmental interpretation. The concept of succession implies that certain facies properties change progressively and systematically in a specific direction either vertically or horizontally (Walker, 2006). The importance of recognizing such successions is that they place individual facies into a larger context. The outcrops with carbonates in Evacuation and Missouri Creeks show distinct sequential ordering of facies vertically. The relationship between facies and facies succession allows an accurate interpretation of depositional processes and the deduction of the depositional environment.

Twenty-one sedimentary facies have been determined in the study area (Tab.2). These facies are characterized by well-defined sedimentary, stratal, and microbialite features (for example, grain size, sedimentary structures, bed geometry, stratal terminations, and

microbialite type) that are the expression of well-defined depositional processes. Genetically related carbonate facies led to the identification of four facies successions deposited in different depositional environments (Tab.2).

3.4.1.1 Carbonate Facies

This paper focuses on the carbonates of the Douglas Creek Member in the Evacuation Creek area, Utah. The carbonates are notable because of the number of distinctive microbialites occurring as biostromes and bioherms and are traceable over several kilometers. There are two types of carbonate facies: microbialite and non-microbialite. Non-microbialite facies are primarily lithofacies, and the microbialite facies are biofacies (Reading and Levell, 1996). Seven microbialite facies were identified based on distinctive microbialite content and defined by using their macro, meso, and microstructural features. Seven non-microbialite carbonate facies were identified based on the size, composition, and textures of the grains that compose the carbonate rock.

3.4.1.1.1 Microbialites

Microbialites are organosedimentary structures produced by the interaction between benthic microbial communities and detrital or chemical sediments (Burne and Moore, 1987). The microbialites recognized in this study are stromatolites (laminated structures) and thrombolites (clotted and not laminated) Two main microbial processes have been recognized to form living microbialites: trapping and binding of detrital sediment (carbonates, e.g., Reid et al 2000, or non-carbonate grains, e.g., Schieber et al, 2007), and mineral precipitation (microbially induced or influenced, e.g., Dupraz et al 2009). Grey and Awramik (2020) was used to assist in describing the microbialites facies types.

Table 2. Summary of Facies, Facies Successions and Interpretations of Douglas Creek Member, Green River Formation, Eastern Uinta Basin.

Facies	ID	Constituents	Bedding	Sedimentary Structures /Fossils	Facies Succession	Interpretation
Layered stromatolite	M1	Complex biostrome with layers of undulatory (T1), pseudocolumnar (T2) and linked domical (T3) stromatolites	Moderately to poorly defined, more or less continuous laminae, ranging from 1 to 5 mm thick		Biostrome (M1, NM1)	Upper littoral
Domical stromatolite	M2	Ochre hemispherical to nodular unlinked domical stromatolite	Laminae are mostly organized into couplets with light and dark laminae	Pits, coated grains		Middle littoral
Fine-grained, domical stromatolite	M3	White hemispherical to nodular unlinked domical stromatolite	Fine-grained, thin, film-bounded laminae, with a smooth to wavy pattern	Pits, *Chlorellopsis* sp	Bioherm (M3, M4,	Middle littoral
Arborescent stromatolite	M4	Centimeter-size, branching columns. Carbonate mudstone and coated 0.5 mm grains compose the interspace sediment.	Stromatolites form layers 2-3 cm thick, delimited by ≤ 1 cm thick bands of coated grains that fill the interspace area	Ostracods		Middle to lower littoral
Branched minicolumnar stromatolite	M5	Minicolumns are thinner, slender, and branch more frequently than stromatolites in M4	Laminae continuity is visible but sometimes irregular. Interspace area filled by fine-grained sediment of quartz grains, calcite crystals and peloids	Ostracods		Middle to lower littoral
Columnar stromatolite	M6	Columns with tapered tops	Heterogeneous laminae pattern: wrinkled laminae alternate in a film bounded texture	Ostracods		Lower littoral to sublittoral
Chlorellopsis stromatolite	M7	Bulbous to turbinate domical structures that in turn are composed of ministromatolites	Laminae couplets: light-colored dolomicrosparitic laminae and dark micritic laminae	*Chlorellopsis* sp, Pits	Bioherm; Mixed microbialites/detrital carbonates	Lower littoral to sublittoral
Thrombolite	M8	Layers of pseudocolumnar thrombolites	Tan to light yellow mesoclots 1 to 3 mm in diameter, with randomly oriented lobate shapes		Mixed microbialites/detrital carbonates	Middle to lower littoral
Intraclastic conglomerate	NM1	Carbonate fragments up to gravel size	Massive			Beach to Upper littoral

Facies	ID	Constituents	Bedding	Sedimentary Structures /Fossils	Facies Succession	Interpretation
Lithoclastic-ooidal grainstone	NM2	Moderately to poorly sorted, grain-supported ooidal grainstone with some quartz sand and intraclasts	Wavy laminitation, cross-lamination, climbing-ripples, micrite drapes	Ostracods, calcareous		Upper littoral
Peloidal grainstone	NM3	Moderately sorted, more or less rounded grains of homogeneous micrite (peloids)	Parallel lamination, climbing ripples	Ostracods	Mixed microbialites/detrital carbonates	Lower littoral
Ostracodal grainstone	NM4	Articulated and inarticulated ostracod valves, range in size from 100μm to 1mm, are moderately to well sorted	Cross-lamination, wavy laminitation, parallel lamination	Inverse graded, Ostracods	Inverse graded	Littoral
Ooidal grainstone	NM5	300 μm to 1.5 mm diameter, grain-supported micritic ooids. Nucleus of skeletal material, commonly ostracods.	Base of inverse-graded, coated-grain cycles, and an infill between microbialite bioherms	Inverse graded, Ostracods		Littoral
Pisoidal rudstone	NM6	Poorly sorted, micrite-rich pisoids ranging in size from 2 to 3 mm	Irregular layers, several cm thick, that are part of the inverse graded cycles	Inverse graded, Ostracods		Upper littoral
Polygonal and elongated pisoidal rudstone	NM7	Well sorted, 3 to 10 mm diameter, pisoids of elongate to polygonal shapes	Lamellar accretion shows polygonal fitting, perched inclusions, and directional elongations	Inverse graded, Ostracods		Upper littoral
Organic poor carbonate mudstone	NM8	Dolomicrite with spare ostracod, ooid grains, and silt-size quartz and feldspar. Usually organic poor.	Tabular; 0.02–2 m thick		Mixed microbialites/detrital carbonates	Littoral to Sublittoral
Organic rich carbonate mudstone	NM9	Moderately organic rich layers of micrite and dolomicrite; fine-grained matrix of phyllosilicates, quartz and feldspar.	Tabular; 0.02–2 m thick		Mixed microbialites/detrital carbonates	Profundal

Facies	ID	Constituents	Bedding	Sedimentary Structures /Fossils	Facies Succession	Interpretation
Erosive sandstone	S1	Fine to medium sandstone	Thin to thick beds up to 1 m thick with scoured and weak erosional bases	climbing-ripple, parallel lamination, wavy or crinkled lamination, intraclasts, carbonaceous fragments, convolute folds		Littoral to Sublittoral
Tabular sandstone	S2	Very fine to fine massive sandstone	Medium beds up to 50 cm thick with planar non-erosional bases. Flaser bedding.	Cross-lamination, climbing-ripple, wavy or crinkled lamination, ostracods		Littoral
Organic poor siliciclastic mudstone	S3	Varying proportions of silt-size quartz, feldspar, and analcime in a fine-grained matrix of phyllosilicates, quartz, analcime, and carbonates.	Commonly laterally continuous with rare, outsized pyrite grains.	Structureless		Sublittoral
Organic rich siliciclastic mudstone	S4	Organic rich layers of S3	Tabular, lenticular; 0.01–3 m thick			Profundal

Layered stromatolite facies (M1)

The layered stromatolite facies (M1) is a complex biostrome characterized by layers of three types of stromatolites: undulatory (T1), pseudocolumnar (T2) and linked domical (T3). The beds making up this facies are up to 50 cm thick (Fig.39A). At the megastructure level, layers of undulatory stromatolites with little or no positive relief dominated with intervening layers of pseudocolumnar stromatolites and linked domical stromatolites (Fig.39A). Type 1 consists of undulatory stromatolites with moderately to poorly defined, more or less continuous laminae, ranging from 1 to 5 mm thick (Fig.39A, B). The degree of inheritance of the laminae is high. In some places dark laminae are thicker than light laminae while in other places the reverse is true (Fig.39B). The microstructure of type 1 stromatolites are couplets composed of a light-colored dolomicrosparitic lamina (with aggrading neomorphism of crystalline anhedral to subhedral dolomite) and a dark micritic lamina (Fig.39C). Type 1 stromatolites often occur overlain and underlain by the coated grains facies. Type 2 are pseudocolumnar to columnar stromatolites that start with small columns that coalesce at the top in a 10 cm thick bed (Fig.39A, D). The stromatolites have wrinkled and discontinuous lamination (Fig.39D). Laminae of the small columns at the base are poorly defined while toward the top are better defined. Dark laminae range from 0.5 to 3 mm in thickness and are composed of one or more micritic films, rich in organic matter (Fig.39F). Dark laminae contain voids that are incompletely filled with blocky calcite. Fenestral porosity is common. Type 3 are linked domical stromatolites with laterally continuous laminae with a high degree of inheritance (Fig.39A, D). Laminae mainly occur in alternating dark and light pairs (couplets of Hofmann, 1969). Microscopically, couplets are composed of light-colored microsparitic laminae and dark micritic laminae (Fig.39E).

Light laminae are thicker (up to 6 mm) than dark laminae (2 to 4 mm). Diagenesis is evidenced by some partial dedolomitization by micrite replacement and pore-filling, blocky calcite cement.

Domical stromatolite facies (M2)

This facies is characterized by domical stromatolites, which are hemispherical to nodular in shape, have pits, and have a very distinctive ochre color. The domes are up to 15 cm tall and 30 cm wide, unlinked, sometimes in clusters (Fig.40A), and make up a single bed, up to 20 cm thick, and traceable for kilometers. Some of the domes grew on large lithoclasts. The domes have pits (steep-sided depressions) (Bradley, 1929) mostly at the top that are filled with ooids.

The margins of the domes are walled with crinkled laminae. Laminae are mostly organized into couplets with light laminae thicker than dark laminae (Fig.40B). Laminae are primarily laterally continuous except where interrupted by pits. Laminae have a grumous microstructure composed of dolomicritic peloids, 50 to 100 μm in diameter, that are clumped together (Fig.40C). Undulating films of organic matter and fenestral primary porosity occurs sporadically. Coated grains, mainly ooids (0.5 to 1mm in diameter) and ostracods, occur within laminae (Fig.40D). Most coated ostracods have their valves closed. Diagenetic cements are composed of dolomite and blocky calcite.

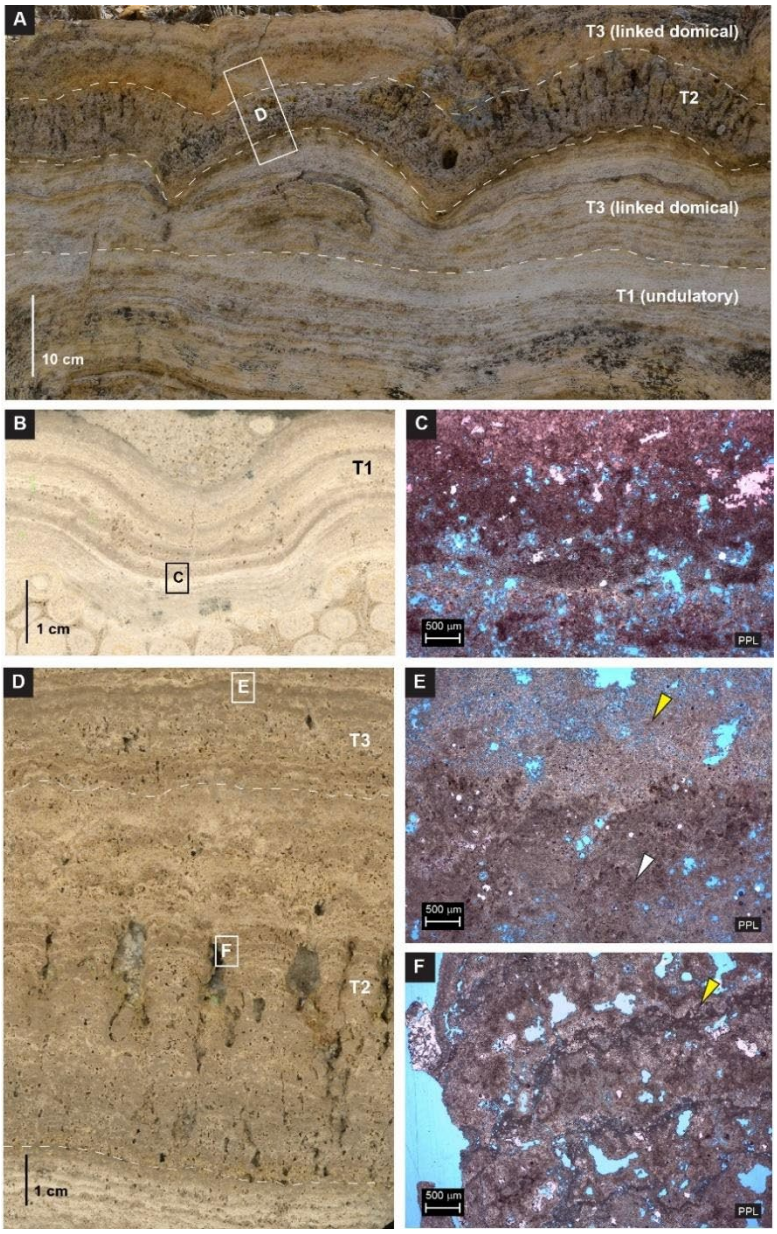

Figure 39. Layered stromatolite facies (M1): A) Outcrop view of complex biostrome composed layered stromatolite facies. Three types of stromatolites are found on a macrostructure scale: undulatory stromatolites (T1), pseudocolumnar to columnar layered stromatolites (T2), and linked domical stromatolites (T3). B) Vertical slab showing stromatolitic mesostructure of undulatory stromatolite (T1). C) Stromatolitic microstructure of T1: well-laminated couplets composed of light-colored microsparitic laminae and dark micritic laminae. All thin sections stained with alizarin red and photos taken under plane-polarized light (PPL). D) Vertical slab showing stromatolitic mesostructure of T2 and T3. E) Stromatolitic microstructure of linked domical stromatolites (T3), showing a couplet composed of a light-colored dolomicrosparitic lamina (yellow arrow) and dark micritic lamina (white arrow). F) Stromatolitic microstructure of pseudocolumnar to columnar layered stromatolites (T2), note micritic texture with films rich in organic matter (yellow arrow), voids incompletely filled by blocky calcite crystals, and fenestral porosity.

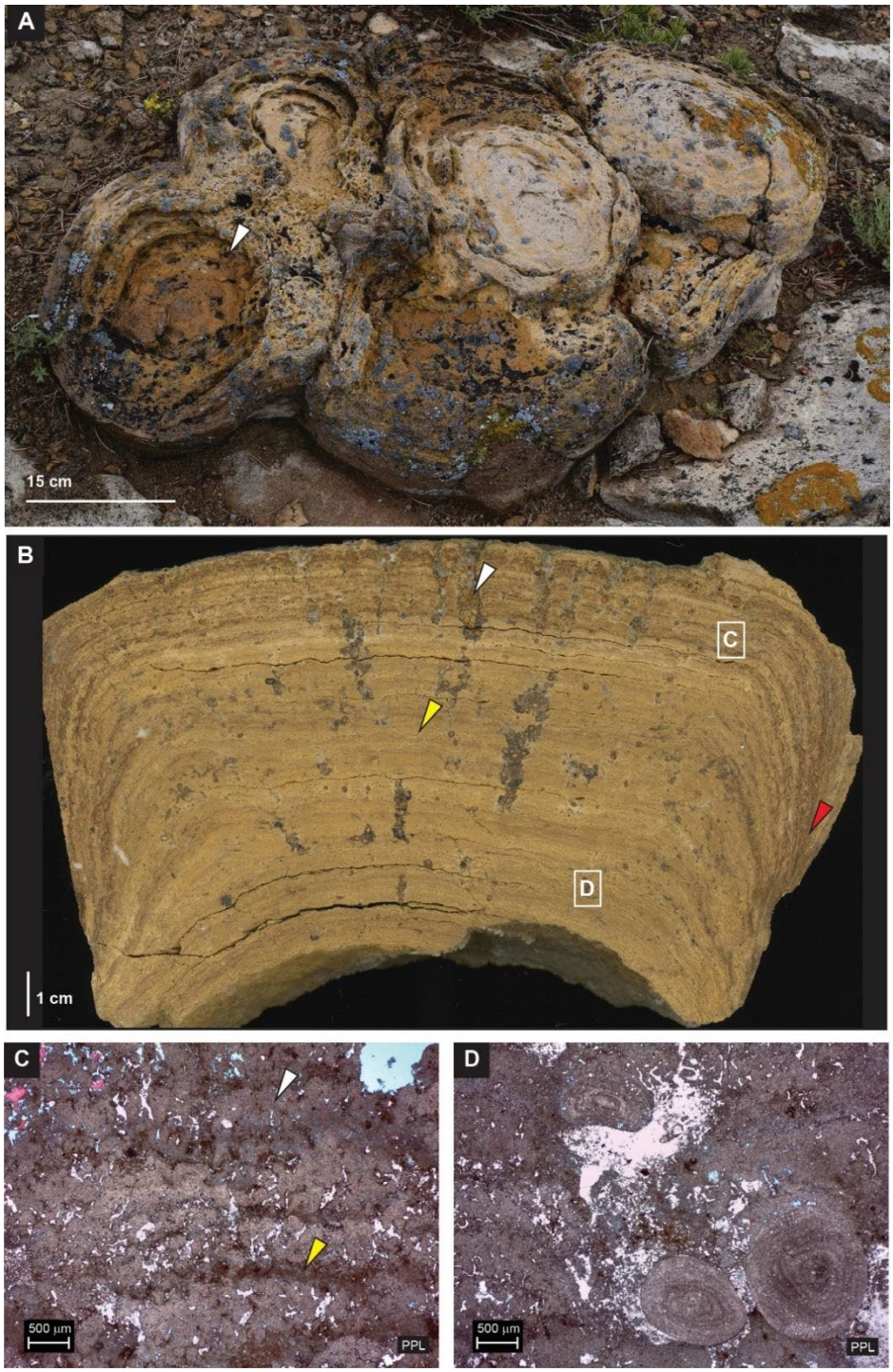

Figure 40. Domical stromatolite facies (M2): A) Plan view of well-developed domical stromatolites reaching up to 30 centimeters in diameter. Note that the domes are grouped together and have pits (white arrow). B) Vertical slab of a domical stromatolite showing crinkled laminae. Couplets with thicker light laminae and thinner dark laminae (yellow arrow). Note the presence of walls (red arrow) and pits with ragged edges (white arrow). C) Grumous microstructure composed of polymorphic dolomicritic peloids often clumped together with undulating films of organic rich carbonate (yellow arrow) and fenestral primary porosity (white arrow). D) Thin section detail of trapped ooids.

Fine-grained, domical stromatolite facies (M3)

Fine-grained, domical stromatolite facies (M3) is complex and characterized by domes, up to 50 cm tall, ranging in shape from hemispherical to nodular, with a distinctive white color (Fig.41A). Domes are unlinked and closely spaced with pits on the top. They formed on a substrate composed of clasts sourced from a variety of origins (see Intraclastic conglomerate facies – NM1). The mesostructure is composed of thin, film-bounded laminae, with a smooth to wavy pattern (Fig.41B). Some laminae contain *Chlorellopsis* sp , spherical microscopic structures of presumed algal origin (Bradley, 1929) (Fig.41C) (The affinity and significance of *Chlorellopsis* are unknown.

Arborescent stromatolite facies (M4)

This facies comprises arborescent stromatolites and their associated coated grains and siliciclastics. The arborescent stromatolites consist of centimeter-size, branching columns (Fig.42A). They vary from 2 to 6 mm in diameter and up to 1.2 cm tall. They form layers, 2 to 3 cm thick, delimited by ≤ 1 cm thick bands of coated grains that fill the interspace areas (Fig.42B). This facies occurs as 10 to 20 cm thick beds. The stromatolites initiate on the positive relief inherited from the underlying fine-grained domical stromatolites facies (M3) or the flat-pebble conglomerate facies (NM2). The interspace sediment and bands are carbonate mudstone (less than 10% silt) and coated 0.5 mm grains. At the mesostructure scale, laminae are poorly defined but are smooth, gently convex with a high degree of inheritance. The microstructure is composed of micrite with rare silt-sized quartz grains floating in the matrix (Fig.42C).

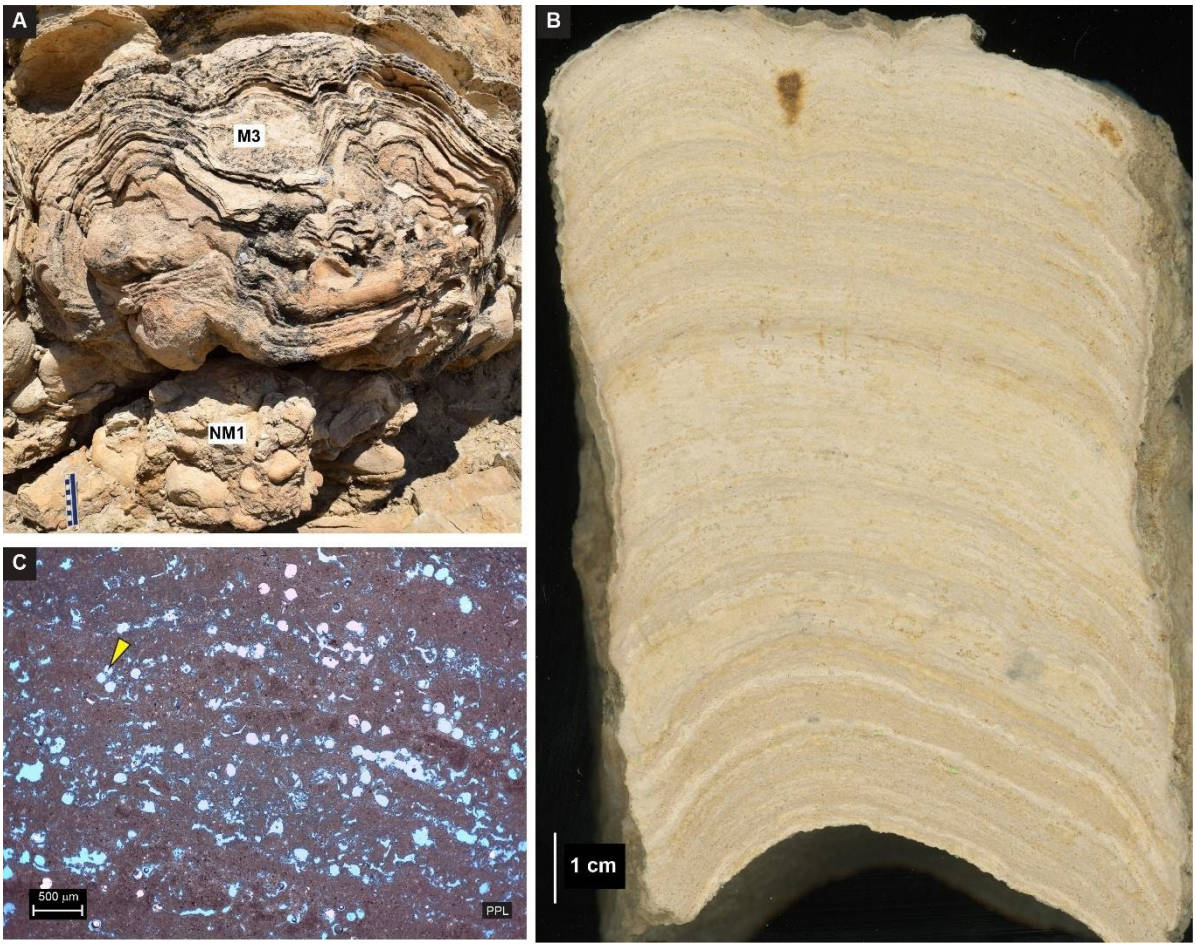

Figure 41. Fine-grained, domical stromatolite facies (M3): A) Outcrop example of M3 facies developed on Intraclastic conglomerate facies (NM1) substrate. Scale is subdivided into 1 cm intervals. B) Vertical slab showing stromatolitic mesostructure of M3. C) Micritic microstructure of laminae with Chlorellopsis sp. (yellow arrow) and fenestrae.

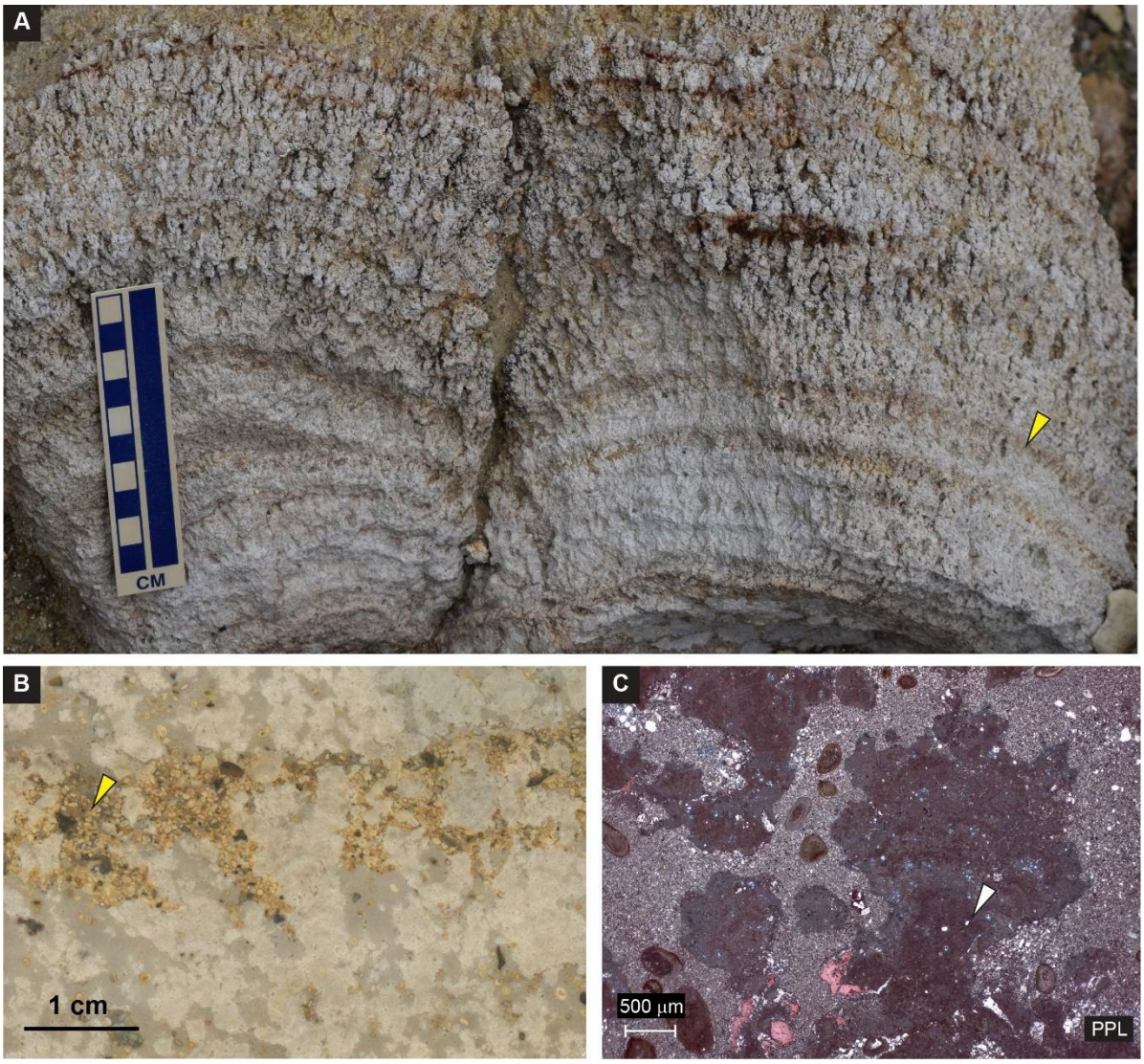

Figure 42. Arborescent stromatolite facies (M4): A) Outcrop view of M4, arborescent stromatolites form layers 2 to 3 cm thick, delimited by interspersed infill of coated grains (yellow arrow). B) Vertical slab of arborescent stromatolite. Note the irregular laminae pattern and the interspace sediment composed of mudstone and infill of coated ~0.5 mm grains (yellow arrow). C) micritic microstructure of arborescent stromatolites. The stromatolitic material is dark gray and the interspace is light gray. Rare trapped and bound silt-sized quartz grains (white arrow).

Branched minicolumnar stromatolite facies (M5)

This facies is characterized by branched minicolumnar stromatolites that form a 20 to 80 cm thick bed (Fig.43A). Some have columns that started out normal to the substrate and then bend to the southeast. Compared to the arborescent stromatolite facies (M4), some features are quite distinct in this facies. First, the branched minicolumns are thinner, ranging from 3 to 20 mm in diameter. Second, the columns are taller (4 to 20 mm tall), with a height-to-width ratio greater than 2 (H>>W). Third, the minicolumnar stromatolites branch more frequently than stromatolites in M4 (Fig.43B). The laminae continuity within the minicolumns is sometimes irregular, but continuity is always visible to the unaided eye. The microstructure of the minicolumns is dolomicritic with distinct laminations, some of which are discontinuous. The interspace area is filled with fine-grained sediment composed by poorly sorted euhedral to anhedral quartz grains, calcite crystals and peloids with inter-particle porosity. Grain size is greater than M4. Few scattered detrital quartz grains are incorporated into the columns (Fig.43C).

Columnar stromatolite facies (M6)

The columnar stromatolites facies is composed of columns with tapered tops (Fig.44A). This facies forms a 10 to 50 cm thick bed. The columns superficially resemble columnar tufa/stromatolites described by Guo and Chafetz (2012; their Fig.1A) from Searles Lake, California. Columns range in size up to 10 cm wide and 40 cm tall and have a bumpy surface. Some columns start out subparallel to the substrate and then bend upward and then to the southeast. The columns have a heterogeneous laminae pattern (Fig.44B), where wrinkled laminae alternate with a film-bounded texture. Some laminae shapes are variable but mostly parabolic. In thin section, laminae are dolomicritic with high fenestral porosity

(Fig.44C). Fenestral and framework pores are partially filled by bitumen. The interspace is filled with poorly sorted, euhedral to anhedral quartz grains (very fine) and peloids. Strong dissolution (recognized by stylolites) and calcite cementation can occur in the stromatolitic microstructure.

Chlorellopsis stromatolite facies (M7)

The *Chlorellopsis* stromatolite facies is composed of bulbous to turbinate domical structures (Fig.45A) that in turn are composed of irregularly shaped minicolumnar stromatolites (Fig.45B). This facies occurs as a 10 to 30 cm thick bed. In outcrop, the ministromatolites superficially resemble large mesoclots and can be misinterpreted as thrombolites. The small columns start out vertical then randomly bend away from the vertical. The ministromatolites are up to 5 mm high and 5 mm wide and branch (Fig.45B). Lamination and *Chlorellopsis* are evident in thin sections (Fig.45C). *Chlorellopsis* consists of sub-millimeter size hollow and microspar-filled spheres (Bradley, 1929). Microstructure ranges from micritic to spherical (Grey and Awramik, 2020). Laminae couplets are composed of light-colored dolomicrosparitic laminae and dark dolomicritic laminae (Fig.45C). The stromatolites of this facies have two large and distinct types of circular pits that occur in the upper layers and in parts of the sides of the domes (Fig.45A, 9A, B, C, E). The first type in vertical view has a cylindrical shape with edges characterized by downward-deflected laminae (Fig.46B). The second type simply shows cone-shaped depressions with rounded bottoms (Fig.46C, E).

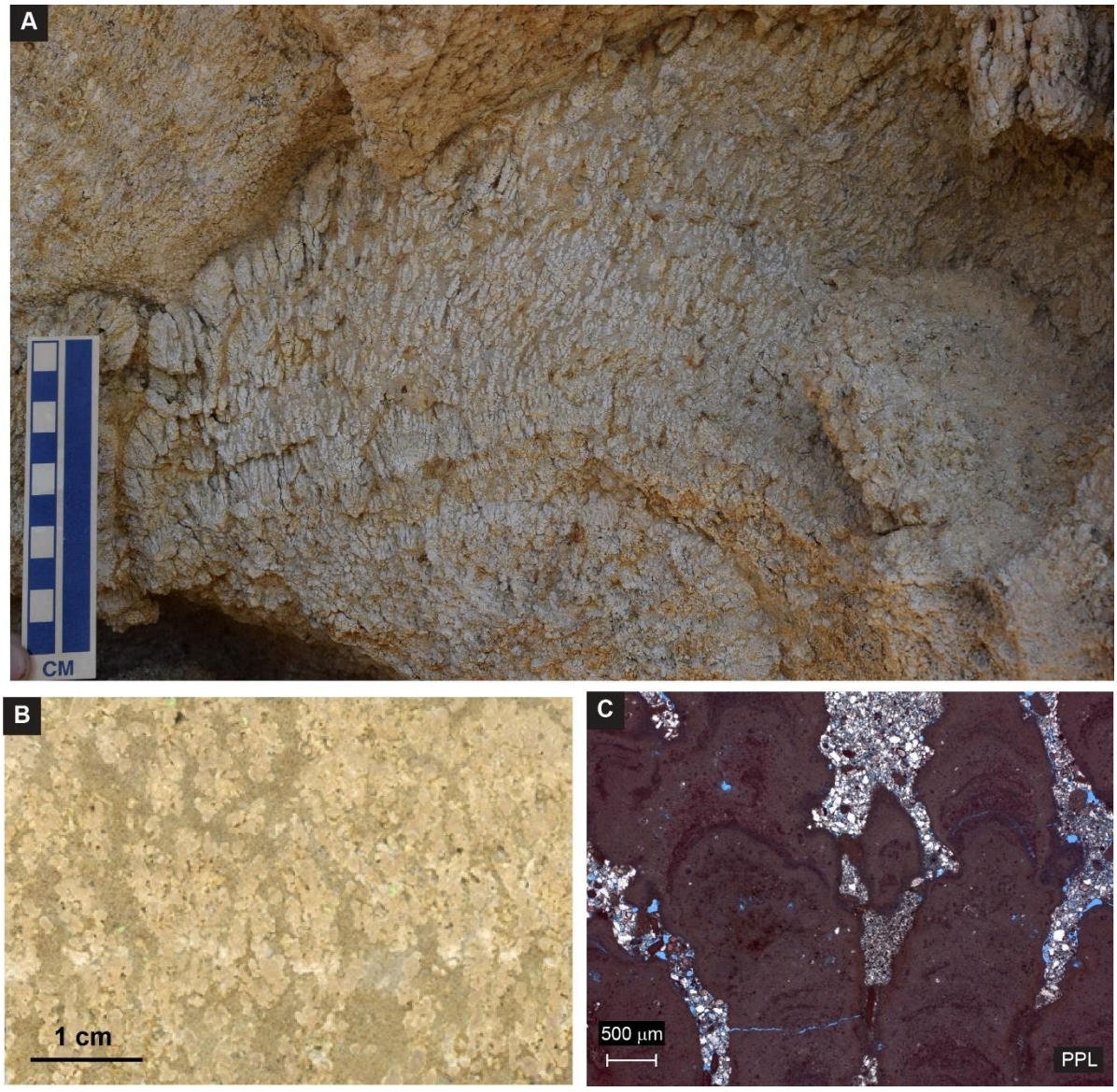

Figure 43. Branched minicolumnar stromatolite facies (M5): A) Outcrop view of branched minicolumnar stromatolites. Note some columns started out normal to the substrate and then bend to the right, which is southeast. B) Vertical slab of branched minicolumnar stromatolite. At the macrostructure level, columns are more slenderer and branch more frequently than stromatolites in M4. Laminae are not very evident. C) In thin section, laminae are evident with well defined, thin dark laminae and much thicker lighter laminae. Some laminae are discontinuous. Microstructure composed of dolomicritic. Note interspace infilled by fine-grained sediments that are coarser than those found in M4 (see Fig.55B for mineral composition).

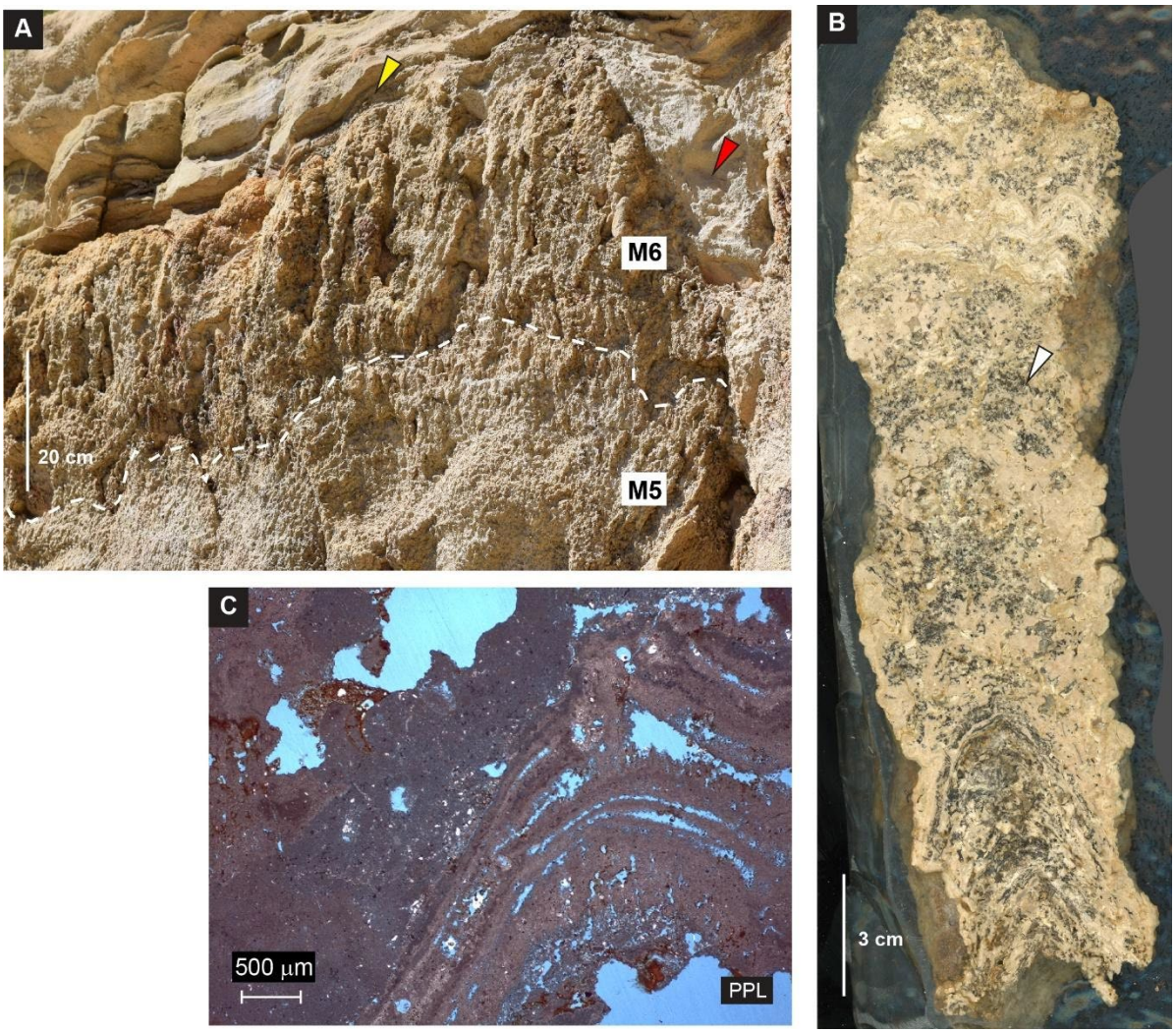

Figure 44. Columnar stromatolite facies (M6): A) Outcrop view of columnar stromatolites. They initiate on the relief (dashed white line) inherited from the underlying branched minicolumnar stromatolite facies (M5). Note siliciclastic mudstone drape (yellow arrow) capping the bioherm and ostracodal grainstone facies (NM4) infilling the interspace between bioherms (red arrow). B) Vertical slab showing the stromatolitic mesostructure, poorly defined heterogeneous laminae (wrinkled to film bounded) with mostly parabolic shape. Fenestral and framework porosity are partially filled by bitumen (white arrow). C) Stromatolitic dolomicritic microstructure with fenestral porosity and bitumen.

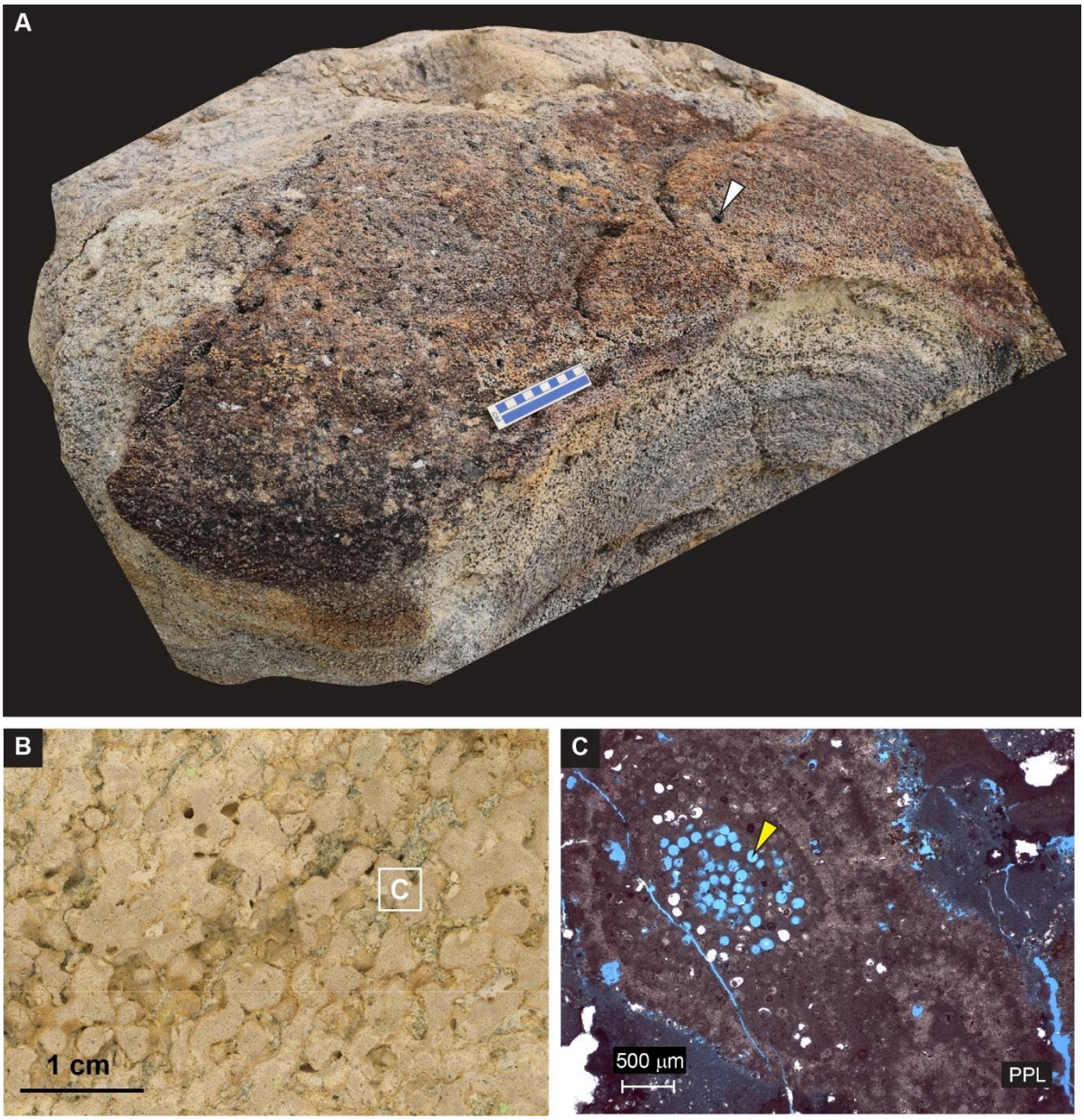

Figure 45. Chlorellopsis stromatolite facies (M7): A) Chlorellopsis stromatolite facies (M7) consists of hemispherical dome of Chlorellopsis-bearing ministromatolites with pits on top (white arrow). B) Stromatolitic mesostructure of M7 showing irregularly shaped minicolumns. C) Stromatolitic microstructure of M7 composed of lamination couplets of light-colored dolomicrosparitic laminae and dark micritic laminae. Note sub-millimeter size hollows of Chlorellopsis sp (yellow arrow).

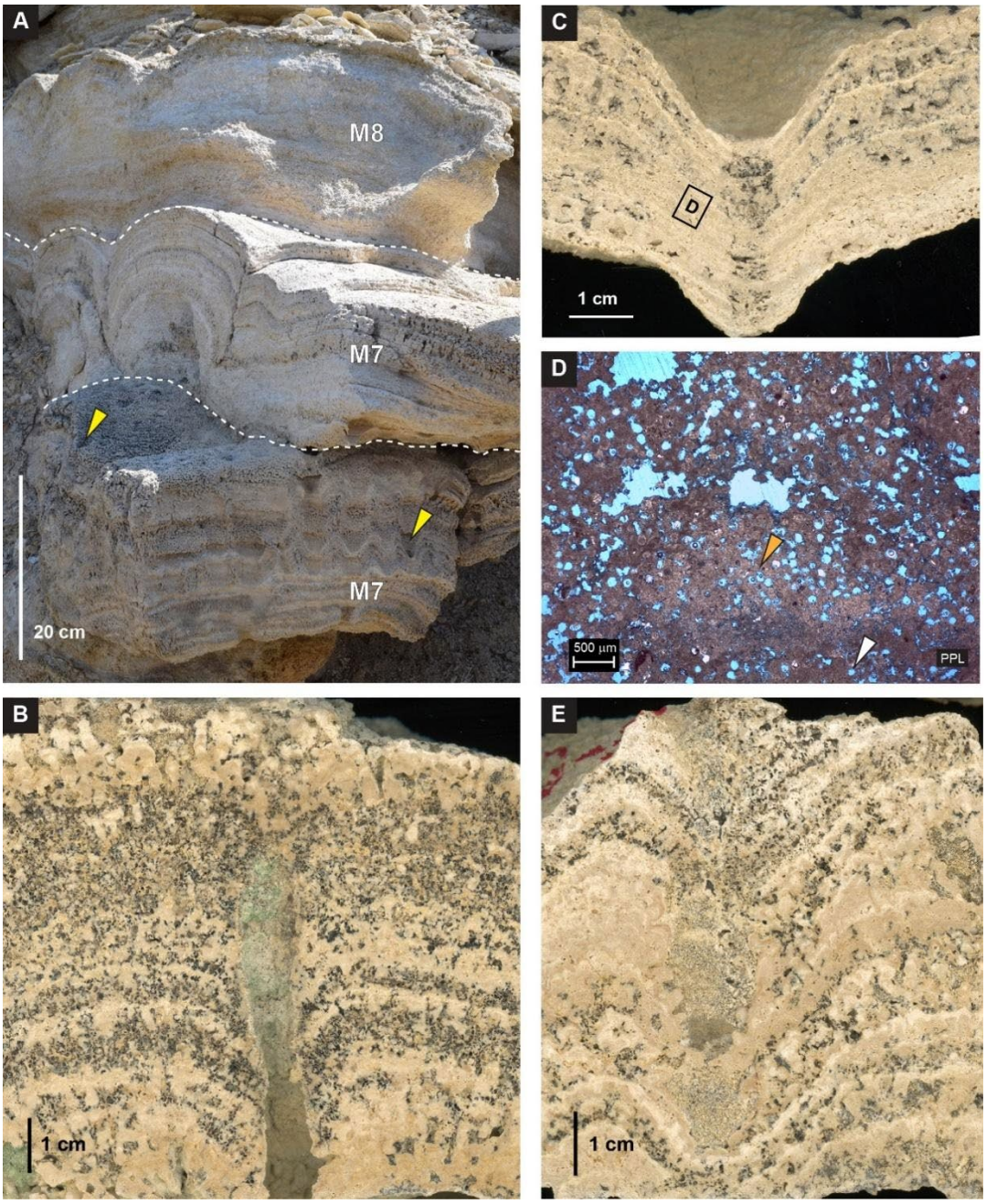

Figure 46. Chlorellopsis stromatolite facies (M7) and Thrombolite facies (M8): A) Outcrop view of two lowermost beds dominated by Chlorellopsis stromatolite facies (M7), overlain by a third bed, the Thrombolite facies (M8). Note presence of cone-shaped pits (yellow arrows) in the lowermost M7 facies bed. Contrasting pits morphologies: B) Vertical slabs of Chlorellopsis stromatolite with cylindrical pit. C) Stromatolitic mesostructure of M7 with cone shape pits. D) Stromatolitic microstructure of Chlorellopsis stromatolite. Microdolosparite laminae with more Chlorellopsis spheres (orange arrow) found directly above a micritic laminae with less Chlorellopsis (white arrow), forming a lamination couplet. E) Another example of Chlorellopsis stromatolite with cone-shaped pits.

Thrombolite facies (M8)

The thrombolite facies is characterized by layers of pseudocolumnar thrombolites (Fig.46A). The thrombolite bed is up to 40 cm thick and can be traced for 2 km. The microbialite is not laminated and does not contain shrubs. Mesoclots vary from 1 to 3 mm in diameter (Fig.47A), are light gray with randomly oriented lobate margins (Kennard, 1994). At the microstructure scale, clots are compound structures, with both mesoclots and miniclots (Fig.47C). Miniclots are up to 500 μm in size.

Heterogeneous microbialite facies (M9)

Heterogeneous microbialite facies consists of morphologically variable microbialites, where the lateral continuity and thickness of the microbialite laminae are different at the center compared to the margins of the microbialite. The beds where M9 occurs can be traced laterally over 10 km and serve as stratigraphic correlation markers.

3.4.1.1.2 Non-microbialites facies

Seven non-microbialite facies were identified based on major carbonate grain types. Grains are bioclasts and non-organic particles that are larger than the groundmass (Flügel, 2010). The terminology used here for the carbonate grains is based on Peryt (1983) and Flügel (2010), whereas the classification is based on depositional texture using the expanded Dunham classification of Embry and Klovan (1971). Some of these grain types and facies grade into one another. Carbonate rocks composed of material of less than 20 μm size areconsidered mudstone.

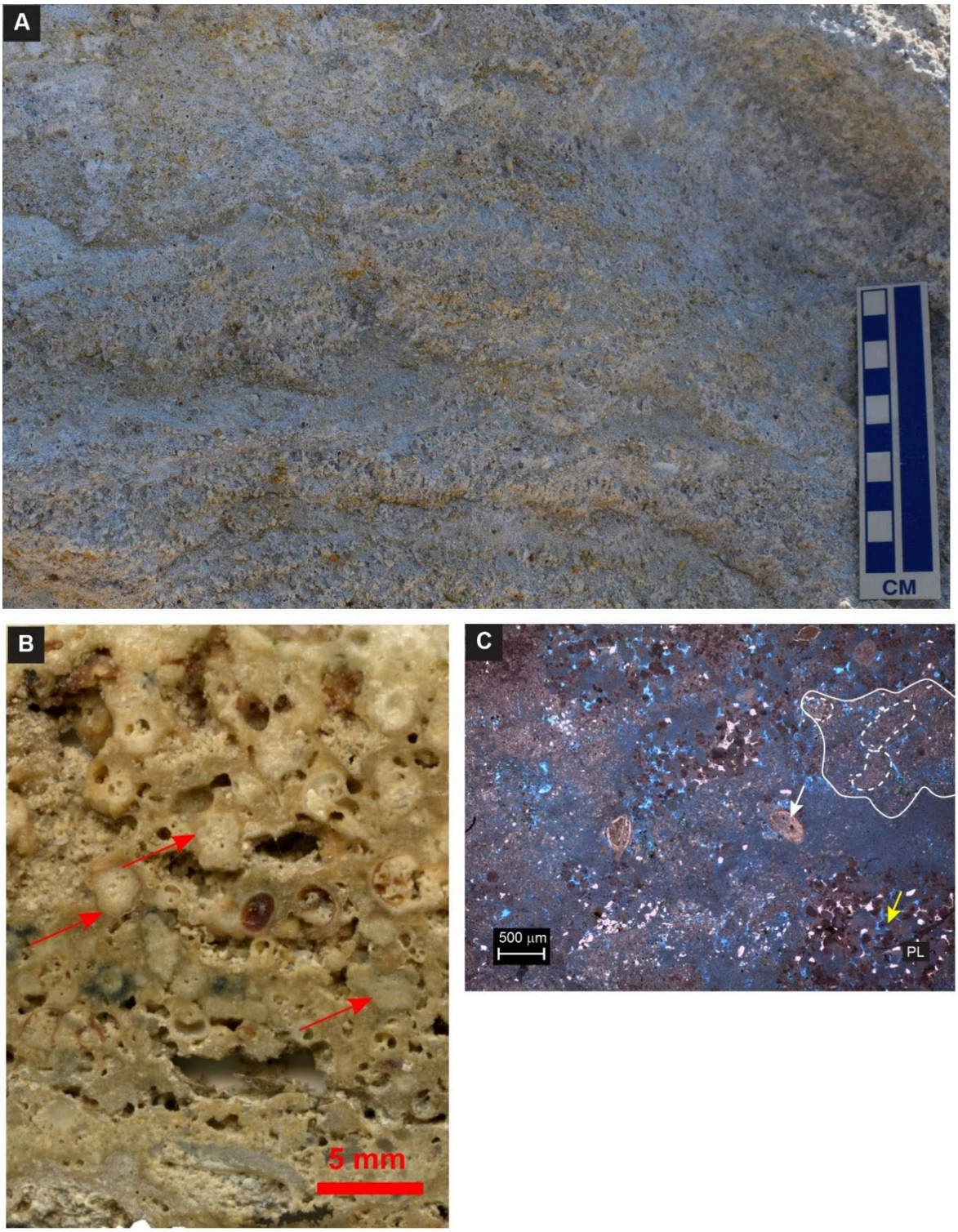

Figure 47. Thrombolite facies (M8): A) Thrombolitic mesostructure, yellow arrow points to a mesoclot. B) Modern lacustrine thrombolite from Rottnest Island, Western Australia. The clots range up to 2 mm in diameter. Compare this to the clots found in Fig.47A. C) Thrombolitic microstructure: mesoclots (white line), microclots (dashed line), peloids (yellow arrow), and ostracods (white arrow).

Intraclastic conglomerate facies (NM1)

The intraclastic conglomerate facies is composed of carbonate fragments up to gravel size (NM1 in Fig.41A). Carbonate clasts are flat with angular edges, along with intraclastic mud chips. The matrix between the clasts is composed of poorly sorted ooids, coated ostracods, and lithoclasts.

Lithoclastic-ooidal grainstone facies (NM2)

The lithoclastic-ooidal grainstone facies is composed of moderately to poorly sorted, grain-supported ooidal grainstone with some quartz sand and intraclasts of mudstone, aggregated peloids, pisoids, cortoids, and microbialite clasts. Intraclasts make up to 20% of the grains. *Chlorellopsis* is present in some microbialite clasts. Ooids are often well laminated and have a well-developed radial structure. They range in size from 100 to 500 μm and these form poorly sorted grainstones.

Peloidal grainstone facies (NM3)

The peloidal grainstone facies is characterized by moderately sorted, more or less rounded grains of homogeneous dolomicrite (peloids) (Fig. 48A, B). The peloids are less than 100 μm in size and closely packed. Scattered articulated coated ostracods and fine to silt-size quartz grains occasionally occur.

Ostracodal grainstone facies (NM4)

The ostracodal grainstone facies consists of articulated and disarticulated coated ostracod valves (Fig. 48C, D). The ostracods range in size from 100μm to 1mm, are moderately to well sorted, and articulated valves are common. They are densely to loosely packed,

generally lacking imbrication. The valves serve as nuclei for coated grains. The carbonate overgrowths tend to decrease the length-height ratio of ostracod valves.

Ooidal grainstone facies (NM5)

The ooidal grainstone facies is composed of 300 μm to 1.5 mm diameter, grain-supported dolomicrite/micrite ooids (Fig.48E, F). The ooids generally have spherical shapes (concentric/tangential ooids), with a nucleus of skeletal material, commonly ostracods, but also peloids (Fig.48F). The original $CaCO_3$ is completely dolomitized, but the traces of concentric laminae may indicate syn-sedimentary dolomitization (Flügel, 2010). The ooidal grainstone is common facies at the base of inverse-graded, coated-grain cycles, and an infill between microbialite bioherms. This facies can also occur as individual beds. In beds of the upper portion of measured stratigraphic sections, the facies shows weak compaction with partly dissolved superficial ooids (oomolds). Intragranular porosity is present, probably the result of dissolution of the carbonate cortices and/or nuclei. This facies has high intergranular porosity, with some pores filled with granular and blocky calcite (cements).

Pisoidal rudstone facies (NM6)

The pisoidal rudstone facies consists of poorly sorted, dolomicrite/micrite pisoids ranging in size from 2 to 3 mm (Fig.48G, H). Pisoidal rudstones occur as irregular layers, several centimeters thick, that are part of inverse graded cycles. Most of this facies has an array of pisoids of different sizes or types (fine-grain coated grains: skeletal, ooildal and peloidal) with an absence of matrix material (Fig.48H). Isopachous and non-isopachous lamellar accretion show evidence of pisoid growth and pisolite cementation. All types may show post-depositional modification by continued accretion of lamellar cement.

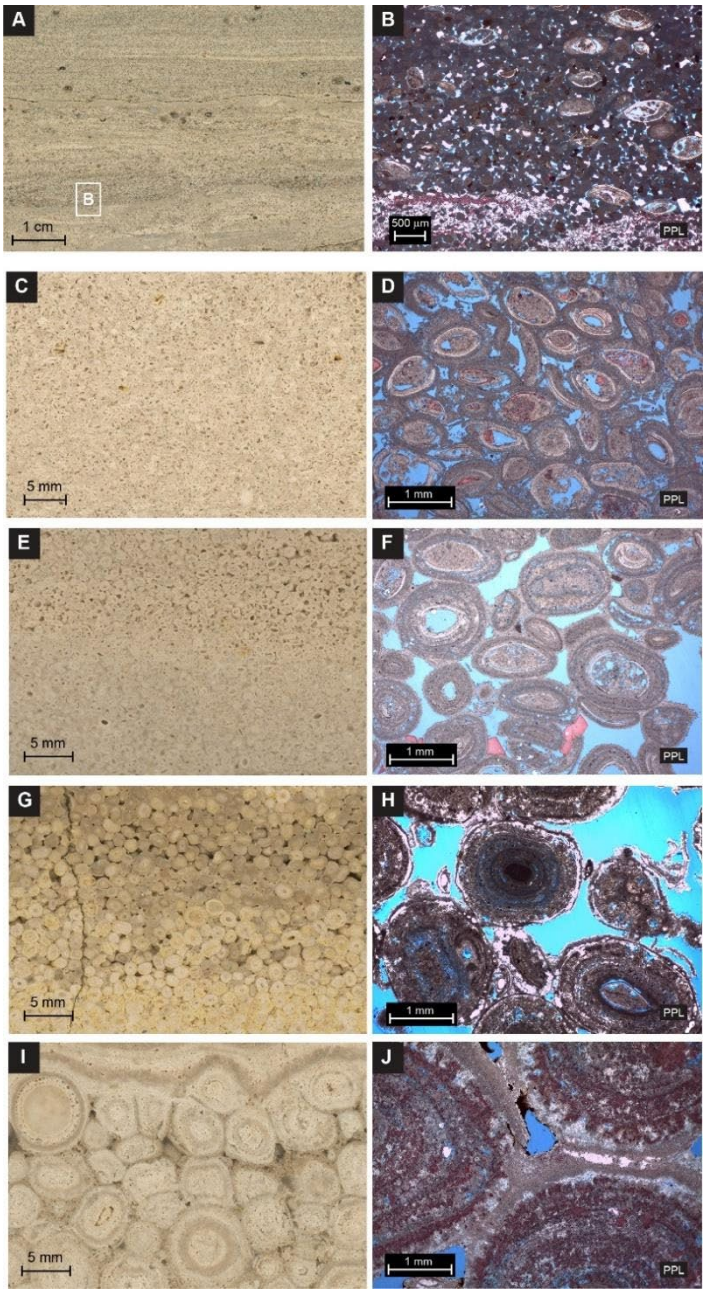

Figure 48. Non-microbialite carbonate facies: A) Slabbed sample of Peloidal grainstone facies (NM3). B) Thin section of NM3 shows the peloidal grainstone (likely fecal pellets) is moderately sorted and has sparse siliciclastics grains and articulated ostracods. C) Slabbed sample of Ostracodal grainstone facies (NM4). D) Thin section of NM4 shows ostracods are mainly articulated and replaced by dolomite. The valves are replaced by very fine dolomite. E) Slabbed sample of Ooidal grainstone facies (NM5). F) Thin section of NM5 shows tangential ooids, commonly with an ostracod nucleus, but also peloids. Note high microporosity. G) Slabbed sample of Pisoidal rudstone facies (NM6) H) Thin section of NM6 shows micrite-rich pisoids, completely dolomitized, ranging in size from 2 to 3 mm. I) Slabbed sample of Polygonal and elongated pisoidal rudstone facies (NM7), note polygonal fitting and elongation of the pisoids. J) Thin section of NM7 shows smooth concentric laminations and linking by cementation.

Polygonal and elongated pisoidal rudstone facies (NM7)

The polygonal and elongated pisoidal rudstone facies is characterized by well-sorted, 3 to 10 mm diameter pisoids of elongate to polygonal shapes (Fig.48I, J). Lamellar accretion shows polygonal fitting (Esteban and Pray, 1983), perched inclusions, and directional elongations. The pisoids are cemented together by a selective placement cementation (Esteban and Pray, 1983) (Fig.48J). Smooth concentric laminations are evident by variations in calcite crystal size. Some laminae show ghosts of radial and radial-concentric arranged crystals. Fabric-selective dissolution and calcite cement occur within the pisoids.

Carbonate mudstone facies (NM8, NM9)

This facies consists of mainly of two types of fine-grained dolomite mudstones. The two types can be distinguished based on the amount of organic matter present: organic-poor carbonate mudstone (NM8) and organic-rich carbonate mudstone (NM9) (Tab.2). Grains include ooids, pisoids, coated oncoids, encrusted intraclasts, and bioclasts.

3.4.1.2 Siliciclastic Facies

Based on measured sections, descriptions of the outcrop, slabbed samples, and thin-sections, four siliciclastic facies were established: Erosive sandstone (S1), Tabular sandstone (S2), Organic-poor siliciclastic mudstone (S3), and Organic-rich siliciclastic mudstone (S4) (Table 2).

3.4.2 Carbonate Facies Successions

Three carbonate facies successions are recognized based on distinct sequential ordering of facies (Dalrymple, 2010) and large-scale morphological characteristics of microbialite-bearing beds.

3.4.2.1 Biostrome facies succession

This facies succession constitutes a tabular biostrome up to 50 cm thick and traceable for kilometers (Fig.49A). It comprises well-developed inverse graded cycles and a biostrome facies succession on top. Each cycle is composed, from bottom to top, by the following facies: ostracodal grainstone (NM4), ooidal grainstone (NM5), pisoidal rudstone (NM6) and polygonal and elongated pisoidal rudstone (NM7) (Fig.49B). Inverse graded beds are 10 to 50 cm thick. All grains are coated and range in size from about 1.0 to 1.5 mm in diameter at the base of the cycle (NM4 facies), increasing in grainsize gradually upward to a maximum grain size of 1.0 to 1.5 cm (NM7 facies). The upper limit of the inverse graded cycle is distinct with no evidence of exposure and generally covered by drapes composed of the layered stromatolite facies (M1). Inverse graded cycles rarely have interparticle matrix material. Fragments of broken grains and intraclasts are uncommon. Most of the nuclei of ooids and pisoids have articulated ostracods. Inverse graded facies succession can persist laterally for kilometers. The biostrome facies succession consists of the sequential order of the following microbialite types of layered stromatolite facies (M1), from bottom to top: undulatory to linked domical (T1), pseudocolumnar (T2), and undulatory to linked domical (T1) stromatolites.

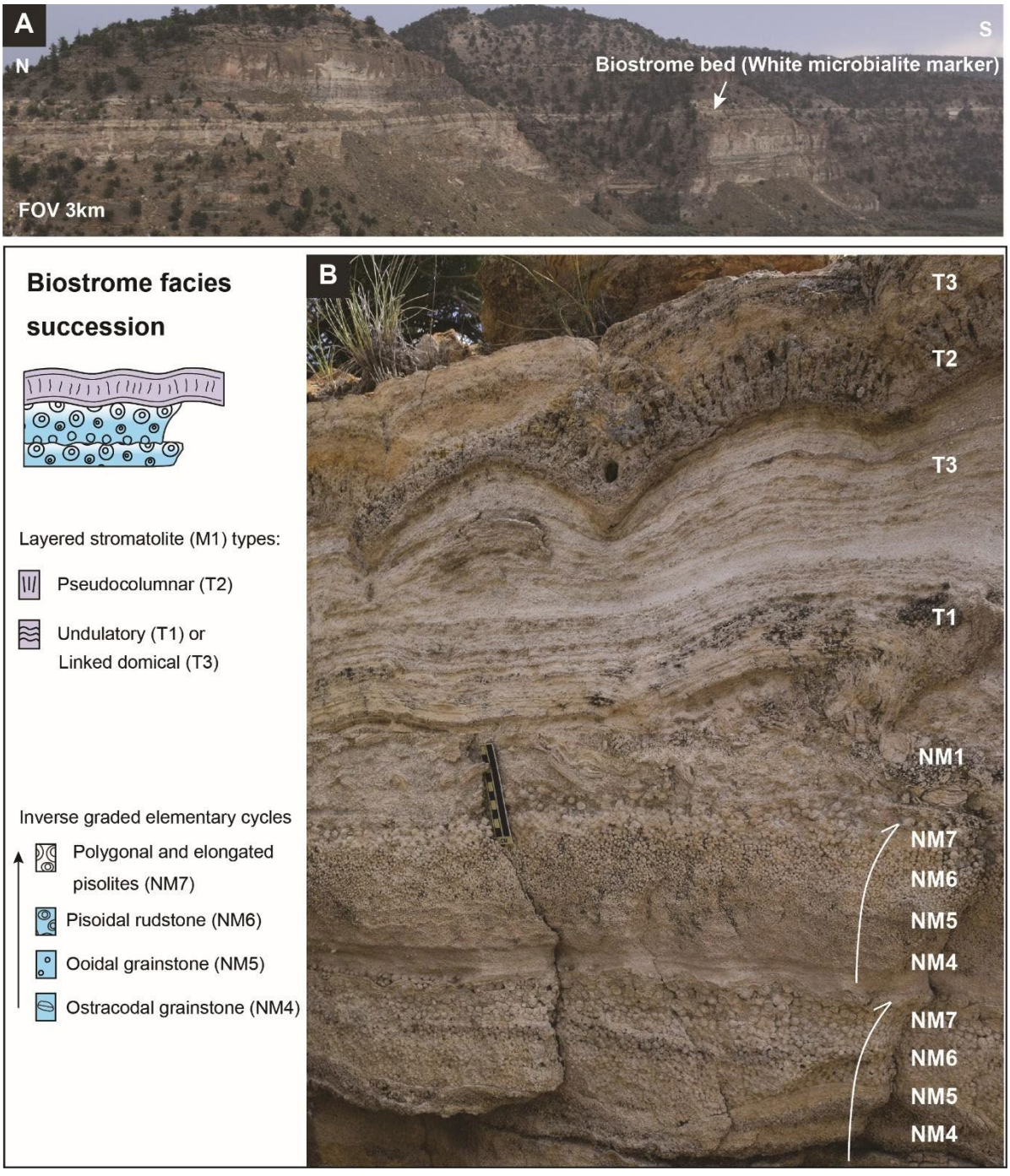

Figure 49. Biostrome facies succession: A) White microbialite marker bed, a tabular biostrome up to meter thick and traceable for kilometers. Photo taken south of Rosewood Section at Evacuation Creek. B) Outcrop view of well-developed inverse graded cycles.

3.4.2.2 Bioherm facies succession

The bioherm facies succession consists of a vertical stacking pattern of microbialite facies within a bioherm (Fig.50). The individual bioherms range in size from 0.4 to 1.5 m in height, and 0.5 to 5 m in diameter. The bioherm height to width ratio is greater than 0.3, resulting in a distinctive domical shape (Fig.50A). The succession starts with the fine-grained domical stromatolite facies (M3) that developed on clasts of the intraclastic conglomerate facies (NM1), followed by arborescent (M4) and branched minicolumnar stromatolites (M5), followed by columnar stromatolites (M6), with the *Chlorellopsis* stromatolite facies (M7) at the top (Fig.50B). Facies vary in thickness laterally, ranging from 5 to 70 cm. Fine-grained domical stromatolite facies (M3) thins laterally toward the western limit of the bioherms' occurrence. The *Chlorellopsis* stromatolite facies is restricted to the tops of the taller (>1m) bioherms (Fig.51A). The sediment infill between the taller bioherms is prone in ostracodal grainstone facies (NM4), while between the northwest smaller bioherms, the main infilling sediment is composed of carbonate mudstone.

3.4.2.3 Mixed microbialite – non-microbialite carbonate facies succession

This succession shows a stacking pattern of microbialites on top of paleo highs. These highs are generally inherited from the taller bioherms below, whose facies change laterally in the paleo lows to non-microbialite facies (intraclastic conglomerate (NM1), peloidal grainstone (NM3), ostracodal grainstone (NM4), and ooidal grainstone (NM5) facies) (Fig.51A). The facies succession consists of *Chlorellopsis* stromatolite facies (M7), Thrombolite facies (M8), Heterogeneous microbialite facies (M9), Lithoclastic-ooidal grainstone facies (NM2),

Peloidal grainstone facies (NM3), Ostracodal grainstone facies (NM4), and carbonate mudstones facies (NM8, NM9). The microbialite facies proportion of the succession comprises 4 beds, ranging in thickness from 20 to 40 centimeters. The two lowermost beds are dominated by *Chlorellopsis* stromatolite facies that change laterally into thin beds (less than 10 cm thick) of the ostracodal grainstone facies (NM4), ooidal grainstone facies (NM5), and carbonate mudstones (NM8, NM9). The *Chlorellopsis* stromatolites beds are overlain by a third bed, up to 40 cm thick, of layered thrombolite facies (M8). Commonly, M8 facies change laterally over a 2 km distance northwest to peloidal grainstones and southeast to ostracodal grainstones and carbonate mudstones (Fig.51B). The fourth microbialite bed consists of up to 30 centimeters of heterogeneous microbialite facies (M9). This facies overlies the thrombolites facies (M8).

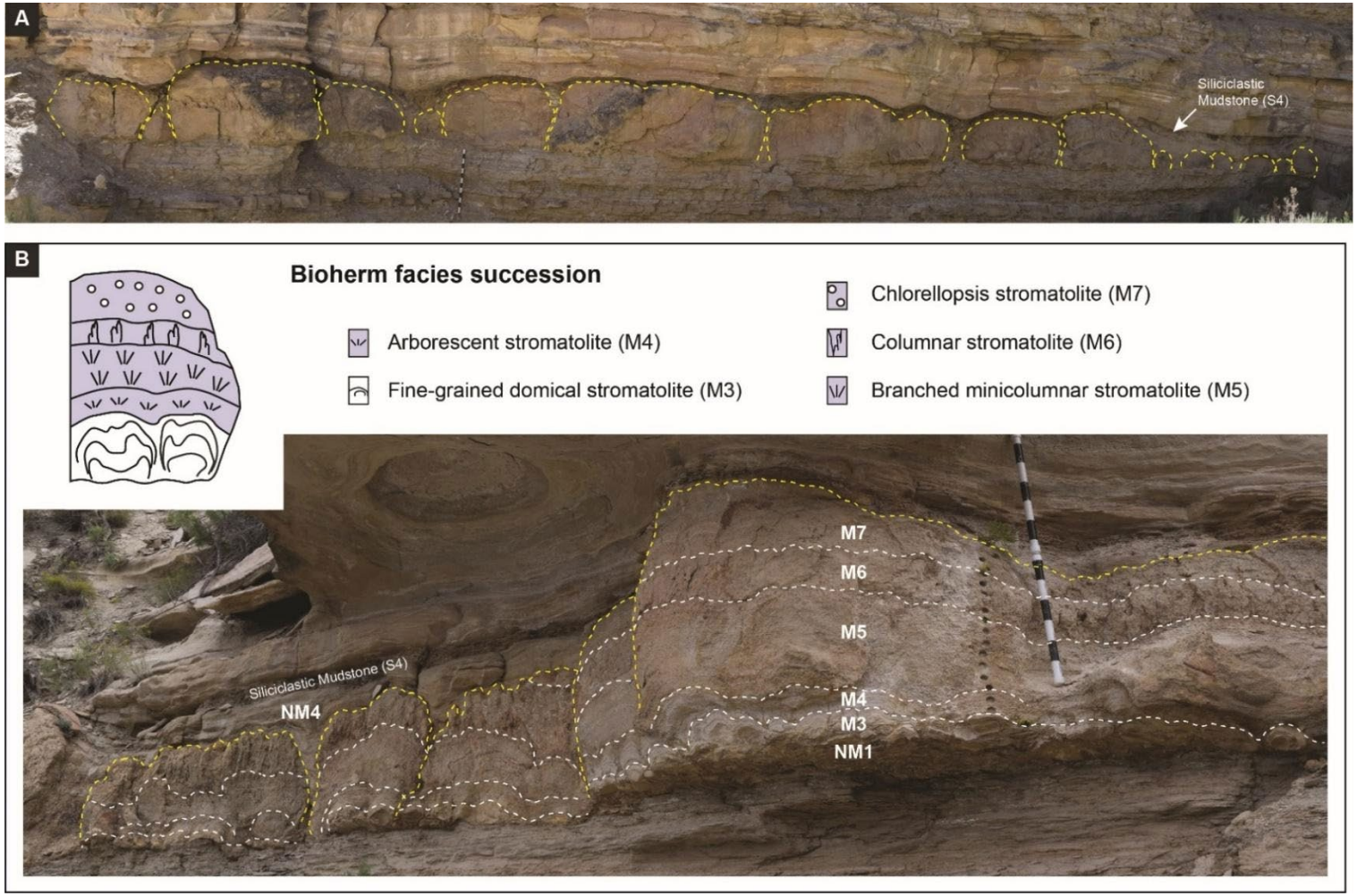

Figure 50. Bioherm facies succession: A) Individuals bioherms, west of Rosewood Section, showing distinctive domical shape (ranging in size from 0.4 to 1.5 m in height, and 0.5 to 5 m in diameter). B) distinctive facies succession within bioherms: fine-grained domical stromatolite facies (M3), followed by arborescent (M4) and branched minicolumnar stromatolites (M5), columnar stromatolites (M6), and Chlorellopsis (M7) facies at the top. Non-microbialite facies: Intraclastic conglomerate facies (NM1) and Ostracodal grainstone facies (NM4).

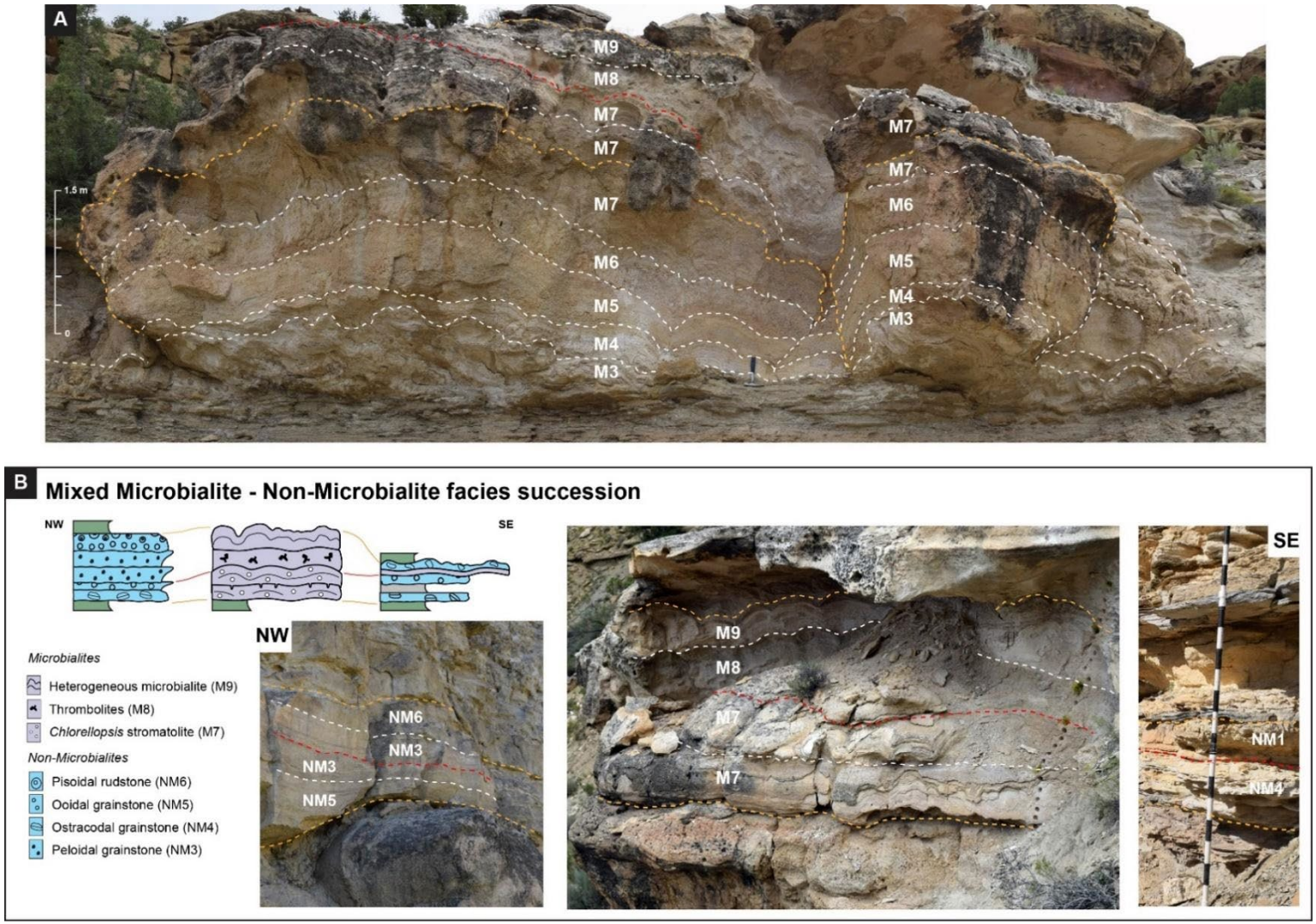

Figure 51. Mixed microbialite – non-microbialite carbonate facies succession: A) Bioherm facies succession with Microbialite facies succession on top at Roosewood Section. B) The microbialite facies commonly changes laterally to non-microbialite facies to northwest and to southeast of the NE Bioherm trend (see Fig.59C).

3.4.3 Mineralogy

The synsedimentary mineralogical variability of saline- alkaline lake deposits of the Green River Formation has been studied by many authors (e.g., Fahey and Rose, 1962; Bradley, 1964; Eugster and Hardie, 1978; Johnson and Brownfield, 2015; Vanden Berg and Birgenheier, 2017; Birgenheier et al, 2020). Aside from detrital minerals, the formation is rich in authigenic minerals formed by neoformation (direct precipitation from ionic solutions), transformation (minerals formed during early to late diagenetic processes), and from microbially-induced mineralization (biomineralization and organomineralization). The Douglas Creek Member of the GRF near Douglas Creek arch differs from more basinward locations of the Uinta Basin in having thick, lake-margin microbial and non-microbial carbonates that record a distinct littoral lacustrine mineral assemblage associated with local fluctuations in the lake chemistry (Smith and Robb, 1966; Cole and Picard, 1978; Moncure and Surdam, 1980; Cole, 1985; Poole, 2014; Boak and Poole, 2015; Tänavsuu-Milkeviciene et al., 2017).

3.4.3.1 Bulk mineralogy

Table 3 presents the average mineralogy of the facies as determined from X-ray-diffraction (XRD) analyses of 142 whole-rock samples. Seven major mineral phases: calcite, dolomite, quartz, potassium feldspar, plagioclase, analcime, and clays were identified. These data are plotted on the stratigraphic columns (Fig.52). To avoid the problematic usage of the name dolomite, dolomite in this paper refers to the mineral and dolostone refers to the rock. Following the carbonate lithology classification of Flügel (2010), the carbonates facies consist of calcitic dolostones (50-90% dolomite) (Tab.3), whereas some pure dolostones (>90% dolomite) occur associated with the microbialite facies (Fig.52). Fine-grained

carbonates, with grain-size <62 μm, comprise the organic-poor and organic-rich carbonate mudstones facies. The organic-poor carbonate mudstones are calcitic dolostones with minor siliciclastic minerals (quartz, k-feldspars). The organic-rich carbonate mudstones are argillaceous limestones (35-65% carbonate) containing calcite (34 wt. %) and dolomite (26 wt. %), with quartz, k-feldspar, clays and minor analcime.

Siliciclastic lithologies (sandstone and siliciclastic mudstone facies) contain quartz (>25 wt. %), potassium feldspar (>11 wt. %), and plagioclase (>8 wt. %) (Tab.3). Tabular sandstone facies (S2) are dolomite-rich (20 wt. %) and contain minor calcite (8 wt. %). Siliciclastic mudstones are fine-grained, nonlaminated rocks that contain variable proportions of detrital silt-sized quartz and feldspar, detrital or authigenic clays, and analcime. Analysis of one tuff from the Ochre Cliffs Section (Douglas Creek Member) indicates that it contains 48 wt. % analcime, plagioclase (27 wt. %) and subordinate calcite (11 wt. %), dolomite (10 wt. %) and quartz (4 wt. %).

3.4.3.2 Ca-Mg carbonates

X-ray diffraction allows fairly accurate determination of the amount of calcium and magnesium substitution in the calcite ($CaCO_3$) or dolomite ($CaMg(CO_3)_2$) lattice. Determination of the mole % $MgCO_3$ content in calcite was based on a single peak displacement in the diffraction pattern (Chave, 1952; Goldsmith et al., 1961). The classification boundaries of Bone and James (1997) are used here, with low Mg-calcite (LMC: 0-4 mol % $MgCO_3$), intermediate Mg-calcite (IMC: 4-12 mol % $MgCO_3$), and high Mg-calcite (HMC: 12-18 mol % $MgCO_3$). For the determination of the mole % $CaCO_3$ content in dolomite the d(104) values of Ca-Mg carbonates reported by Brown (1980) were followed. Samples with higher than 50 mol % $CaCO_3$ are classified as Ca-dolomite. Recent

work has shown that microbially influenced mineralization processes in benthic microbial communities are involved in the precipitation of carbonate minerals, such as high-magnesium calcite and Ca-dolomite, in lacustrine environments (Vasconcelos and McKenzie, 1997; Wright, 1999; Van Lith et al., 2003; Dupraz et al., 2004), marine environments (Bontognali et al 2010), and laboratory experiments (Warthmann et al, 2000; Aloisi et al, 2006; Bontognali et al 2014). XRD and SEM-EDS analyses were performed to evaluate the origin and diagenesis of Ca-Mg carbonates in the Douglas Creek Member.

Analysis by XRD of 94 carbonate samples found that each of the individual minerals consist of low-Mg calcite and Ca-dolomite (Fig.53A, B). The main displacement of the calcite d(104) peak is toward the 3.0269 Å value (low-Mg calcite), while the main shifts of the dolomite d(104) are between 2.89 and 2.90 Å values (Ca-Mg 50:50 mol % and Ca-Mg 55:45 mol %, respectively). All dolomite are ordered dolomites, as the 101, 015, and 021 reflections (corresponding to the conventional hexagonal, and Bravais-Miller indices) are systematically present (Fig.53C). To complement this characterization and understand better the genesis of these non-stoichiometric carbonate compositions, automated mineralogical mapping was performed by scanning electron microscopy coupled to two EDS detectors (QEMSCAN), deploying quantitative evaluation of minerals in the thin sections. Parizek-Silva (2019), combining QEMSCAN with electron microprobe results, was able to construct a mineralogical database mainly for the correct identification and grouping of non-stoichiometric carbonates. The QEMSCAN results from the carbonate facies show mainly Ca-dolomites mineral phases with 54 to 60 mol % $CaCO_3$, which correspond to an approximate chemical formula of $Ca_{1,21}Mg_{0,79}(CO_3)_2$ to $Ca_{1,08}Mg_{0,92}(CO_3)_2$ according to Parizek-Silva (2019). The occurrence of these microcrystalline Ca-dolomites is non-fabric

selective (Fig.55). Low-Mg calcite with 0 to 2.4 mol % MgCO3 ($CaCO_3$ to $Ca_{0,976}Mg_{0,024}(CO_3)$, according to Parizek-Silva, 2019) occurs as pore-filling cement (Fig.55B).

Two populations of Ca-dolomite rhombs, all of them preserving the original texture, were identified in the carbonate facies of the Douglas Creek Member in the Evacuation Creek area. Both populations are very finely crystalline (<100 μm in size) (Fig.56A-D). In the first population (P1), the dolomite consists of smaller, anhedral to subhedral crystals, commonly less than 3 μm in size (Figs.56D). Nano Ca-dolomite mineral phases less than 500 nm also occur. Nanocrystals and microcrystals coexist locally. P1 displays planar-s dolomite shape (Sibley and Gregg, 1987), while some dolomite crystals have irregular faces. Viewed in thin section, the microdolomites have a cloudy aspect and portions have a very thin film of organic matter (Fig.56B). Larger fabric-preserving planar subhedral dolomite crystals (Sibley and Gregg, 1987), up to 4 μm in size, occur as clusters in the microdolomite matrix. These crystals can form closely arranged small rhombs (Fig.56D). Complex shapes result from a coalescence of recrystallized microscrystals, which can produce subhedral, larger Ca-dolomite crystals up to 4 μm in size. No partially degraded EPS (extracellular polymeric substance) matrices or microbial fossils were found during SEM scanning.

The second type (P2) is characterized by rhombs larger than 3 μm. Many crystals are euhedral to subhedral (Figs.19A, C). This type exhibits straight crystal growth faces and well-defined rhombohedral habit, characteristic of planar-e dolomite shape according to Sibley and Gregg (1987). Sharp edges and corners indicate no evidence of dissolution (Fig.56C). Higher magnification shows that the dolomite surfaces are composed of rhombic, frequently oriented sub crystals.

Table 3. Average mineralogical composition of facies by X-ray powder diffraction.

Facies	Calcite	Dolomite	Quartz	Potassium feldspar	Plagioclase	Analcime	Clay	Number of samples
	Mean weight percent							
All microbialite carbonate facies	9	85	3	0	1	0	0	39
All non-microbialite carbonate facies	13	76	5	1	2	0	0	38
Organic Poor Carbonate Mudstone	1	76	8	11	0	2	0	3
Organic Rich Carbonate Mudstone	34	26	13	10	0	4	7	2
Erosive Sandstone	3	8	38	15	25	6	4	14
Tabular Sandstone	8	20	42	11	20	0	0	4
Organic Poor Siliciclastic Mudstone	4	4	25	14	10	23	19	30
Organic Rich Siliciclastic Mudstone	3	0	27	15	8	15	31	6
Tuff	11	10	4	0	27	48	0	1

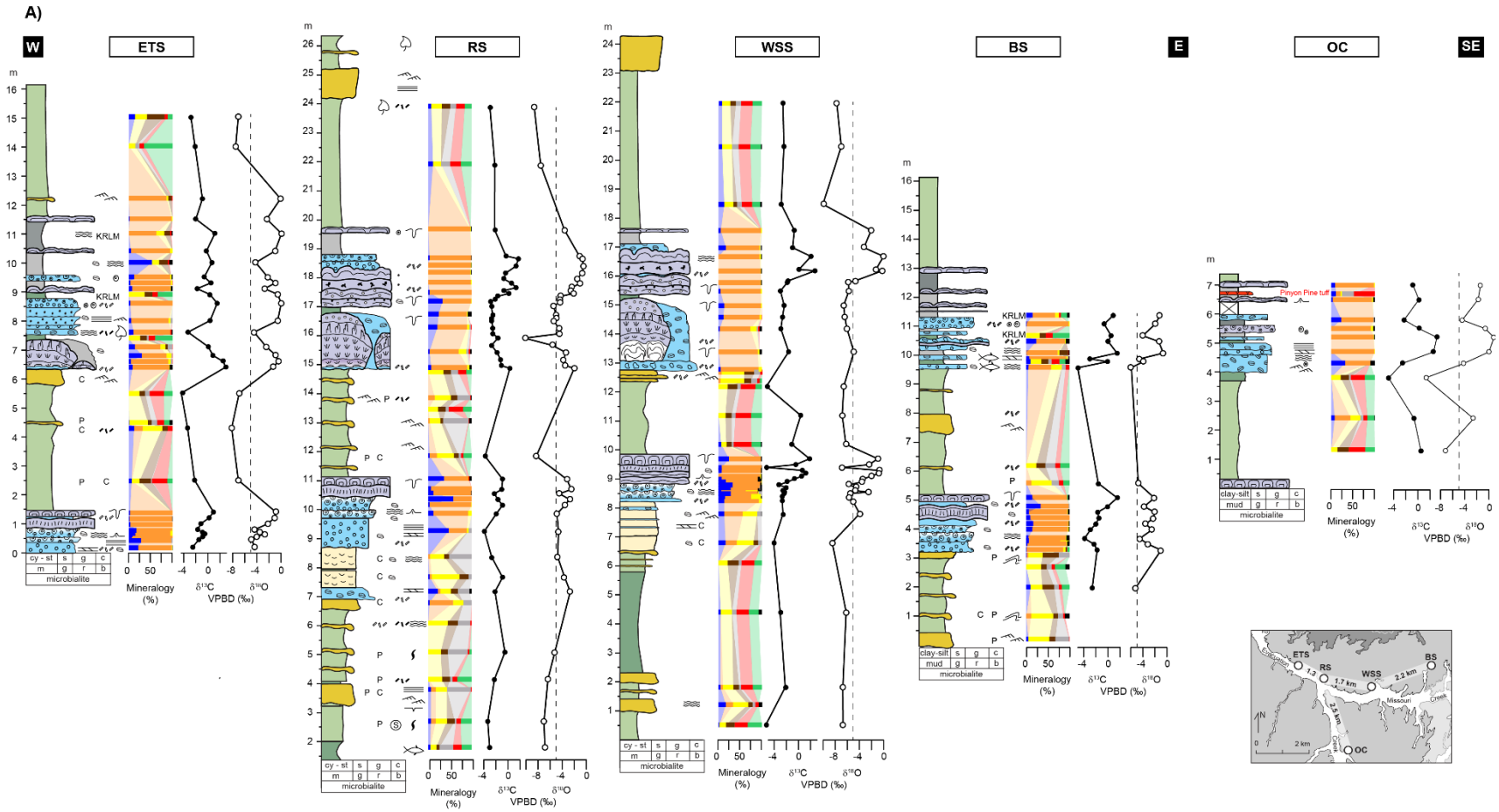

Figure 52. A) Synthesis of lithostratigraphy, bulk mineralogy, stable isotopes (C and O) of the upper section of the Douglas Creek Member of the Green River Formation in the Evacuation Creek area. Measured sections: ETS – East Temple Section, RS – Roosewood Section, WSS – West Stadium Section, BS – Barrel Section.

B)

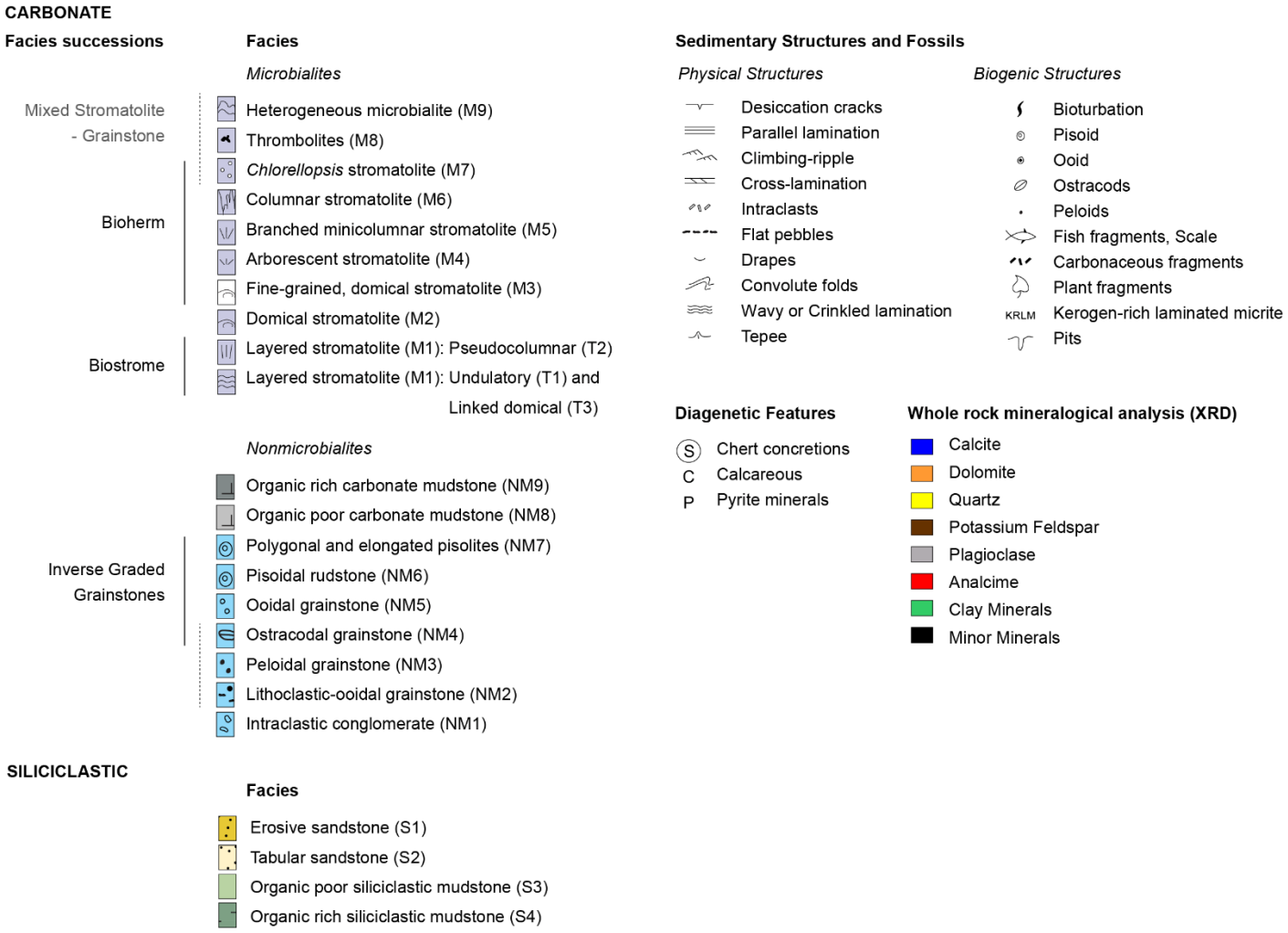

Figure 52. B) Legend for Fig.52A and 58.

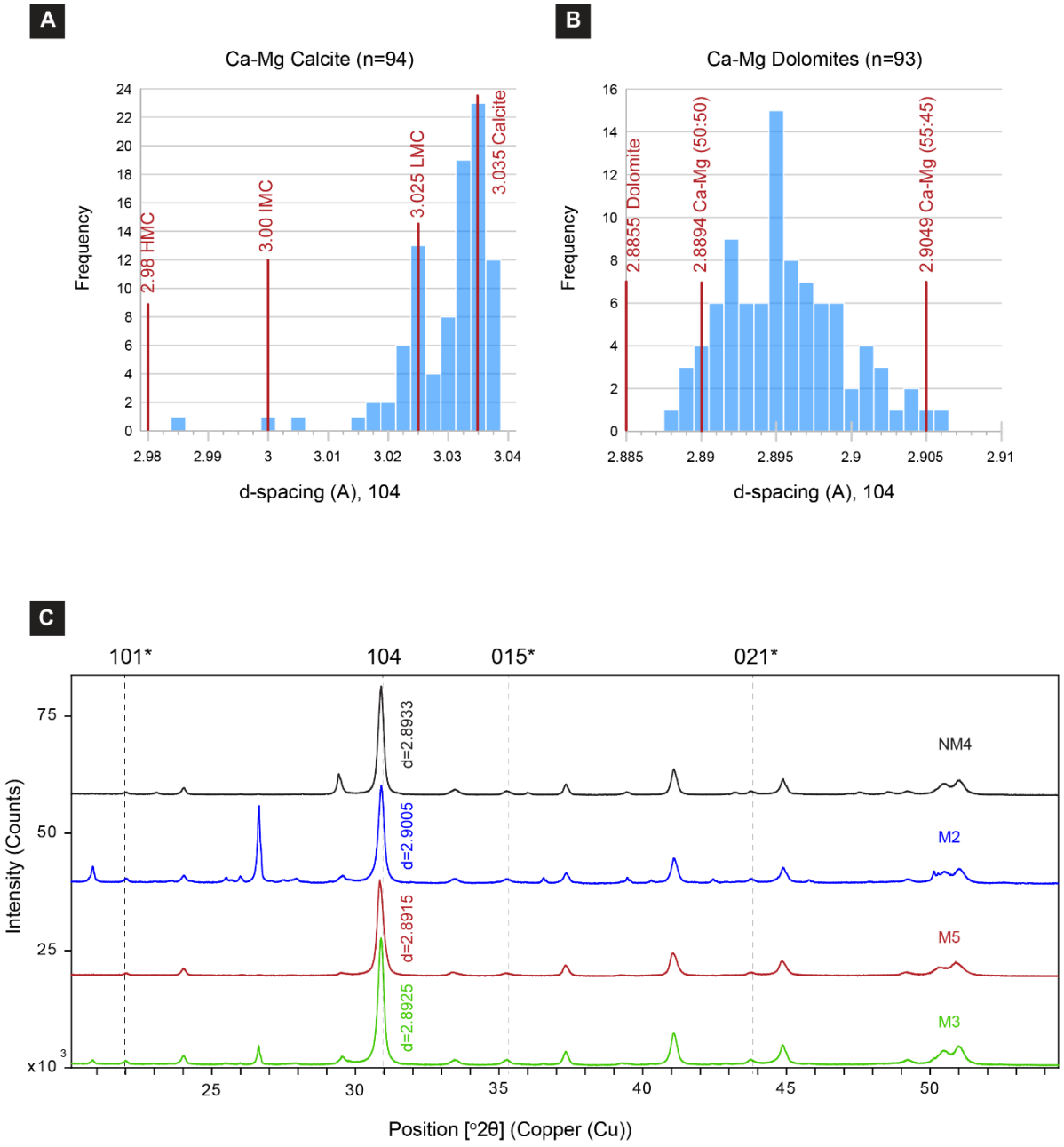

Figure 53. Ca-Mg carbonate mineralogy based on XRD measurements: A) Unimodal and left-skewed distribution of the d-spacing low-Mg Calcites values, d(104) peaks ranging from 3.025 to 3.035 Å. B) Unimodal and fairly symmetric distribution of the d-spacing Ca-Dolomite values, d(104) peaks ranging from 2.89 to 2.90 Å. C) Powder XRD patterns from 20 to 55o 2θ of bulk samples: Ostracodal grainstone facies (NM4, sample ETS-12A), Domical stromatolite facies (M2, sample ETS-13C), Branched minicolumnar stromatolite facies (M5, sample RS-Q5) and, Fine-grained domical stromatolite facies (M3, sample WSS-18). Dolomite ordering reflections indicated by an asterisk.

3.4.3.3 Analcime-rich siliciclastic mudstones

Analcime is a cubic sodium-rich zeolite with an ideal structural formula of $Na_{16}Al_{16}Si_{32}O_{96}.16H_2O$. It is a common authigenic silicate mineral that forms under saline-alkaline lake conditions (Surdam and Sheppard, 1978; Eugster and Hardie, 1978). Authigenic analcime has been reported in tuffs and mudstones of the GRF by different authors (Goodwin and Surdam, 1967; Brobst and Tucker, 1973; Cole and Picard, 1978). Its occurrence has been attributed to an early diagenetic transformation of precursor alkali zeolites inherited from silicic glass in tuff beds (Surdam and Parker, 1972) or by precursor clay minerals (Remy and Ferrel, 1989).

Large amounts of analcime (up to 40 wt%) associated with clay minerals within the siliciclastic mudstone facies were detected by XRD (Fig.52). In organic-poor siliciclastic mudstone, analcime occurs at 23 wt % average and in organic-rich siliciclastic mudstone at 15 wt % average (Tab.3). The analcime-rich siliciclastic mudstones (Fig.54) and associated sandstones and siltstones lack volcanic detritus and zeolites other than analcime. In addition, varying proportions of K-feldspar (up to 25 wt %; 15 wt % average) are found in the siliciclastic mudstone facies. The clay-size material in this facies is on average composed of quartz, k-feldspar, plagioclase, analcime, and clay minerals as detected by XRD (Tab.3)

Petrographic and SEM observations show that analcime grains are discrete and range from 10 to 80 μm in size, mainly 25–50 μm (coarse to very coarse silt) (Fig.54). They are moderately sorted. Grains are dominantly subrounded with moderate to high sphericity. Rarely do they exhibit an equant, trapezohedral crystal form (Fig.54). Pristine subhedral to euhedral analcime crystals show an isotropic extinction under cross-polarized light (Fig.54D). Some analcime crystals are engulfing and replacing the clay matrix (Fig.54C).

Under the SEM, the analcime display characteristics of detrital grains, appearing like reworked subhedral granular crystals, often showing smooth surfaces (Fig.54E). EDS data show that the analcime contains Na, Al, Si, and O, with no other elements detected (Fig.54E, F).

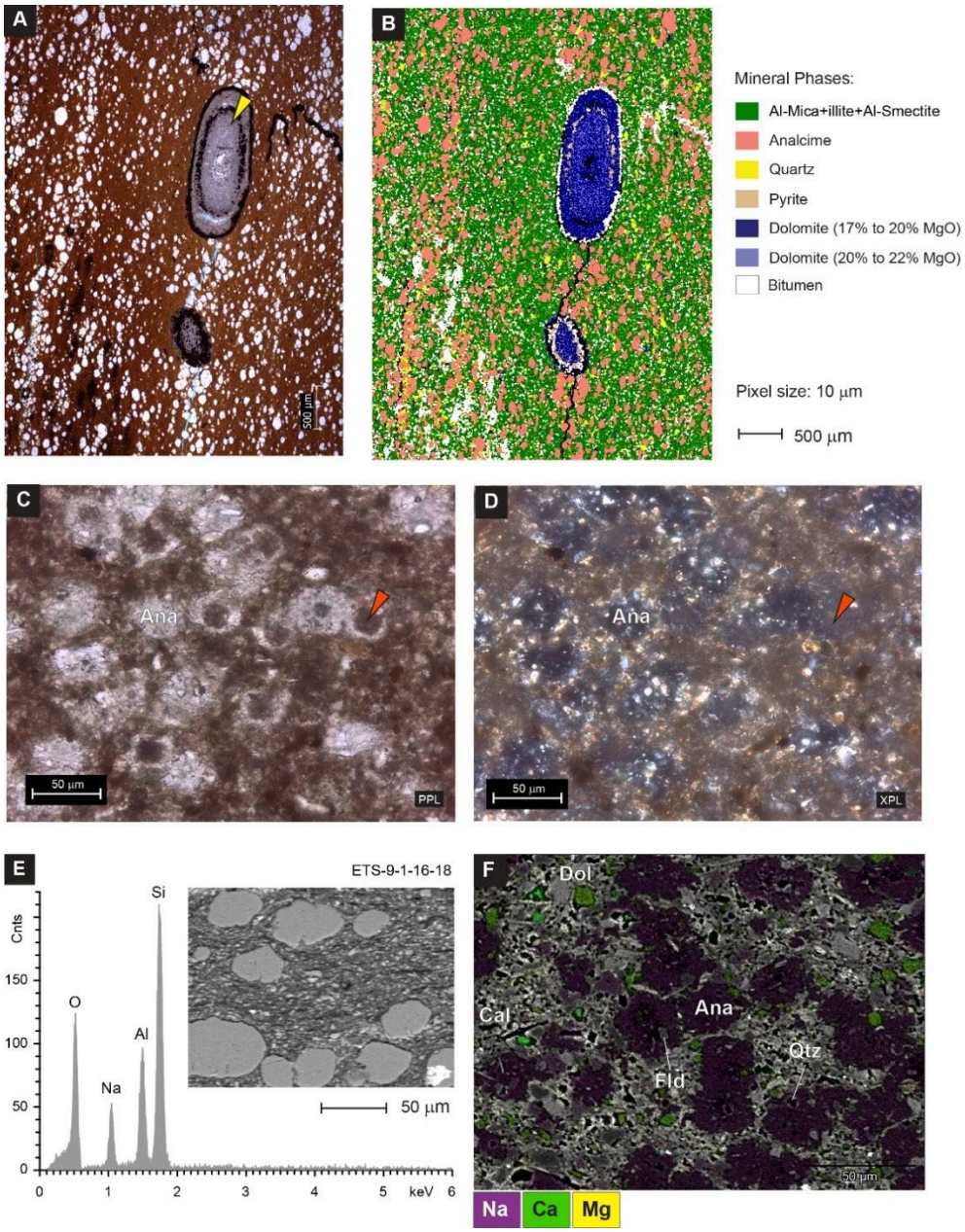

Figure 54. Analcime-rich siliciclastic mudstones: A) Thin-section photomicrograph showing amount and size of discrete analcime grains (10 to 80 µm), ostracods (yellow arrow) and fine-grained minerals. Alizarine-red stained. B) QEMSCAN image of Fig.54A, showing analcime minerals in a detrital clay matrix. Note ostracods grains replaced by Ca-dolomite. C) Thin-section photomicrograph of analcime-rich siliciclastic mudstones, showing subhedral analcime grains (Ana). Note authigenic analcime replacing the detrital clay mineral matrix (red arrow). D) Analcime minerals of Fig.54C with isotropic extinction under crossed-polarized light (XPL). E) EDS spectrum typical for analcime grains present in siliciclastic mudstone facies (S3, S4). BSC-SEM Close-up of subhedral analcime granular crystals, note smooth surfaces; crystals are under 80 µm. F) BSC-SEM image and elemental maps from Fig.54C. EDS Na element map (purple) showing grains fully composed by analcime mineral phase. EDS Ca element map (green) and EDS Mg element map (yellow) show occurrence of calcite (Cal) and dolomite (Dol) crystals.

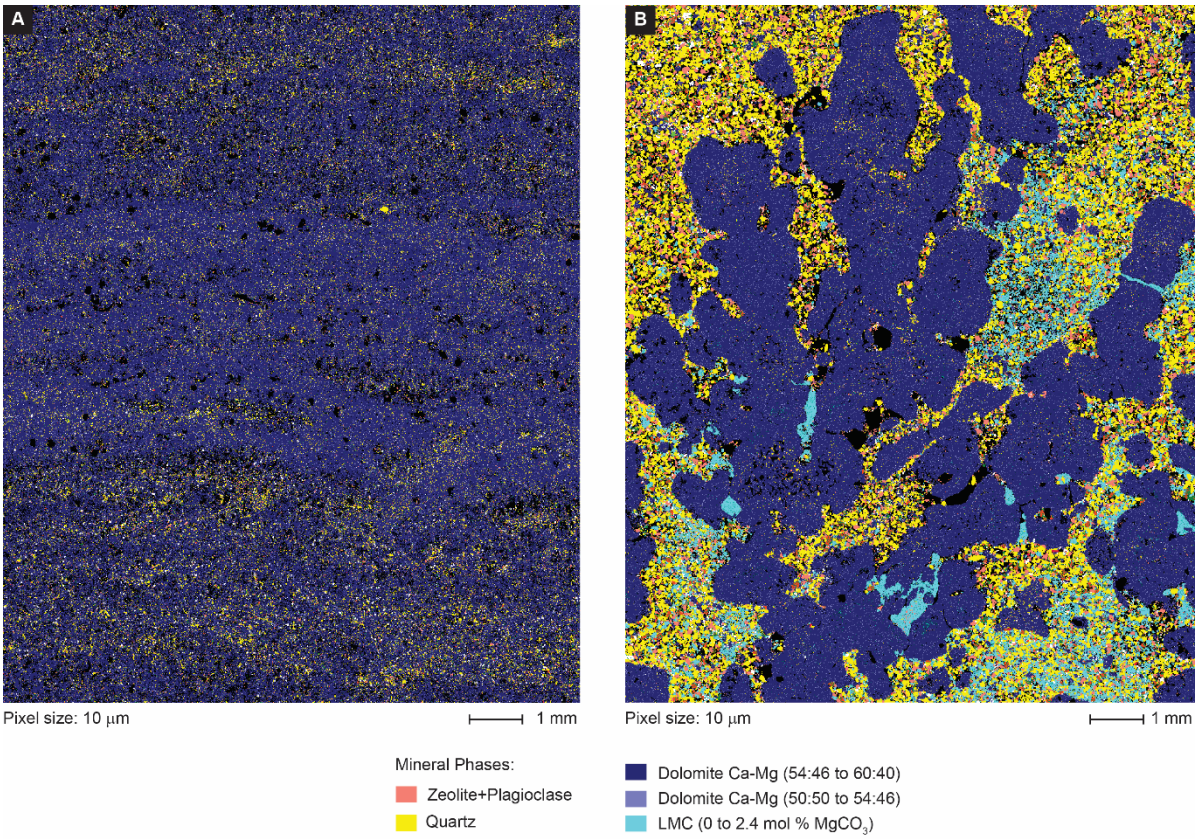

Figure 55. QEMSCAN images showing structural, textural, and fabric features of some microbialite facies: A) Fine-grained domical stromatolite facies (M3, sample WSS-18) intensely dolomitized (dark blue) with minor quatz (yellow) trapped by microbialite laminae; B) Branched minicolumnar stromatolite facies (M5, sample RS-Q5) composed of Ca rich dolomicrite (dark blue) with macrocrystalline quartz (yellow) and analcime/plagioclase (orange) grains infilling the interspace area. Pores filled by low magnesium calcite (LMC, light blue).

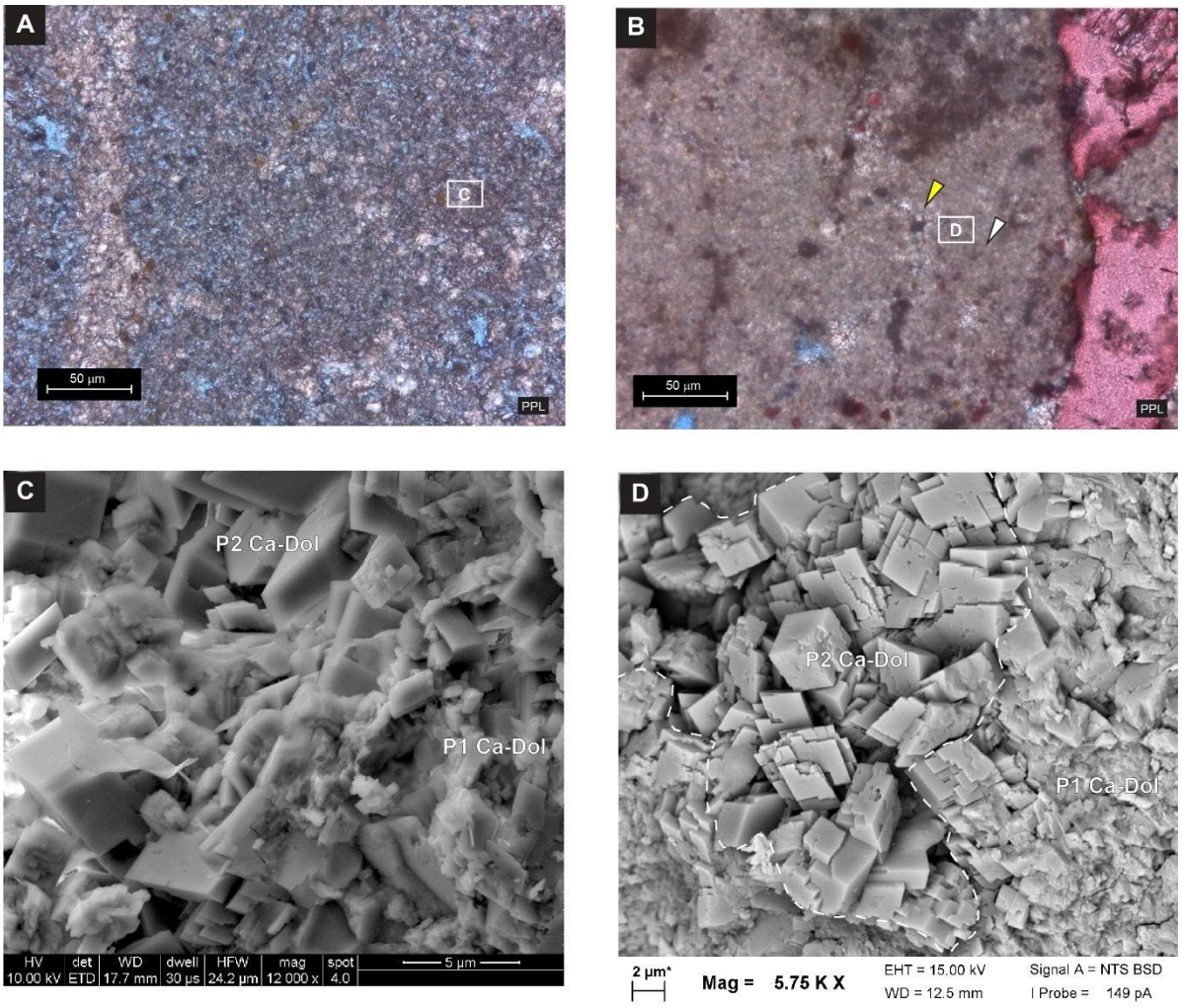

Figure 56. Two populations of Ca-dolomite microcrystals. A) Thin-section photomicrograph of Fine-grained domical stromatolite facies (M3, sample WSS-18) showing very fine dolomicrite texture (mainly P2) with intraparticle porosity. B) Photomicrograph Branched minicolumnar stromatolite facies (M5, sample RS-Q5) showing a texture-preserving Ca-dolomite microrhombs (mainly P1): light brown zones (white arrow) composed of very fine dolomicrite (P1), whereas the dark brown are enclosed zones of organic matter; P2 crystals are present (yellow arrow). The void between the stromatolites here is filled by blocky calcite. C) SEM image of Fig.56A, note planar-e dolomite texture associated to P2 (>3 µm rhombs): flat dolomite faces and well-defined rhombohedral habit. D) SEM image of Fig.56B, planar-s dolomite texture associated to P1, very small Ca-dolomite rhombs (<3 µm) amidst in the anhedral to subhedral clusters of Ca-dol microcrystals and nanocrystals (<1 µm). Texture-preserving P1 Ca-dololomite microrhombs.

3.4.4 Stable Isotope Geochemistry

Isotope records of $\delta^{18}O$ and $\delta^{13}C$ in carbonates have provided important evidence for environmental change (salinity, hydrological inputs, biologic activity) over time in lake basins, especially in deposits that have not been diagenetically altered (Deocampo, 2010). Isotope values are products of isotopic fractionation, which is controlled by three primary factors: temperature, water chemistry, and organic processes (Leng and Marshall, 2004).

The $\delta^{18}O$ and $\delta^{13}C$ values of carbonate samples from four stratigraphic sections in the Evacuation Creek area are shown in Figure 52. Both $\delta^{18}O$ and $\delta^{13}C$ co-vary and show similar trends of increasing and decreasing isotopic values in vertical profile. Values of δ13C range between −5.6‰ and 2.9‰ (VPDB), with an average of −1.3‰ and a mode of −2.6‰. δ18O values range from −8.6‰ to 0‰ (VPDB), with an average of −3.7‰ and a mode of −4.8‰. There is a correlation between isotopic values and sample lithology. In general, carbonates in siliciclastic facies show enrichment of 12C and 16O (negative excursions) with δ13C and δ18O mean values of −1.7‰ and −5.2‰, respectively. Carbonate facies isotopic trends show depletion of lighter isotopes resulting in positive δ excursions, with mean δ13C values of −1.2‰, and δ18O of −3.2‰. The trend of the isotope values of the 1.5 m tall carbonate bioherm facies succession is slightly lower on average compared to the trend of other carbonate facies.

Paleohydrological interpretation of lake carbonate stable isotopic records has shown that suites of lacustrine carbonates with high covariance of δ13C and δ18O data ($r \geq 0.7$), normally form from closed, and often evaporative lake hydrology (Talbot, 1990; Horton et al, 2016). Analysis of the Evacuation Creek area's carbonate stable isotopic compositions shows strong positive linear covariance between δ13C and δ18O values (n=88, R=0.83,

R2=0.69, p-value<0.0001) (Fig.57A). A low covariant carbon and oxygen isotopic trend (n=32, R=0.68, R2=0.47, p-value<0.0001) is observed in carbonate in siliciclastic samples indicating a hydrologically open system (Talbot, 1990) (Fig.56B).

Paleohydrological interpretation of lake carbonate stable isotopic records has shown that suites of lacustrine carbonates with high covariance of $\delta^{13}C$ and $\delta^{13}O$ data ($r \geq 0.7$), normally form from closed, and often evaporative lake hydrology (Talbot, 1990; Horton et al, 2016). Analysis of the Evacuation Creek area's carbonate stable isotopic compositions shows strong positive linear covariance between $\delta^{13}C$ and $\delta^{18}O$ values (n=88, R=0.83, R2=0.69, p-value<0.0001) (Fig.57A). A low covariant carbon and oxygen isotopic trend (n=32, R=0.68, R2=0.47, p-value<0.0001) is observed in carbonate in siliciclastic samples indicating a hydrologically open system (Talbot, 1990) (Fig.56B).

Because of the differences in temperature-dependent oxygen isotope fractionation between dolomite and calcite at low temperatures, concern has been raised about making corrections on stable isotope values for dolomite versus calcite (Vasconcelos et al, 2005; Petrash et al, 2017). Due to the inability to physically separate discrete carbonate phases in samples from the WC1 drill core from the Green River Formation, Pitman (1996) used a timed-dissolution procedure based on Walters and others' (1972) different reaction rates for chemically distinct calcite and dolomite phases to obtain carbon and oxygen isotope ratios for distinct carbonate phases. Douglas Creek Member in the WC1 drill core has $\delta^{13}C$ and $\delta^{18}O$ values of calcite that tend to show on average an enrichment of the lighter isotopes compared to dolomite δ-values. Calcite shows on average a 1.5‰ decrease for $\delta^{13}C$ and a 3.0‰ decrease for $\delta^{18}O$ (VPBD) compared to dolomite δ-values in the same sample (Pitman, 1996). These differences between calcite and dolomite might seem large. In fact, the results of various

isotopic studies of calcite-dolomite pairs elsewhere showed considerable scatter 0‰ to 9.0‰ (Fritz and Smith, 1970; Land, 1980; McKenzie, 1981; Vasconcelos et al, 2005). However, correction of the isotope values is largely ignored in lacustrine carbonate studies. The overall trends, not so much the absolute values (corrected or not) in the variation of the stable isotopes, have been used to interpret the lake conditions (Sarg et al, 2013; Swierenga, 2014, Frantz et al, 2014; Eljalafi, 2017) and this has been followed here.

It has long been recognized that the presence of dolomite and high Mg/Ca ratio in lacustrine carbonates indicates evaporative evolution of lake waters (Bradley, 1964; Eugster and Hardie, 1978; Deocampo, 2010; Symcox, 2015). Continued precipitation of calcium carbonate in the closed lake system leads to progressive increase in the Mg/Ca ratio of lake water, which in turn gives rise to deposition of progressively more Mg-rich carbonate until authigenic dolomite is precipitated. In the Douglas Creek Member in the Evacuation Creek area, an indication of evaporative concentration is that the most $\delta^{18}O$-depleted samples are often accompanied by an increase in dolomite mineral phases (Fig.57C).

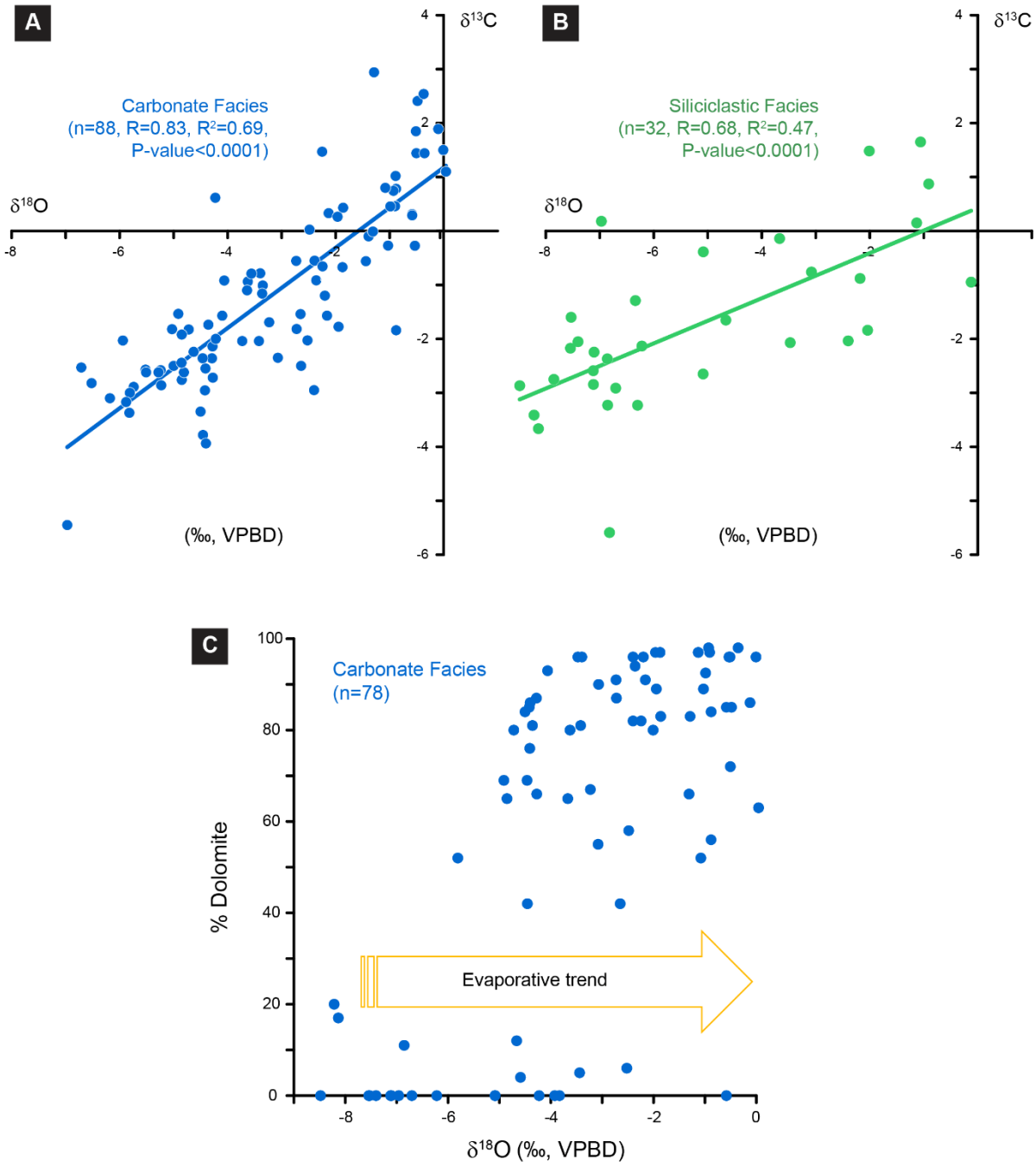

Figure 57. Stable isotope geochemistry: A) Carbonate facies: covariance of d13C and d18O data (R>0.7) consistent with closed basin lake conditions (Talbot, 1990). Low p-value (<0.05) means that the correlation is strong or important. (N = number of samples). B) Siliciclastic facies: d13C versus d18O plot with weak covariant trend (R<0.7). C) Moderate-to-strong correlation between oxygen isotopic composition and dolomite content, indicative evaporative concentration (Arenas et al, 1997).

3.5 Discussion

Two siliciclastic-carbonate deepening-shallowing up cycles defined by unique microbialites-contaiing benches at the top were recognized in the Douglas Creek Member (Fig.15). Each one shows distinct depositional trends (facies evolution and stacking pattern), mineralogical composition, and chemostratigraphic trends (stable isotope geochemistry) (Figs.16, 22).

3.5.1 Cyclical Record and Carbonate Lacustrine Environment

The Douglas Creek Member in the study area can be subdivided into a hierarchy of stratigraphic cycles that record superimposed long-term and short-term physico-chemical fluctuations of the lake to provide paleoclimatic conditions. The carbonate-rich zone one (R1) suggests a long-term, relatively colder condition with less monsoonal precipitation, and repetitive (cyclic) carbonate and siliciclastic sediment deposition (Fig.58). This high-frequency alternation may reflect short-term climate oscillations. The carbonate-rich zone one (R1) is composed of two short-term cycles, each up to 8 m thick. Short-term transgressive-regressive cycles (C1 and C2; Fig.58) always start with siliciclastic mudstones with occasional sandstones related to a more distal portion of a deltaic system deposited in a sublittoral lake environment. This interpretation relies on Rosencrans (2015), who studied the siliciclastic-dominated intervals in the area and interpreted them as mouth bar sediments, deposited tens of kilometers from the shoreline by hyperpycnal currents related to monsoonal floods. Short-term transgressive-regressive cycles (C1 and C2) end up with shoreline to shallow lacustrine carbonates, deposited in a littoral lake environment. The carbonate facies successions are separated by periods of episodic fluvial discharge, recording reduced fluvial deposition between warming events. The cycles are incomplete in

places. The carbonate successions are unique in each cycle but show a lateral extension of kilometers. Exposure surfaces are very rare in the carbonate facies successions.

The short-term cyclicity of R1 is interpreted as an alternation of carbonate-dominated intervals deposited in a closed lake phase and siliciclastic-dominated intervals deposited in a less closed lake phase. This is supported by oxygen and carbon stable isotopic data (Fig.57). The average linear regression slope of 88 carbonate facies samples show a significant positive covariation trend of 0.83 between $d^{18}O$ and $d^{13}C$, with statistical significance ($p < 0.05$) (Fig.57A). Meanwhile, 32 siliciclastic facies samples show weak significant isotopic covariation indicating a less closed system hydrology (Fig.57B). A review of Quaternary Lake carbonate stable isotopic data covering a broad range of lacustrine systems (e.g., high and low latitude environments, closed and open basin hydrology, low and high altitudes, and humid to arid hydroclimates) have shown statistically significant positive covariation trends between $d^{18}O$ and $d^{13}C$ associated with evaporative enrichment of lake waters in closed basins (e.g., Horton et al, 2016).

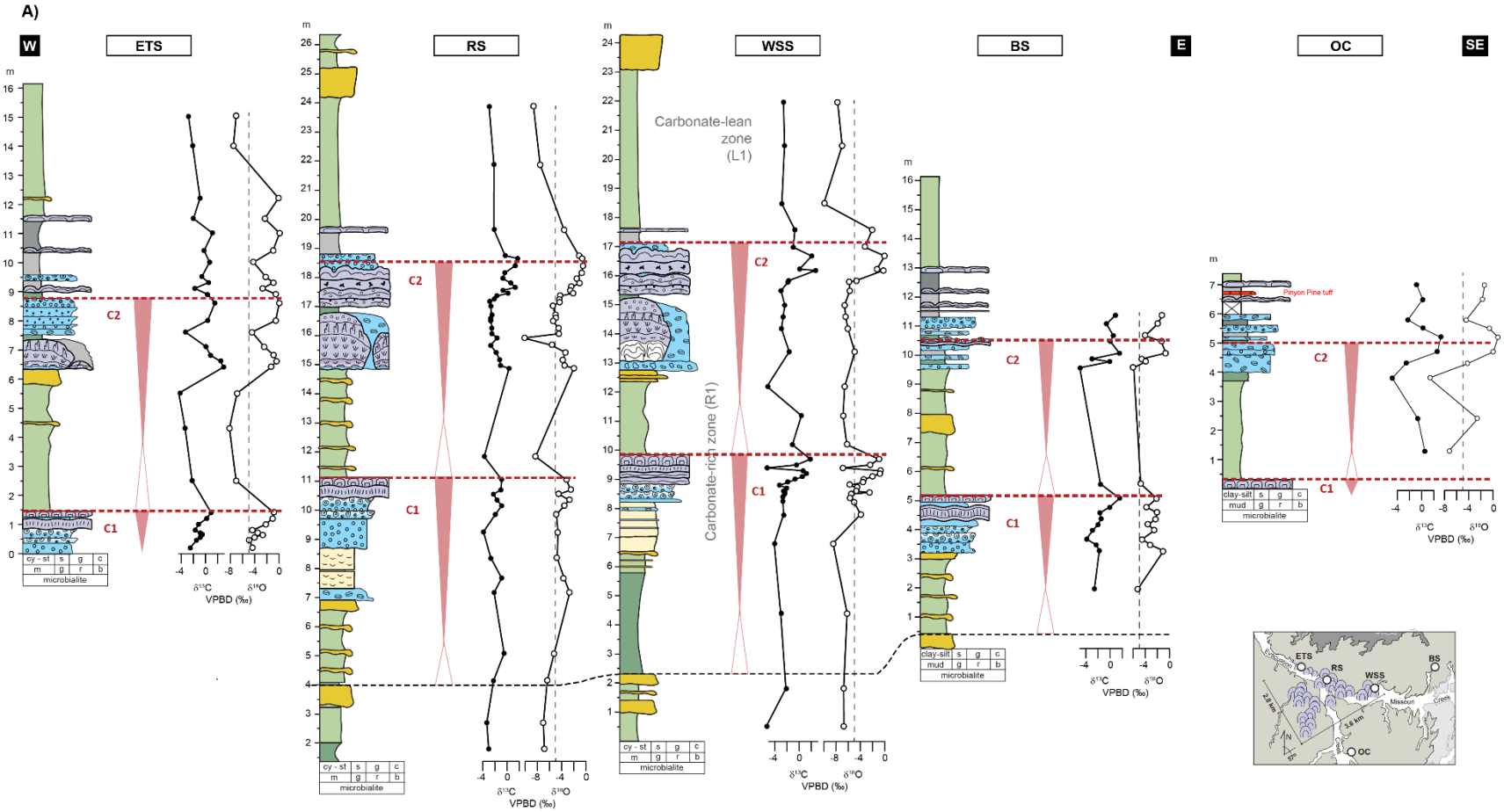

Figure 58. Cyclical record in upper Douglas Creek Member: Long-term periods of highly seasonal river dominated lake (yellow) and perennial lake (blue) corroborate with the distribution of organic-rich (R1) and organic-poor (L0/L1) zones (after Cashion and Donnell, 1972; Tänavsuu-Milkeviciene et al., 2017). Short-term deepening upward cycles (C1, C2, C3 and C4) associated to perennial lake phase in gray triangles. See Fig.59B for legend.

$\delta^{18}O$ data plotted adjacent to the measured sections in figure 15 show positive and negative excursion that are well-tuned on average with the long-term cycles. The average range in $d^{18}O$ values of the carbonate facies is -3.2‰, while the average in the siliciclastic facies is -5.2‰ (Fig.52). The relationship of the oxygen isotope record and lake levels in a closed basin is shown by Lister and others (1991) in Lake Qinghai, China. In a lake flooding setting (transgression) or humid phase, the $\delta^{18}O$ value for the lake water decreases (becomes enriched in ^{16}O) as the inflow and precipitation increase, resulting in a $\delta^{18}O$ negative excursion. Once the evaporative loss from the total lake surface exceeds the total input waters, an arid phase, the residual lake waters will face an evaporative enrichment for $\delta^{18}O$ value, resulting in $\delta^{18}O$ positive excursion. The evolution of long-term cycles in the Douglas Creek Member to the Parachute Creek Member show an overall trend of increasing in water level and salinity of Lake Uinta (Rosenberg et al., 2015, Ricketts, 2015, Tänavsuu-Milkeviciene et al 2017, Gall et al 2017). Gall and others (2017) suggested that this overall transgressive trend is manly controlled to climatic factors, like hyperthermal events associated with the Early Eocene Climate Optimum (EECO), which generated a monsoonal continental climate and extreme seasonal variation.

Lakes can be divided into regions related to light penetration (Renault and Gierlowisk-Kordesch, 2010). The zonation of the lake environment applied here is based on Cohen (2003), where the lake floor in the photic zone is called the littoral zone. Intermediate depths where photosynthesis occurs exclusively by benthic algae and cyanobacteria is called sublittoral zone, and the area of lake floor below the depth of the photic zone is called profundal zone. It is noteworthy that growth of photosynthesizing organisms depend not strictly on depth but mainly on light penetration. It is influenced by other variables like

turbidity, plankton, and nutrients in the dissolved solid content in the water. Careful attention must be taken to use the photic zonation as a proxy for paleolake level depth. Therefore, the use of comparative sedimentology, mineralogy, and stable isotopes allow better understanding of depositional processes and lake level fluctuations. This makes it possible to determine lacustrine sub-environments (e.g,. mudflat, shoreline, shallow lake and deep lake) and, consequently, paleolake depth assumptions.

The distinct carbonate facies succession of each short-term cycle is interpreted to have been deposited in a range of saline-alkaline subaqueous environments of the littoral zone; all within the photic zone over the Douglas Creek Arch (Fig.59). Lower to moderate energy conditions prevailed with these carbonate deposits, which tend to become readily affected by wave and storm energies when the lake level falls. At this time the arch was never exposed and a brine flow of water from the Uinta Basin across the arch into the Piceance Basin occurred (Dyni, 1996). Under a dry climate, all microbial carbonate facies were deposited in this phase of the lake.

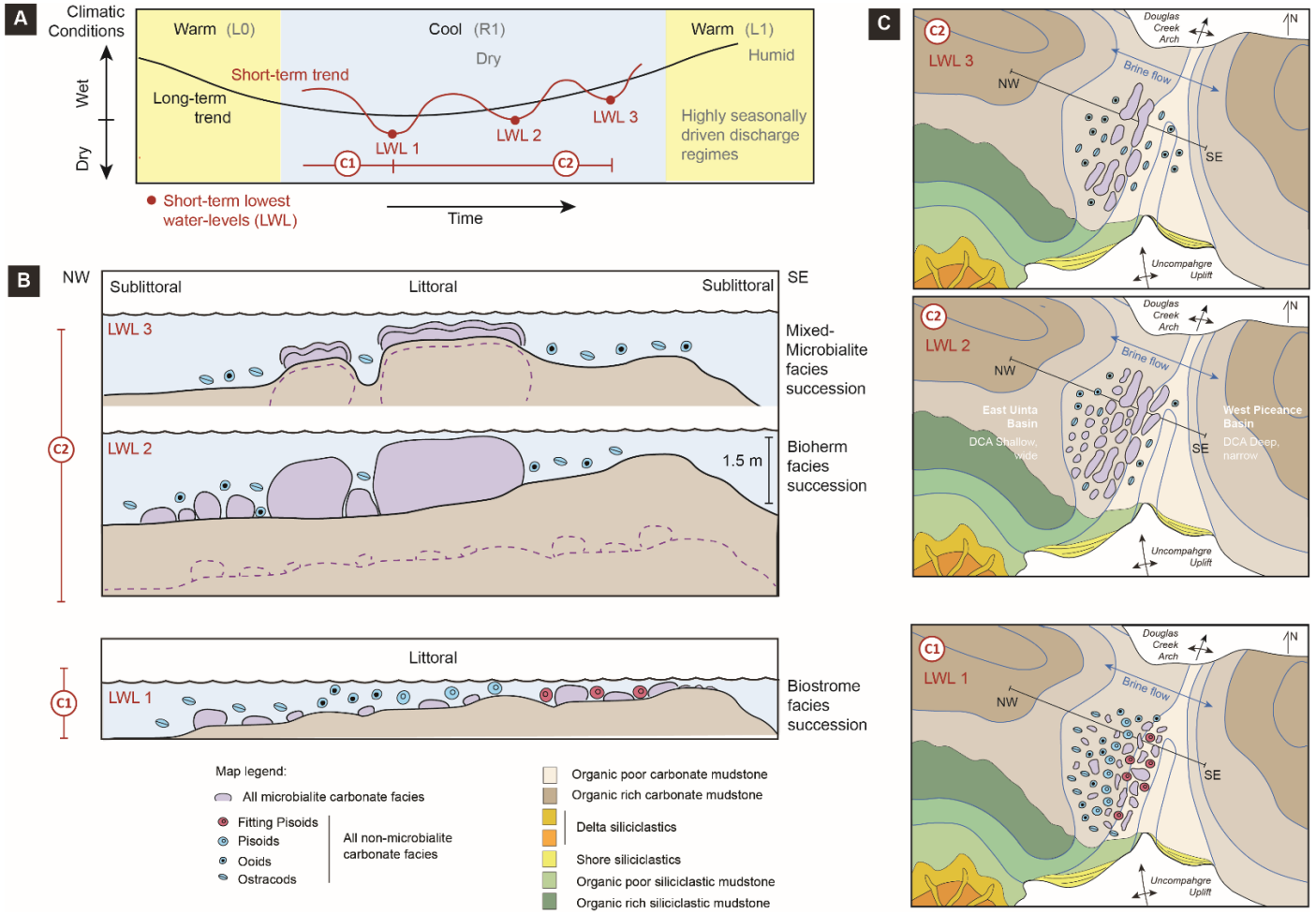

Figure 59. Carbonate lacustrine environment: A) Hypothetical long and short-term climatic oscillations associated to monsoonal continental climate. Cycle amplitudes estimated from measured sections at Evacuation Creek area (Fig.22). B) Depositional profiles and distribution of microbialite and non-microbialite facies at distinct relative lowest water levels (LWL) associated with successive short-term cycles (C1, C2 and C3). C) Paleogeography maps and main depositional environments observed in Douglas Creek member at C1, C2 and C3 short-term LWL.

C1 Short-term cycle: Biostrome facies succession and analogs

The first short-term cycle is the most laterally continuous and includes carbonate inverse graded and biostrome facies successions. It starts by local pulsed fluvial siliciclastic input into the area of the Douglas Creek arch, which relatively increases the lake level. The tabular sandstones (S2) and ostracodal grainstone facies (NM4) indicate that, at the beginning of C1, the southern arm of the arch acted as shoreline with moderate energy. Carbonate shoals with minor microbialites were dominated by coated grains such as coated ostracods (NM4), ooids (NM5), and pisoids (NM6,7). Such facies are composed inverse graded sub-cycles, forming kilometer-long tabular beds. The similarity of the inverse graded sub-cycles with their occurrence in hypersaline waters the peritidal environment in the Permian shelf crest of Guadalupe Mountains as reported by Esteban and Pray (1983) is used as a model. These authors interpreted the formation of the inverse graded pisolites associated with depositional sorting and in-place pisoid growth processes. Where the coated grains pass through different growth stages, always precipitating in subaqueous setting, starting from a ‘free to move’ environment toward a ‘free to jostle’, but not rotate environment where the pisods grewThe presence of polygonally fitted nature of the pisoids implies a constrained, in-situ growth. By the end of the pisolite evolution, the pisoids were linked by in-place cement accretion (Fig.59). In the Douglas Creek Member, well-developed inverse graded cycles within the biostrome facies succession represent nearshore shallow lacustrine deposits.

The inversed graded cycles are overlain by layered stromatolites that represent the shallowest water of the carbonate facies. Laguna Negra, a modern shallow (<2 m) hypersaline lake in Argentina with a strongly negative water balance, shows a belt of

microbialite biostromes where carbonate precipitation and microbial mats occur at a shallow lake margin (Gomez et al, 2014). Modern and ancient laterally extensive carbonate laminites, without evidence of subaerial exposure, indicate subaqueous deposition under fluctuating surface water chemisrty (Warren, 2016).

Domical stromatolite facies (M2) marks the transition from very shallow water dominated deposition to transgressive dominated deposition related to the next short-term cycle (Fig.58). A possible analog to the domical stromatolites facies is the pitted domical stromatolites from Lake Turkana, Kenya, deposited in a transgressive phase of the lake (Hicks, 2012). In the Douglas Creek Member, very similar layering and pits with no evidence of exposure.

Most of the carbonate beds show shallowing upward elementary cycles in a thickening-up trend. All carbonates are dominated by dolomite (Avg=80%). An overall positive excursion of $\delta^{18}O$ and $\delta^{13}C$, from the base of the cycle to the top of the carbonate bedset, is interpreted as an increase in aridity and biological productivity in a hydrographically closed lake basin (Figs.58, 59). This increasing salinity fostered microbialite growth.

The lowest relative water level (LWL) is associated with the first short-term cycle (C1) under a dry climate as recorded by the biostrome facies succession and nearshore sandstones. These facies successions were deposited in a shallow hypersaline region, under one of the several quiescent fluvial discharge regimes of Lake Uinta. Despite the fall in lake level and the increase in alkalinity and salinity, the inflow of groundwater, springs and perennial rivers kept the Douglas Creek arch from exposure and drying out.

C2 Short-term cycle: Bioherm and Mixed microbialite – non-microbialite carbonate facies successions

The second short-term cycle (C2) is marked by carbonate facies that vary laterally ranging from well-developed large bioherms (central area), to smaller bioherms and ostracodal-ooidal grainstones to the northwest, with kerogen-rich mudstones to the southeast (Fig.58). The second short-term cycle (C2) is asymmetric with two relative lowest water levels (LWL2, LWL3) (Fig.59A). The initiation of the C2 cycle starts with transgressive conditions toward relative high lake level represented by widespread distal siliciclastic mudstone deltaic deposits (Fig.58). This overall freshening of the lake is recorded by negative excursions of $\delta^{18}O$ and $\delta^{13}C$, which reflects high fluvial water inflow into the basin during short-term, wetter climate conditions. The deltaic system source point of the distal siliciclastic mudstone (S4) deposition is mostly related to a southwest area on the side of Douglas Creek arch (Rosencrans, 2015; Gall et al, 2017) (Fig.59C). Large bioherms record the first, lowest water level of cycle 2 (LWL2) that formed during the regressive phase of C2. This carbonate bed is dominated by dolomite (Avg =70%) with ≤10% quartz grains and begins with a debris layer that is the substrate for the overlying bioherms (Fig.58). The initiation of the Bioherm facies succession is characterized by scoured basal contacts of the intraclastic conglomerate facies (NM1) marking ravinement lag deposition over the surrounding, low gradient mudstones (Fig.58; WSS). The NM1 beds are laterally continuous across the area (10 km^2) bellow the bioherms, with individual disconnected bioherms occurring on the top. The internal layering of the bioherms can be divided into four microbialite facies, as described previously in the Bioherm facies succession section. The differences of microbialite facies, which build the bioherm, are controlled by distinct

microbial communities according to their position in the photic zone. The succession of M3, M4, M5, and M6 facies is related to a short-term (high frequency) increase in water level (Fig.59A) and a consequentl reduction of the photic zone. This interpretation is supported by the carbonate fabric and stable oxygen stable isotopic data (Fig.58). Holocene microbial deposits of Western Australia's Hamelin Pool in Shark Bay, a hypersaline marine embayment, show similar features where fabrics are controlled by substrate gradient and water levels (Jahnert and Collins, 2012). The Hamelin Pool bioherms show different microbialite facies according to their relative position in relation to water depth fluctuations. At Evacuation Creek, bioherms, the stubby microbialite facies (M3, M7) formed in a relative low lake level in the littoral zone, while the slender microbialite facies were formed in a transgressive, higher lake-level phase. The interspace of the bioherms is filled by syndepositat intraclasts (NM2) and ostracoidal grainstones (NM4) due to continued agitation by wave and current action. The absence of erosion surfaces, desiccation cracks or carbonate mud within these facies indicates deposition in subaqueous lacustrine wave-dominated littoral to sublittoral zones. Dramatically fresher and relatively deeper-water, profundal conditions in a sublittoral zone inhibited the microbial carbonate factory (Fig.59B) and is recorded by organic-rich siliciclastic mudstone (S4) (Fig.58).

The second lowest water level of cycle 2 (LWL3) is represented by mixed microbialite – non-microbialite carbonate facies succession that formed during an additional regressive phase of C2 (Fig.58). Mounds composed of *Chlorellopsis* stromatolite facies (M7) and Thrombolite facies (M8) formed on top of bioherms' paleo highs (Fig.59B). They show elongation with NE trend (Fig.59C). *Chlorellopsis* stromatolite and thrombolite mounds occur along the western DCA shore and developed microatoll-like morphologies surrounded

by ostracods and ooids. At Lake Clifton, Western Australia, microatoll-like microbialites occur on the lake shore and extend to 1m depth (Burne and Moore, 1993); however, they are not elongate. In the deeper water, they form mounds that develop flat tops on reaching current lake level.

The overall $\delta^{18}O$ values in the mixed microbialite – non-microbialite carbonate facies succession (Fig.58) shows a trend of increasing $\delta^{18}O$ from the base of the *Chlorellopsis* stromatolite facies (M7) to Thrombolite facies (M8). The $\delta^{18}O$ positive excursion suggests minor inflow with increase in evaporation. The lake apparently increased its hyper salinity at lowest water level (LWL3).

3.5.2 Mineralogy and Diagenetic Considerations

Even with the lake fluctuations recorded by high frequency and low frequency cyclicity, the upper part of the Douglas Creek Member in the Evacuation Creek area was always deposited under saline-alkaline conditions. This is supported by the presence of near-surface, authigenic minerals, like analcime and abundant dolomite, which occur throughout the area investigated with mineralogy varying with stratigraphic positions (Fig.52). At the Douglas Creek arch, analcime is always disseminated in the siliciclastic mudstone facies, while dolomite occurs within carbonate facies. The lacustrine episode in which stromatolites formed is also of great importance in examining the variation of the chemistry of Lake Uinta.

The origin of the mineral dolomite has been a focus of many investigations (e.g., Machel, 2004; Petrash et al., 2017) including several of them on the Green River Formation (Boak

and Poole, 2015; Rueda Chaparro, 2018). Over the years, many dolomitization models have been proposed, among them the evaporation models (e.g., Adams and Rhodes, 1960; Butler, 1970; Eugster and Surdam, 1973) and the microbial model (e.g., Vasconcelos et al., 1995). Natural diagenetic environments prevail in the nearshore conditions of the SW portion on the Douglas Creek arch. At the perennial lake phase, two different dolomite textures were found based on petrography and SEM analyses (Fig.56). Both textures have overall very small dolomite crystal size (< 10 μm). Sibley and Gregg (1987) indicate that temperature regulates nucleation and growth rates of dolomite crystal size. Very small dolomite crystal size can be controlled by high nucleation rates paired with low growth rates, frequently associated with evaporitic (syndepositional) environments (Machel, 2004).

The presence of calcium excess in the dolomites of the upper Douglas Creek Member (Fig.53) allows a near-surface formation interpretation. Ca-Mg carbonate minerals can have either calcite symmetry (disordered cation arrangement) or dolomite symmetry (ordered cation arrangement (Kaczmarek et al, 2017). That laboratory study s showed ordered cation arrangements and thus dolomite (Fig.53C). Laboratory experiments by Petrash et al (2017) indicate that microbes and organic matter can catalyze precipitation of Mg-rich carbonate precursors of dolomite. Very high Mg calcite and imperfectly ordered Ca-dolomite reflect a raise in the total alkalinity and buffering of the pH (Petrash et al, 20 17). Nevertheless, Mg-rich carbonate precursors of dolomite are like the initial Ca- Mg carbonate phases formed in high-temperature abiotic dolomitization experiments (Kaczmarek et al, 2017). The role, if any, of high temperature in abiotic dolomitization for the Green River carbonates is uncertain.

Even if microbially induced or influenced dolomite mineralization occurred, the main mechanism for the dolomite formation was most likely triggered by evaporation. The first population of dolomite crystals with a size < 4 μm conforms to brine-direct precipitation and formed in the sediment/water interface as a mud or by early dolomitization, calcite to dolomite mineral replacement in unconsolidated sediments. Due to evaporation, the lake water became denser, which forced it to move downward replacing the already deposited metastable calcium carbonate sediments by dolomite. This type of dolomitization is called the reflux model (Adams and Rhodes, 1960). With the evolution of the reflux dolomitization process, the second population of dolomite crystals > 4 μm (Fig.56A, C) took place. The level of supersaturation with respect to dolomite would have been moderated along with the dolomitization forming nearly stoichiometric Ca-rich crystals. However, later recrystallization could overprint this pattern.

The presence of analcime in the highly seasonal, river-dominated lake phase indicate that saline, highly alkaline conditions prevailed in the siliciclastic-rich succession (Figs.16, 20). No volcanic detritus or zeolites, other than analcime, are present in these stratigraphic intervals. Authigenic analcime is common in non-tuffaceous claystones of saline, highly alkaline lakes (Hay and Sheppard, 2001). Analcime-rich siliciclastic mudstones along the southern shore of Lake Uinta have been reported by Remy and Ferrel (1989). At high lake levels, moderately saline, alkaline lake water induced analcime formation by phyllosilicate transformation in shallow lacustrine environments. During low lake levels, intense evaporation on exposed mudflats triggered evaporative pumping of Na-rich brines, which enhanced authigenic analcime formation by phyllosilicate transformation. Analcime has been also found in fine-grained siliciclastic and carbonate, non-volcanogenic lacustrine

rocks of the Carboniferous Rocky Brook Formation, Canada (Gall and Hyde, 1989). There, analcime was formed either by direct lake-water precipitation or by reaction of these waters with one or more clay mineral types or plagioclase. The analcime associated to the upper part of Douglas Creek Member at Evacuation Creek area display two populations: 1) most of analcime crystals are engulfing and replacing the clay matrix; 2) some analcime crystals display characteristics of detrital grains, appearing like reworked subhedral granular crystals. Since evidence of volcanic material associated with the analcime is appears to be lacking, clay minerals seem the most likely precursor for analcime. The overall reaction for the formation of the authigenic analcime likely comes from the transformation of detrital clays in the presence of Na-Mg brine flowing by seepage reflux. A saline, highly alkaline, shallow lacustrine environment seems to be an y environment for these deposits, where some authigenic analcime crystals could be reworked by seasonal river discharge.

3.6 Conclusions

The different facies successions of the microbial lacustrine beds of the Green River Formationare interpreted to have been deposited in a range of subaqueous environments from upper littoral to upper sublittoral - all within the photic zone over the Douglas Creek arch (Fig.59). Low to moderate energy conditions prevailed with these carbonate deposits, which tended to become affected by wave and storm action s when the lake level fell. The stacking pattern of facies for each microbialite-bearing carbonate cycle is distinctive and each bed's microbialite assemblage is unique. Microbialites of the Douglas Creek Member show a wide range of microbialite mesostructures, but millimeter- to centimeter-scale

microbialite microstructures do not appear to reflect changes in lake-water chemistry. The overall small-scale microbialite cycles reflect chemostratigraphic evolution of the lake. The meter- to several meter-scale microbialite beds display distinct depositional trends. One of the overall patterns seen is that microbialite morphology is strongly correlated with lake conditions. If the stability of the paleolake is relatively short, microbialites uniformly cover hard substrates and form a poorly diversified biostrome. Differently, long-lasting lacustrine episodes lead to stable microbiological niches according to depth, which results in bioherms showing a distinct facies succession.

Most of the identified authigenic mineral phases took place in saline, highly alkaline lake water. Diagenetic mineral phases took place in near-surface and shallow diagenetic settings. Some distinctive features stand out: 1) All the carbonate facies are dolomite rich, and their percentage varies within different facies; 2) The two populations of dolomite crystals indicate, first, a direct precipitation and/or microbially mediated dolomite crystal formation and, second, an early formation with shallow burial diagenetic dolomitization: 3) All dolomite is Ca-rich and ordered, probably subsequently stabilized from disordered dolomite precursor phases under near-surface conditions. The small amount of tuffaceous claystones and the presence of analcime along the siliciclastic mudstone facies suggest the formation of analcime by reaction of detrital clays with saline, highly alkaline lake and pore water.

The various generations of microbialites show comparable stable carbon and oxygen isotope values and were deposited align to NE-SW trend in the littoral zone along the subaqueous western shoulder of Douglas Creek arch This indicates a similar physical environment and paleolake stabilization levels (Fig.59B, C). $\delta^{13}C$ and $\delta^{18}O$ isotope results indicate that evaporative and closed hydrological conditions were necessary for the development of the

carbonate microbial and non-microbial facies. Highly evaporative lake conditions were promoted by a cooler monsoonal period of relative fluvial quiescence. The low amount of siliciclastics suggests a depositional environment located relatively far away from the source of siliciclastic input (rivers). Episodic discharge events do occur in this cooler monsoonal, long-term period, evidenced by siliciclastic filling the interspace between some stromatolites, the presence of siliciclastic mudstone beds, and the short-term cycles (C1, C2, C3 and C4). Based on interpretations made by Gall et al (2017), warm and wet periods promoted high discharge regimes creating deltaic, mouth bar complexes. In the Evacuation Creek area, these long-term wet periods were recorded by distal mouth bar sediments, associated with southwestern distributary channels (Rosencrans, 2015).

The variability and cyclicity of the upper Douglas Creek Member deposits highlight the paleoenvironmental dynamics in the subaqueous shallow littoral zone of a saline-alkaline lake. Microbialites of the Douglas Creek Member show a wide range of microbialite mesostructures, but millimeter to centimeter scale microbialite microstructures do not reflect changes in lake-water chemistry. The overall small-scale microbialite cycles reflect chemostratigraphic evolution of the lake. The meter to several meter scale microbialite beds display distinct depositional trends. The evolution of marginal Lake Uinta with Eocene climate at the Douglas Creek Arch emphasizes the importance of microbialite occurrence for climatic interpretation and the utility of microbialite morphology to reconstruct lake conditions.

3.7 Acknowledgments

We acknowledge Petrobras (Brazil) for support and funding this research. We are grateful to R. Biaggi, Y. Parizek-Silva, and K. Wright for discussions, constructive reviews, and assistance in the field related to this study. We are most grateful to the late H.P.Bucheim, whose experience in the Green River Formation greatly influenced this research. We thank S.C. Anjos, P. M. Magalhaes, and R.J. Jahnert for encouraging this project to take place.

CHAPTER 4

4. Lacustrine paleoenvironmental controls on layering variations within giant stromatolites of the Eocene Green River Formation, Sand Wash Basin, Colorado.

Daniel Cupertino, Michael Vanden Berg, Roberto Biaggi, Stanley M. Awramik

4.1 Abstract

Detailed microbialite characterizations were performed on some of the largest known lacustrine columnar stromatolites. These occur in the upper LaClede Bed, Laney Member of the Eocene Green River Formation at Vermillion Creek, northwest Colorado. The four stromatolite bioherms studied occur in a biostrome. These stromatolites are unusual regarding the 3-10 cm thick layers composed of columnar and layered stromatolites. Very detailed and precise analyses were performed to determine the relationship between stromatolite morphology at several observational levels and environmental conditions. Three major stromatolite macrostructures (columnar, domical, coniform) were indentified. The layers were examined in terms of their microbialite content from a macrostrucutural, mesostructural and microstructural perspective and classified nine distinct microbialite types. Combined sedimentological, mineralogical, and stable isotope ($\delta^{13}C$ and $\delta^{18}O$) analyses allowed identification of two depositional phases. This suggested that these phases reflect distinct paleoenvironmental conditions: an arid phase in a closed lake and humid phase in a closed lake. These lake phases resulted from short-term changes in climate that modulated the water and sediment flux into the southeast margin of the Sand Wash basin of

Lake Gosiute in northwest Colorado. The layering patterns and their contained microbialite types resulted from lake-water fluctuation due to changing climatic conditions (primarily arid vs. humid) and provide critical indicators for paleoenvironmental analysis.

4.2 Introduction

Lacustrine systems preserve sensitive depositional environments that reflects regional and global climate and tectonics. Lake capture and record the weathering products of continental uplifts, spring, groundwater, and rivers, as well as other climatic and environmentally influenced conditions (Renaut and Gierlowski-Kordesch, 2010). Lacustrine carbonate sediments, especially those from environments in which microbialites form, provide high-resolution time-archives of lacustrine paleoenvironmental conditions and variations. Some of these factors have been observed in lacustrine stromatolites (Abell et al., 1982; Hillaire-Marcel and Casanova, 1987; Casanova and Hillaire-Marcel, 1992; Lettéron et al, 2018).

Stromatolites in the Vermillion Creek area, Sand Wash basin Colorado, are the largest known lacustrine columnar stromatolites (Awramik and Buchheim, 2015). They reach up to 5.5m high and 7m in diameter, occurring over an area of ~1 km^2 (Fig.60) in the upper LaClede Bed, Laney Member, of the Green River Formation. The stromatolites formed during a regional expansion (transgression) of Lake Gosiute, soon after the Early Eocene Climatic Optimum (EECO), 52–50 Ma. This large-scale transgression was recorded by several well-defined, small-scale depositional cycles in the LaClede Bed found elsewhere (Surdam and Stanley, 1979). The Laney Member in the study area spans less than a 1 m.y. interval, from 49.9 Ma to 49.0 Ma (extrapolated from data and figures in Smith and Carroll,

2015). The Analcite Tuff in the upper LaClede Bed (Rhodes, 2002) has been dated at 49.25 ±0.12 Ma by using $^{40}Ar/^{39}Ar$ on sanidine (Smith and Carroll, 2015).

The giant stromatolites were first noted by Korngay and Surdam in 1980 and then by Roehler in 1993, who illustrated them and suggested the bioherms (columns) formed on erect trees in a flooded woodland. The microbialites-coated residual stumps are usually hollow cylinders with some having petrified wood. The trees were substrates for the microbialites.

A stratigraphic section, here called the Stump Grove Section, was measured along Vermillion Bluffs in the Sand Wash Basin (Fig.61). Domical, columnar, and coniform stromatolites of the bioherms occur in a complex biostrome bed (Awramik and Buchheim, 2015). A peculiar feature of these giant stromatolites, some >5m tall, is the distinctive, cm-thick layers that can be traced from the base to the top of column with layers thickening at the tops of the columns. A single occurrence of erosion (subareal exposure) was found in the layering of one of the columns indicating they formed primarily in water at least 5+ meters deep. The layers are composed of one or more types of microbialites. Layering and microbialite types are considered to reflect variation in the environmental conditions driven by climate. Analysis of the layering allows the reconstruction of local environmental conditions and can be extended regionally and possibly basin-wide during the time of their formation.

4.3 Methods

Drones were used to determine the spatial distribution of the giant and other stromatolites as well as the biostrome. To determine specific factors that influenced the microbialite layering

within the giant stromatolites, 4 giants were sampled. The sampling campaign was focused on three major kinds of stromatolite macrostructures: columnar (Site 4 and Core), domical (Site 2) and coniform (Site 5). Fifty hand samples were collected from outcrop and a 1.5 m core was sampled (Fig.62).

Detailed morphological descriptions from the outcrop and hand and core samples were performed using the methodology for stromatolite descriptions recommended by Grey and Awramik (2020). This included four scales or levels of observation: (1) megastructure - large-scale features of the stromatolite, here based on outcrops; (2) macrostructure - the individual microbialite at the outcrop (e.g., the domes or columns); (3) mesostructure - internal microbialite features visible with the naked eye in the hand samples (e.g., laminated or shrubs); and (4) microstructure - microscopic features (e.g., textures and fabrics) as viewed in thin section. Seventy-eight, oriented thin sections were made. They were vacuum impregnated with blue epoxy, stained with Alizarin Red S, and analyzed under a petrographic microscope. Eighty-four 500g powder samples were prepared by milling, using a 4 mm carbide drill bit. These were prepared from layers in the bioherms for mineralogical analyses using XRD. Analyses were performed on Panalytical Empyrean Powder Diffractometer (UCSB-Material Research Laboratory) and interpreted using MDI Jade 2010 Software (ICDD PDF-2 Database) at Loma Linda University.

$\delta^{13}C$ and $\delta^{18}O$ Analyses

Stable oxygen and carbon isotope analyses were performed on 185 carbonate powder samples, that were carefully microdrilled with a 1 mm carbide bit in Weldeab's Lab (UCSB Earth Science). Care was taken to drill only a targeted mesostructure (microbialites and

detrital infill) avoiding cements. Isotope ratios ($\delta^{13}C$ and $\delta^{18}O$) are referenced to Vienna-Pee Dee Belemnite (PDB). Seventy mg of the microdrilled powder were anayzed using a Thermo-Finnigan DELTAplusXP MAT isotope ratio mass spectrometer (IRMS) coupled to GasBench at the Marine Science Institute Analytical Lab (UCSB). Analytical uncertainties (1σ) are assessed by repeat analyses of NBS 19 standard and accounts for ± 0.07 ‰ and ± 0.18 ‰ $\delta^{13}C$ and $\delta^{18}O$, respectively.

Sr Isotopes and REE+Y Analyses

Analyses of $^{87}Sr/^{86}Sr$ ratios and rare earth elements (REE+Y) were carried out by Dual LA-ICP-MS (LASS) Facility at University of California, Santa Barbara, following the methods outlined in Kylander-Clark et al., (2013). Well-polished cored samples were analyzed using Inductively Coupled Plasma Mass Spectrometry (ICPMS) with Laser Ablation Split-Stream (LASS) technique. The laser-ablation split-stream system combines a Photon Machines 193 nm ArF Excimer laser, equipped with a Hel-Ex ablation cell, with a Nu Instruments HR Plasma high-resolution MC- ICP-MS system for collecting Sr isotope data, and an Agilent 7700 quadrupole ICP-MS for determining trace-element concentrations. The laser parameters for analysis consisted of a 25 µm spot ablated at ~1 j/cm^2 and 4 Hz for 15 seconds, following a 20 second baseline and two-shot pre-ablation.

Ground-Penetrating Radar

The GPR data were collected using a hand-towed Sensors & Software pulse EKKO PRO GPR system (Sensors & Software Inc., Mississauga, Canada) courtesy of Alexander Simms, UCSB. Common-offset surveys were collected using 100 MHz, 200 MHz, and 500 MHz transducers. The frequencies obtain resolutions of 0.15 m, 0.10 m, and 0.03 m and

penetrated to depths of up to 7 m, 5 m, and 2 m, respectively. There is no ground-water table at the plato. GPR data were processed using Sensors & Software EkkoView Deluxe by applying dewow, automatic gain control (AGC), bandpass filter, and a synthetic aperture image reconstruction migration to focus scattered signals. Elevation data were collected simultaneously using a HiPer Lite Plus RTK-GPS system (Topcon Positioning Systems Inc., Livermore, California). After processing, GPR data were topographically corrected using a simple vertical shift of traces to correct for terrain using elevations obtained from the GPS survey and the average velocity of sediments obtained from the common midpoint (CMP) surveys. GPR profiles were interpreted in IHS's Kingdom software. GPR data presented in this paper are from the 200 MHz transducers which provided the highest resolution images of the bioherms.

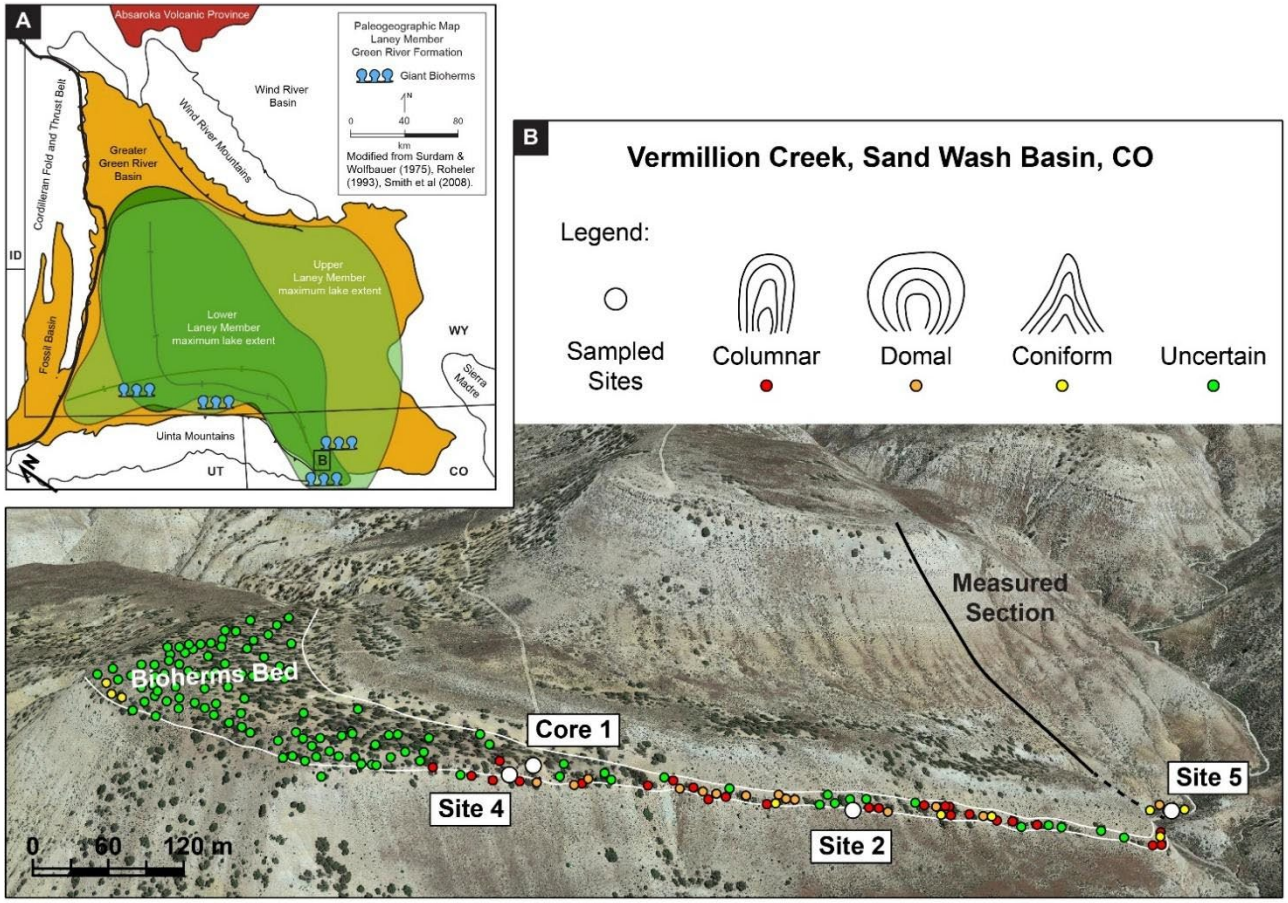

Figure 60. A) Palegeographic map of the LaClede Bed, Laney Member, Green River Formation (modified from Roehler 1993) showing the maximum extension and depositional axis of the Eocene Lake Gosiute between 49.25 ±0.12 and 49.9 Ma. The location of the studied area at Vermillion Creek in Sand Wash Basin is shown in a box labeled B. B). Satellite view and location of the stromatolite bioherms bed (Upper LaClede). The location of four stromatolite macrostructures sampled is shown in white circles. Measured stratigraphic section in black line. Image modified from Google Earth.

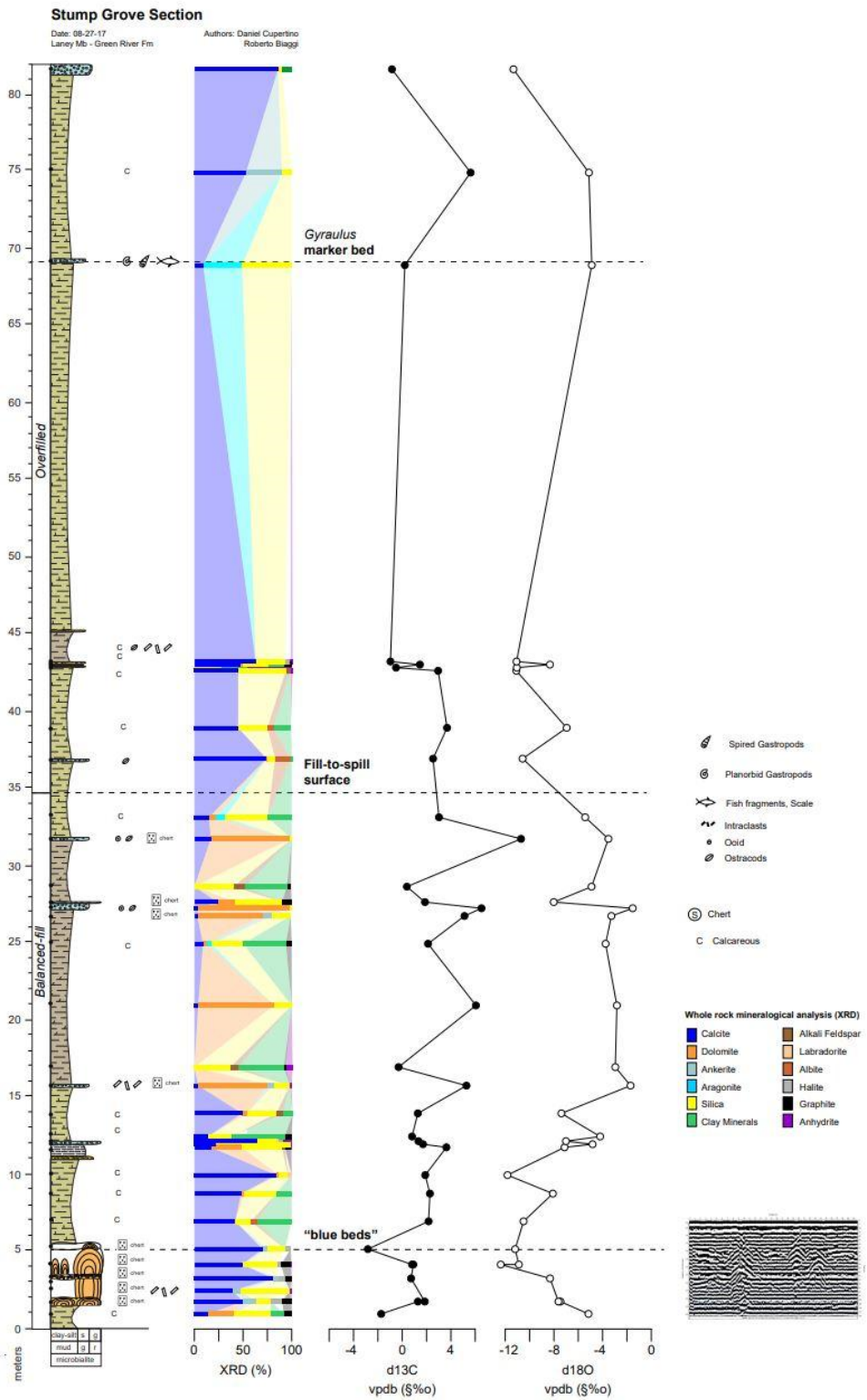

Figure 61. Stump Grove Section of Lower LaClede Bed of the Green River Formation in the Vermillion Creek area. Note detailed lithology, XRD measurements, bulk rock (weight percent), and $\delta^{13}C$ and $\delta^{18}O$ stable isotopes.

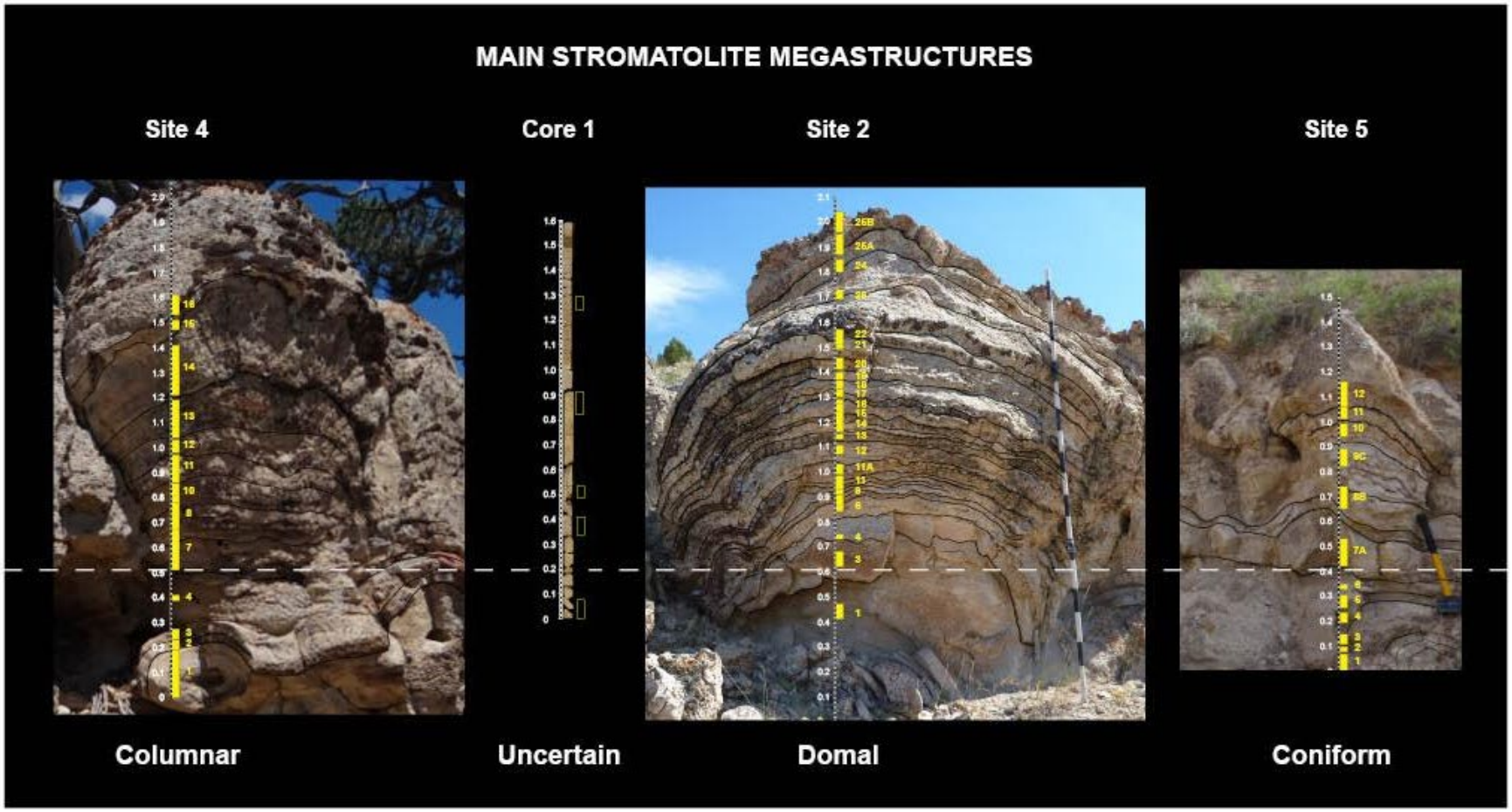

Figure 62. Main stromatolite megastructures sampled: columnar (site 4), uncertain (core 1), domical (site 2) and coniform (site 5). Samples are shown in yellow with respective identification number. Vertical scale (white numbers) in meters. Dashed white line is the correlation datum.

4.4 Results

4.4.1 Ground-Penetrating Radar

With the aim of imaging the bioherms and understand their vertical succession, over 500 m (four lines) of ground-penetrating radar (GPR) profiles were collected on top of the overburden of the biostrome bed (Fig.63). GPR provides a useful tool for imaging the subsurface structure of sediment layers. Carbonate mound structures, and their internal layering of limestone and chert are clearly imaged by the GPR data where they appear as mound-shaped semicontinuous, high to medium amplitude (Fig.64). The reflections exhibit good continuity and facilitate 2-D mapping of the mounds over the area. The largest distance between two mound summits observed in the GPR data is approximately 40 m. The GPR profiles indicate that the mounds have heights of 2 m and within two depositional beds (Fig.64).

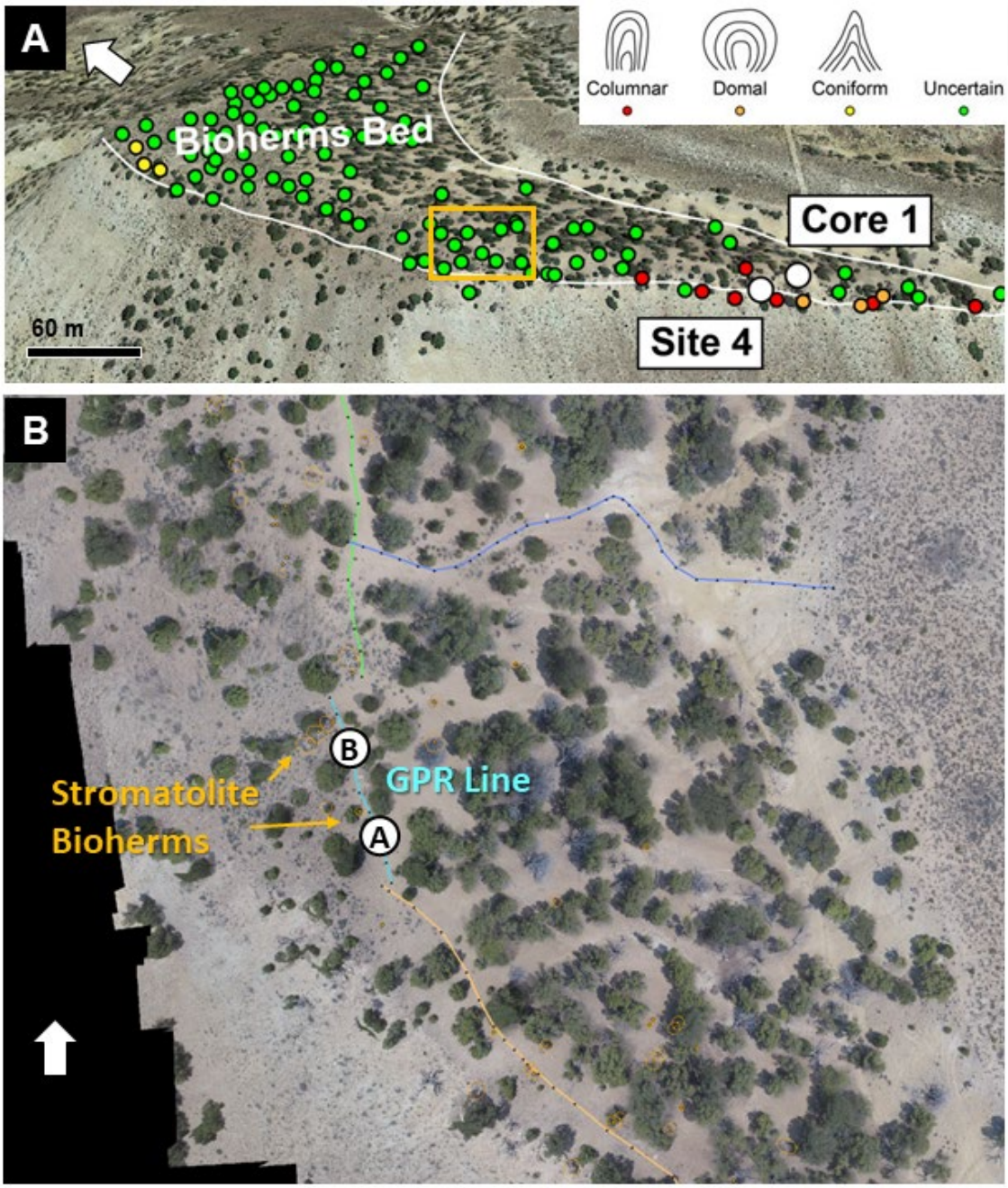

Figure 63. A) Satellite view of Vermillion Creek area showing stromatolite macrostructures in colored circles (see legend) and GRP accquisiton area in orange rectangle. Image modified from Google Earth. B) Drone photomosaic of GRP accquisiton area from July 2015 displaying locations of GPR transects as color lines.

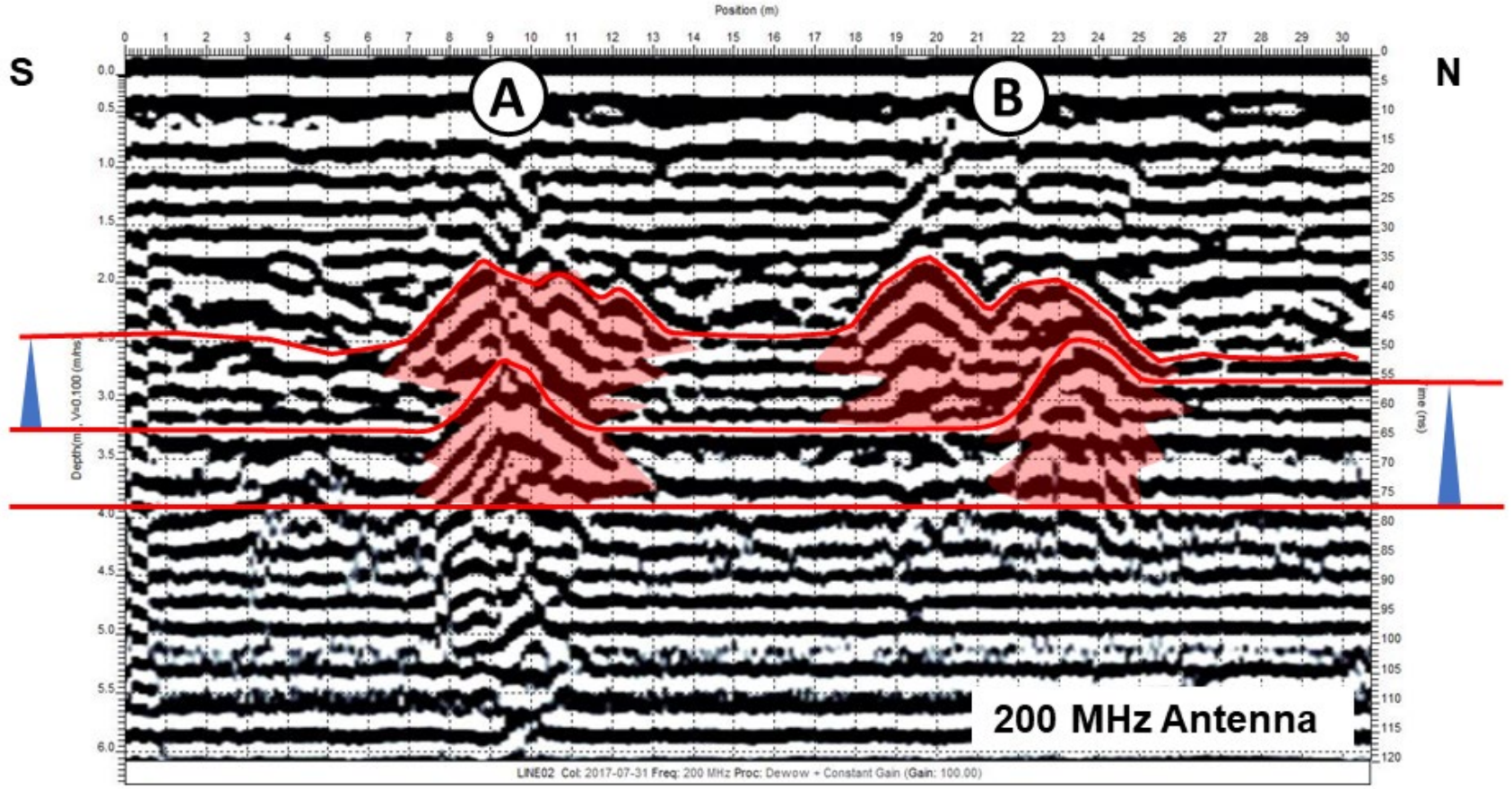

Figure 64. Interpreted GPR profile with bioherm elements overlain in red. Note two bioherms depositional events are separated by onlap terminations. This GPR transect is located in Fig.63 as a light blue line.

4.4.2 Description of the Microbialites

Four stromatolite bioherms were studied at sites designated as Site 4, Core1, Site 2, and Site 5 (Fig.60B). They occur in a complex biostrome made up of the bioherms, stromatolite coated logs, and contain individual stromatolite bioherms up to 5.5 m tall, but average about 3 m. From outcrop observations, three major stromatolite macrostructures were identified: columnar, domical, and coniform (Fig.62). Spatial distribution of columnar, domical, and coniform stromatolites is shown in Figure 60B. It is noted that the structures described above are based on limited outcrop exposures and the tops of giant columns. Detailed, centimeter-scale measured sections of the individual bioherms were conducted. The stromatolite bioherms initiate on stromatolite-coated logs or on older, lithified microbialites. The bioherms are discrete structures enclosed in sediment infill. They do not intergrade with infill sediment. The growth direction is perpendicular to the plane of the substrate. The stromatolites are composed of layers, a few centimeters thick, in turn the layers are composed of a variety of microbialites (Fig.65). Altogether, up to 50 layers were recognized and described per bioherm, and a total of 108 samples plus one 1.6-meter-long core were collected (Fig.62). Only in one bioherm, a clear erosion surface has been identified.

Each bioherm is composed of 3-10 cm thick layers. Six distinct microbialite types were identified in the layers: (1) Microbial boundstone, (2) Stratiform Stromatolites, (3) Domical and Columnar Stromatolites, (4) Bulbous and Stubby Stromatolites, (5) Shrubby Stromatolites and (6) Slender Columnar Microbialites (Fig.67). Each layer is composed of microbialites, mostly stromatolites. Only two types of layers are not composed of stromatolites: one has unlaminated branching, slender columns (presumably a microbialite) and the other is composed of grainstone and represents a microbial boundstone. The

identification of patterns of the microbialite types in the layers turn out as a valuable tool for the correlation of the bioherms at Sites 4, 2, 5 and Core 1.

The types of microbialites in the layers were determined based on mesostructural and microstructural features. For stromatolites, laminae were examined in terms of stacking pattern, profile, waviness, synoptic relief, lateral continuity, thickness; and by the composition of the lamina (microstructure). In the other microbialites, macrostructure, mesostructure, and microstructure, and sedimentary grains were used. This terminology is based on Grey and Awramik (2020). Figure 65 illustrates key features that applied to the classification of mesostructure and microstructure.

(1) **Microbial boundstone**. "Grainstone" Microbial Boundstone, microbial boundstone are formed by trapping and binding of ooids, peloids and detrital minerals grains (Kenter et al, 2005). (Fig.68A, B, C)

(2) **Stratiform stromatolites**, occur in two variations. First as micro-undulations to lateral linked domes and have continuous laminae across the domes (Fig.68D, E). Second, are discrete, vertically stacked discrete hemispheroids that are not laterally linked with other hemispheroids. (Fig.68F, G)

(3) **Domical and columnar stromatolites**, Columnar describes discrete structures in which the height is greater than the maximum width (Fig.69A, B). Domical, discrete structures approximately as high as they are wide (Fig.69C, D).

(4) **Bulbous and stubby stromatolites**, Bulbous refers to a shape variation of columnar in which the diameter of the base is much less than the maximum diameter, frequently the structure may appear to be almost detached from the substrate (Fig.69E, F). Stubby

Stromatolites, a variation of branched columnar microbialite where the height to width ratio is approximately equal to 1 (Fig.69G, H).

(5) **Shrubby stromatolites**, type of branched stromatolite with highly irregular morphology, but with a characteristic shrub-like appearance. The microstructure consists of laminae composed of fan-shaped carbonate crystals (Fig.70A, B).

(6) **Slender columnar microbialites**, are columnar branched microbialites where the elongation (height to width ratio) of a column is much greater than 1 (Fig.70C, D). Branching can be infrequent to frequent. Slender Columnar microbialites are formed mainly by peloids, sometimes laminated (stromatolite) (Fig.70E, F).

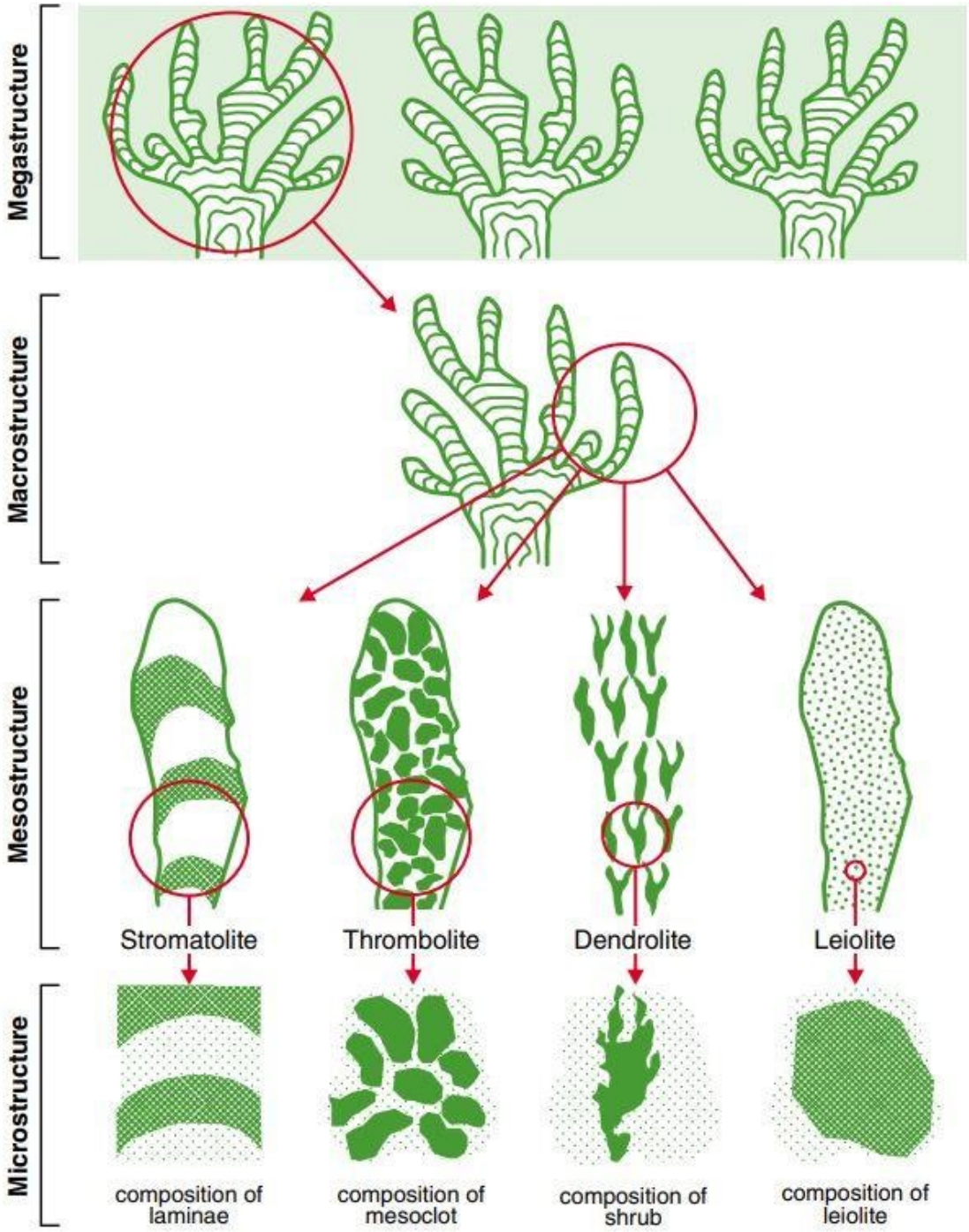

Figure 65. Hierarchy of observational levels for microbialites (Grey and Awramik, 2020).

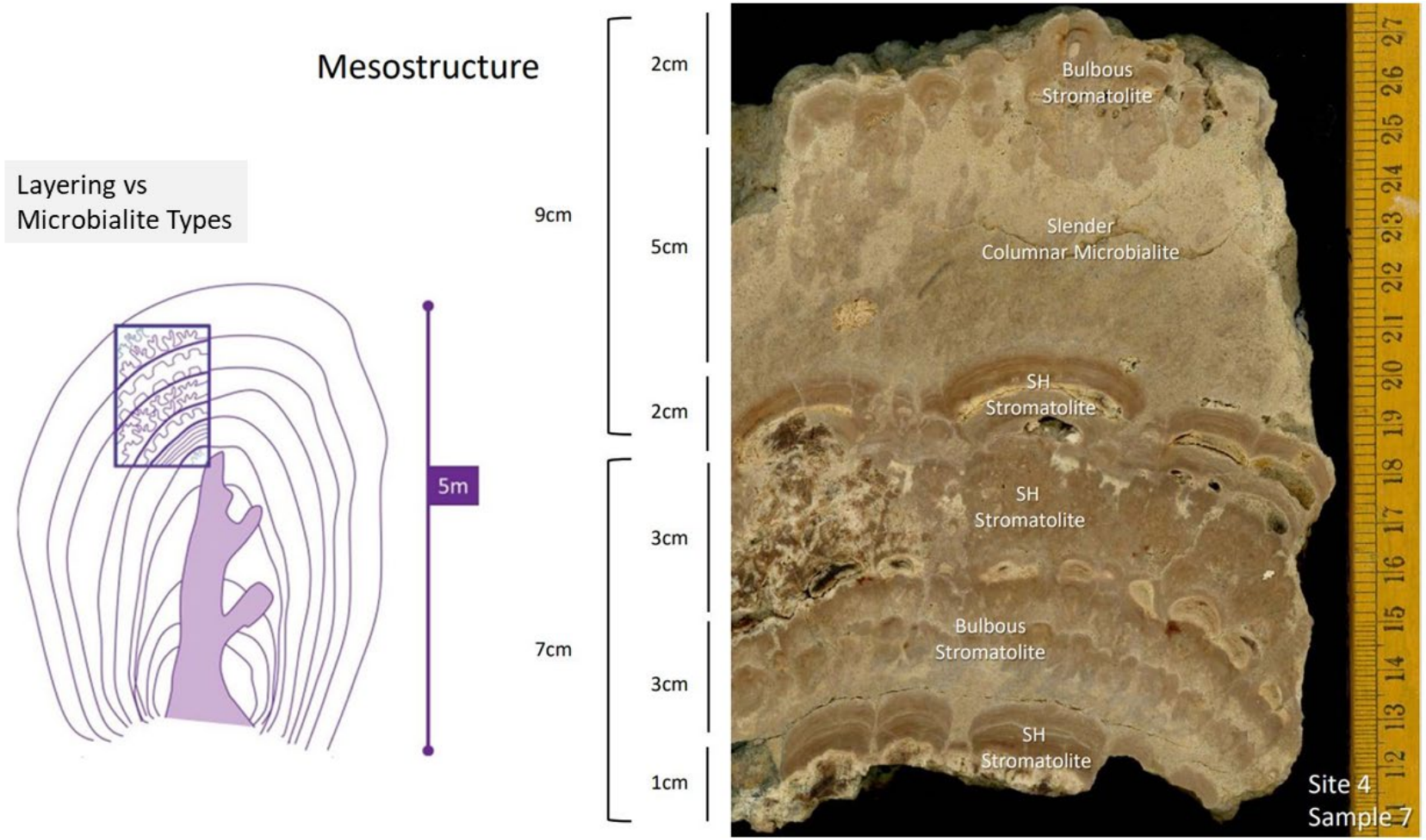

Figure 66. Vermillion Creek multi-meter stromatolites formed by layers composed by microbialite types. The initiation of giant stromatolite growth required availability of large accretionary substrates within the photic zone.

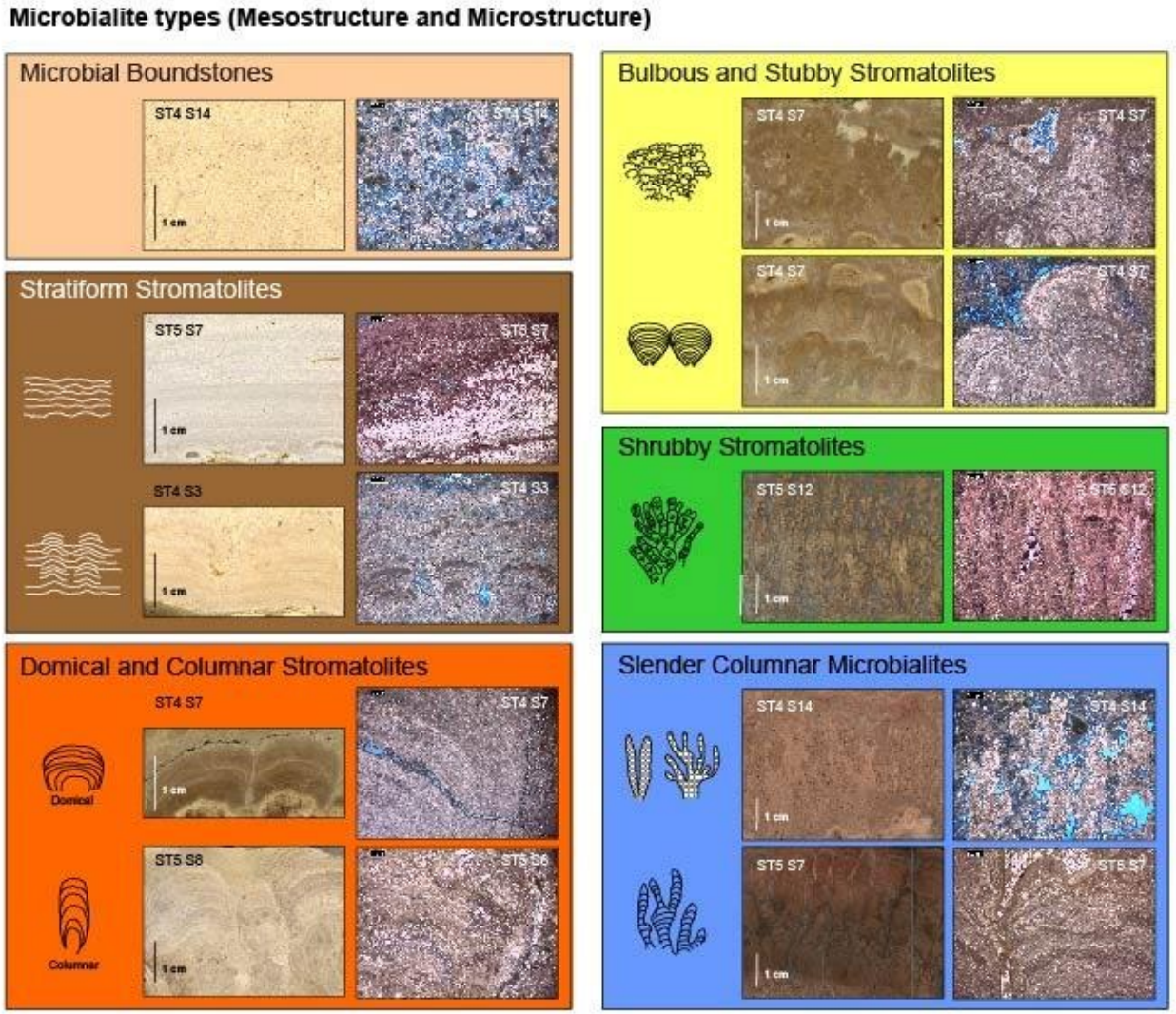

Figure 67. Microbialite types at the mesostructural and microstructural level. The occurrence of these different types of microbialites in layers is graphically presented in figure 71, 72.

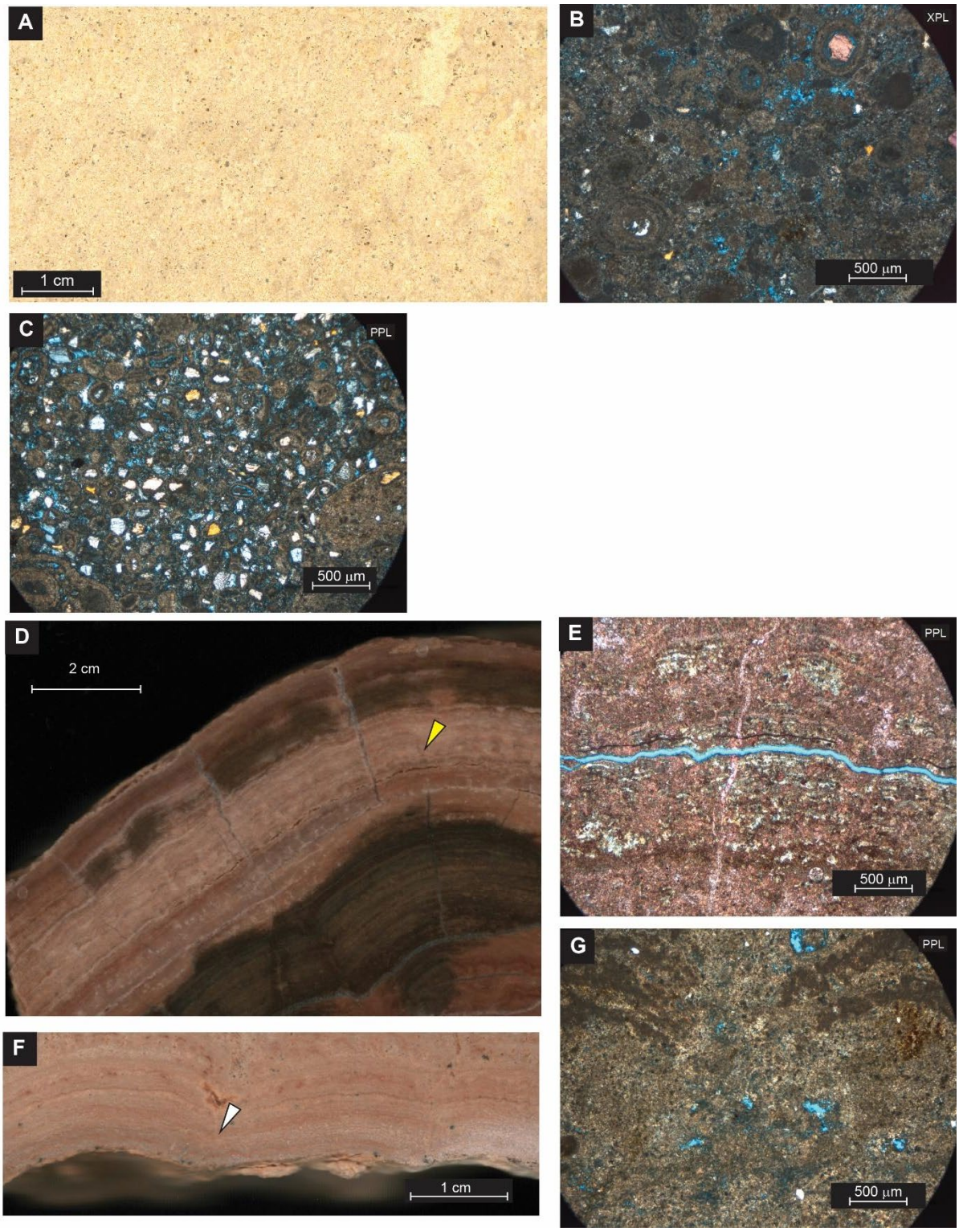

Figure 68. Microbial boundstone at (A) slabbed section (SS), (B) Polarized light microscopy (XPL), (C) Non-polarized light microscopy (PPL). Stratiform stromatolites: D) micro-undulations to lateral linked domes, SS and E) PPL. Stratiform stromatolites: F) discrete hemispheroidal and G) PPL.

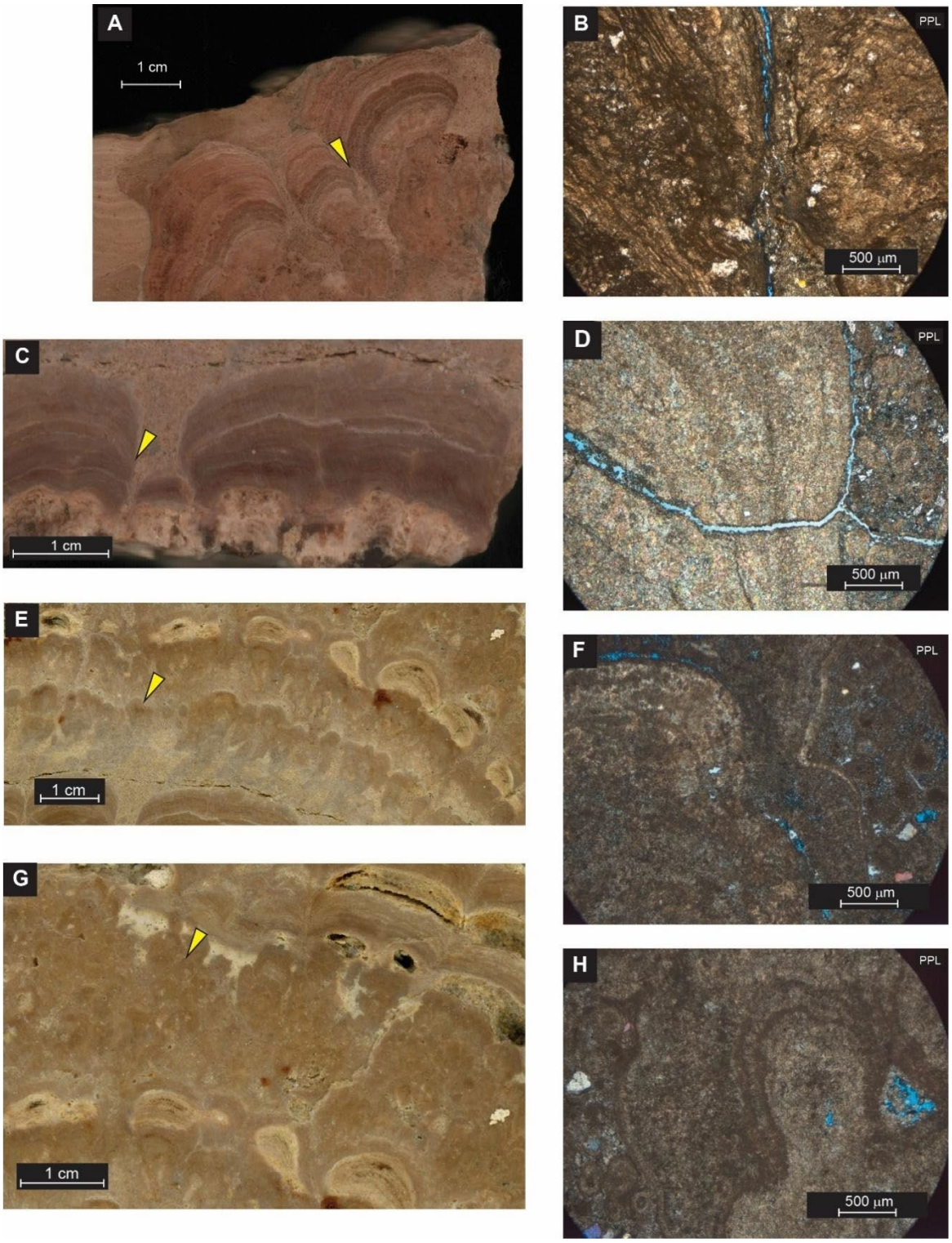

Figure 69. Domical stromatolites: A) mesostructural level, slabbed section (SS), note laminae terminations yellow arrow and B) microstructural level, non-polarized light microscopy (PPL). Columnar stromatolites: C) SS, note laminae synoptic relief and D) PPL. Bulbous Stromatolites: E) SS, note bulbous short base diameter (yellow arrow) and F) PPL. Stubby Stromatolites: SS, note bulbous short base diameter (yellow arrow) and F) PPL.

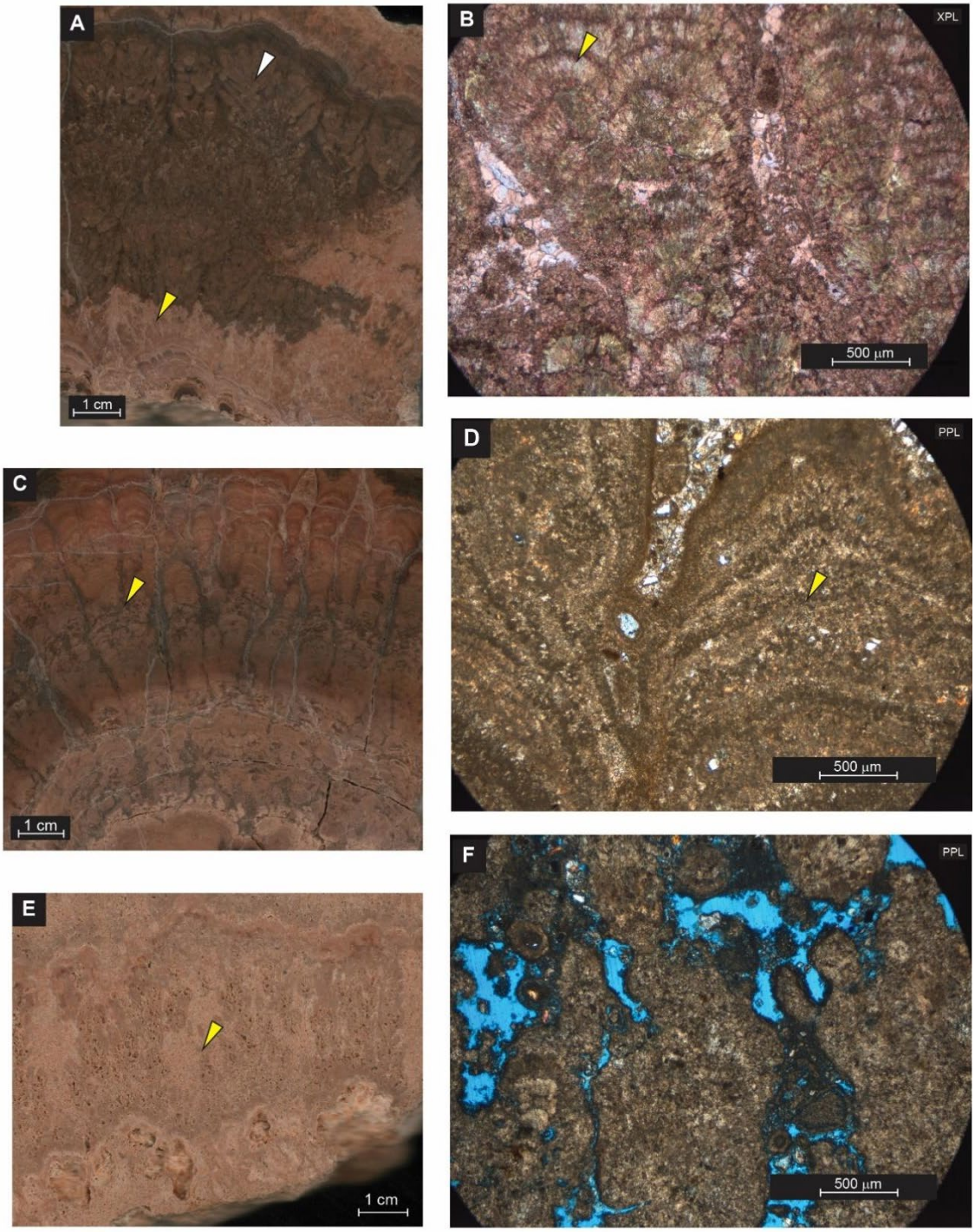

Figure 70. Shrubby Stromatolites: A) mesostructural level, slabbed section (SS), shrub-like branching columns (yellow arrow), shrub-like columns in a silicified portion (white arrow); B) microstructural level, partially dolomitized fabric of fibro-radial calcite/aragonite polycrystals, polarized light microscopy (XPL). Slender Columnar stromatolites: C) column elongation greater than width (yellow arrow) (SS); D) peloids and lamination (PPL). Slender Columnar Microbialites: E) branched columns (SS), F) micritic matrix, absence of lamination (PPL).

4.4.3 XRD Mineral Identification and Quantification

Over ten minerals were identified in the sampled material from Vermillion Creek using quantitative X-Ray Diffraction (XRD) bulk analysis. Four major mineral phases occur at over 50 wt% average in 84 samples. The major mineral phases are primarily assemblages of calcite ($CaCO_3$), dolomite ($CaMg(CO_3)_2$), detrital quartz and chert (SiO_2), and Clay Minerals. Minor minerals identified are: ankerite $Ca(Fe,Mg,Mn)(CO_3)_2$, aragonite ($CaCO_3$), albite ($NaAlSi_3O_8$), and Ca-albite $(Na,Ca)Al(Si,Al)_3O_8$).

The Stump Grove Section shows variation in mineralogy and their variation in stratigraphic position (Fig.61). X-Ray Diffraction (XRD) bulk analysis in the measured section starts at the biostrome microbialite bed and ends at the *Gyraulus* (gastropod) regional marker bed. Several distinctive features of lake margin fluctuation mineralogy stand out in Stump Grove Section and provide important reference points for examining the variation of the chemistry of SE margin of Lake Gosiute. Calcite is the only mineral that is present along the entirely section. Calcite decreases in abundance between 15 and 25 m in the section lining up with a positive $\delta^{18}O$ excursion (Fig.61). Dolomite increases for the same interval. Dolomite occurs mainly in this interval, between 15 to 25 m of Stump Grove Section. Dolomite is also found in the biostrome microbialite bed in smaller amounts (see Dolomite/Dolomite+Calcite ratio) (Fig.71). Calcite and dolomite major phases are very important for the interpretations and conclusions regarding the environment of deposition. The Dolomite/Dolomite+Calcite ratio in the biostrome microbialite bed show values up to 50%, usually increasing associated with positive $\delta^{18}O$ excursions (except at site 4) (Fig.71). No XRD data were acquired for Core 1. Upward in the Stump Grove Section, after the high dolomite portion, at 33 m, clay mineral and dolomite content decreases and calcite and silica content increase between the fill-to-

spill surface and *Gyraulus* marker bed. However, bellow the fill-to-spill surface, clay minerals show a relative higher content. Silica is present throughout the Stump Grove Section.

4.4.4 Stable Isotopes

The $\delta^{13}C$ and $\delta^{18}O$ values for the Stump Grove Section range from -4‰ to 6‰ (V-PDB) and -12‰ to -2‰ (V-PDB). Three main isotope excursions occur (Fig.61). An overall negative $\delta^{18}O$ excursion near the bottom of the section within the biostrome microbialite bed with values starting at -4‰ near the bottom to a minimum of less than -10‰ upper section close to blue beds marker. There is subsequently a positive $\delta^{18}O$ excursion with an overall increase in the $\delta^{18}O$ values to -2‰ through 15 to 35 m in the section. Thereafter, a new trend is present in which the $\delta^{18}O$ values shift erratically more negative, overall, by -6‰ to almost the *Gyraulus* marker bed.

The amplitudes of short-term changes in $\delta^{13}C$ and $\delta^{18}O$ values in the biostrome microbialite bed allow to correlate distinct layers with different types of microbialites. Within that interval, several large deviations of $\pm<3$‰ are present (Fig.72). Stable Isotope values were determined from the powders made from three categories of samples: (1) the distinct types of microbialites in the layer, (2) from the infill between microbialites, and (3) in a few cases, a mixture of infill and microbialite (was not able to differentiate). The $\delta^{13}C$ and $\delta^{18}O$ values vary from -2‰ to 6‰ and -12‰ to -2‰, respectively, and their correlation variations are showed in figure 72. At this scale, two oxygen excursions occur in major kinds of stromatolite macrostructures like columnar (Site 4 and Core), domical (Site 2) and coniform

(Site 5). The first one is a positive $\delta^{18}O$ excursion near the bottom in all sites, up to -6 to -4‰ values, followed by a negative $\delta^{18}O$ excursion with values less than -10‰ by the upper section of all sites.

Lastly, overall stable isotopic data show strong positive linear covariance between $\delta^{13}C$ and $\delta^{18}O$ values from microbialite samples of Site 4 ($r = 0.86$) and Site 2 ($r = 0.93$) (Fig.73).

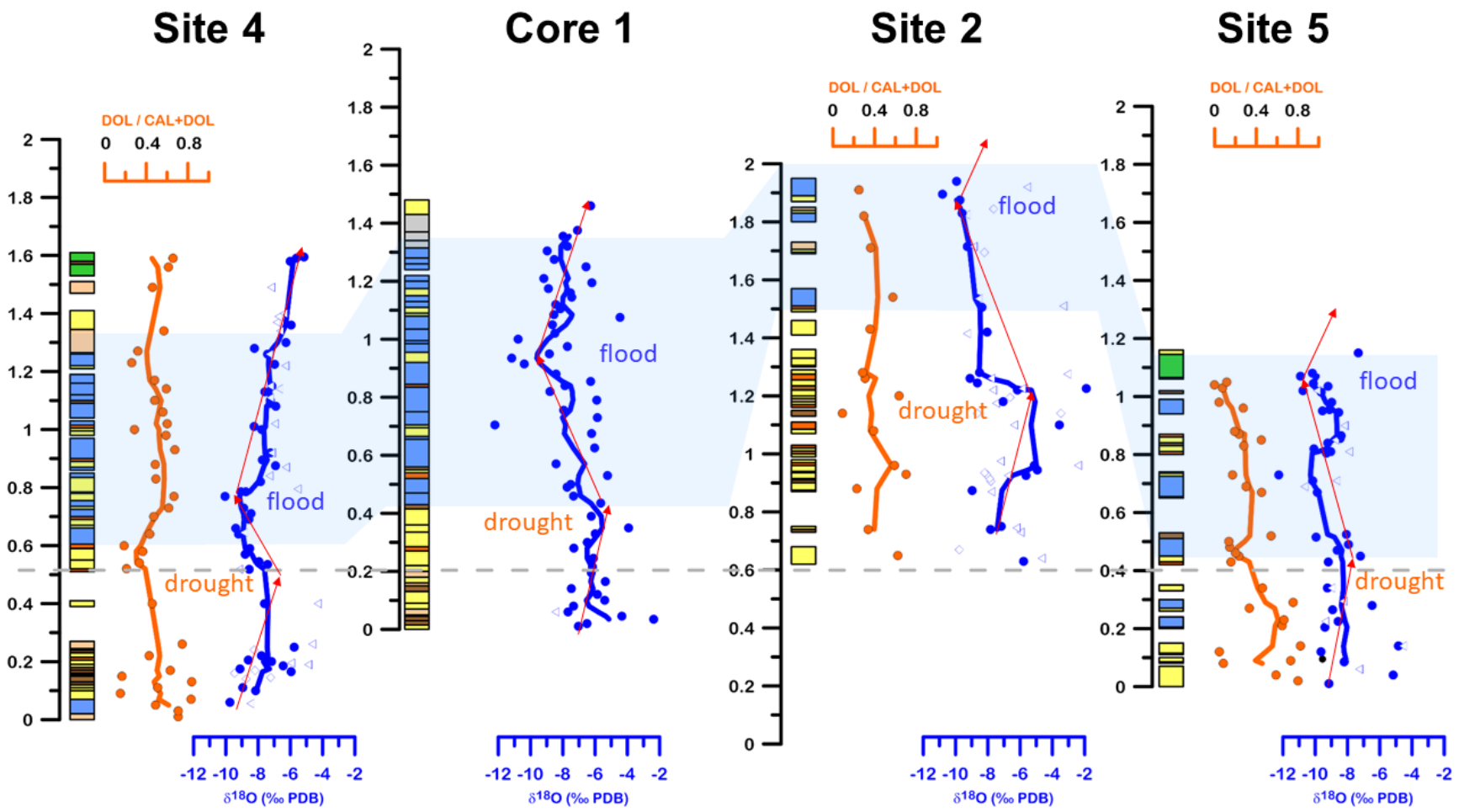

Figure 71. Microbialite types, left column (see figure 67 for color legend) and Dolomite/ Dolomite+Calcite ratio and oxygen isotope composition within individual layers of the major stromatolites. Blue area highlights flood events, which are interpreted as controlled by short-term changes in climate.

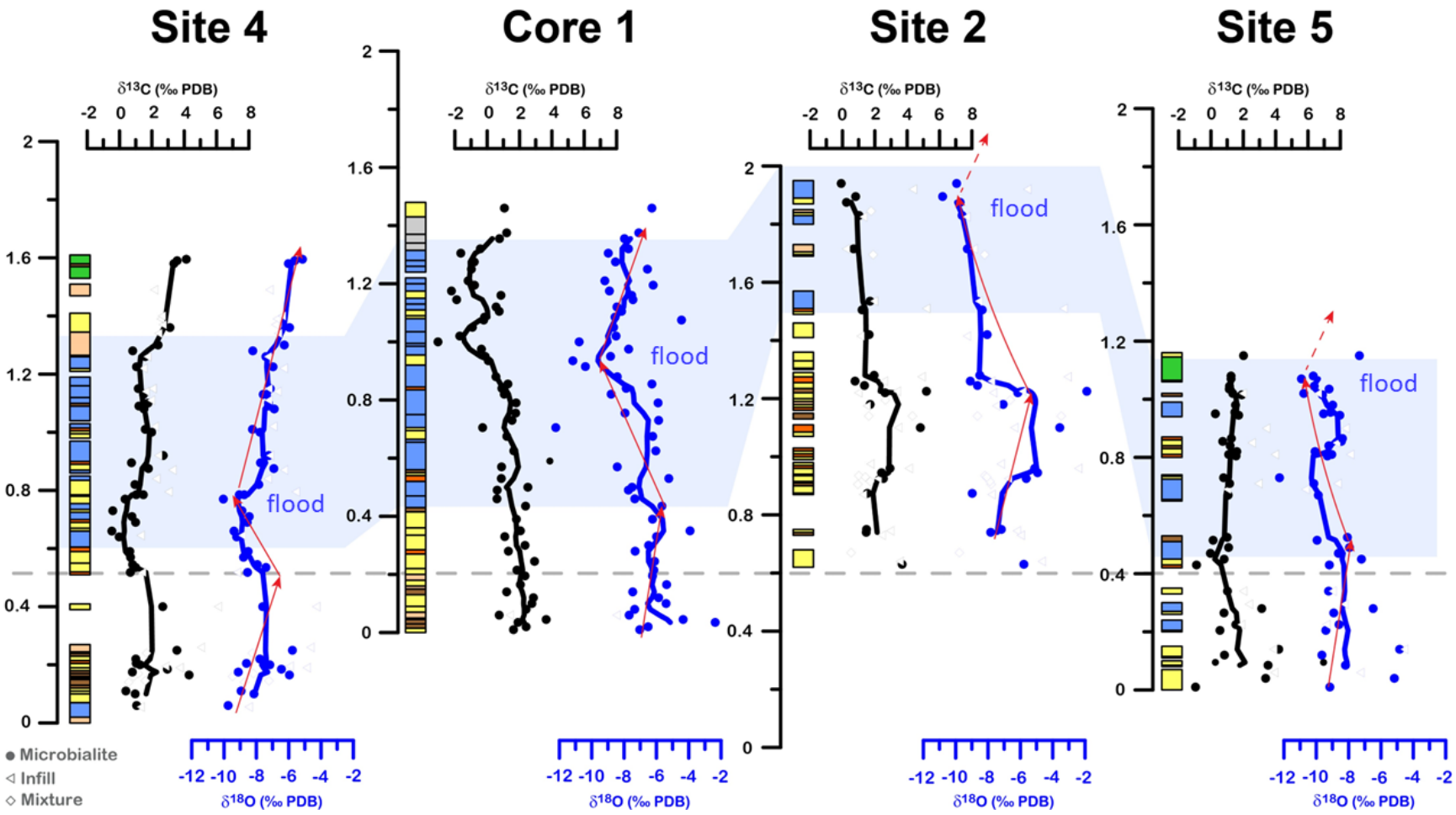

Figure 72. Microbialite types, left column (see figure 67 for color legend) and carbon and oxygen isotope composition within individual layers of the major stromatolites. Blue area highlights flood events, which are interpreted as controlled by short-term changes in climate.

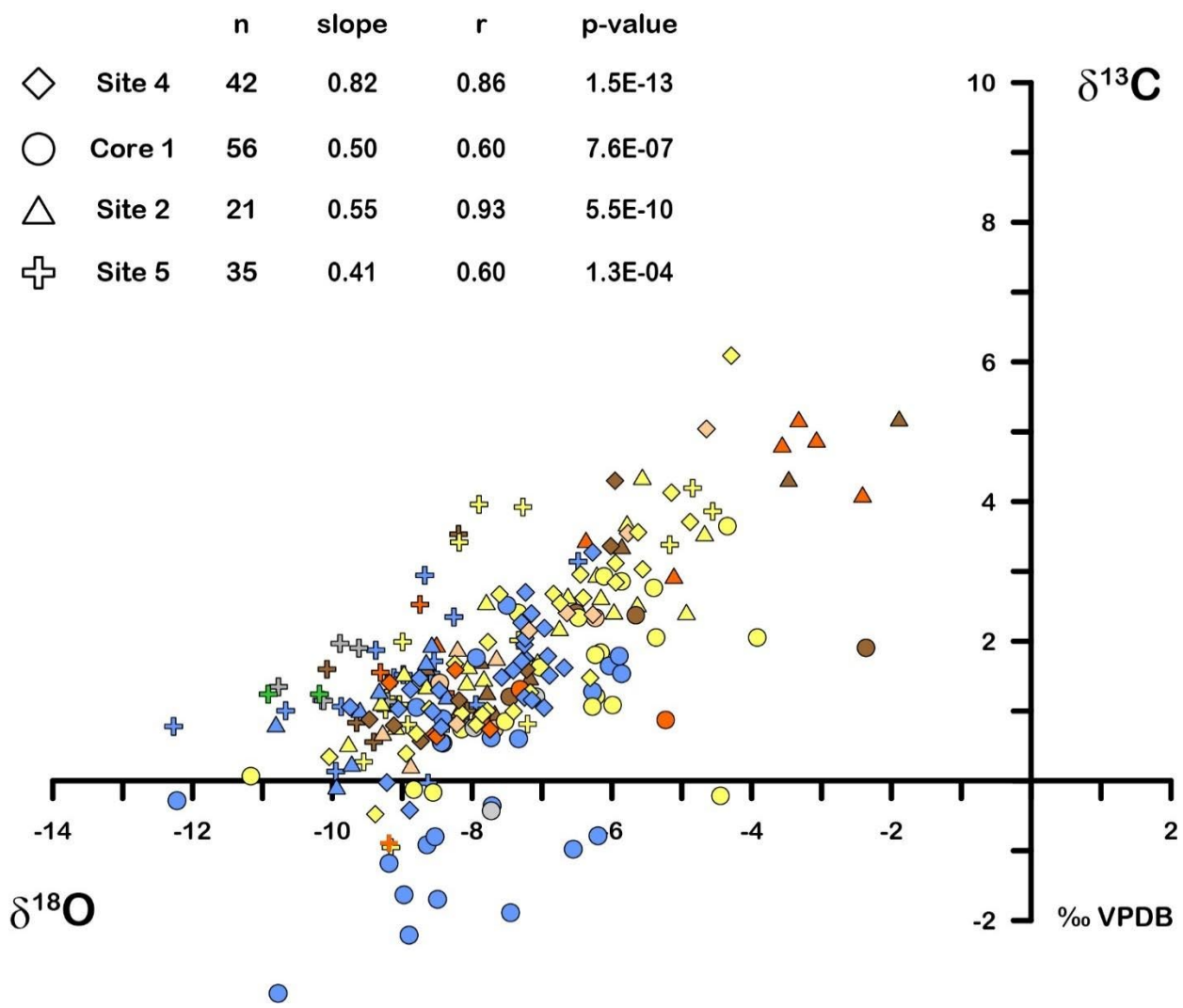

Figure 73. Covariant trends between $\delta^{18}O$ and $\delta^{13}C$ (see figure 67 for color legend). An r > 0.7 indicates carbonate precipitation and accumulation in closed lakes (Talbot 1990). An r < 0.7 may reflect springs.

4.4.5 87Sr/86Sr and REE+Y

Five samples from Core 1 were examined using $^{87}Sr/^{86}Sr$ ratios, Rare Earth Elements (REE+Y), and $\delta^{18}O$ and $\delta^{13}C$ values in trying to detect groundwater and lake water signatures. The isotope geochemistry at the centimeter-scale of the microbialite types in the core were used to determine any short-term changes in lake water. Data from the sampled interval are typically calcitic and have high Sr concentrations (median = 3415 ppm) and stratigraphically constant $^{87}Sr/^{86}Sr$ ratios that range from 0.7125 to 0.7135, with an average around 0.7130 (Fig.74A). Overall, there is no correlation of carbonate mineralogy with Sr concentration or isotopic composition. Strontium isotope ratios were obtained from 4 microbialite types and 2 carbonate infilled sediment beds. These data demonstrated $^{87}Sr/^{86}Sr$ measured on average of 0.7131 for Stratiform Stromatolites, 0.7130 for Domical and Columnar Stromatolites, 0.7130 for Bulbous and Stubby Stromatolites, 0.7132 for Slender Columnar Microbialites and, 0.7130 and 0.7132 for the Carbonate infill sediments.

Rare Earth Elements and Ytrium (REE+Y) patterns of Core 1 microbialites and infilled sediments show (1) a relatively higher proportion of HREE, (2) no anomalies in Ce, Gd and Pr; positive anomalies in Eu and Y, and negative anomalies in La, and (3) a low Y/Ho ratio (Fig.75). These results were compared with date from modern sclerosponges following a suggestion from Matthew Jackson from which solid/solution fractionation patterns for marine waters could be determined and compared (Fig.75).

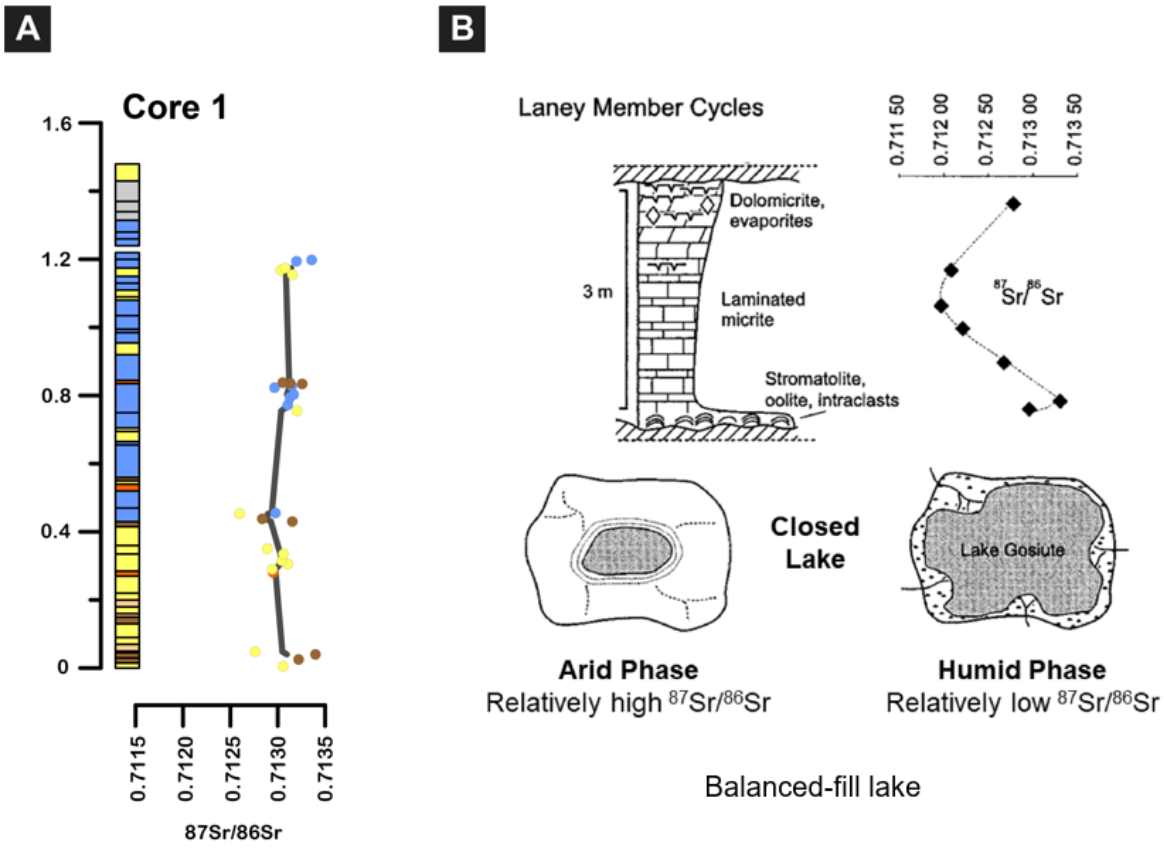

Figure 74. A) Different microbialite types from Core 1 showing relatively high $^{87}Sr/^{86}Sr$ (see figure 67 for color legend). B) Lake cycle and strontium ratios from lake margin in Laney Member (Rhodes 2002).

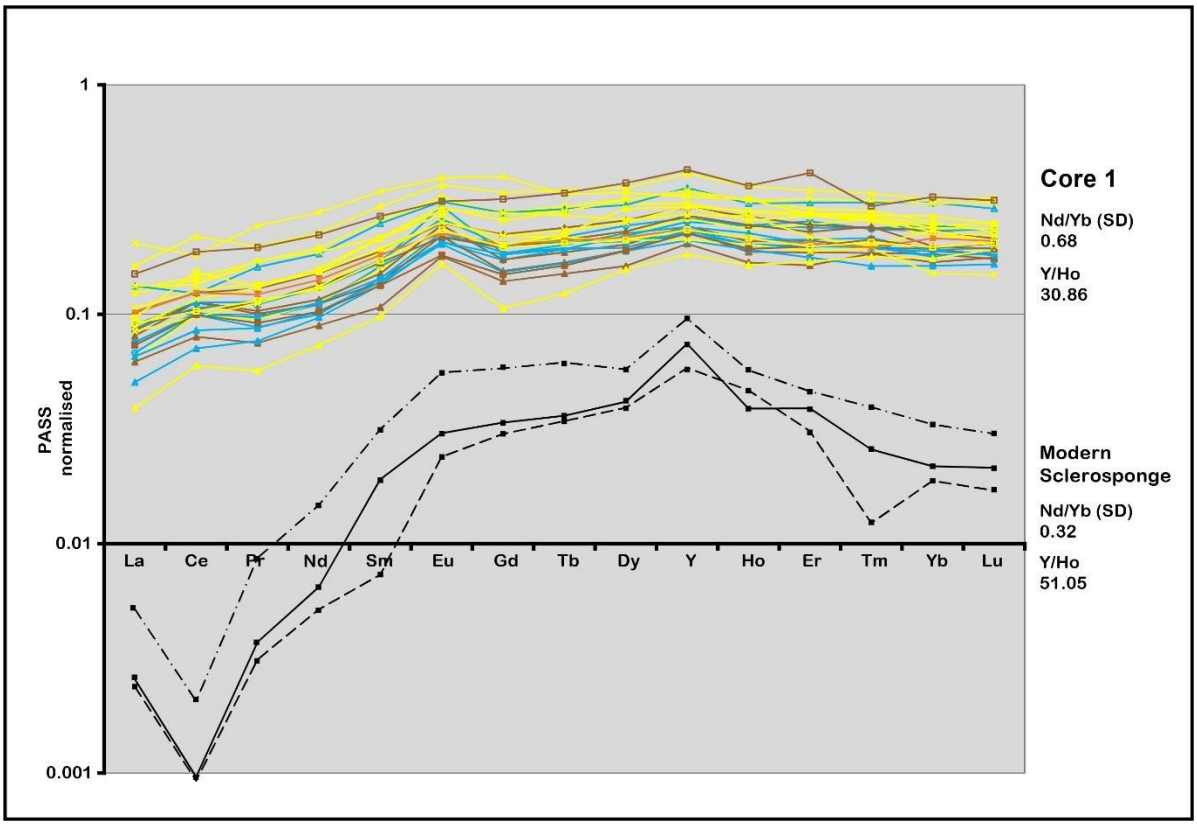

Figure 75. Rare earth elements and yttrium from different microbialite types in Core 1 (see figure 67 for color legend) and a modern marine sclerosponge (standard data supplied by Matthew Jackson).

4.5 Discussion

Lakes are very dynamic systems. Stump Grove Section data from the Lower LaClede Bed at Vermillion Creek show fluctuations in a balanced-fill lake (Fig.61). It presents a fluctuating-profundal facies association (carbonate and kerogen rich) due to the depth and salinity variation of the lake water, recording the balance between rates of subsidence (accommodation space) and sediment + water fill, mostly as function of precipitation (I) and evaporation (E). Mineral assemblage and stable isotopic analysis show a lake-flooding setting (transgression) or humid phase (I > E) in the lower portion of the Stump section (Fig.61). $\delta^{18}O$ values for the lake water decreases (becomes enriched in ^{16}O) as the water inflow and precipitation increase, resulting in a $\delta^{18}O$ negative excursion. The high calcite content indicates increases in the carbonate precipitation rate along with microbial activity seen in the complex biostrome bed. Once the evaporative loss (E) from the total lake surface exceeds the total input waters (I) indicating an arid phase (E > I), the residual lake waters will have an evaporative enrichment for $\delta^{18}O$ value, resulting in $\delta^{18}O$ positive excursion (Fig.61). This was a low frequency drought phase and followed by an increase in the dolomite mineral assemblage. Again, this is in a balanced fill portion of Lake Gosiute. At least, on the upper part of Stump Grove Section, a second $\delta^{18}O$ negative excursion occurs increasing the calcite minerals occurrence, waning dolomite minerals, and recording the freshwater fossils indicators, like gastropods, which occurs in the *Gyraulus* marker bed in strata above this marker.

The Vermillion Creek bioherms, in the lower part of Stump Grove Section, consist of columnar, domical, and coniform stromatolites (Fig.60B). The formation of these stromatolite bioherms generally initiates on in-situ stumps or broken-off tree trunks and

branches which form substrate for microbially induced carbonate precipitation (Fig.62, site 4) (Awramik and Buchheim, 2015; Ingalls et al, 2021). Domical macrostructures, like the one described from the Stump Grove Section (Fig.61), show cyclicity. It starts with development of a domical stromatolite enveloping tree parts. It ends, with a resumption of the domical stromatolite. Since most of the domical stromatolites are buried in the outcrop (relative poor exposure), GPR provided detailed imaging and mapping of the domical structures. GPR reflectivity of the structures and reflectors terminations, like downlaps, onlaps and truncations, indicate that there are two stratigraphic levels of domical structures (Fig.64). The mounds imaged by GPR typically have widths of ~1-2 m and heights of ~1-4 m. These findings agree with outcrops in Vermillion Creek area.

One significant observation to be drawn from mineralogical and isotopic variation in the layering is that most $\delta^{18}O$-depleted samples are often accompanied by a progressive decrease in dolomite relative to calcite (Fig.71). It has been recognized that the presence of dolomite and high Mg/Ca ratios in lacustrine sediment indicates evaporative evolution of lake waters (Eugster and Hardie, 1978). Continued precipitation of calcium carbonate in closed lake systems leads to progressive increase in the Mg/Ca ratio of lake water, which in turn gave rise to deposition of progressively more Mg-rich carbonate sediment until authigenic dolomite is precipitated. This relationship within Vermillion Creek bioherms is present in part in samples from Site 5 and Site 2 (Fig.77). Stable isotopic data show strong positive linear covariance between $\delta^{13}C$ and $\delta^{18}O$ values from all sites (Fig.72), especially from samples of Site 4 ($r = 0.82$) and Site 2 ($r = 0.93$) (Fig.73). Talbot (1990) notes that suites of lacustrine carbonates that display high covariance of $\delta^{13}C$ and $\delta^{18}O$ data ($r \geq 0.7$), normally precipitate from closed lakes. Carbonates from

hydrologically open lakes show little or no correlation between $\delta^{13}C$ and $\delta^{18}O$ data (Talbot, 1990). Similar positive correlation was obtained by Ingalls et al., (2022) for some of the bioherms at Vermillion Creek.

Strontium isotope ratios ($^{87}Sr/^{86}Sr$) are reliable geochemical tracers for modern and ancient spring discharge in lacustrine basins (Peterman et al., 2012). $^{87}Sr/^{86}Sr$ ratios are not fractionated by temperature or evaporation, and hence are not directly influenced by climate, although climate-induced changes in weathering may affect Sr isotope compositions (Doebbert et al, 2014). Strontium isotopes ratios measured from Core 1, range from 0.7125 to 0.7135, with an average around 0.7130. On average, there is almost no strontium isotope ratio differentiation obtained from microbialite types and carbonate infill sediments (Fig.74A). Rhodes et al. (2002) showed an idealized lake cycle and $^{87}Sr/^{86}Sr$ ratio responses of humid and arid phases of Lake Gosiute in Laney Member cycles in the Delaney Rim area. They observed relatively low $^{87}Sr/^{86}Sr$ ratios (0.7130) in stromatolite samples, and relatively high $^{87}Sr/^{86}Sr$ ratios (0.7120) for kerogen-rich laminated micrites. The most radiogenic isotope compositions are associated with stromatolites, recording a higher proportion of runoff from the surrounding Precambrian uplifts. Doebbert (2014) reported $^{87}Sr/^{86}Sr$ ratios of modern streams and weighted averages for basement uplifted terrain around the east catchments of Vermillion Creek area from Sierra Madre show 0.7100 values, while west catchments associated with Uinta uplift have 0.7157 values (Fig.76). Differential weathering within the drainage basin of Lake Gosiute would therefore drive $^{87}Sr/^{86}Sr$ ratios lower for lake water during wetter periods (lacustrine highstands) and higher during drier periods (lacustrine lowstands).

The potential origins of REE signatures of Vermillion Creek bioherms were evaluated with a comparative analysis between modern sclerosponge (marine signature) and aqueous solutions of modern microbialites-- dominated lakes (Zeyen et al, 2021). All studied microbialite types at Vermillion Creek showed no strong differentiation of REE fractionation patterns (Fig.75). No fractionation during the incorporation of these elements into the microbialites are suggested since the patterns are mostly flat. Cerium is sensitive to changes in the redox conditions of water because oxidized Ce is tetravalent, less soluble, and more easily absorbed onto particles (Bolhar and Van Kranendonk, 2007). Negative Ce anomalies are therefore commonly interpreted as indicative of oxygenated conditions at the time of the deposition (Kamber and Webb, 2001). Most of the Core 1 microbialites showed positive Ce anomalies. Overall, such positive anomalies are consistent with poorly oxygenated conditions observed at shallow depth in saline lakes. This anomaly may record the input of poorly oxygenated groundwater fluids at or close to the formation site of this sample. All studied microbialites showed a positive Eu anomaly. Moreover, strong Eu enrichment of Vermillion Creek samples could be seen compared to the marine sclerosponge results (Fig.75). The positive Eu anomaly is influenced by groundwater discharge, which have leached the basement. Vermillion Creek bioherms were enriched in heavy REE relative to light REE. Similarly, Johannesson et al. (2014) observed a fractionation between recent Cuatro Cienegas microbialites from Mexico and ambient continental water with preference for HREE.

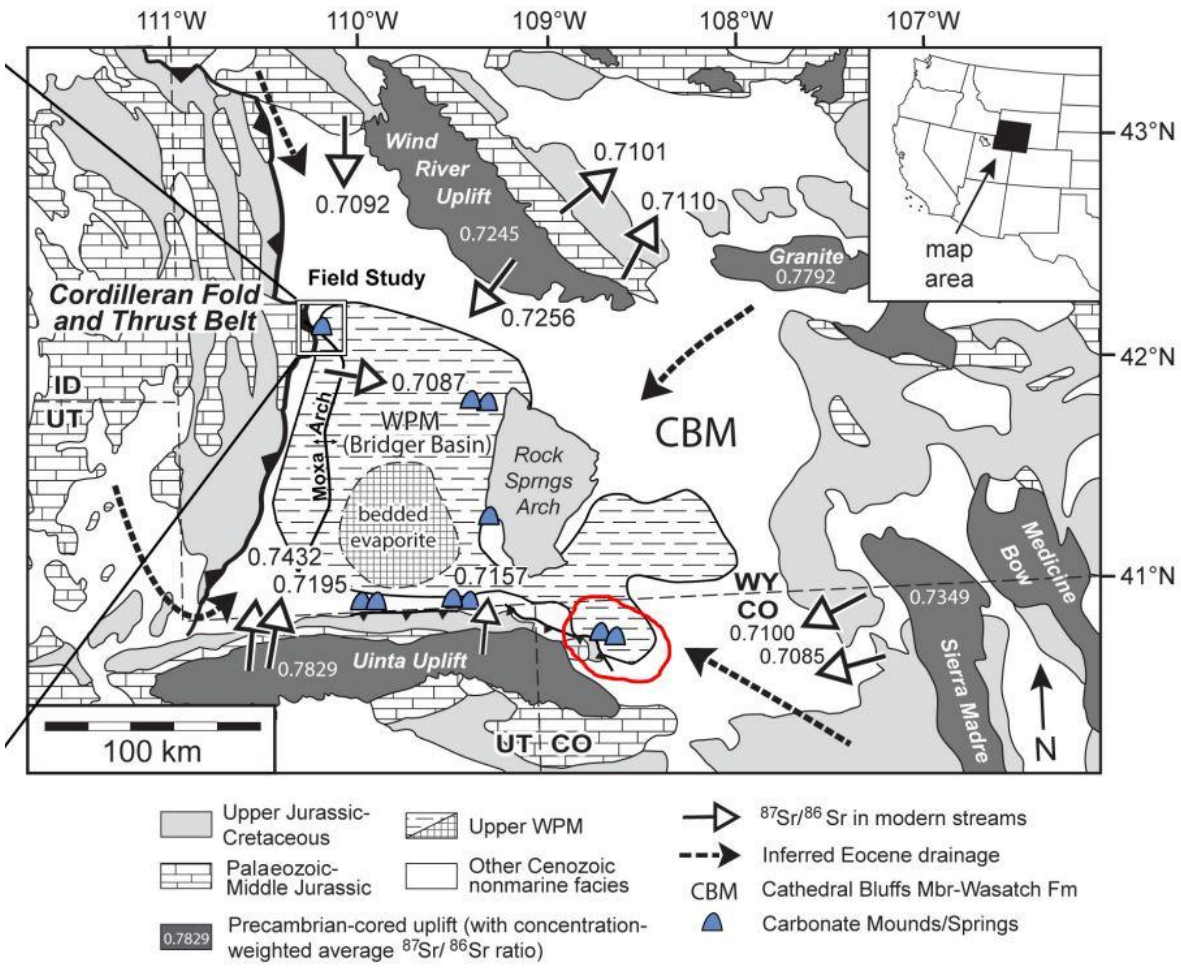

Figure 76. Greater Green River Basin geologic map with carbonate mounds highlighted at basin margins and basin-bounding faults (blue symbols). Note the Vermillion Creek area in red (modified from Jagniecki et al., 2021). $^{87}Sr/^{86}Sr$ ratios of modern streams (white arrows) and weighted averages for Precambrian cored uplifted terrain (dark grey) are plotted from Doebbert et al. (2014).

Significant input of freshwater during humid phases can occur at the margin of saline alkaline lakes. At times, unusual salinity patterns can occur from lake margin to offshore (Awramik and Buchheim, 2015). In response to these and other environmental conditions, saline-alkaline lakes register an unusual variety of carbonate microbialite sediments. Combined lithological, mineralogical, and isotopic data from the four bioherms (Fig.62) were organized into six microbialite types (Fig.67) and into two microbialite associations: Short microbialites, and Tall microbialites (Fig.77, 78). The Short-Microbialite Association occurs in the arid phase of the lake (E > I) and has the following assemblage of microbialite types: Stratiform Stromatolites, Bulbous and Stubby Stromatolites, Domical and Columnar Stromatolites. The Tall Microbialite Association occurs in the humid phase of the lake (I > E) and has Slender Columnar Microbialite, Bulbous and Stubby Stromatolite, and Domical and Columnar Stromatolites.

$\delta^{13}C$ and $\delta^{18}O$ covariation, oxygen isotopic composition, dolomite/calcite ratio and microbialite associations within layers of Core 1, Site 4, 2 and 5 indicated a cyclical pattern. Two depositional cycles were identified: Arid and Humid phase (Fig.71) and are associated with one lake hydrological type: closed lake. These lake phases result from short-term changes in climate that served to control the flux of water and fluvial sediment into the subsiding basin. An arid phase in a hydrologically closed lake is well represented at Sites 2 and 4 (Fig.71). It recorded an event that brought in microbial-coated logs where the laminated and short microbialite association and the $\delta^{18}O$ positive excursion show a changing trend from humid phase, when the logs were transported and deposited, to an arid phase, where the laminated short stromatolites developed. It signals a regional drying in a hydrologically closed phase of the balanced-fill lake type with a $\delta^{18}O$ positive excursion

(Sites 4, 2 and 5). This in turn gave rise to deposition of more Mg-rich carbonate sediments and dolomite precipitation (Sites 4 and 2; Fig.71), in response to an increase Mg/Ca ratio of lake water. The laminated and short stromatolites, (e.g, stubby, bulbous, stratiform) (Sites 4 and 2, Fig.64 and Fig.71) show changes in layering patterns presumably due to a diminishing water depth, but still at least 5m deep, and consequent increase in salinity and alkalinity. Site 2 records high carbonate productivity, probably triggered by Ca^{2+} and HCO^{3-} rich groundwater spring inflow and an erosion surface (subaerial exposure) during this phase. We consider the upper part of the arid phase, where $\delta^{18}O$ shows values of - 7‰ PDB, our correlation datum and the initiation growth surface for columnar and coniform stromatolitic bioherms. A humid phase in a hydrologically closed lake has a $\delta^{18}O$ negative excursion and substantial precipitation of calcium carbonate (Sites 4, 2 and 5; Fig.71). Layers composed of Slender Columnar Microbialites are associated with the most ^{18}O-depleted values (-10‰ V PDB). Slender Columnar Microbialites are the chief components in the layering of this phase (Core 1 and Site 4, Fig.71). A slight mineral preeminence of calcite over dolomite is observed. This pattern reflects the humid phase of the lake, distinguishing it from the arid phases recorded in subsequent layering.

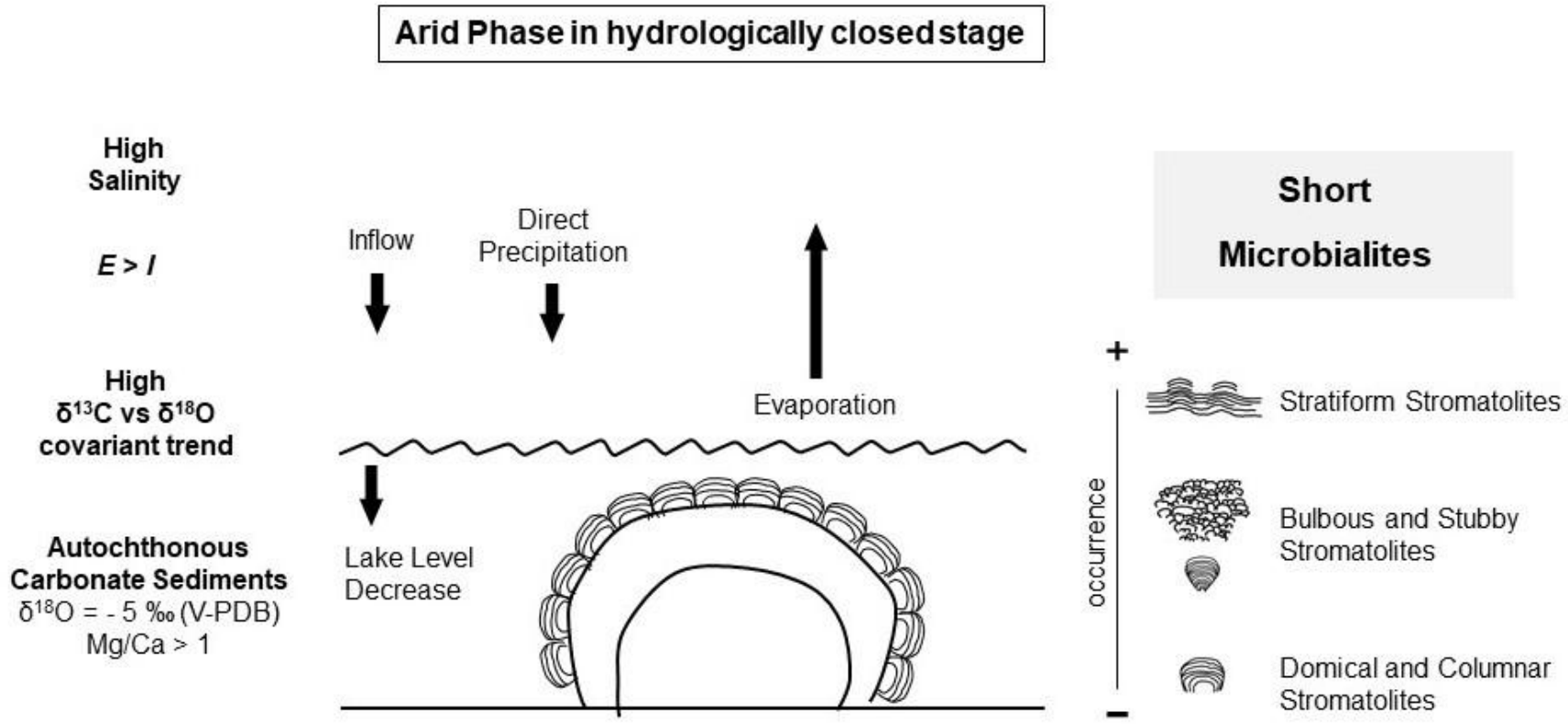

Figure 77. Short microbialite association controlled by the balanced-fill lake environmental conditions. Combined lithological (microbialite types), mineralogical and isotopic data support this interpretation.

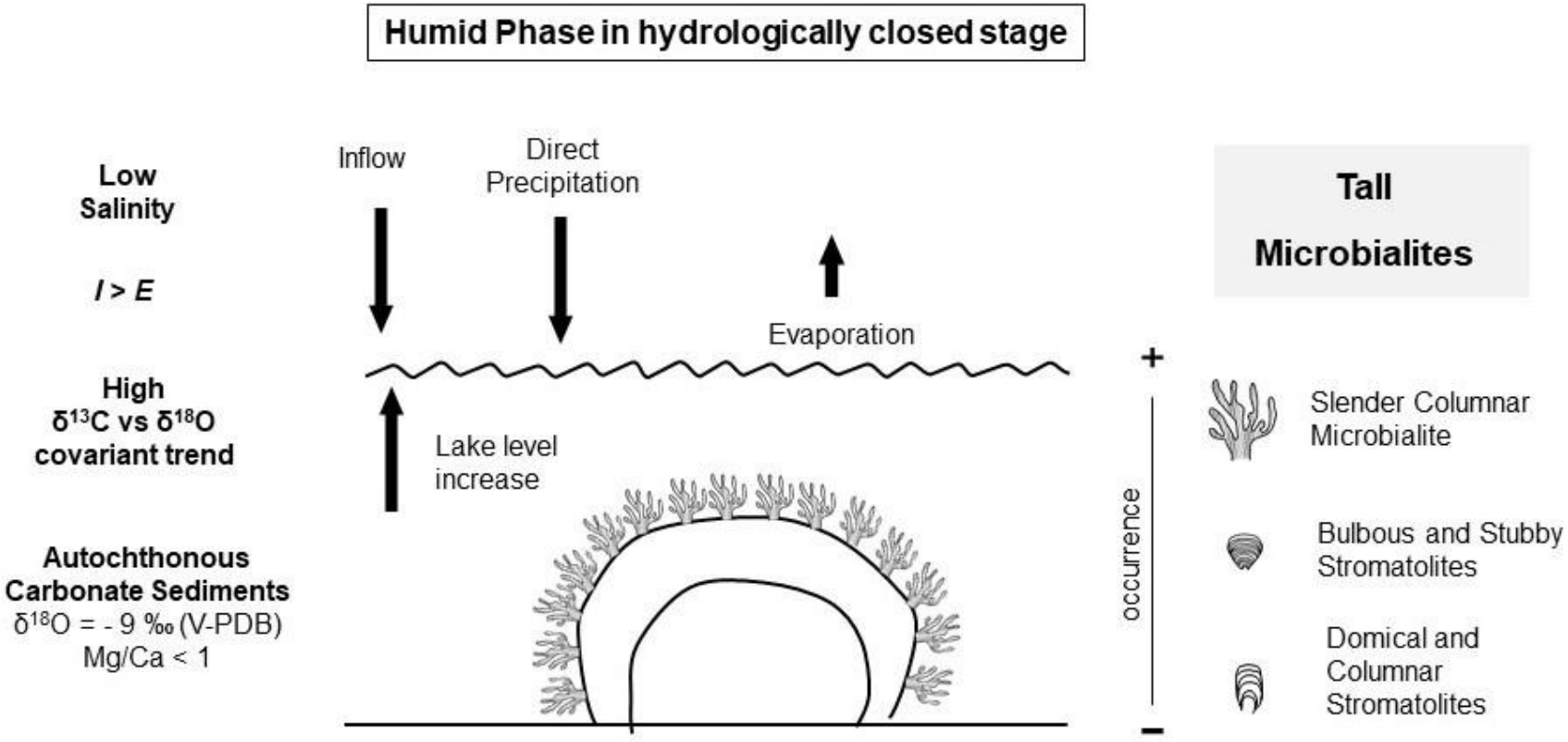

Figure 78. Tall microbialites association – controlled by the balanced-fill lake environmental conditions. Combined lithological (microbialite types), mineralogical and isotopic data support this interpretation.

4.6 Conclusions

Giant lacustrine stromatolites present a special case to understand chemical and physical lake-basin dynamics. Since they are much larger than most stromatolites, they record a longer period of continuous growth. The large stromatolites studied in the biostrome provide a high-resolution history of lake-level oscillation and are thus proxies for past regional climatic variations and can be integrated with regional or global patterns.

The layering patterns, chemical and isotope changes recorded in these large stromatolites, indicate successive changes in hydrological balances most likely in response to changing climatic conditions. The drainage might had varied, but the bioherms were formed in a closed basin, where water inflow could periodically fill the basin, but not always balanced by outflow. The instability of the lake level was mainly driven by climatic fluctuations.

Combined sedimentological, mineralogical and isotope results indicate that there were alternating arid and humid cycles that controlled the occurrence of different types of microbialites in the layers of the stromatolites. Arid phases (E > I) are inferred from δ18O positive excursions, high dolomite/calcite, and laminated and short microbialite association. δ18O negative excursions that were accompanied by an increase in calcium carbonate precipitation and tall microbialite association are interpreted to indicate positive hydrological balance (I+P > E) in a closed lake phase of the balanced-fill lake type. Slender Columnar Microbialites are characteristic of this stable lake environment.

4.7 Acknowledgments

We acknowledge Petrobras (Brazil) for support and funding this research. We are grateful to R. Biaggi, Alex Simms and Victor Schmidt for discussions, and assistance in the field. To Alex Simms for the GPR acquisition campaign and Julie Zurbuchen for all the support on GPR data processing. We are most grateful to the late H.P.Bucheim, whose experience in the Green River Formation greatly influenced this research. We thank S.C. Anjos, P. M. Magalhaes, and R.J. Jahnert for encouraging this project to take place.

5. References

Abell, P.I., Awramik, S.M., Osborne, R.H., and Tomellini, S., 1982. Plio-Pleistocene lacustrine stromatolites from Lake Turkana, Kenya: Morphology, stratigraphy and stable isotopes: Sedimentary Geology, v. 32, p. 1–26.

Adams, J.E. and Rhodes, M.L., 1960. Dolomitization by seepage refluxion. AAPG Bulletin, 44(12), pp.1912-1920.

Allwood, A. C., Burch, I. W., Rouchy, J. M., and Coleman, M. (2013). Morphological biosignatures in gypsum: Diverse formation processes of Messinian (~ 6.0 Ma) gypsum stromatolites. Astrobiology, 13(9), pp. 870-886.

Aloisi, G., Gloter, A., Kruger, M., Wallmann, K., Guyot, F. and Zuddas, P., 2006. Nucleation of calcium carbonate on bacterial nanoglobules. Geology, 34(12), pp.1017-1020.

Arenas, C., Casanova, J., and Pardo, G., 1997, Stable-isotope characterization of the Miocene lacustrine systems of Los Monegros (Ebro Basin, Spain): Palaeogeographic and palaeoclimatic implications: Palaeogeography, Palaeoclimatology, Palaeoecology, v. 128.

Armelenti, G., Goldberg, K., Kuchle, J., and De Ros, L. F. 2016. Deposition, diagenesis and reservoir potential of non-carbonate sedimentary rocks from the rift section of Campos Basin, Brazil. Petroleum Geoscience, 22(3), pp. 223-239.

Aswasereelert, W, Carroll, A.R., Feigl, K.L., Peters, S.E., Meyers, S.R., and Smith, M.E., 2013. Basin-scale cyclostratigraphy of the Green River Formation, Wyoming: GSA Bulletin, v. 125, pp. 216–228.

Awramik, S. M., and Buchheim, H. P., 2014. Microbialites in the Eocene Green River Formation, Sanpete Valley, Uinta Basin, Utah. In: Proceedings of the AAPG Annual Convention and Exhibition, Houston, TX, USA, pp. 6-9.

Awramik, S.M., and Buchheim, H.P., 2015, Giant stromatolites of the Eocene Green River Formation (Colorado, USA): Geology, v. 43, pp. 691–694.

Baddouh, M., Meyers, S.R., Carroll, A.R., Beard, B.L., and Johnson, C.M., 2016, Lacustrine 87Sr/86Sr as a tracer to reconstruct Milankovitch forcing of the Eocene hydrologic cycle: Earth and Planetary Science Letters, v. 448, pp. 62–68.

Bader, J.W., 2009, Structural and tectonic evolution of the Douglas Creek arch, the Douglas Creek fault zone, and environs, northwestern Colorado and northeastern Utah: Implications for petroleum accumulation in the Piceance and Uinta basins: Rocky Mountain Geology, v. 44, pp. 121–145.

Beerling, D. J., and Royer, D. L., 2011. Convergent cenozoic CO2 history. Nature Geoscience, 4(7), pp. 418-420.

Berelson, W. M., Corsetti, F. A., Pepe-Ranney, C., Hammond, D. E., Beaumont, W., and Spear, J. R., 2011. Hot spring siliceous stromatolites from Yellowstone National Park: assessing growth rate and laminae formation. Geobiology, 9(5), pp. 411-424.

Best, M.G., Barr, D.L., Christainsen, E.H., Gronme, C.S., Deino, A.L., and Tingey, D.G., 2009. The Great Basin alitplano during the Middle Cenozoic ignimbrite flareup: insights from volcanic rocks. Int. Geol. Rev., 51, pp. 580–633.

Bijl, P. K., Schouten, S., Sluijs, A., Reichart, G.-J., Zachos, J. C., and Brinkhuis, H., 2009. Early 596 Palaeogene temperature evolution of the southwest Pacific Ocean, Nature, 461, 776- 779.

Birgenheier, L., and Vanden Berg, M.D., 2011. Core-based integrated sedimentologic, stratigraphic, and geochemical analysis of the oil shale bearing Green River Formation, Uinta Basin, Utah, p. 30.

Birgenheier, L.P., Vanden Berg, M.V., Plink-Björklund, P., Gall, R.D., Rosencrans, E., Rosenberg, M.J., Toms, L.C. and Morris, J., 2020. Climate impact on fluvial-lake system evolution, Eocene Green River Formation, Uinta Basin, Utah, USA. GSA Bulletin, 132(3-4), pp. 562-587.

Blakey, R. C., and Ranney, W. D., 2017. Ancient landscapes of western North America: A geologic history with paleogeographic maps. Springer.

Boak, J., and Poole, S., 2015. Mineralogy of the Green River Formation in the Piceance Creek Basin, Colorado. In Smith, M.E. and Carroll, A.R., eds., Stratigraphy and Paleolimnology of the Green River Formation, Western USA, Dordrecht, Springer Netherlands, pp. 183–209.

Bohacs, K.M., Carroll, A.R., Neal, J.E., and Mankiewicz, P.J., 2000 Lake-Basin Type, Source Potential, and Hydrocarbon Character: an Integrated Sequence-Stratigraphic–Geochemical Framework, In: Gierlowski-Kordesch, E.H. and Kelts, K.R., eds., Lake Basins Through Space and Time, American Association of Petroleum Geologists, v. 46.

Bohacs, K.M., Carroll, A.R., and Neal, J.E., 2003. Lessons from large lake systems — Thresholds, nonlinearity, and strange attractors.

Bohaty, S.M. and Zachos, J.C., 2003. Significant Southern Ocean warming event in the late middle Eocene. Geology, 31(11), pp. 1017-1020.

Bone, Y. and James, N.P., 1997. Bryozoan stable isotope survey from the cool-water Lacepede Shelf, southern Australia. Special Publications of SEPM

Bontognali, T.R.R., Vasconcelos, C., Warthmann, R.J., Bernasconi, S.M., Dupraz, C., Strohmenger, C.J., and McKenzie, J.A., 2010. Dolomite formation within microbial mats in the coastal sabkha of Abu Dhabi (United Arab Emirates). Sedimentology, 57, pp. 824–844.

Bontognali, T.R., McKenzie, J.A., Warthmann, R.J. and Vasconcelos, C., 2014. Microbially influenced formation of Mg-calcite and Ca-dolomite in the presence of exopolymeric substances produced by sulphate-reducing bacteria. Terra Nova, 26(1), pp.72-77.

Bradley, W.H., 1929. The varves and climate of the Green River epoch. U.S. Geological Survey Professional Paper 158-E, pp. 872-110.

Bradley, W.H., 1930. The varves and climate of the Green River epoch: Professional Paper Report 158E.

Bradley, W.H., 1931 Origin and microfossils of the oil shale of the Green River formation of Colorado and Utah: Professional Paper Report 168.

Bradley W.H., 1964. Geology of the Green River Formation and associated Eocene rocks in southwestern Wyoming and adjacent parts of Colorado and Utah. U. S. Geol. Surv. Prof. Pap., 496-A, pp. 1 –71.

Bradley, W. H. and Eugster, H. P., 1969. Geochemistry and paleolimnology of the trona deposits and associated authigenic minerals of the Green River Formation of Wyoming (No. 496-B).

Bradley, W. and Fahey, J.J., 1962. Occurrence of stevensite in the Green River Formation of Wyoming. American Mineralogist: Journal of Earth and Planetary Materials, 47, pp. 996–998.

Brake, S. S., Hasiotis, S. T., Dannelly, H. K., and Connors, K. A., 2002. Eukaryotic stromatolite builders in acid mine drainage: Implications for Precambrian iron formations and oxygenation of the atmosphere? Geology, 30(7), pp. 599-602.

Bristow, T.F., Kennedy, M.J., Morrison, K.D., and Mrofka, D.D., 2012. The influence of authigenic clay formation on the mineralogy and stable isotopic record of lacustrine carbonates. Geochimica et Cosmochimica Acta, 90, pp. 64–82.

Brobst, D.A. and Tucker, J.D., 1973. X-ray mineralogy of the Parachute Creek Member, Green River Formation, in the northern Piceance Creek basin, Colorado (No. 803). US Govt. Print. Off.

Brown, Brindley, and Brindley, G.W., 1980. Crystal Structures of Clay Minerals and Their X-ray Identification. London: Mineralogical Society, Print. Monograph (Mineralogical Society (Great Britain)); No. 5

Buchheim, H.P. Surdam, R.C., 1977. Fossil catfish and the depositional environment of the Green River Formation, Wyoming. Geology, 5(4), pp. 196-198.

Buchheim, H P., 2014. f Inverted Indexes on the UNIX System, Bell Laboratories internal memorandum, Murray Hill, New Jersey (1978).

Bunevich, R.B., Borghi, L., Gabaglia, G.P., Terra, G.J., Freire, E B., Lykawka, R., and Fragoso, D.G., 2017. Microbialitos da Sequência Balbuena IV (Daniano), Bacia de Salta, Argentina: caracterização de intrabioarquiteturas e de microciclos. Pesquisas em Geociências, 44(2), pp. 177-202.

Buongiorno, J., Gomez, F.J., Fike, D.A., and Kah, L.C., 2018, Mineralized microbialites as archives of environmental evolution, Laguna Negra, Catamarca Province, Argentina: Geobiology

Burne, R.V. and Moore, L.S., 1987. Microbialites: Organosedimentary deposits of benthic microbial communities. Palaios 2, pp. 241–254

Burne, R.V. and Moore, L.S., 1993. Microatoll microbialites of Lake Clifton, Western Australia: Morphological analogues of Cryptozoön proliferum Hall, the first formally-named stromatolite. Facies, 29(1), pp.149-168.

Burne, R.V., Moore, L.S., Christy, A.G., Troitzsch, U., King, P.L., Carnerup, A.M., and Hamilton, P.J., 2014. Stevensite in the modern thrombolites of Lake Clifton, Western Australia: A missing link in microbialite mineralization? Geology, 42(7), pp. 575-578.

Butler, G.P., 1970. Holocene gypsum and anhydrite of the Abu Dhabi sabkha, Trucial Coast: an alternative explanation of origin. In: Third Symposium on Salt,Vol. 1, pp. 120-152. Cleveland, Ohio Northern Ohio Geological Society.

Calvo, J.P., Blanc-Valleron, M.M., Rodríguez-Aranda, J.P., Rouchy, J M., and Sanz, M. E., 1999. Authigenic clay minerals in continental evaporitic environments. Zaragoza. International Association of Sedimentologists Special Publications, v. 27, pp. 129-151.

Calvo, J.P. and Pozo, M., 2015 Geology of magnesian clays in sedimentary and non-sedimentary environments In Pozo, M. and Galan, E., eds., Magnesian Clays: Characterization, Origins and Applications, Association Internationale pour l'Etude des ´Argiles, Educational Series, 380 p.

Carminatti, M., Wolff, B., and Gamboa, L., 2008. New exploratory frontiers in Brazil. In: World Petroleum Congress 19, Spain. New Frontier Exploration. Forum 01.

Carramal, N.G., Oliveira, D.M., Cacela, A.S., Cuglieri, M.A., Rocha, N.P.Viana, S.M., Toledo, S.L., Pedrinha, S. and de Ros, L.F., 2022. Paleoenvironmental insights from the deposition and diagenesis of Aptian pre-salt magnesium silicates from the Lula Field, Santos Basin, Brazil. Journal of Sedimentary Research, 92(1), pp. 12-31.

Carroll, A.R. and Bohacs, K M., 1999. Stratigraphic classification of ancient lakes: Balancing tectonic and climatic controls. Geology, 27(2), pp. 99-102.

Carvalho, A.M.A., Hamon, Y., De Souza Jr, O.G., Carramal, N G., and Collard, N., 2022. Facies and diagenesis distribution in an Aptian pre-salt carbonate reservoir of the Santos Basin, offshore Brazil: A comprehensive quantitative approach. Marine and Petroleum Geology, 141.

Casanova, J., 1986. East African Rift stromatolites. Geological Society, London, Special Publications.

Casanova, J. and Thouin, C., 1990. Biosedimentologie des stromatolites du lac Tanganyika (Burundi); implications hydrologiques: Bulletin de la Société Géologique de France, v. VI, pp. 647–656.

Casanova, J., and Hillare-Marcel, C., 1993, Carbon and Oxygen Isotopes in African Lacustrine Stromatolites: Palaeohydrological Interpretation, in Climate Change in Continental Isotopic Records, American Geophysical Union (AGU), p. 123–133.

Cashion, W.B. and Donnell, J.R., 1972. Chart showing correlation of selected key units in the organic-rich sequence of the Green River Formation, Piceance Creek basin, Colorado, and Uinta Basin, Utah. Oil and Gas Investigation Chart Report 65.

Cashion, W.B. and Donnell, J.R., 197., Revision of nomenclature of the upper part of the Green River Formation, Piceance Creek Basin, Colorado, and eastern Uinta Basin, Utah: Bulletin Report 1394G.

Chamberlain, C.P., H. T. Mix, A. Mulch, M.T. Hren, M.L. Kent-Corson, S.J. Davis, T.W. Horton, and 2012., The Cenozoic climatic and topographic evolution of the western North American Cordillera, Am. J. Sci., 312, pp. 213–262.

Chase, C.G., Gregory-Wodzicki, K.M., Parrish, J.T., and Zachos, P.G., 1998. Topographic history of the western Cordillera of North America and controls on climate: Oxford Monographs on Geology and Geophysics, v. 39, pp. 73–99.

Chave, K.E., 1952. A solid solution between calcite and dolomite. Journal of Geology, 60(2), pp.190-192.

Cohen, A.S., 2003. Paleolimnology: the history and evolution of lake systems: Oxford University Press.

Cohen, A.S., Talbot, M.R., Awramik, S.M., Dettman, D.L., and Abell, P., 1997. Lake level and paleoenvironmental history of Lake Tanganyika, Africa, as inferred from late Holocene and modern stromatolites: Geological Society of America Bulletin, v. 109, pp. 444–460

Cole, R.D., 1985. Depositional environments of oil shale in the Green River Formation, Douglas Creek arch, Colorado and Utah, p. 17.

Cole, R.D., 1998. Possible Milankovitch cycles in the Lower Parachute Creek Member of Green River Formation (Eocene), North-Central Piceance Creek Basin, Colorado: an analysis

Cole, R.D. and Picard, M.D., 1978. Comparative mineralogy of nearshore and offshore lacustrine lithofacies, Parachute Creek Member of the Green River Formation, Piceance Creek Basin, Colorado, and eastern Uinta Basin, Utah. Geol Soc Am Bull 89, pp. 1441–1454.

Dalrymple, R.W., 2010. Interpreting Sedimentary Successions: Facies, Facies Analysis And Facies Models. In: James N.P., Dalrymple R.W. (Eds). Facies Models 4, 2nd Edn. Geological Association of Canada, St. John's, pp. 3–18.

Darragi, F. and Tardy, Y., 1987. Authigenic trioctahedral smectites controlling pH, alkalinity, silica and magnesium concentrations in alkaline lakes. Chemical Geology, 63, pp. 59–72.

Deocampo, D.M., 2015. Authigenic clay minerals in lacustrine mudstones. In: Geological Society of America Special Papers, Geological Society of America, 515, pp. 49–64.

DeCelles, P.G., 2004. Late Jurassic to Eocene evolution of the Cordilleran thrust belt and foreland basin system, western U.S.A. Am. J. Sci., 304, pp. 105–168.

De Wet, C B., Mora, C.I., Gore, P.W., Gierlowski-Kordesch, E.H., and Cucolo, S.J., 2002. Deposition and geochemistry of lacustrine and spring carbonates in Mesozoic rift basins, eastern North America. Special Publication -SEPM, 73, 309-326.

Dickinson, W.R., Klute, M.A., Hayes, M.J., Janecke, S.U., Lundin, E.R., McKITTRICK, M.A., and Olivares, M.D., 1988. Paleogeographic and paleotectonic setting of Laramide sedimentary basins in the central Rocky Mountain region: Geological Society of America Bulletin, v. 100, pp. 1023–1039.

Dickinson, W.R., 2004. Evolution of the North American Cordillera: Annual Review of Earth and Planetary Sciences, v. 32, pp. 13–44.

Doebbert, A.C., Carroll, A.R., Mulch, A., Chetel, L.M., and Chamberlain, C.P., 2010.Geomorphic controls on lacustrine isotopic compositions: Evidence from the Laney Member, Green River Formation, Wyoming. Geological Society of America Bulletin, v. 122, pp. 236–252.

Dupraz, C., Visscher, P.T., Baumgartner, L.K. and Reid, R.P., 2004. Microbe–mineral interactions: early carbonate precipitation in a hypersaline lake (Eleuthera Island, Bahamas). Sedimentology, 51(4), pp.745-765.

Dupraz, C., Reid, R.P., Braissant, O., Decho, A.W., Norman, R.S., and Visscher, P.T.,2009., Processes of carbonate precipitation in modern microbial mats. Earth-Science Reviews, 96, pp. 141–162.

Dyni, J.R. (1976) Trioctahedral Smectite in the Green River Formation, Duchesne County, Utah. USGS Professional Paper 967

Dyni, J.R., 1996. Sodium carbonate resources of the Green River Formation. US Geological Survey Open-file Report, 729, p.39

Eljalafi, A. ,2017. Lithofacies, diagenesis, and chemostratigraphy of the microbialite and marginal lacustrine carbonate units within the Green River Formation, eastern Uinta Basin, Colorado and Utah. Master Thesis. Colorado School of Mines. Department of Geology and Geological Engineering. pages?

Embry, A.F. and Klovan, J.E., 1971. A Late Devonian reef tract on northeastern Banks Island, NWT. Bull. Can. Pet. Geol. 19, pp. 730–781.

Esteban, M., Pray, L.C., 1983. Pisoids and Pisolite Facies (Permian), Guadalupe Mountains, New Mexico and West Texas. In Peryt, T., ed., Coated Grains, Springer-Verlag, New York, pp. 109-115.

Eugster, H.P. and Surdam, R.C., 1973. Depositional environment of the Green River Formation of Wyoming: A preliminary report. Geological Society of America Bulletin, 84(4), pp. 1115-1120.

Eugster, H.P. and Hardie, L.A., 1975. Sedimentation in an ancient playa-lake complex: the Wilkins Peak Member of the Green River Formation of Wyoming. Geological Society of America Bulletin, 86(3), pp. 319-334.

Eugster H.P. and Hardie LA., 1978. Saline lakes. In: Lerman A (ed), Lakes: Chemistry, Geology, and Physics. Springer, New York, pp 237–293

Fahey, J.J. and Rose, M.E., 1962. Saline Minerals of the Green River Formation: With a Section on X-Ray Powder Data for Saline Minerals of the Green River Formation. US Government Printing Office,

Faulk, N.R.,1948. The Green River Formation in the Manti-Spring City Area of Central Utah. Master of Science Thesis, The Ohio State University Libraries.

Fischer, A.G., and Roberts, L.T., 1991,. Cyclicity in the Green River Formation (Lacustrine Eocene) of Wyoming, p. 9

Flügel, E., 2010. Microfacies of Carbonate Rocks: Analysis, Interpretation and Application, 2nd ed. Springer-Verlag, Berlin Heidelberg.

Frantz, C.M., Petryshyn, V.A., Marenco, P.J., Tripati, A., Berelson, W.M., and Corsetti, F.A., 2014. Dramatic local environmental change during the Early Eocene Climatic Optimum detected using high resolution chemical analyses of Green River Formation stromatolites. Palaeogeography, Palaeoclimatology, Palaeoecology, 405, pp.1-15.

Fritz, P. and Smith, D.G.W., 1970. The isotopic composition of secondary dolomites. Geochimica et Cosmochimica Acta, 34(11), pp.1161-1173.

Galán, E., and Pozo, M. (2011). Palygorskite and sepiolite deposits in continental environments. Description, genetic patterns, and sedimentary settings. In: Developments in Clay Science, Vol. 3, pp. 125-173, Elsevier.

Gall, Q. and Hyde, R., 1989. Analcime in lake and lake-margin sediments of the Carboniferous Rocky Brook Formation, Western Newfoundland, Canada. Sedimentology, 36(5), pp.875-887.

Gall, R.D., Birgenheier, L.P., and Vanden Berg, M.D., 2017. Highly seasonal and perennial fluvial facies: Implications for climatic control on the Douglas Creek and Parachute Creek Members, Green River Formation, southeastern Uinta Basin, Utah, U.S.A.:Journal of Sedimentary Research, v. 87, pp. 1019–1047

Goldsmith, J.R., Graf, D.L., and Heard, H.C., 1961. Lattice constants of the calcium magnesium carbonates. Mineralogical Society of America.

Gomes, J.P., Bunevich, R.B., Tedeschi, L.R., Tucker, M.E., and Whitaker, F.F., 2020. Facies classification and patterns of lacustrine carbonate deposition of the Barra Velha Formation, Santos Basin, Brazilian pre-salt. Marine and Petroleum Geology, 113, 104176.

Gomez, F.J., Kah, L.C., Bartley, J.K., and Astini, R.A., 2014, Microbialites in a high-altitude Andean lake: Multiple Controls on Carbonate Precipitation and Lamina Accretion high Altitude Lacustrine Microbialites.PALAIOS, v. 29, pp. 233–249

Goodwin, J.H. and Surdam, R.C., 1967. Zeolitization of tuffaceous rocks of the Green River Formation, Wyoming. Science, 157(3786), pp.307-308.

Grey, K. and Awramik, S.,2020. Handbook for theSstudy and Description of Microbialites. Geological Survey of Western Australia Bulletin 147, 290 pp.

Guo, X. and Chafetz, H.S., 2012. Large tufa mounds, Searles Lake, California. Sedimentology, v. 59, pp. 1509–1535.

Haberyan, K.A. and Hecky, R.E., 1987. The late Pleistocene and Holocene stratigraphy and paleolimnology of Lakes Kivu and Tanganyika. Palaeogeography, Palaeoclimatology, Palaeoecology, v. 61, pp. 169–197.

Hay, R.L. and Sheppard, R.A., 2001. Occurrence of zeolites in sedimentary rocks: An overview. Reviews in Mineralogy and Geochemistry, 45(1), pp.217-234.

Hardy, R. and Tucker, M.E., 1988. Techniques in sedimentology. Blackwell Scientific Publications, 844, pp.191-228.

Harris, P., Diaz, M.R., and Eberli, G.P., 2019. The formation and distribution of modern ooids on Great Bahama Bank. Annual Review of Marine Science, 11, pp. 491-516.

Herlinger, R., Zambonato, E.E., and De Ros, L.F.,2017. Influence of diagenesis on the quality of Lower Cretaceous pre-salt lacustrine carbonate reservoirs from northern Campos Basin, offshore Brazil. Journal of Sedimentary Research, 87, pp. 1285–1313.

Hillaire-Marcel, C. and Casanova, J., 1987. Isotopic hydrology and paleohydrology of the Madagi (Kenya)-Natron (Tanzania) basin during the late Quaternary. Palaeogeography, Palaeoclimatology, Palaeoecology, v. 58, pp. 155–181.

Hicks, M., 2012. Microbialites from around Lake Turkana: Macro-, meso-, and microstructures, p. 44.

Hofmann, H.J., 1969. Attributes of stromatolites. Geological Survey of Canada, Paper 69–39, 58 p.

Horton, T.W., Defliese, W.F., Tripati, A.K., and Oze, C., 2016. Evaporation induced 18O and 13C enrichment in lake systems: A global perspective on hydrologic balance effects. Quaternary Science Reviews, 131, pp. 365-379.

Ingalls, M., Fetrow, A.C., Snell, K.E., Frantz, C.M., and Trower, E.J., 2022. Lake level controls the recurrence of giant stromatolite facies. Sedimentology, 69(4), pp. 1649-1674.

ICDD. PDF-2, Release 2013. Pennsylvania: International Centre for DiffractionDdata. 2013. CD-ROM.

Jackson, S.E., Pearson, N., J., Griffin, W.L., and Belousova, E.A., 2004. The application of laser ablation-inductively coupled plasma-mass spectrometry to in situ U–Pb zircon geochronology. Chemical Geology, 211(1-2), pp. 47-69.

Jagniecki, E.A., Lowenstein, T.K., Demicco, R.V., Baddouh, M.B., Carroll, A.R., Beard, B.L., and Johnson, C.M., 2021. Spring origin of Eocene carbonate mounds in the Green River Formation, Northern Bridger Basin, Wyoming, USA. Sedimentology, 68(6), pp. 2334-2364.

Jahnert, R.J. and Collins, L.B., 2012. Characteristics, distribution and morphogenesis of subtidal microbial systems in Shark Bay, Australia. Marine Geology, 303, pp.115-136.

Johnson, R.C., 1984. New names for units in the lower part of the Green River Formation, Piceance Creek basin, Colorado.

Johnson, R.C. and Finn, T.M., 1986. Early Cenozoic history of the Uinta and Piceance Creek Basins, Utah and Colorado, with special reference to the development of Eocene Lake Uinta. pp. 247–276

Johnson, R.C., Nichols, D.J., and Hanley, J.H., 1988. Stratigraphic sections of lower Tertiary strata and charts showing palynomorph and mollusk assemblages, Douglas Creek Arch area, Colorado and Utah. Miscellaneous Field Studies Map Report 1997.

Johnson, R.C. and Johnson, S.Y., 1991. Stratigraphic and time-stratigraphic cross sections of phanerozoic rocks along line B-B', Uinta and Piceance basin area, west-central Uinta basin, Utah to eastern Piceance basin, Colorado. IMAP Report 2184B,

Johnson, R.C., Mercier, T.J., Brownfield, M.E., Pantea, M.P., and Self, J.G., 2010. Oil shale and nahcolite resources of the Piceance Basin, Colorado. U.S. Dept. of the Interior, U.S. Geological Survey.

Johnson, R.C., Mercier, T.J., Ryder, R.T., and Self, J.G., 2011. Assessment of In-Place Oil Shale Resources of the Eocene Green River Formation, Greater Green River Basin, Wyoming, Colorado, and Utah: 68 p.

Johnson, R.C. and Brownfield, M.E., 2015. Development, evolution, and destruction of the saline mineral area of Eocene Lake Uinta, Piceance Basin, western Colorado (No. 2013-5176). Scientific Investigations Report, 76-76, 2 sheets. US Geological Survey.

Jones, B.F., 1986. Clay mineral diagenesis in lacustrine sediments. United States Geological Survey Bulletin, 1578, pp. 291–300.

Jones, B.F. and Weir ,1983. Clay Minerals of Lake Abert, an Alkaline, Saline Lake. Clays and Clay Minerals, 31, pp. 161–172.

Keighley, D., Flint, S., Howell, J., and Moscariello, A., 2003. Sequence Stratigraphy in Lacustrine Basins: A Model for Part of the Green River Formation (Eocene), Southwest Uinta Basin, Utah, U.S.A. Journal of Sedimentary Research, v. 73, pp. 987–1006.

Kelts, K., 1988, Environments of deposition of lacustrine petroleum source rocks: an introduction. Geological Society, London, Special Publications, v. 40, pp. 3–26.

Kennard, J.M., 1994. Thrombolites and stromatolites within shale-carbonate cycles, Middle-Late Cambrian Shannon Formation, Amadeus Basin, central Australia. In Phanerozoic Stromatolites II, J. Bertrand-Sarfati and C.L.V. Monty, eds., Kluwer Academic Publishers, Dordrecht, Netherlands, pp. 443–471.

Kylander-Clark, A.R., Hacker, B., and Cottle, J.M., 2013. Laser-ablation split-stream ICP petrochronology. Chemical Geology, 345, pp. 99-112.

Land, L.S., 1980. The Isotopic and Trace Element Geochemistry of Dolomite: The State of the Art. In: Zenger, D.H., Dunham, J.B., Ethington, R.L. Concepts and Models of Dolomitization. SEPM Society for Sedimentary Geology.

Lawton, T.F., 2008 Laramide Sedimentary Basis, in Miall, A.D. ed., Sedimentary Basins of the World, Chapter 12, Elsevier, v. 5p, p. 429–450.

Leng M.J. and Marshall, J.D., 2004. Palaeoclimate interpretation of stable isotope data from lake sediment archives. Quaternary Science Reviews, 23(7-8), pp. 811-31.

Lindsay, C.R. and Feeley, T.C., 2003. Magmagenesis at the Eocene Electric Peak–Sepulcher Mountain complex, Absaroka Volcanic Province, USA. Lithos, 67(1-2), pp. 53-76.

Lister, G.S., Kelts, K., Zao, C.K., Yu, J.-Q., and Niessen, F., 1991. Lake Qinghai, China: Closed-basin lake levels and the oxygen isotope record for ostracoda since the latest Pleistocene. Palaeogeography, Palaeoclimatology, Palaeoecology, 84, pp. 141–162.

Liu, Y., Hu, Z., Zong, K., Gao, C., Gao, S., Xu, J., and Chen, H., 2010. Reappraisement and refinement of zircon U-Pb isotope and trace element analyses by LA-ICP-MS. Chinese Science Bulletin, 55(15), pp. 1535-1546.

Lowenstein, T.K., Jagniecki, E.A., Carroll, A.R., Smith, M.E., Renaut, R.W., and Owen, R.B., 2017. The Green River salt mystery: What was the source of the hyperalkaline lake waters? Earth-Science Reviews, 173, pp. 295-306.

Machel, H.G., 2004. Concepts and models of dolomitization: A critical reappraisal: Geological Society, London, Special Publications, 235, pp. 7–63.

Machlus, M., Hemming, S.R., Olsen, P.E., and Christie-Blick, N., 2004. Eocene calibration of geomagnetic polarity time scale reevaluated: Evidence from the Green River Formation of Wyoming. Geology,. 32, p. 137.

Machlus, M.L., Olsen, P.E., Christie-Blick, N., and Hemming, S.R., 2008. Spectral analysis of the lower Eocene Wilkins Peak Member, Green River Formation, Wyoming: Support for Milankovitch cyclicity. Earth and Planetary Science Letters, 268, pp. 64–75.

McKenzie, J.A., 1981. Holocene dolomitization of calcium carbonate sediments from the coastal sabkhas of Abu Dhabi, UAE: a stable isotope study. Journal of Geology, 89(2), pp. 185-198.

MDI, 2015. Jade 9, versão 9.6. Livermore: Materials Data, 2015. CD-ROM.

Mederos, S., Bankey, V., and Tikoff, B., 2005. Geometry, timing, and continuity of the Rock Springs uplift, Wyoming, and Douglas Creek arch, Colorado: Implications for uplift mechanisms in the Rocky Mountain foreland, U.S.A. Rocky Mountain Geology, 40, pp. 167–191.

Meyers, S.R., 2008 Resolving Milankovitchian controversies: The Triassic Latemar Limestone and the Eocene Green River Formation: Geology, 36, p. 319.

Miller, T.S., Crockett, F.J., and Hollis, S.H., 1992. Wyoming Oil and Gas Fields Symposium, Greater Green River Basin and Overthrust Belt.

Moncure, G., and Surdam, R.C., 1980, Depositional environment of the Green River Formation in the vicinity of the Douglas Creek Arch, Colorado and Utah. Rocky Mountain Geology, 19, pp. 9–24.

Netto, P.R.A., Pozo, M., da Silva, M.D., Mexias, A S., Gomes, M.E.B., Borghi, L., and Rios-Netto, A.M., 2022. Authigenic Mg-clay assemblages in the Barra Velha Formation (Upper Cretaceous) from Santos Basin (Brazil): The role of syngenetic and diagenetic process. Applied Clay Science, 216, 106339.

Norris, R.D., Jones, L.S., Corfield, R.M., and Cartlidge, J.E., 1996. Skiing in the Eocene Uinta Mountains? Isotopic evidence in the Green River Formation for snow melt and large mountains. Geology, 24(5), pp. 403-406.

Norris, R.D., Corfield, R.M., and Hayes-Baker, K., 2000. Mountains and Eocene climate. In Huber, B.T., Macleod, K.G., and Wing, S.L.E., eds., Warm Climates in Earth History, Cambridge University Press, New York, pp. 161–196.

Parizek-Silva, Y. M., 2019. Métodos avançados para caracterização de mineralogia, porosidade e de parâmetros petrofísicos em reservatórios carbonáticos. MSc Thesis, Universidade Federal do Rio de Janeiro/Museu Nacional, Rio de Janeiro, RJ, Brazil.

Paton, C., Hellstrom, J., Paul, B., Woodhead, J., and Hergt, J., 2011. Iolite: Freeware for the visualisation and processing of mass spectrometric data. Journal of Analytical Atomic Spectrometry, 26(12), pp. 2508-2518.

Peryt, T., 1983. Coated Grain.: Springer-Verlag, New York, 655 p.

Petrash, D.A., Bialik, O.M., Bontognali, T.R., Vasconcelos, C., Roberts, J.A., McKenzie, J.A. and Konhauser, K.O., 2017. Microbially catalyzed dolomite formation: from near-surface to burial. Earth-Science Reviews, 171, pp. 558-582.

Petryshyn, V.A., Corsetti, F.A., Berelson, W.M., Beaumont, W., and Lund, S.P., 2012, Stromatolite lamination frequency, Walker Lake, Nevada: Implications for stromatolites as biosignatures. Geology, 40, pp. 499–502. doi:10.1130/G32675.1.

Picard, M.D., and High, L.R., 1968. Sedimentary cycles in the Green River Formation (Eocene), Uinta Basin, Utah. Journal of Sedimentary Research, 38, pp. 378–383.

Pietras, J.T., Carroll, A.R., Singer, B.S., and Smith, M.E., 2003. 10 k.y. depositional cyclicity in the early Eocene: Stratigraphic and 40Ar/39Ar evidence from the lacustrine Green River Formation: Geology, 31, pp. 593–596

Pitman, J.K., 1996. Origin of primary and diagenetic carbonates in the lacustrine Green River Formation (Eocene), Colorado and Utah (Vol. 2157). US Government Printing Office.

Planavsky, N., Rouxel, O., Bekker, A., Shapiro, R., Fralick, P., and Knudsen, A., 2009. Iron-oxidizing microbial ecosystems thrived in late Paleoproterozoic redox-stratified oceans. Earth and Planetary Science Letters, 286(1-2), pp. 230-242.

Poole, S., 2014. Quantitative mineralogy and distributions of minerals of the Green River Formation, Piceance Creek Basin, western Colorado. MSc Thesis, Colorado School of Mines, Golden CO.

Pozo, M. and Calvo, J.P., 2018. An overview of authigenic magnesian clays. Minerals, 8(11), 520.

Ramnani, C.W., Santos, J.F., Parizek-Silva, Y., Madrucci, V., Araújo, C.C., Vasquez, G.F., Morschbacher, M.J., Bonzanini, L.A.F, Viana, S.M., Souza, R.S, Alves, D.B., Anjos, S.M.C., 2021. Magnesian Clay Minerals in Brazilian Pre-salt Province. In adapted from extended abstract at 2021 SEG AAPG Image International meeting for applied geoscience & energy, Denver, Colorado.

Reading, H.G.and Levell, B.K., 1996. Controls on the sedimentary rock record. In Sedimentary Environments: Processes, Facies and Stratigraphy, Reading, H.G. (ed.), Wiley, pp. 5-35.

Reid, R.P., Visscher, P.T., Decho, A.W., Stolz, J.F., Bebout, B.M., Dupraz, C., Macintyre, I.G., Paerl, H.W., Pinckney, J.L., Prufert-Bebout, L., Steppe, T.F., DesMarais, D.J., 2000. The role of microbes in accretion, lamination and early lithification of modern marine stromatolites. Nature, 406, pp. 989–992.

Remy, R.R., 1992. Stratigraphy of the Eocene part of the Green River Formation in the south-central part of the Uinta Basin, Utah.

Remy, R.R. and Ferrell, R.E., 1989. Distribution and origin of analcime in marginal lacustrine mudstones of the Green River Formation, south-central Uinta Basin, Utah. Clays and Clay minerals, 37(5), pp. 419-432.

Renault R.W. and Gierlowisk- Kordesch E. 2010. Lakes. In: James N.P., Dalrymple R.W. (eds.) Facies models 4. Geological Association of Canada, pp. 541-577.

Reynolds, R.C. Jr., 1985. NEWMOD, a computer program for the calculation of basal diffraction intensities of mixed layer clay minerals. Reynolds, R.C., Ed. 8 Brook Rd., Hanover, New Hampshire 03755, USA.

Renault R.W. and Gierlowisk- Kordesch E., 2010. Lakes. In: James N.P., Dalrymple R.W. (eds.) Facies models 4. Geological Association of Canada, pp. 541-577.

Renaut, R.W., Tiercelin, J.J., and Owen, R.B., 1986. Mineral precipitation and diagenesis in the sediments of the Lake Bogoria basin, Kenya Rift Valley. Geological Society, London, Special Publications, 25, pp. 159–175.

Ricketts, L., 2015. Sedimentology of the Douglas Pass section of the lower Eocene Green River Formation, Piceance Creek Basin; implications for lake levels in ancient Lake Uinta [PhD Thesis]

Rietveld, H.M., 1969. A profile refinement method for nuclear and magnetic structures. Journal of Applied Crystallography, 2, pp. 65–71.

Roehler H.W., 1992. Correlation, composition, areal distribution, and thickness of Eocene stratigraphic units, greater Green River basin, Wyoming, Utah, and Colorado. U.S. Geological Survey Professional Paper, 1506-E, 49 p.

Roehler, H.W., 1993. Eocene climates, depositional environments, and geography, greater Green River Basin, Wyoming, Utah, and Colorado. U. S. Geological Survey, Professional Paper, 1506-F.

Rossi, C., Lozano, R. P., Isanta, N., and Hellstrom, J., 2010. Manganese stromatolites in caves: el Soplao (Cantabria, Spain). Geology, 38(12), pp. 1119-1122.

Rosencrans, E.M., 2015. Stratigraphic architecture of deltaic mouth bar deposits during the early Eocene Climatic Optimum, Green River Formation, Uinta Basin, Utah. MSc Thesis, University of Utah, Salt Lake City, UT, United States.

Rosenberg, M.J., 2013. Facies, stratigraphic architecture, and lake evolution of the oil shale bearing Green River Formation, eastern Uinta Basin, Utah. PhD Thesis, 152 p.

Rueda Chaparro, F., 2018. Dolomitization in the Uteland Butte Member of the Eocene Green River Formation, Uinta Basin, Utah.

Sarg, J.F., Tänavsuu-Milkeviciene, K. and Humphrey, J.D., 2013. Lithofacies, stable isotopic composition, and stratigraphic evolution of microbial and associated carbonates, Green River Formation (Eocene), Piceance Basin, Colorado. AAPG bulletin, 97(11), pp.1937-1966.

Schieber, J., Bose, P.K., Eriksson, P.G., Banerjee, S., Sarkar, S., Altermann, W., and Catuneanu, O. (Eds.), 2007. Atlas of microbial mat features preserved within the siliciclastic rock record. Elsevier.

Sheliga, C.M., 1980. Sedimentology of the Eocene Green River Formation in Sevier and Sanpete Counties, central Utah. MScThesis, The Ohio State University.

Silva, M.D., Gomes, M.E.B., Mexias, A.S., Pozo, M., Drago, S.M., Célia, R.S., Silva, L.A.C., Netto, P., Gomes, L.B., Porcher, C.C. and Dani, N., 2021. Mineralogical study of levels with magnesian clay minerals in the Santos Basin, Aptian pre-salt Brazil. Minerals, 11(9), pp. 970

Sibley, D.F. and Gregg, J.M., 1987. Classification of dolomite rock textures. Journal of Sedimentary Research, 57(6), pp.967-975.

Sláma, J., Košler, J., Condon, D.J., Crowley, J.L., Gerdes, A., Hanchar, J.M., Horstwood, M.S., Morris, G.A., Nasdala, L., Norberg, N., Schaltegger, U., Schoene, B., Tubrett, M.N., and Whitehouse, M.J., 2008. Plešovice zircon—a new natural reference material for U–Pb and Hf isotopic microanalysis. Chemical Geology, 249(1-2), pp. 1-35.

Smith, M.E. and Carroll, A.R., 2015. Introduction to the Green River Formation,.In Smith, M.E. and Carroll, A.R., eds., Stratigraphy and Paleolimnology of the Green River Formation, Western USA, Dordrecht, Springer Netherlands, pp. 1–12.

Smith J.W. andRobb, W.A., 1966. Ankerite in the Green River Formation's Mahogany zone. Journal of Sediment Petrol 36(2), pp.486–490.

Smith, M.E., Singer, B., and Carroll, A., 2003. 40Ar/39Ar geochronology of the Eocene Green River Formation, Wyoming. Geological Society of America Bulletin, p. 17.

Smith, M.E., Carroll, A.R., Scott, J.J., and Singer, B.S., 2014. Early Eocene carbon isotope excursions and landscape destabilization at eccentricity minima: Green River Formation of Wyoming. Earth and Planetary Science Letters, 403, pp. 393–406.

Smith, M.E., Carroll, A.R., and Singer, B.S., 2008. Synoptic reconstruction of a major ancient lake system: Eocene Green River Formation, western United States. Geological Society of America Bulletin, 120, pp. 54–84.

Smith, M.E., Chamberlain, K.R., Carroll, A.R., and Singer, B.S., 2010. Eocene clocks agree: Coeval 40Ar/39Ar, U-Pb, and astronomical ages from the Green River Formation. Geology, 38, pp. 527–530.

Smoot, J.P., 1983. Depositional subenvironments in an arid closed basin; the Wilkins Peak Member of the Green River Formation (Eocene), Wyoming, USA. Sedimentology, 30(6), pp. 801-827.

Sprinkel, D.A., 2018. Interim Geologic Map of the Duchesne 30' x 60' Quadrangle, Duchesne and Wasatch Counties, Utah. Utah Geological Survey Open-File Report OFR-689.

Straccia, F.G., Wilkinson, B.H., and Smith, G.R., 1990. Miocene lacustrine algal reefs—southwestern Snake River Plain, Idaho. Sedimentary Geology, 67, pp. 7–23.

Surdam, R.C. and Parker, R.D., 1972. Authigenic aluminosilicate minerals in the tuffaceous rocks of the Green River Formation, Wyoming. Geological Society of America Bulletin, 83(3), pp.689-700.

Surdam, R.C. and Sheppard, R.A., 1978. Zeolites in saline, alkaline-lake deposits: Natural zeolites: Occurrence, properties, use, 145, pp. 145–174.

Surdam R.C. Stanley K.O., 1979. Lacustrine sedimentation during the culminating phase of Eocene Lake Gosiute, Wyoming (Green River Formation). Geological Society of America Bulletin, 90, pp. 93–110.

Surdam R.C. and Stanley K.O., 1980. Effects of changes in drainage-basin boundaries on sedimentation in Eocene Lakes Gosiute and Uinta of Wyoming, Utah, and Colorado. Geology, 8, pp. 135–139.

Surdam, R. C., and Wolfbauer, C. A., 1975. Green River Formation, Wyoming: A playa-lake complex. Geological Society of America Bulletin, 86(3), pp. 335-345.

Swierenga, M., 2014. Depositional history and lateral variability of microbial carbonates, Three Mile Canyon and Evacuation Creek, eastern Uinta basin, Utah. MSc Thesis, Colorado School of Mines

Symcox, C., 2015. Facies, stratigraphy, and mineralogy of the carbonate marker and D marker units, Lower Green River Formation, Uinta Basin, Utah. Colorado School of Mines.

Talbot, M.R., 1990. A review of the palaeohydrological interpretation of carbon and oxygen isotopic ratios in primary lacustrine carbonates. Chemical Geology, Isotope Geoscience Section, 80, pp. 261–279.

Talbot, M.R. and Allen, P.A., 1996. Lakes. In: Reading, H. (ed.), Sedimentary Environments: Processes, Facies, and Stratigraphy. Blackwell Science, Oxford, pp. 83–124.

Tänavsuu-Milkeviciene, K., and Sarg, J.F., 2012. Evolution of an organic-rich lake basin - stratigraphy, climate, and tectonics: Piceance Creek basin, Eocene Green River Formation: Evolution of an organic-rich lake. Sedimentology, 59, pp. 1735–1768.

Tänavsuu-Milkeviciene, K., Sarg, J.F., and Bartov, Y., 2017. Depositional Cycles and Sequences In An Organic-Rich Lake Basin: Eocene Green River Formation, Lake Uinta, Colorado and Utah, U.S.A.Journal of Sedimentary Research, 87, pp. 210–229.

Tank, R.W., 1972. Clay minerals of the Green River Formation (Eocene) of Wyoming. Clay Minerals, 9, pp. 297–308.

Tettenhorst, R. and Moore, G E., 1978. Stevensite oolites from the Green River Formation of central Utah. Journal of Sedimentary Research, 48(2), pp. 587-594.

Thrasher, B.L, and Sloan, L.C., 2009. Carbon dioxide and the early Eocene climate of western North America. Geology, 37(9), pp. 807-810.

Tosca, N.J. and Masterson, A.L,. 2014. Chemical controls on incipient Mg-silicate crystallization at 25°C: Implications for early and late diagenesis. Clay Minerals, 49, pp. 165–194.

Tosca, N.J. and Wright, V.P., 2014. The formation and diagenesis of Mg-clay minerals in lacustrine carbonate reservoirs. In Adapted from oral presentation given at 2014 AAPG Annual Convention and Exhibition, Houston, Texas.

Tosca, N.J. and Wright, V.P., 2018. Diagenetic pathways linked to labile Mg-clays in lacustrine carbonate reservoirs: a model for the origin of secondary porosity in the Cretaceous pre-salt Barra Velha Formation, offshore Brazil. Geological Society, London, Special Publications, 435, pp. 33–46.

Thiry, M. 1974. Technique de préparation des mineraux argileux en vue de l'ánalyse aux rayons X. Centre de Sédimentologie et Géochimie de la Surface, Strasbourg, 25p

Van Lith, Y., Warthmann, R., Vasconcelos, C. and McKenzie, J.A., 2003. Microbial fossilization in carbonate sediments: A result of the bacterial surface involvement in dolomite precipitation. Sedimentology, 50(2), pp.237-245.

Vanden Berg, M.D. and Birgenheier, L.P., 2017. An examination of the hypersaline phases of Eocene Lake Uinta, upper Green River Formation, Uinta Basin, Utah. Journal of Paleolimnology, 58(3), 353

Vasconcelos, C. and McKenzie, J.A., 1997. Microbial mediation of modern dolomite precipitation and diagenesis under anoxic conditions (Lagoa Vermelha, Rio de Janeiro, Brazil). Journal of Sedimentary Research, 67(3), pp. 378-390.

Vasconcelos, C., McKenzie, J.A., Warthmann, R., and Bernasconi, S.M., 2005. Calibration of the δ18O paleothermometer for dolomite precipitated in microbial cultures and natural environments. Geology, 33(4), pp.317-320.

Walker, R.G., 1992. Facies, facies models and modern stratigraphic concepts. Facies models response to sea-level change, pp.1-14.

Walker, R.G., 2006. Facies models revisited: Introduction. Special Publication-SEPM, 84, p.1.

Walters, L.J., Jr., Claypool, G.E., and Choquette, P.W., 1972. Reaction rates and ^{18}O variation for the carbonate-phosphoric acid preparation method. Geochimica et Cosmochimica Acta, 36, pp. 129-140

Warthmann, R., Van Lith, Y., Vasconcelos, C., McKenzie, J.A. and Karpoff, A.M., 2000. Bacterially induced dolomite precipitation in anoxic culture experiments. Geology, 28(12), pp. 1091-1094.

Warren, J. K., 2006. Evaporites: Sediments, Resources, and Hydrocarbons. Springer Science & Business Media.

Whiteside, J.H. and Van Keuren, M.A., 2009. Multiproxy environmental characterization of lake level cycles in the Green River Formation of Utah and Colorado.

Wiedenbeck, M.A.P.C., Alle, P., Corfu, F.Y., Griffin, W.L., Meier, M., Oberli, F.V., Quadt, A.V., Roddick, J.C., and Spiegel, W., 1995) Three natural zircon standards for U-Th-Pb, Lu-Hf, trace element and REE analyses. Geostandards Newsletter, 19(1), pp. 1-23.

Wilf, P., 2000. Late Paleocene–early Eocene climate changes in southwestern Wyoming: Paleobotanical analysis. Geological Society of America Bulletin, 112(2), pp. 292-307.

Wright, P. V. (1992) A revised classification of limestones. Sedimentary Geology, 76, 177–185.

Wright, D.T., 1999. The role of sulphate-reducing bacteria and cyanobacteria in dolomite formation in distal ephemeral lakes of the Coorong region, South Australia. Sedimentary Geology, 126(1-4), pp.147-157

Yonkee, W.A. and Weil A.B., 2015. Tectonic transect of the Sevier and Laramide belts, North American Cordillera: Evolution of a complex orogenic system. Earth Sci. Rev., 150, pp. 531– 593.

Young, R.A., 1995. The Rietveld method. International Union of Crystallography, Oxford University Press, Oxford,

Zachos, J.C., Dickens, G.R., and Zeebe, R.E., 2008. An early Cenozoic perspective on greenhouse warming and carbon-cycle dynamics. Nature, 451, pp. 279–283.

Zachos, J., Pagani, M., Sloan, L., Thomas, E., and Billups, K., 2001. Trends, rhythms, and aberrations in global climate 65 Ma to present. Science, 292(5517), pp. 686-693.